

**SIMULATION OF THE HEATER TEST ROOM
DEFINED BY EN 442 STANDARD AND VIRTUAL
TESTING OF DIFFERENT TYPE OF HEATERS**

**A Thesis Submitted to
the Graduate School of Engineering and Sciences of
İzmir Institute of Technology
in Partial Fulfillment of the Requirements for the Degree of**

**DOCTOR OF PHILOSOPHY
in Mechanical Engineering**

**by
Abdullah Berkan ERDOĞMUŞ**

January 2011

İZMİR

We approve the thesis of **Abdullah Berkan ERDOĞMUŞ**

Prof. Dr. Zafer İLKEN

Supervisor

Prof. Dr. Barış ÖZERDEM

Co-Supervisor

Assoc. Prof. Dr. Selahattin YILMAZ

Committee Member

Assoc. Prof. Dr. Moghtada MOBEDİ

Committee Member

Assist. Prof.Dr. Hüseyin GÜNERHAN

Committee Member

Assist. Prof. Dr. Ünver ÖZKOL

Committee Member

07 January 2011

Prof. Dr. Metin TANOĞLU

Head of the Department of
Mechanical Engineering

Prof. Dr. Durmuş Ali DEMİR

Dean of the Graduate School of
Engineering and Sciences

ACKNOWLEDGMENTS

First of all, I would like to express my sincere gratitude and deepest respect to my supervisor Prof. Dr. Zafer İLKEN for his support throughout PhD program. Working under the supervision of Prof. Dr. Zafer İLKEN is a great honor for me. I am heartily thankful to my co-supervisor, Prof. Dr. Barış ÖZERDEM, whose constant encouragement; friendly personality enabled me to complete this study. He gave me invaluable recommendations throughout my academic studies.

I would like to thank Assoc. Prof. Dr. Moghtada MOBEDİ for giving insightful feedback to improve the contents of this study. He helped me to understand fundamental concepts and shows me applying different approaches to accomplish a research problem. I would like to thank Assoc. Prof. Dr. Selahattin YILMAZ for giving valuable recommendations. His constructive comments led to substantial improvements of the study. I would like to thank thesis committee members. Their suggestions helped me to clarify my ideas and strengthen my research.

It is my great pleasure to thank the management board of ELBA Inc. for permission to use radiator test room and collaboration. Their supports to scientific works are admirable. I am extremely thankful to Okan EROĞLU, the production manager of ELBA Inc., and Serdar ELÇE. Their endless supports were unforgettable. I would like to show my gratitude to Cihan ŞAHİN and Ümit AYANDIN. Their experiences shortened the test period and accelerate this study.

I would like to thank İhsan ÖZSOY, Dr. Ali M. ÇOLAKOĞLU, and Birol ERENTURK for giving a chance to deal with related problems in ASELSAN Inc. Researches increased my experiences in computational heat transfer and fluid dynamics applications. It is a pleasure to thank my colleagues Erkin GEZGİN, A. Cem GÖZÜKARA, Mustafa OCAK, A. Levent AVŞAR and Murat ŞAHİN for understanding and contributions in various stages of this study. I would like to express my gratitude to my other colleagues working in MGEO Division of ASELSAN Inc., sincere and scientific atmosphere and their motivations increased my concentration. I am also grateful to Emre OZTURK and ANOVA Company for giving supports whenever I required.

Finally, I would like to thank my family for their endless and complimentary support especially in distressful times.

ABSTRACT

SIMULATION OF THE HEATER TEST ROOM DEFINED BY EN 442 STANDARD AND VIRTUAL TESTING OF DIFFERENT TYPE OF HEATERS

Heat outputs of radiators are determined experimentally in specific conditions. Many standards have been developed to identify test conditions. EN442 standard specifies test room properties, temperature measurements and heat output calculations for radiators. In this study, the heat dissipation capabilities of three different panel radiators were determined by using numerical methods. The height and length of the tested radiators were 600 mm and 1000 mm, respectively. An experimental study was conducted in the standard test room in order to determine boundary conditions for computational study and verify numerical results. Tests were carried out in three different operating conditions. Twelve measurements were performed in each condition when test room reached steady state. Turbulent typed air flow in the test room and water flow inside the tested radiators were simulated. Temperature and velocity contours in virtual test room are also investigated in this study. Non uniform temperature distribution on the front surface of tested radiators was observed. It is seen that the symmetricity in velocity contours is distorted by using more complex radiator models and increasing excess temperature. The difference between experimental and computational heat output fluctuates between 0.4% and 13.6% for the simplest model, 3.4% and 11.1% for the second radiator, 4.5% and 12.9% for most complicated model investigated in this study. Good results are obtained for the excess temperature of 50°C and 60°C. For the lowest excess temperature, results are also in acceptable range. The study shows that computational methods can be applicable in the design of new heater types.

ÖZET

EN 442 STANDARDI İLE TANIMLANMIŞ ISITICI TEST ODASININ SİMULASYONU VE DEĞİŞİK TİPTEKİ ISITICILARIN SANAL TESTLERİ

Radyatörlerin ısı yayma kapasiteleri belirli koşullar için deneysel çalışmalar ile belirlenir. Test koşullarını belirlemek için birçok standart geliştirilmiştir. EN 442 standardı ile radyatörler için test odasının özellikleri, sıcaklık ölçümleri ve ısı yayma kapasitelerini hesaplanma detayları tanımlanmıştır. Test edilen radyatörlerin yükseklik ve uzunlukları sırayla 600 mm ve 1000 mm dir. Bu çalışmada üç farklı panel radyatörün ısı yayma kapasitesi sayısal yollarla hesaplanmıştır. Nümerik çalışmada kullanılacak sınır şartlarını belirlemek ve nümerik yollarla elde edilen sonuçları doğrulamak için deneysel bir çalışma gerçekleştirilmiştir. Testler üç farklı aşırı sıcaklık çalışma şartına dayanarak yapılmıştır. Her bir aşırı sıcaklık testi için kararlı hal durumuna erişildiğinde oniki sıcaklık ölçümü yapılmıştır. Türbülanslı hava akışı ve radyatör içindeki suyun akışı birlikte simüle edilmiştir. Bu çalışmada aynı zamanda test odası içindeki sıcaklık ve hız dağılımları da incelenmiştir. Test edilen radyatör yüzeylerindeki sıcaklığın her bölgede aynı olmadığı gözlenmiştir. Karmaşık radyatör modellerinde ve yüksek aşırı sıcaklıklarda çizdirilen hız eğrilerinin radyatör eksenine simetrikliklerinin bozulduğu görülmüştür. Deneysel ve nümerik yollarla hesaplanan ısı yayma kapasiteleri arasındaki farkın radyatör I için %0.4 ile %13.6 arasında, radyatör II için %3.4 ile %11.1 arasında, radyatör III için %4.5 ile %12.9 değiştiği bulunmuştur. 50°C ve 60°C aşırı sıcaklıklar için nümerik yollarla elde edilen sonuçların oldukça iyi, 30°C aşırı sıcaklıkta ise kabul edilebilir bir aralıkta olduğu değerlendirilmiştir. Bu çalışma yeni ısıtıcı tiplerinin geliştirilmesinde sayısal metotların kullanımının uygulanabilir olduğunu göstermektedir.

TABLE OF CONTENTS

LIST OF FIGURES	x
LIST OF TABLES	xiv
LIST OF SYMBOLS	xvii
CHAPTER 1. INTRODUCTION	1
1.1. Central Heating	1
1.2. Heating Devices in Central Heating Systems	2
1.3. Types of Radiators	3
1.3.1. Stainless Steel Radiators	4
1.3.1.1. Panel Radiators	6
1.3.1.1.1. Single Panel Radiators	7
1.3.1.1.2. Double Panel Radiators	7
1.3.1.1.3. Panel Radiators with Extended Surfaces	8
1.4. Heat Transfer from Radiators	9
1.5. Heat Requirement of Buildings	10
1.6. Heat Output of Radiators	10
1.7. Unique Contribution and Parts of the Study	12
CHAPTER 2. THEORY	14
2.1. Convective Heat Transfer	14
2.2. Radiative Heat Transfer	17
2.3. Flow Types and Properties	18
2.4. Governing Equations	19
2.4.1. Continuity Equation	20
2.4.2. Momentum Equations	20
2.4.3. Energy Equation	22
2.5. Boussinesq Approximation	23
2.6. Turbulent Flows	24
2.6.1. Continuity Equation for Turbulent Flows	25

2.6.2. Reynolds Average Navier Stokes Equations	25
2.7. Boussinesq Hypothesis	27
2.8. Turbulence Modeling.....	27
2.8.1. Two Equation Turbulence Models.....	28
2.8.1.1. The k- ϵ Turbulence Model.....	28
2.8.1.1.1. Standard k- ϵ Turbulence Model.....	29
2.8.1.1.2. Realizable k- ϵ Turbulence Model.....	30
2.8.2. Energy Equation in the k- ϵ Models.....	32
2.9. Modeling Near Wall Regions	32
2.10. Radiative Transfer Equation	35
2.10.1. The Discrete Ordinates Radiation Model	37
2.11. Basics of Computational Fluid Dynamics	37
2.11.1. Geometry Preparation	38
2.11.2. Mesh Generation.....	39
2.11.3. Selection of Numerical Method	41
2.11.3.1. Finite Difference Method.....	42
2.11.3.2. Finite Volume Method.....	44
2.11.4. Identification of Flow Conditions and Properties.....	46
2.11.5. Defining Initial and Boundary Conditions.....	47
2.11.6. Solver Selection	49
2.11.7. Selection of Numerical Scheme.....	54
2.11.8. Under-Relaxation Factor Settings.....	56
2.11.9. Termination Criteria and Convergence.....	57
2.11.10. CFD Errors.....	59
2.11.11. Post-Processing	59

CHAPTER 3. STANDARDS ON DETERMINATION OF RADIATORS HEAT

OUTPUT	60
3.1. Previous Standards.....	60
3.2. European Standard EN 442 Part 2	60
3.2.1. The Characteristics of Heater Test Room Specified in EN 442	61
3.2.2. The Determination of Standard Characteristic Equation and EN 442 Heat Output	62

CHAPTER 4. LITERATURE REVIEW	66
4.1. Studies on Two Dimensional Heat Transfer and Fluid Flows	67
4.2. Studies on Three Dimensional Heat Transfer and Fluid Flows	80
CHAPTER 5. EXPERIMENTAL STUDY	85
5.1. Test Procedure	85
5.2. Measured Values	88
5.3. Calculation of Experimental Heat Outputs	92
5.4. Calculation of EN 442 Standard Heat Outputs	95
CHAPTER 6. VERIFICATION OF TWO DIMENSIONAL NATURAL CONVECTION IN CAVITY	97
6.1. Two Dimensional Differential Heating	97
CHAPTER 7. BOUNDARY CONDITIONS AND COMPUTATIONAL DETAILS	118
7.1. Pre-Analysis	118
7.1.1. Natural Convection in Cavity with Three Cold and One Hot Sides	118
7.1.2. Cavity with Three Cold and One Partially Heated Sides	121
7.1.3. Natural Convection in the Cavity with Internal Heated Body	123
7.1.4. Natural Convection in a Three Dimensional Enclosure with an Internal Heated Body	125
7.2. CFD Analysis of Tested Radiators	130
7.2.1. ICEPAK Models for Tested Radiators	130
7.2.2 Mesh Details	132
7.2.3. Boundary Conditions	135
7.2.4. Assumptions and Solver Settings	137
7.2.5. Convergence Criteria	138
7.2.6. Comparison of Results	140
CHAPTER 8. RESULTS AND DISCUSSION	141
8.1. CFD Results for Radiator I	141
8.2. CFD Results for Radiator II	148
8.3. CFD Results for Radiator III	155

CHAPTER 9. CONCLUSION	162
REFERENCES	166
APPENDICES	
APPENDIX A. TABLES FROM EN 442 STANDARD	170
APPENDIX B. MEASURED DATA.....	171
APPENDIX C. ADDITIONAL CODE USED IN FLUENT	180

LIST OF FIGURES

<u>Figure</u>	<u>Page</u>
Figure 1.1. Different connection styles of radiators.....	3
Figure 1.2. Sectional view from panel radiators.....	6
Figure 1.3. Schematic view of single and double panel radiators.....	7
Figure 1.4. Schematic view of different type of panel radiators which include fins.	9
Figure 2.1. Cell shapes used in 2D geometries (a) Triangle (b) Quadrilateral	39
Figure 2.2. Cells used in 3D geometries (a) Cube (b) Rectangular Prism (c) Tetrahedron (d) Hexahedron (e) Prism (f) Pyramid	40
Figure 2.3. Discrete grid points for finite difference method	42
Figure 2.4. A finite volume in one dimension.	45
Figure 2.5. Segregated solution procedure.....	49
Figure 2.6. Coupled solution procedure.....	49
Figure 2.7. Unsteady solution procedure	50
Figure 2.8. Overview of the density-based solution methods.....	50
Figure 2.9. Overview of the pressure-based solution methods.	51
Figure 2.10. SIMPLE algorithm in steady state.....	53
Figure 2.11. SIMPLE algorithm in transient solutions	53
Figure 2.12. Upwind, central differencing, power law and quick schemes.....	55
Figure 3.1. Water channels in test room panels.....	61
Figure 3.2. Cooling of test room panels.....	62
Figure 3.3. Schematic view of test set up when weighting method is applied.	64
Figure 4.1. Temperature contours (isotherms) at different Rayleigh numbers.....	69
Figure 4.2. Stream functions at different Rayleigh numbers.	70
Figure 4.3. Experimental set up performed by Tian and Karaannis.	73
Figure 4.4. The Principle of a laser doppler anemometer.....	74
Figure 4.5. Local Nusselt numbers on vertical and horizontal walls.....	75
Figure 4.6. Wall temperatures found by Ampofo and Karaannis.	76
Figure 4.7. Vertical velocity profile near the hot wall.....	77
Figure 4.8. Experimental set up performed by Beck.	78
Figure 4.9. Configurations investigated by Beck.....	79
Figure 4.10. Velocity profiles with no, one and two sheets in the gap.....	80

Figure 4.11. Wall temperatures of the fully coupled radiator models.	82
Figure 5.1. View from tested radiators.	85
Figure 5.2. Placement of a radiator during a test procedure.	86
Figure 5.3. Measuring of air temperature inside the test room.	86
Figure 5.4. Thermal camera view from the flexible connections.	87
Figure 5.5. Flow rates in tests of radiator I.	89
Figure 5.6. Reference air temperatures in tests of radiator I.	89
Figure 5.7. Mean water temperatures in tests of radiator I.	89
Figure 5.8. Flow rates in tests of radiator II.	90
Figure 5.9. Reference air temperatures in tests of radiator II.	90
Figure 5.10. Mean water temperatures in tests of radiator II.	90
Figure 5.11. Flow rates in tests of radiator III.	91
Figure 5.12. Reference air temperatures in tests of radiator III.	91
Figure 5.13. Mean water temperatures in tests of radiator III.	91
Figure 5.14. Temperature distributions on the front surface of radiator I.	92
Figure 5.15. Experimental heat outputs of radiator I (W).	93
Figure 5.16. Experimental heat outputs of radiator II (W).	93
Figure 5.17. Experimental heat outputs of radiator III (W).	93
Figure 5.18. Enhancement in the heat transfer rates when radiator II is compared with radiator I (in percentage).	94
Figure 5.19. Enhancement in the heat transfer rates when radiator III is compared with radiator I (in percentage).	94
Figure 6.1. Contours obtained for $Ra=10^2$	100
Figure 6.4. Contours obtained for $Ra=10^5$	103
Figure 6.5. Contours obtained for $Ra=10^6$	104
Figure 6.6. Contours obtained for $Ra=10^7$	105
Figure 6.7. Change in middle point temperature for $Ra=10^8$	106
Figure 6.8. Contours obtained for $Ra=10^8$	107
Figure 6.9. Velocity vectors for $Ra=10^8$	107
Figure 6.10. Contours obtained for $Ra=10^{10}$	108
Figure 7.1. Contours obtained for the cavity whose three side is cold and the other side is hot.	120
Figure 7.2. Contours obtained for the cavity which has three cold and one partially heated side.	122

Figure 7.3.	The schematic view of cavity with internal heated body.	123
Figure 7.4.	Contours for cavity with internal heated body.	124
Figure 7.5.	The sectional view of grid created for 3D domain (Grid II).	126
Figure 7.6.	The temperature contour ($^{\circ}\text{C}$) at vertical plane (II-II) whose normal is in the z direction (Grid II).....	126
Figure 7.7.	The velocity contour ($^{\circ}\text{C}$) at vertical plane (II-II) whose normal is in the z direction (Grid II).....	127
Figure 7.8.	The temperature contour ($^{\circ}\text{C}$) at vertical plane (III-III) whose normal is in the x direction (Grid II).....	127
Figure 7.9.	The temperature contour at vertical plane (I-I) whose normal is in the x direction (Grid II and $x=2.398$)	128
Figure 7.10.	Y velocity contours at vertical plane (I-I) whose normal is in x direction (Grid II).	128
Figure 7.11.	Velocity vectors (Grid II).	129
Figure 7.12.	ICEPAK models of tested radiators.....	131
Figure 7.13.	Details of CFD model of single panel.	131
Figure 7.14.	Comparison of real and CFD models.	132
Figure 7.15.	A cross sectional view of grid created in the virtual test room which includes radiator I.	133
Figure 7.16.	The grid density around radiator I.	133
Figure 7.17.	A cross sectional view of grid created for the test room includes radiator II.	134
Figure 7.18.	The grid density around radiator II.....	134
Figure 7.19.	A cross sectional view of grid created for the test room includes radiator III.....	135
Figure 7.20.	The grid density around radiator III.	135
Figure 7.21.	Residuals in the final CFD run for radiator II (Case 1).	139
Figure 7.22.	Reference point temperature in the final CFD run for radiator II (Case 1).....	139
Figure 7.23.	Air velocities in the final CFD run for radiator II (Case 1).....	139
Figure 8.1.	Temperature distribution on vertical mid plane of radiator I ($z=0.4559$ m).	142
Figure 8.2.	Temperature distributions at three different horizontal cross sections of radiator I.	143

Figure 8.3.	Temperature contours on the vertical mid plane of virtual test room whose normal is in z direction ($z=2.405$ m).....	144
Figure 8.4.	Temperature contours on the vertical mid plane of virtual test room whose normal is in x direction ($x=2.398$ m).....	145
Figure 8.5.	Temperature contours on the horizontal mid plane of virtual test room whose normal is in y direction ($y=1.867$ m).....	146
Figure 8.6.	Velocity contours on the vertical mid plane of virtual test room whose normal is in z direction ($z=2.405$ m).	147
Figure 8.7.	Temperature distribution on vertical mid plane of panel used in radiator II.	149
Figure 8.8.	Temperature distribution on a horizontal cross section of radiator II.	150
Figure 8.9.	Temperature contours on the vertical mid plane whose normal is in z direction ($z=2.405$ m).	151
Figure 8.10.	Temperature contours on the vertical mid plane whose normal is in x direction ($x=2.398$ m).....	152
Figure 8.11.	Velocity contours on the vertical mid plane whose normal is in z direction ($z=2.405$ m).	153
Figure 8.12.	Path lines for the air motion in virtual test of radiator II.....	154
Figure 8.13.	Pathlines for the air motion in virtual test of radiator III.....	155
Figure 8.14.	Temperature distribution on radiator III in case 1.....	156
Figure 8.15.	Temperature distribution on radiator III in case 2.....	157
Figure 8.16.	Temperature distribution on radiator III in case 3.....	158
Figure 8.17.	Velocity contours on the vertical mid plane whose normal is in z direction ($z=2.405$ m).	159
Figure 8.18.	Temperature contours on the vertical mid plane whose normal is in z direction ($z=2.405$ m).	160

LIST OF TABLES

<u>Table</u>	<u>Page</u>
Table 1.1. Proportion of heat emitted as radiation and convection (in an isothermal cooled surface-enclosure).	10
Table 1.2. Factors affect the heat output of radiators.	11
Table 2.1. The ratio of the emissivity in accordance with surface characteristics.....	18
Table 2.2. Default under relaxation factors in FLUENT and ICEPAK.....	57
Table 4.1. Results of simulation performed by Gritzki for the first radiator model.	83
Table 4.2. Results of simulation performed by Gritzki for the second radiator model.	83
Table 5.1. Mean experimental heat outputs (Φ_{exp}) of investigated radiators(W).....	95
Table 5.2. The radiated heat output factor (S_k), the exponent n_p and test pressure for investigated radiators.	95
Table 5.3. Coefficients used in Equation (3.7) and (3.8) for tested radiators.	95
Table 5.4. Standard characteristic equations for tested radiators.....	96
Table 5.5. EN 442 heat outputs (Φ) of tested radiators (W).....	96
Table 5.6. Comparison of experimental and EN 442 heat outputs of tested radiators in three cases (in percentage).....	96
Table 6.1. Details about two dimensional domains in investigated Rayleigh numbers.....	98
Table 6.2. Coefficients used for the calculation of Rayleigh numbers.....	98
Table 6.3. Air properties in two dimensional computational runs.....	98
Table 6.4. Discretization scheme employed in the computational runs of two dimensional problems.	99
Table 6.5. Heat transfer rates and mean Nusselt number on hot and cold walls for different number of elements and $Ra=10^2$	99
Table 6.6. Heat transfer rates and mean Nusselt number on hot and cold walls for different number of elements and $Ra=10^3$	100

Table 6.7.	Heat transfer rates and mean Nusselt number on hot and cold walls for different number of elements and $Ra=10^4$	101
Table 6.8.	Heat transfer rates and mean Nusselt number on hot and cold walls for different number of elements and $Ra=10^5$	102
Table 6.9.	Heat transfer rates and mean Nusselt number on hot and cold walls for different number of elements and $Ra=10^6$	103
Table 6.10.	Heat transfer rates and average Nusselt number on hot and cold walls for different number of elements and $Ra=10^7$	104
Table 6.11.	Comparison of the predicted mean Nusselt number on the hot or cold walls of a cavity	105
Table 6.12.	Total heat transfer rates and mean Nusselt number on hot and cold walls for $Ra=10^8$	106
Table 6.13.	Total heat transfer rates and mean Nusselt number on hot and cold walls for $Ra=10^{10}$	108
Table 6.14.	Total heat transfer rates on hot and cold walls for different number of cells (W)	111
Table 7.1.	Total heat transfer rates from the walls and reference temperatures in different number of elements for two dimensional cavity which has three cold and one hot sides (W)	119
Table 7.2.	Total heat transfer rates (W) from the walls and reference temperatures for two dimensional domain which has three cold and one partially heated side.	121
Table 7.3.	Total heat transfer rates from the walls (W) and reference temperatures for cavity with internal heated body.....	123
Table 7.4.	Number of elements in two different grid structures generated for 3D enclosure with internal body.....	126
Table 7.5.	Total heat transfer rates in different grid structures.....	129
Table 7.6.	Mesh details for Radiator I.	132
Table 7.7.	Mesh details for three cases of Radiator II.	134
Table 7.8.	Mesh details for three cases and Radiator III.	135
Table 7.9.	Boundary conditions at radiator inlet.....	136
Table 7.10.	Boundary conditions for the walls of virtual tests room (except wall behind tested radiators).....	137

Table 8.1.	Computational heat outputs of radiator I in different grid structures (W).	148
Table 8.2.	Compared heat outputs for radiator I (W).	148
Table 8.3.	Computational heat outputs (W) of radiator II in two different grid structures	154
Table 8.4.	Compared heat outputs for radiator II.....	154
Table 8.5.	Computational heat outputs of radiator III in two different grid structures (W).	161
Table 8.6.	Experimental heat outputs of radiator III (W).	161
Table 8.7.	Comparison of heat outputs of tested radiators.	161

LIST OF SYMBOLS

a	:Absorption coefficient
a_p	:Coefficient
a_{nb}	:Coefficient
C	:Specific heat (J/kgK)
$C_\mu, C_2, C_{1\varepsilon}$:Constants of turbulence models
ΔT_e	:Excess temperature
E	:Total energy
f_x, f_y, f_z	:Source terms
f_p	:Correction factor
g	:Gravitational acceleration
G_b	:Generation of turbulence kinetic energy due to buoyancy
G_k	:Generation of turbulence kinetic energy due to mean velocity
	Gradients
Gr	:Grashof number
h	:Heat transfer coefficient (W/m ² K)
h_{ext}	:External heat transfer coefficient defined by users
h_f	:Fluid-side local heat transfer coefficient
i	:Enthalpy
I	:Radiation intensity
I_λ	:Spectral intensity
k	:Thermal conductivity (W/mK) or Turbulence kinetic energy (m ² /s ²)
k_t	:Turbulent thermal conductivity
K_m	:The radiator output constant
L	:Length (m)
\dot{m}	:Mass flow rate (kg/s)
n	:Refractive index
N	:Number of test points
Nu	:Nusselt number
p	:Static pressure (kPa)
Pe	:Peclet number

Pr	:Prandtl number
Q	:Heat output (W)
\vec{r}	:Position vector
R	:Universal gas constant
R_p	:Imbalance
Ra	:Rayleigh number
q	:Heat flux (W/m ²)
q _{rad}	:Radiative heat flux
s	:Path length for Radiation transport equation
S _h	:Source term (volumetric)
S _k	:User defines source term or radiated heat output factor
S _e	:User-defined source terms.
\vec{s}	:Direction vector
\vec{s}'	:Scattering direction vector
T	:Temperature (°C or K)
T _∞	:Ambient temperature (°C or K)
T _{rom}	:Reference air temperature (°C or K)
u, v, w	:Velocity components (m/s)
U _T	:The friction velocity
V	:Velocity (m/s) or Volume (m ³)
\vec{V}	:Velocity vector
y _p	:The distance between first cell and wall
Y _M	:Contribution of the fluctuating dilatation incompressible turbulence to the overall dissipation rate

Greek Symbols

α	:Thermal diffusivity or under relaxation factor
β	:Expansion coefficient (K ⁻¹)
ν	:Kinematic viscosity (m ² s ⁻¹)
Δn	:Distance between wall surface and cell center
ε	:Energy dissipation rate (m ² /s ³)
λ	:Bulk viscosity coefficient
Ø	:Any flow property

$\bar{\phi}$:Average value of any flow property
ϕ'	:Instantaneous value of any flow property
μ	:Dynamic viscosity (kg/ms)
μ_t	:Turbulent (eddy) viscosity
ρ	:Density (kg/m ³)
σ_s	:Scattering coefficient
Γ	:Diffusion coefficient
τ	:Shear stress
$(\tau_{ij})_{\text{eff}}$:Deviatoric stress tensor
Φ	:Dissipation function or corrected (EN 442 standard) heat output
Φ_{me}	:Uncorrected heat output (W)
Ω'	:Solid angle

Subscripts

c	:Cold
comp	:Computational
eff	:Effective
exp	:Experimental
f	:Fluid
h	:Hot
in	:Inlet
out	:Outlet
x, y, z	:Spatial coordinate directions
o	:Operating temperature and standard test conditions.
i, j, k	:Suffix notation for x, y and z directions
k	:Turbulence kinetic energy
nb	:Neighbor cells
s	:Solid
w	:Water or wall
∞	:Fluid sufficiently far from the hot or cold surfaces.

CHAPTER 1

INTRODUCTION

Human beings feel comfortable in buildings in case of specific indoor temperature; relative humidity and air velocities are maintained. In cold seasons, thermal comfort is mainly provided with different kind of heating devices in buildings. Local or joint heat sources are used for heating process. In local heating applications, spaces are separately heated by using different appliances like electric heaters, radiative heaters, heat pumps, electrically heated oil-filled radiators and gas-fired or wood fueled stoves. In central heating applications, joint heat sources are used. Heat generated in one place is distributed to all spaces of buildings in those applications. Although the investment cost of a central heating is higher than the cost of local heating, desired or uniform temperatures can be ensured in whole building and people feel more comfortable.

1.1. Central Heating

A medium is required in order to carry the heat generated as a result of combustion of fossil fuel in a joint heat source. Steam or hot water can be utilized as a primary medium in such applications. When a medium carries the heat, long pipes or some special devices can be used in order to transfer heat.

Air can also be used as a secondary medium in buildings which have many zones and different thermal conditions are required like shopping centers, sport centers or airports. In such systems, air is conditioned first by using previously conditioned water and then distributed to each zone by insulated ductwork.

Generally, hot water is used as a medium in heating systems of dwellings. In those systems, tap water is used directly without exposed to any treatment process. Water treatment can be employed to prevent scaling or corrosion caused by dissolved gasses, freezing of the water, the growth of mold in complicated heating systems.

1.2. Heating Devices in Central Heating Systems

Heat can be discharged to indoor environment by using different equipment from straight or finned pipes to special heating appliances like radiators. Straight pipes can be assumed as basic heat exchangers. However heat transfer rates from straight pipes are very low when they are in contact with stir air. Therefore, the length of piping line becomes crucial to overcome the required energy.

The heat emitted from the pipe surface can be increased by using finned pipes. Finned pipes are generally used in convectors or air handling units in which speed of air is high.

Because of relatively lower investment cost and easy installation, radiators are widespread heating devices in households when a joint heat source is used. In case radiators which do not used any external force are utilized in the heating system, air circulation in indoor environment occurs without using external force.

Radiators are installed to areas such as under windows, along cold walls, or at doorways where great heat losses occur. Generally, freestanding radiators or radiators in decorative enclosures are placed symmetrically below the windows or on the external walls. Different researches show that enclosures affect their effectiveness (Ashrae 2000) The size of radiator, connection style of supply and return lines, and places can be different in each project. However radiator dimensions are standard and correct one is selected from the producers catalogues according to required energy amount. Height of radiators usually changes between 200 mm and 900 mm while length changes between 400 mm and 3000 mm. The size of a radiator is not important for HVAC engineers only. Building engineers and architects want to use smaller heaters since smaller ones use less wall space.

Different supply and return connections can be applied as seen in Figure 1.1 (Radiator Connection 2010). Hot water can enter the radiator from the top and exits from the bottom of the same side as shown in Figure 1.1 a.) which is one of the frequently seen connection type. Connection shown in Figure 1.1 b.) is generally applied when long radiators whose length is 4 or 5 times more than its height are used in the system. When a radiator is connected from bottom opposite ends as shown in Figure 1.1 c.), the performance of the radiator can decrease depending on the height of the radiator.

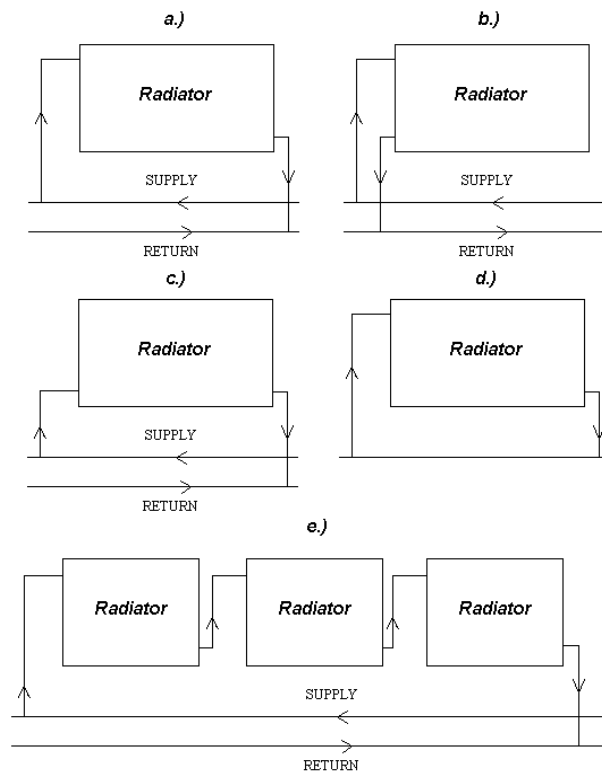


Figure 1.1. Different connection styles of radiators.

In Figure 1.1 d.), radiators are connected to circuit constructed from single pipe line. The surface temperatures of radiators are different from each other in this type of connection. In the last figure, serial connection is schematically shown. It should be noted that this connection is not frequently used (Radiator Connection 2010).

1.3. Types of Radiators

Design, material, size and colors of radiators can be different. Comparisons between different radiators are based on volume and projection area, weight, thermal inertia, ease of installation, water volume, life, corrosion, aesthetic, security, the required amount of heating surface, pressure resistance and price. It is possible to classify radiators according to construction material as cast iron radiators, steel radiators and aluminum radiators. Panel radiators, panel radiators with extended surfaces, convectors, low surface temperature radiators and towel radiators are examples of steel radiators.

Even though steel is the more common material in radiators, aluminum is also used in the production of radiators. Better heat conductivity properties of aluminum

improves heat dissipation rate. Short heat-up period and immediate response to desired temperature make In addition, better corrosion resistance is achieved by using aluminum item since formation of surface layer of aluminum oxide when exposed to air. Reduced load of aluminum radiators ease to place them.

Cast iron is the first material used for radiators. It contains 3-4.5 wt % C and other alloying elements (Callister 1985). The heat can be kept for longer time by using cast iron in the construction of radiators. As compared with aluminum radiators, longer time is required for initial heating and slow response is given to sudden changes in temperature. For this reason, they are especially proper for continuous heating requirement. On the other hand, they are extremely heavy and cannot be placed on a wall easily. Their lives are approximately fifty years.

Hot water and steam can be used as a medium in cast iron radiators. Their large sizes increase the overall water content of a heating system and the operating cost. Also, oversized pipes can be required in addition to large capacities of boilers, pumps and expansion tanks. As a consequence, the investment cost will be higher when cast iron radiators are used.

Column type cast iron radiators which is the main type of cast iron radiators is made from separate sections since number of sections is important in the heat dissipation capability of a radiator. Sections are connected to each other. Therefore there is a wide range of length option. The length is selected according to the required heating output. The number of columns identifies the type of column radiators like 2 column, 3 column or 4 column radiators.

Only panel radiator which is one type of stainless steel radiators are taken into consideration in this study. In the following section, stainless steel radiators are briefly introduced.

1.3.1. Stainless Steel Radiators

Steel alloy with a concentration of at least 11% Chromium (Cr) is called stainless steel. A passive film of chromium oxide which is created by chromium prevents corrosion in stainless steels. Corrosion resistance of steels may also be enhanced by addition of nickel and molybdenum (Callister 1985). Rapid heating periods for stainless steel radiators increase the usage of stainless steel radiators. Several

designs can be seen for those types of radiators. Commonly used stainless steel radiators are column type radiators. They are similar to column type cast iron radiators. They are produced from welded sections of tubular steel. The advantages of using tubular steel column radiators are lightness, inexpensiveness and esthetical appearance. Their different colors enable to use them all in various conditions and prevent corrosion. Convectors are one type of stainless steel radiators. They can be classified in two groups: natural convective convectors and fan assisted convectors. In the natural convective convectors, the air movement occurs as a result of chimney effect. They are made from finned pipes which are placed inside a cabinet in order to create a chimney effect. Cold air enters from the bottom of cabinet and heated by finned pipes. Chimney effect increases the air velocity. The rising hot air flows from the upper tray. As a result of air velocity increment, the proportion of convection heat transfer increases. In these types, air outlet openings and the height of the layout are very important for thermal efficiency. Heating power is adjusted by air valves used to control the airflow or valves used to control the amount of water entering to convectors. Fan assisted convectors use centrifugal fans to provide air movement. A fan speed control unit is also installed on a wall. Because of their relatively smaller size, they are suitable where wall space is limited. However, their electricity consumption increases the operating cost in the heating system. In this arrangement the fan is located in the below while the heater is placed above. In some types, outside air is connected to air inlet to fulfill the function of ventilation. Low surface temperature radiators include a protective casing which limits the surface temperature to prevent injuries. They release heat to the room via grills at the top of the casing while cooler air enters the casing through grills at the bottom. They are used in special buildings where vulnerable people at risk of burning themselves lives or where the maximum operating temperature must be controlled such as hospitals, clinics, and schools. A towel radiator consists of steel tubular pipes. They are used to serve a double function in the bathrooms: drying of towels and heating. The water passing through a towel radiator flows in a separate loop from the heating circle. Both loops are connected to a boiler separately. Heat is dissipated even the central heating is off. By this way, the bathroom can be kept warm.

1.3.1.1. Panel Radiators

Panel radiators are common type of stainless steel radiators and used in heating of buildings. They are made of steel sheets which are bended by using machine press to shape water flow channels. There are different types of panel radiators. Basically they include only one or more panels. Some configurations have extended surfaces (fins) to increase convection heat transfer on the surface as shown in Figure 1.2.

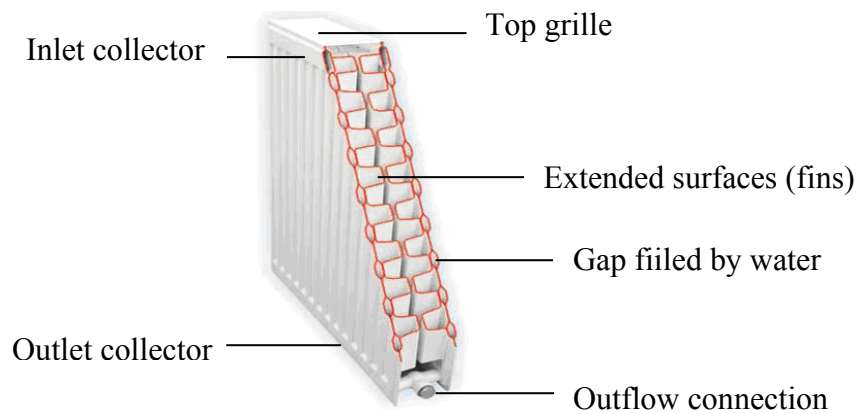


Figure 1.2. Sectional view from panel radiators.

Generally, the surface of a radiator panel is cleaned by degreasing iron phosphate coating and passivation process in accordance with DIN 55900. Then radiators are primed with water-based paint and dried in the oven. At the last stage, they are painted with Epoxy-Polyester electrostatic powder coating method and kiln dried again. By this way, panel radiators become resistant to the corrosion and all weather conditions. As a standard application, panel radiators are painted with white (RAL 9016) color.

Low water content of panel radiators decrease the overall water content of heating systems. Therefore, the operating cost of panel radiators is lower than the operating cost of cast iron column radiators. Their lives change between 15 and 20 years. Different number of panels can be used in the design of panel radiators. They are named according to number of panels like single-panel radiators or double-panel radiators. Increasing number of panel reduces the size of the required device but increases the heat output.

1.3.1.1.1. Single Panel Radiators

Single panel radiators are comprised from one panel. There are not any extended surfaces attached to the rear surface of the radiator. Radiation is dominant heat transfer mechanism in single panel radiator. A schematic view of a single panel radiator is shown in Figure 1.3 a.) The symbol P or the number 10 stands for single panel radiators. In numeric notation, the first digit shows the number of panels. Since it is the simplest type of radiator, the panel radiators are selected as a beginning point in this study.

1.3.1.1.2. Double Panel Radiators

Double panel radiators are composed of two panels. Those single panels are welded together and work in tandem. The gap between the panels increases the convection heat transfer. The symbol PP or the number 20 stands for double panel radiators. Schematic view of a double panel radiator is shown in Figure 1.3 b.) This type is not investigated in this study.

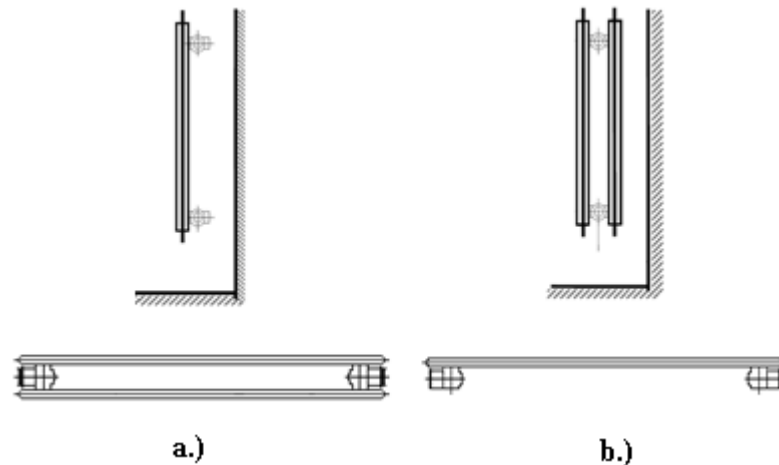


Figure 1.3. Schematic view of single and double panel radiators.

1.3.1.1.3. Panel Radiators with Extended Surfaces

Radiators with extended surfaces or fins are similar with single and double panel radiators in front view. They differ from single and double panel radiators only by the fact that they equipped with extended surfaces to improve the heat output. Fins produced from steel sheets and attached to the rear side to form vertical chimneys in order to draw up and warm the air. Extended surfaces increase the surface area of heat dissipation and increase the convection heat transfer rate. These types of radiators emit most of heat via convection, with a small amount radiation direct from the steel panel. Common types of radiators with extended surfaces: single panel with single fin, double panel with single fin, double panel with double fin, and triple panel with triple fin.

Radiators with single panel and single fin are made from one panel covered with fin. The symbol PC or the number 11 stands for single convector radiators. In numeric notation, the first digit shows the number of panel as in panel radiators while the second one indicates the number of extended surface attached to panels. Schematic view of a radiator with single panel and single fin is shown in Figure 1.4-a (Dağsöz 1998). Radiators with double panel and single fin consist of double panel and single convector. The symbol PCP or the number 21 stands. Their schematic view is given Figure 1.4-b (Dağsöz 1998). As it is seen in Figure 1.4 c.) (Dağsöz 1998), radiators with double panel and double fin contain two single-panel radiators with two sets of convectors between them. They can be called as PCCP or type 22, simply. Radiators with triple panel and triple fin are constructed from the combination of a radiator with single panel and single fin and a radiator with double panel and double fin. They can be called as PCPCCP or type 33, simply. A schematic view of a radiator with triple panel and triple fin is given in Figure 1.4 d.).

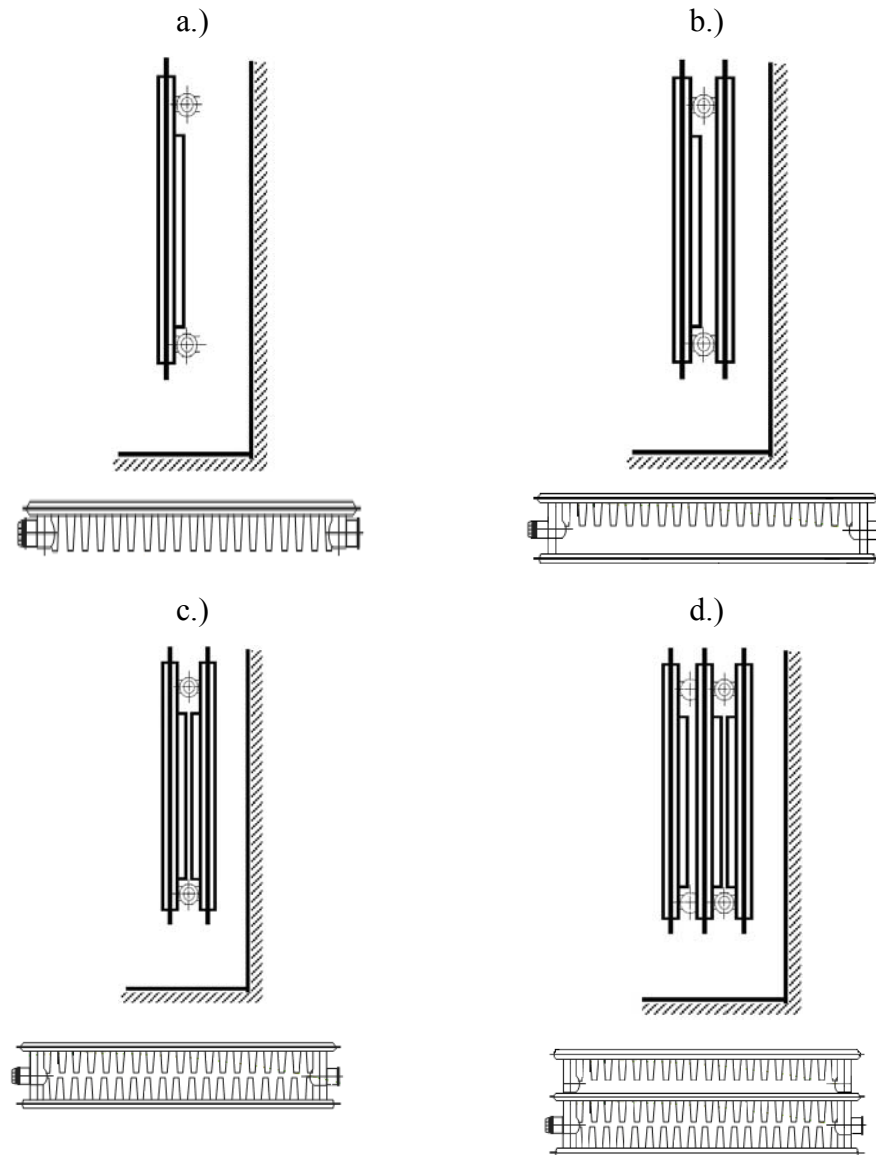


Figure 1.4. Schematic view of different type of panel radiators which include fins.
(Source: Dağsöz 1998)

1.4. Heat Transfer from Radiators

Heat is transferred by the combination of conduction, convection and radiation from radiators. Radiators have two surfaces: wet heating and dry heating surfaces. Wet heating surface is always in contact with the medium. As medium flows through the hollow sections of radiators, heat is emitted from the medium. Wet heating surface conducts heat to dry heating surface which is in contact with air only. Then, the heat is emitted by the dry heating surface. As heat emitted from the dry heating surface, heat is discharged over the surface to ambient, hot water becomes colder and surrounding air

circulates. Although the radiative heat transfer is important in this phenomenon, natural convection plays crucial role. It is illustrated that the proportion of convective heat transfer changes between 50% - 90% by Peach (Peach 1972). Maximum convection heat transfer occurs by using a convector type radiator as seen in Table 1.1.

Table 1.1. Proportion of heat emitted as radiation and convection (in an isothermal cooled surface-enclosure) (Source: Peach 1972).

Type	Average proportion of total emission	
	Radiation (%)	Convection (%)
Single panel	50	50
Double panel	30	70
Triple panel	25	75
2-column	30	70
3-column	22	78
4 column	19	81
6-column	17	83
Convector/radiator	15-10	85-90

1.5. Heat Requirement of Buildings

The energy requirement of a space is determined by heat loss calculations. Heat loss from a space includes fabric and ventilation heat losses. Fabric heat loss involves heat flow through walls, floors, roofs, windows, and between rooms of dissimilar temperatures. Because of air quality concerns, there is an air replacement in spaces. Replaced air brings an extra load to heating systems. Accurate radiator size is selected with regard to heat loss calculations.

1.6. Heat Output of Radiators

The heat output of radiators depends on excess temperature (ΔT_e) which is the difference between mean water and the indoor temperatures as expressed in Equation (1.1).

$$\Delta T_e = \frac{1}{2}(T_{in} + T_{out}) - T_{room} \quad (1.1)$$

The Equation (1.2) is used to express the heat output of a radiator (Ward 1991).

$$Q = K_m \Delta T_e^n \quad (1.2)$$

where K_m is the radiator output constant. Values of K_m and n are usually established from experimental measurements.

It is known that radiators are sold according to their lengths in Turkey. However, their prices are determined according to their heating capabilities in many countries. For this reason, correct determination of heat output of radiators is quite important for producers. They try to improve heating capabilities of their products.

As a result of the first law of Thermodynamics, the heat output of radiators depends on the heat input directly in steady state conditions. Some parameters which affect heat output of radiators (Beck et al 2004) are shown in Table 1.2. In the first column (I), factors increase the heat output are given. In the second column (II), factors decrease the heat output are summarized.

Table 1.2. Factors affect the heat output of radiators.

I	II
<ul style="list-style-type: none"> • Decreasing the distance between the radiator and the ground • Increasing the space between radiator and back side wall • Attachment of fins • Connecting support line to the top of the radiator • Applying a reflector to the wall behind the radiator 	<ul style="list-style-type: none"> • Decreasing the water flow rate • Fouling • Facing the wall adjacent to the radiator with insulated reflector can lower the heat loss through the wall by 70%. However it decrease the heat output from the radiator as the heated wall acts as another convecting surface • Use of metallic paint can reduce the radiant component of radiator heat outputs by up to 10%

Although heat output is very important characteristics of radiators, it is generally taken into consideration only in the selection of proper radiator. However, the price level of radiators is determined according to their unit heat outputs in many countries. Therefore attempts to increase heat outputs become crucial.

Radiators dissipating heat further than the requirement can increase the overall cost of a heating system. For this reason, selecting proper sized radiators which directly depends on the correctness of heating output values listed in catalogues becomes very

important. Publishing comparable and repeatable values for the heat dissipation capabilities of radiators is only possible with using standard measurement techniques. In order to determine heat output of radiators, different legal frameworks like BSI in the UK, DIN in Germany, TS 4310 in Turkey had been used. In the countries of European union, EN 442 part 2 has been used since 1997.

1.7. Unique Contribution and Parts of the Study

In this investigation, flow occurs in a radiator and buoyancy induced flow during the test of a radiator in a test room had been investigated. The aim of this study is to find the heat dissipation capability of radiators and simulation of air flow around them by using computational methods. The results obtained from computational methods were compared with experimental results and results of characteristic equations derived in accordance to EN 442 part 2 standard.

Because of the difficulties encountered in the computational analysis of turbulent type of natural convection problems, some two dimensional natural convection problems were solved by commercial software initially. Two dimensional problems were solved directly in FLUENT. GAMBIT software was used to create two dimensional CFD models and computational grids. The results are validated with the results of benchmark solutions published in literature.

Then, natural convection heat transfers from a three dimensional object whose surface temperatures were constant was found computationally. The surface temperature was assumed by using the average water temperature measured in test of single panel radiator. This three dimensional problem was solved with two different grid structures. Different turbulence models were tried. The velocity and temperature distributions were examined in each case.

Next, single panel radiator whose dimensions were 600 mm (height) and 1000 mm (length) had been investigated by using numerical methods. The problem was solved by using three different operating conditions as mentioned in EN 442 part 2. Finally the heat outputs of other two types of radiators (single panel with single extended surface and double panels with double extended surfaces) with same dimensions (high and wide) were determined. Although the height and length of the investigated models are same, widths differ since different configurations.

ICEPAK software is used to create the CFD models and the computational grids in the CFD simulations of these radiators. Also ICEPAK software is used for the numerical solutions. Numerical findings are verified by an experimental study performed in the test room suitable to EN 442 part 2 standard. The standard thermal outputs calculated with regard to the least squares regression method mentioned in the standard and measured temperature data.

Fundamental knowledge on heat transfer and an overview on computational fluid dynamics (CFD) are presented in the second chapter to clarify the subject.

In chapter 3, EN 442 part 2 standard is introduced.

Literature review is presented in chapter 4.

The experimental studies performed in a test room constructed according to EN 442 part 2 are explained in chapter 5. The measured values are tabulated and catalogue values are calculated with regard to the least squares regression method. Comparisons between experimental and standard results are also presented in this chapter.

In chapter 6, the results for verification of two dimensional natural convection solutions are presented in details.

In chapter 7, the two and three dimensional pre-analysis and ICEPAK models of tested radiators are given. Details of generated meshes, boundary conditions used in the analysis, and computational details are explained.

Results obtained by computational methods are given in chapter 8.

The study is concluded with chapter 9.

CHAPTER 2

THEORY

2.1. Convective Heat Transfer

Temperature distribution is critical information in many engineering design. The motion of fluid plays an important role in heat transfer process since the determination of temperature field in fluid flow requires knowledge of velocity distribution. In addition to temperature distribution, the rate of heat transfer is another important criterion for decision makers.

Newton law of cooling is used for finding convection heat transfer from surface at uniform temperature. Local or mean heat transfer coefficients are used in Newton law of cooling. Dimensionless parameter that characterizes the intensity of convective heat exchange between the surface of a body and a fluid flow is expressed by Equation (2.1). It represents the ratio of convection heat transfer for fluid in motion to conduction heat transfer for a motionless layer of fluid (Cengel 2006).

$$Nu = \frac{hL}{k_f} \quad (2.1)$$

where k_f is the thermal conductivity of the fluid and h is the convective heat transfer coefficient.

Heat flux can be derived from the temperature field. When a flow of hot fluid with a temperature of T_∞ over a cold plate whose surface temperature is T_s is considered, the fluid layer in contact with the solid surface sticks to the surface. There is a very thin layer of fluid whose velocity is zero. The heat transfer from a wall surface to adjacent fluid layer is governed by pure conduction. The conduction heat flux at the wall surface from fluid to wall is defined by Equation (2.2).

$$q(x) = -k_f \left. \frac{\partial T(x, y)}{\partial y} \right|_{y=0} \quad (2.2)$$

where $\left. \frac{\partial T}{\partial y} \right|_{y=0}$ is temperature gradient at the surface

Local and average Nusselt numbers on walls can be determined by using the measured temperature data in the thermal conductive boundary layer where the heat flux is constant.

Heat transfer coefficient can be computed only on the surface of objects not for plane cuts or iso-surfaces by Equation (2.3).

$$h = \frac{q}{T - T_{ref}} \quad (2.3)$$

where q is the heat flux for the surface and T_{ref} is a reference temperature

As a result of continual replacement of the heated and cooler fluid, natural convection currents occur. This current improves the heat transferred from a heated surface and the heat transfer mechanism is known as natural convection heat transfer (Cengel 2006) and faced in many practical applications like in design of efficient heating devices, the cooling of electronic equipment (Balaji and Venkateshan 1993). Many experimental and numerical studies on natural convection heat transfer have been performed and reported in the literature.

In heating applications, buoyancy force and natural convection current are expected due to the temperature difference between the air adjacent to heated surface and the air away from it. Light air places with heavier air because of varying density of air. Buoyancy force is proportional to the density difference of air.

When the flow around a radiator is examined, it is seen that the air velocity will increase from the bottom to the top. As the velocity increases, flow becomes unstable and enters the transition region. When the velocity further increases, eddies form and the flow becomes turbulent (Peach 1972).

The magnitude of the natural convection heat transfer between the heated surface and ambient depends on the flow rate of the fluid. However, the flow rate

cannot be controlled from outside since it occurs dynamically by buoyancy and friction effects.

The flow regime in natural convection heat transfer is usually expressed in terms of Rayleigh number. Rayleigh number is found by multiplication of the Grashof (Gr) and Prandtl (Pr) numbers (Özışık 1997).

The flow regime in natural convection heat transfer is usually expressed in terms of Rayleigh number. Rayleigh number is found by multiplication of the Grashof (Gr) and Prandtl (Pr) numbers (Özışık 1997).

The Grashof number is the ratio of the buoyancy and viscous force acting on a fluid (Özışık 1997). For vertical flat plates, it is calculated by using Equation (2.4).

$$Gr = \frac{g\beta}{\nu^2}(T_s - T_\infty)L^3 \quad (2.4)$$

where L is the length scale and β is the volume expansion coefficient of the fluid. Volume expansion represents the variation of the density of a fluid with temperature at constant pressure and it is defined by Equation (2.5).

$$\beta = -\frac{1}{\rho} \left(\frac{\partial \rho}{\partial T} \right)_p \quad (2.5)$$

At constant pressure, the volume expansion coefficient can be calculated from Equation (2.6).

$$\beta \approx -\frac{1}{\rho} \frac{\Delta \rho}{\Delta T} = -\frac{1}{\rho} \frac{\rho_\infty - \rho}{T_\infty - T} \quad (2.6)$$

The density difference can be found by Equation (2.7).

$$\rho_\infty - \rho = \rho\beta(T_\infty - T) \quad (2.7)$$

Prandtl number which is found by Equation (2.8) describes the relationship between momentum and thermal diffusivities. It depends on fluid state and controls the

relative thickness of the momentum and thermal boundary layers. When it is small, heat diffuses fast compared to the velocity.

$$\text{Pr} = \frac{\nu}{\alpha} = \frac{c_p \mu}{k} \quad (2.8)$$

The Rayleigh can be found by Equation (2.9) for vertical flat plate.

$$\text{Ra} = \frac{\rho g \beta \Delta T L^3}{\mu \alpha} \quad (2.9)$$

where ρ is the fluid density, g is the gravitational acceleration, ΔT is the difference between the surface and free stream temperature, μ is the dynamic viscosity and α is the thermal diffusivity.

2.2. Radiative Heat Transfer

Heat can be emitted as electromagnetic waves in the wavelength range of 0.1 to 100 microns. Heat emittance as electromagnetic waves is called radiative heat transfer and depends on the surface characteristics of objects like surface conditions (roughness, finish, etc.) and composition.

The radiation flux incident on a surface from all directions over all wavelengths is named irradiation. Irradiated heat can be reflected, absorbed, and sometimes transmitted.

Radiative energy transferred per unit time, solid angle, spectral variable, and area normal to the pencil of rays is called the radiative intensity (I). The spectral radiative intensity I_λ is the total radiative intensity per unit wavelength interval about λ .

The emission characteristics of surfaces can be described by blackbodies which are perfect emitter or absorber of radiative energy. The emissivity of a surface is the ratio of the radiation emitted by the surface at a given temperature to the radiation emitted by a blackbody at the same temperature. It shows the closeness to a blackbody and varies with the temperature of surface, wavelength and the direction of the emitted radiation (Cengel 2006).

The emissivity of surface increases with the surface temperature for metallic surfaces. The emissivity values (Peach 1972) in accordance with surface characteristics are given in Table 2.1.

Table 2.1. The ratio of the emissivity in accordance with surface characteristics.
(Source: Peach 1972)

Surface characteristic	Emissivity
Non-metalling coatings	0.8 – 0.95
Metallic paints	0.4 – 0.7
Oxidized metals	0.8 – 0.9
Clean metals	0.1 -0.4
Polished metals	0.1

2.3. Flow Types and Properties

When the fluid friction has significant effects, the flow is referred as viscous. When the viscous forces are dominant, the flow is smooth and adjacent layers of fluid slide over each other orderly. When the inertial forces govern the flow instead of viscous forces, the flow is turbulent. The turbulent flow is one of the complicated phenomena encountered in the nature. Most natural convection flows in the engineering applications are turbulent.

Under constant temperature conditions, Reynolds number which is the ratio of inertia to viscous forces determines the flow characteristic. Above the critical value of the Reynolds number, there are variations in flow characteristics. When the ratio between Grashof and Reynold numbers surpasses unity, strong buoyancy is expected. In pure natural convection, the strength of the buoyancy-induced flow is measured by the dimensionless Rayleigh number as expressed in section 2.1. The Rayleigh number is around 10^6 and 10^8 in most engineering applications.

Critical Rayleigh number determines the transition from laminar to turbulent flow in pure natural convection flow and depends on the geometry and boundary conditions. Rayleigh numbers less than 10^8 indicate a buoyancy-induced laminar flow. Turbulent flow occurs when Rayleigh number is greater than 10^8 (Ansys Fluent 2009). In turbulent flow, particles exhibit additional transverse motion which enhances the rate of energy and momentum exchange between them thus increasing the heat transfer and the friction coefficient.

A fluid flow is said to be compressible when the pressure variation in the flow field is large enough to cause substantial changes in the density of fluid.

Many flows are naturally time-dependent. Because of instability, flows with stationary boundaries become time-dependent.

In most studies, distributions of pressure, velocity or temperature through flow fields are wanted to predict (Kakac 1997). For a long time, correlations, tables and nomograms have been used to find flow properties. Because of limitations in applicability of such tools, geometric, kinematic and dynamics similarities between models have been used to achieve empirical information (Bilir 2009).

There are three approaches used in the determination of flow properties: analytical, experimental, and numerical methods. Analytical methods are limited to highly simplified problems especially with simple geometries. The entire surface of the geometry should be described mathematically in a coordinate system by setting variables equal to constant. Also, thermal conditions should be sufficiently simple in addition to simple geometry (Bilir 2009).

Reliable results can be obtained by conducting experiments. In experimental methods, one variable is changed while trying to keep all other variables constant. Replicability of experiments with the same results is important since generalization from the results of a single experiment is not healthy. In some instances, because of impossibility of conducting experiments or costly setups of experiments computational methods are preferred.

Computational methods enable to see unobtainable properties during experiments. Comparing numerical results with theoretical or experimental results data is used in verification. Development in computer speed and memory capacity increases the usage of computational methods in practice. Parallel to the development of algorithm more realistic simulations can be performed.

2.4. Governing Equations

Governing equations in CFD include continuity, momentum and energy equations. In this section, the governing equations for an unsteady, three-dimensional, compressible, viscous flow are introduced.

2.4.1. Continuity Equation

Since mass is conserved within the control volume or infinitesimal fluid element, the rate of increase of mass within a volume is equal to the net rate at which mass crosses its bounding surface. The conservation of mass can be defined by a scalar equation. Velocity components in x, y and z directions are represented by u, v, and w. The components of velocity vector are functions of space and time. The continuity equation is given in Equation (2.10) (Von Karman Institute 2010).

$$\frac{\partial \rho}{\partial t} + \rho \nabla \cdot \vec{V} = 0 \quad (2.10)$$

where ρ is the density and \vec{V} is the velocity field in three dimensional rectangular Cartesian coordinate system.

The second term is divergence of the velocity and named as convective term. It represents the difference between the mass flows into and the mass flows out from boundaries. It must be balanced with the first term which describes the accumulation. If the fluid is incompressible, then density is constant in both location and time.

2.4.2. Momentum Equations

Even in steady flow field, particles of fluid may be accelerated. Their velocity can change as they move to new positions. Momentum Equation (Navier-Stokes equations) is obtained by the application of conservation of momentum principle. It describes the relationship between velocity, pressure, and density of a moving fluid. Since it is a vector equation, there are separate scalar equations for each coordinate direction. In these equations, changes in momentum of particles of a fluid are equal to the sum of two kinds of forces acting on fluid: body and surface forces. Body forces like gravitational, electrical, and magnetic act directly on the volumetric mass of the fluid element and defined as a source term. Surface forces act directly on the surface of the fluid element. The momentum equations in Cartesian coordinates are expressed by Equations (2.11), (2.12), and (2.13).

$$\frac{\partial(\rho u)}{\partial t} + \nabla \cdot (\rho u \vec{V}) = -\frac{\partial p}{\partial x} + \frac{\partial \tau_{xx}}{\partial x} + \frac{\partial \tau_{yx}}{\partial y} + \frac{\partial \tau_{zx}}{\partial z} + \rho f_x \quad (2.11)$$

$$\frac{\partial(\rho v)}{\partial t} + \nabla \cdot (\rho v \vec{V}) = -\frac{\partial p}{\partial y} + \frac{\partial \tau_{xy}}{\partial x} + \frac{\partial \tau_{yy}}{\partial y} + \frac{\partial \tau_{zy}}{\partial z} + \rho f_y \quad (2.12)$$

$$\frac{\partial(\rho w)}{\partial t} + \nabla \cdot (\rho w \vec{V}) = -\frac{\partial p}{\partial z} + \frac{\partial \tau_{xz}}{\partial x} + \frac{\partial \tau_{yz}}{\partial y} + \frac{\partial \tau_{zz}}{\partial z} + \rho f_z \quad (2.13)$$

For Newtonian fluids in which shear stress components are proportional to velocity gradients, Equations (2.14) and (2.15) can be used (Von Karman Institute 2010).

$$\tau_{xx} = \lambda \nabla \cdot \vec{V} + 2\mu \frac{\partial u}{\partial x}, \tau_{yy} = \lambda \nabla \cdot \vec{V} + 2\mu \frac{\partial v}{\partial y}, \tau_{zz} = \lambda \nabla \cdot \vec{V} + 2\mu \frac{\partial w}{\partial z} \quad (2.14)$$

$$\tau_{xy} = \tau_{yx} = \mu \left(\frac{\partial v}{\partial x} + \frac{\partial u}{\partial y} \right), \tau_{xz} = \tau_{zx} = \mu \left(\frac{\partial u}{\partial z} + \frac{\partial w}{\partial x} \right), \tau_{yz} = \tau_{zy} = \mu \left(\frac{\partial w}{\partial y} + \frac{\partial v}{\partial z} \right) \quad (2.15)$$

where μ is the molecular viscosity coefficient and λ is the bulk viscosity coefficient. For most gases, bulk viscosity coefficient is found by using Equation (2.16).

$$\lambda = -\frac{2}{3}\mu \quad (2.16)$$

Momentum equations can be expressed by vector form by Equation (2.17).

$$\rho \frac{D\vec{V}}{Dt} = -\nabla P + \mu \nabla^2 \vec{V} + \rho \vec{g} \quad (2.17)$$

Momentum equations are second order, non-homogenous, non-linear partial differential equations. The nonlinearity is due to acceleration associated with the change in velocity over position. Acceleration associated with the change in velocity is present

in most flows except creeping flow and incompressible flow in one dimension. Therefore any convective flow, whether laminar or turbulent, involves nonlinearity.

2.4.3. Energy Equation

The energy of a fluid is defined as the sum of internal energy (u), kinetic energy, and gravitational potential energy. The energy equation which is scalar represents that the rate of change of energy inside the fluid element is equal to the sum of the rate of heat transfer (ignoring radiation effects) to the element and the rate of work by the fluid element against to body and surface forces. The conservation form of the energy equation written in terms of the internal energy (e) is given by Equation (2.18).

$$\begin{aligned} \rho \frac{De}{Dt} = & \rho \cdot \dot{q} + \nabla \cdot (k \nabla T) - p \nabla \cdot \vec{V} + \lambda \left(\frac{\partial u}{\partial x} + \frac{\partial v}{\partial y} + \frac{\partial w}{\partial z} \right)^2 + \\ & \mu \left[2 \left(\frac{\partial u}{\partial x} \right)^2 + 2 \left(\frac{\partial v}{\partial y} \right)^2 + 2 \left(\frac{\partial w}{\partial z} \right)^2 + \left(\frac{\partial u}{\partial y} + \frac{\partial v}{\partial x} \right)^2 + \left(\frac{\partial u}{\partial z} + \frac{\partial w}{\partial x} \right)^2 + \left(\frac{\partial v}{\partial z} + \frac{\partial w}{\partial y} \right)^2 \right] \end{aligned} \quad (2.18)$$

The conservation form of the energy equation written in terms of the total energy ($E = e + \frac{V^2}{2}$) is given by Equation (2.19).

$$\begin{aligned} \rho \frac{DE}{Dt} = & \rho \cdot \dot{q} + \nabla \cdot (k \nabla T) - p \nabla \cdot \vec{V} + \frac{\partial (u \tau_{xx})}{\partial x} + \frac{\partial (u \tau_{yx})}{\partial y} + \frac{\partial (u \tau_{zx})}{\partial z} + \\ & \frac{\partial (v \tau_{xy})}{\partial x} + \frac{\partial (v \tau_{yy})}{\partial y} + \frac{\partial (v \tau_{zy})}{\partial z} + \frac{\partial (w \tau_{xz})}{\partial x} + \frac{\partial (w \tau_{yz})}{\partial y} + \frac{\partial (w \tau_{zz})}{\partial z} + \rho (u f_x + v f_y + w f_z) \end{aligned} \quad (2.19)$$

The energy equation can be also written in terms of enthalpy ($i = e + \frac{p}{\rho}$). Ideal gas assumption can be used for incompressible gas flow. The ideal gas equation (Equation (2.20)) is the sixth equation in addition to continuity, Navier Stokes and energy equations in case ideal gas assumption is used.

$$p = \rho RT \quad (2.20)$$

Six unknown flow-field variables in the governing equations: u , v , w , p , ρ , T can be solved by using six equation given above.

2.5. Boussinesq Approximation

Buoyant flows differ from subsonic forced convective flows in some significant aspects. In subsonic forced convective flows, the coupling between the momentum and energy equations tends to be one way with momentum affecting the advection term in the energy equation. The energy equation typically does not feed back into the momentum equation directly. In buoyant flows, the coupling is direct and two-way with the density gradient in a gravity field appearing in the momentum equations (Kakaç 1997).

Several approximations like Boussinesq or the boundary layer are used to simplify equations given above since solving process of natural convection is quite difficult.

In the boundary-layer approximation in natural convection, the flow and the energy transfer are predominantly restricted to a thin region close to the surface. Beyond this region, the fluid is stationary. The main consequences of the boundary-layer approximations are that the axial diffusion terms in momentum and energy equations are neglected. The transverse momentum balance is neglected, since it is found to be of negligible importance compared to the axial balance (Kakaç 1997).

Boussinesq approximation states that in a flow where the density changes (not by compressibility effects, but by temperature differences) are small but not zero, the density change is important only in relation to the body force. This body force is usually gravity, and is typically important only in the vertical momentum equation. All other density gradients and fluctuations may be neglected. The density difference is estimated by Equation (2.6). When a vertical hot flat plate located in y axis is taken into the consideration in two dimensional rectangular coordinate systems,

$$\text{In the outside of the boundary layer: } u=0 \text{ and } \frac{\partial P_{\infty}}{\partial y} = -\rho_{\infty} g$$

$$\text{In the boundary layer region, } P = P(x) = P_{\infty}(x) \text{ and } \frac{\partial P}{\partial y} = \frac{\partial P_{\infty}}{\partial y} = -\rho_{\infty} g$$

The momentum equation in vertical direction can be expressed by Equation (2.21).

$$\rho \frac{Dv}{Dt} = \mu \left[\frac{\partial}{\partial x} \left(\frac{\partial v}{\partial x} \right) + \frac{\partial}{\partial y} \left(\frac{\partial v}{\partial y} \right) + \frac{\partial}{\partial z} \left(\frac{\partial v}{\partial z} \right) \right] + g\rho\beta(T - T_\infty) \quad (2.21)$$

For many natural-convection flows, using Boussinesq approximation provide faster convergence according to setting up the problem with fluid density as a function of temperature. The constant density assumption reduces the nonlinear nature of the governing equations. Boussinesq approximation is accurate as long as temperature variations are small.

While pressure variations are small but temperature variations are large, the incompressible ideal gas law can also be used in Fluent. The incompressible ideal gas option for density treats the fluid density of a fluid is a function of temperature only. It is claimed that the incompressible ideal gas law generally gives better convergence compared to the ideal gas law.

2.6. Turbulent Flows

Because of irregular movement of particles of the fluid, the velocity, temperature, and pressure fluctuate in turbulent flow. Therefore, turbulent flows can be described by time-averaged values and fluctuations. Time average values are found by integrating the local instantaneous value of particular quantity at a given point over a sufficiently long time interval. For steady turbulence, time averaged quantities do not vary with time. For unsteady turbulence, the time averaged quantities vary with time. Most engineering models of turbulent flow assume that the velocity at a given point in space and a given time can be made up of the superposition of mean velocity, which may vary slowly with time, and a random component which varies rapidly.

Turbulent flows are computed either by solving the Reynolds-averaged Navier-Stokes equations with suitable models for turbulent fluxes or by computing the fluctuating quantities directly. Linear eddy-viscosity models (EVM), Non-linear eddy-viscosity models (NLEVM) and Differential stress models (DSM) are Reynolds-averaged Navier-Stokes (RANS) models. With Large-eddy simulation (LES) and Direct numerical simulation (DNS) fluctuating quantities are computed. In Reynolds averaging, the solution variables are decomposed into mean and fluctuating components. If ϕ is any flow variable like u , v , w , p , T , the instantaneous value can be

constituted from two components: time average values of the quantity ($\bar{\phi}$) and fluctuations ($\phi'(t)$) as written in Equation (2.22).

$$\phi(t) = \bar{\phi} + \phi'(t) \quad (2.22)$$

The mean values are predictable variables while the turbulent fluctuations are stochastic variables. Governing equations are written in terms of time average values alone in below sections.

2.6.1. Continuity Equation for Turbulent Flows

For incompressible turbulent flow, the continuity equation is given by Equation (2.23). In the continuity, instantaneous velocity components are replaced by the time-averaged ones.

$$\frac{\partial \bar{u}}{\partial x} + \frac{\partial \bar{v}}{\partial y} + \frac{\partial \bar{w}}{\partial z} = 0 \quad (2.23)$$

2.6.2. Reynolds Average Navier Stokes Equations

Reynolds Averaged Navier-Stokes (RANS) equations have the same general form as the instantaneous Navier-Stokes equations. Additional terms appear arise due to the presence of the fluctuating velocity components in RANS equations. These terms are often named as turbulent or Reynolds stress terms and represent the effects of turbulence. The Reynolds Averaged Navier-Stokes Equation for the turbulent flow is given by Equation (2.24) for the x direction.

$$\begin{aligned} \bar{u} \frac{\partial \bar{u}}{\partial x} + \bar{v} \frac{\partial \bar{u}}{\partial y} + \bar{w} \frac{\partial \bar{u}}{\partial z} = -\frac{1}{\rho} \frac{\partial \bar{p}}{\partial x} - \\ \left[\frac{\partial \overline{(u')^2}}{\partial x} + \frac{\partial \overline{(v'u')}}{\partial y} + \frac{\partial \overline{(w'u')}}{\partial z} \right] + \nu \cdot \left(\frac{\partial}{\partial x} \left(\frac{\partial \bar{u}}{\partial x} \right) + \frac{\partial}{\partial y} \left(\frac{\partial \bar{u}}{\partial y} \right) + \frac{\partial}{\partial z} \left(\frac{\partial \bar{u}}{\partial z} \right) \right) \end{aligned} \quad (2.24)$$

The Reynolds Averaged Navier-Stokes Equation for the turbulent flow is given by Equation (2.25) for the y direction.

$$\begin{aligned} \bar{u} \frac{\partial \bar{v}}{\partial x} + \bar{v} \frac{\partial \bar{v}}{\partial y} + \bar{w} \frac{\partial \bar{v}}{\partial z} = -\frac{1}{\rho} \frac{\partial \bar{p}}{\partial y} - \\ \left[\frac{\partial}{\partial x} (\overline{u'v'}) + \frac{\partial}{\partial y} (\overline{v'^2}) + \frac{\partial}{\partial z} (\overline{w'v'}) \right] + \nu \cdot \left(\frac{\partial}{\partial x} \left(\frac{\partial \bar{v}}{\partial x} \right) + \frac{\partial}{\partial y} \left(\frac{\partial \bar{v}}{\partial y} \right) + \frac{\partial}{\partial z} \left(\frac{\partial \bar{v}}{\partial z} \right) \right) \end{aligned} \quad (2.25)$$

The Reynolds Averaged Navier-Stokes Equation for the turbulent flow is given by Equation (2.26) for the z direction.

$$\begin{aligned} \bar{u} \frac{\partial \bar{w}}{\partial x} + \bar{v} \frac{\partial \bar{w}}{\partial y} + \bar{w} \frac{\partial \bar{w}}{\partial z} = -\frac{1}{\rho} \frac{\partial \bar{p}}{\partial z} - \\ \left[\frac{\partial}{\partial x} (\overline{u'w'}) + \frac{\partial}{\partial y} (\overline{v'w'}) + \frac{\partial}{\partial z} (\overline{w'^2}) \right] + \nu \cdot \left(\frac{\partial}{\partial x} \left(\frac{\partial \bar{w}}{\partial x} \right) + \frac{\partial}{\partial y} \left(\frac{\partial \bar{w}}{\partial y} \right) + \frac{\partial}{\partial z} \left(\frac{\partial \bar{w}}{\partial z} \right) \right) \end{aligned} \quad (2.26)$$

In tensor notation, momentum equation is given by Equation (2.27).

$$\frac{\partial \bar{u}_i}{\partial t} + \bar{u}_j \frac{\partial \bar{u}_i}{\partial x_j} = -\frac{1}{\rho} \frac{\partial \bar{p}}{\partial x_i} + \frac{\partial \tau_{vij}}{\partial x_j} + \frac{1}{\rho} \frac{\partial \tau_{Rij}}{\partial x_{\partial j}} + g_i \quad (2.27)$$

where τ_{vij} and τ_{Rij} are viscous stress tensor and Reynold stress tensors, respectively.

$$\tau_{vij} = \nu \left(\frac{\partial \bar{u}_i}{\partial x_j} + \frac{\partial \bar{u}_j}{\partial x_i} \right) \quad (2.28)$$

$$\tau_{Rij} = -\rho \overline{u'_i u'_j} \quad (2.29)$$

Reynolds stress which are time-averaged products of fluctuating velocity components and are responsible for considerable momentum exchange in turbulent flow. Reynolds stresses are usually large compared to the viscous stresses.

2.7. Boussinesq Hypothesis

Many turbulence models are based upon the Boussinesq hypothesis since Reynolds stresses are modeled easily (Equation (2.30)). Reynolds stress tensor expressed in terms of the time-averaged velocity gradients and the turbulent viscosity. A new quantity the turbulent viscosity (eddy viscosity) μ_t (Pa.s) appears in the Equation (2.30). The turbulent viscosity is used to close the momentum equations.

$$-\rho u'_i u'_j = \mu_{eff} \left(\frac{\partial \bar{u}_j}{\partial x_i} + \frac{\partial \bar{u}_i}{\partial x_j} \right) \quad (2.30)$$

The turbulent viscosity is not homogeneous. However, it can be assumed to be isotropic. This assumption is valid for many flows.

2.8. Turbulence Modeling

Typically boundary layer flow relies on the mixing length model for analytical solutions. Computer turbulence modeling often relies on complicated models, but they are difficult to solve analytically. The solution of unknowns in turbulent flow depends on the turbulence model employed which includes additional equations to simulate turbulence effect. The following models can be used to predict the turbulent viscosity:

- Zero-equation/algebraic models like mixing length, Cebeci-Smith, Baldwin-Lomax, Johnson-King, a roughness-dependent
- One-equation models like Wolfstein, Baldwin-Barth, Spalart-Allmaras, k-model, etc.
- Two-equation model like k- ϵ , k- ω , k-t, k-L, etc.
- Three-equation models like k-e-A
- Four-equation models (Ansys Fluent).

2.8.1. Two Equation Turbulence Models

Two equation turbulence models (k- ϵ and k- ω) are used frequently in applications. Convection and diffusion of turbulent energy effects are taken into consideration by using two extra partial differential equations which describe the relationship between the turbulent viscosity and the tangible flow quantities (Ansys Fluent 2009).

2.8.1.1. The k- ϵ Turbulence Model

Two extra equations are utilized in this semi-empirical turbulence model: transport equations for the turbulent kinetic energy (k) and the dissipation rate or the rate of k destruction (ϵ). Turbulent kinetic energy is defined by Equation (2.31).

$$k = \frac{1}{2} \left(\overline{u'^2} + \overline{v'^2} + \overline{w'^2} \right) \quad (2.31)$$

Turbulent kinetic energy is complemented by a model for the momentum eddy diffusivity.

$$\epsilon_M = c_\mu k^{1/2} L \quad (2.32)$$

C_μ is an experimentally determined constant and L is a length scale similar to the mixing length. The dissipation rate of turbulent kinetic energy is defined by Equation (2.33).

$$\epsilon = C_D \frac{k^{3/2}}{L} \quad (2.33)$$

The length scale can be eliminated by using these two equations and setting C_D to be 1.

$$\varepsilon_M = C_\mu \frac{k^2}{\varepsilon} \quad (2.34)$$

This model is only valid in fully developed turbulent regions. Three different k-ε models can be used in FLUENT: standard, RNG and realizable (Ansys Fluent 2009). In the following section, some information on standard and realizable k-ε models is summarized. Detailed knowledge about turbulence models can be found in FLUENT Theory Guide (Ansys Fluent 2009).

2.8.1.1.1. Standard k- ε Turbulence Model

In this model, the Reynolds stresses are linked to the mean flow and coefficient for turbulent viscosity depends on the turbulent kinetic energy k and dissipation ε. The standard k- ε model calculates the turbulent viscosity from Equation (2.35).

$$\mu_t = \rho \cdot \varepsilon_M \quad (2.35)$$

Where c_μ is a constant and equal to 0.09.

The governing differential equations are given in Equation (2.36) and (2.37).

$$\frac{Dk}{Dt} = \frac{\partial}{\partial y} \left[\left(\mu + \frac{\mu_t}{\sigma_k} \right) \frac{\partial k}{\partial y} \right] + G_k + G_b - \rho \varepsilon - Y_M + S_k \quad (2.36)$$

$$\frac{D\varepsilon}{Dt} = \frac{\partial}{\partial y} \left[\left(\mu + \frac{\mu_t}{\sigma_\varepsilon} \right) \frac{\partial \varepsilon}{\partial y} \right] + C_{1\varepsilon} \frac{\varepsilon}{k} (G_k + C_{3\varepsilon} G_b) - C_{2\varepsilon} \rho \frac{\varepsilon^2}{k} + S_\varepsilon \quad (2.37)$$

where G_k represents the generation of turbulent kinetic energy due to the mean velocity gradients and it calculated from Equation (2.38), G_b is the generation of turbulent kinetic energy due to buoyancy and found by using Equation (2.39), Y_M is found by Equation (2.40) represents the contribution of the fluctuating dilatation in compressible turbulence to the overall dissipation rate, $C_{1\varepsilon}$, $C_{2\varepsilon}$ and $C_{3\varepsilon}$ are constants, σ_k and σ_b are

Prandtl numbers for turbulent kinetic energy and turbulent dissipation, S_k and S_ϵ are user-defined source terms.

$$G_k = -\rho \overline{u'_i u'_j} \frac{\partial u_j}{\partial x_i} \quad (2.38)$$

$$G_b = -\beta g_i \frac{\mu_t}{\rho \text{Pr}_t} \frac{\partial T}{\partial x_i} \quad (2.39)$$

Where Pr_t is turbulent Prandtl number and equal to 0.85

$$Y_M = 2\beta \epsilon M_t^2 \quad (2.40)$$

Where M_t is turbulent mach number and defined by Equation (2.41).

$$M_t = \sqrt{\frac{k}{\alpha^2}} \quad (2.41)$$

where α is the speed of sound

Model constants are

$$C_{1e} = 1.44, C_{2e} = 1.92, C_\mu = 0.09, \sigma_k = 1.0, \sigma_\epsilon = 1.3$$

2.8.1.1.2. Realizable k- ϵ Turbulence Model

Certain mathematical constraints on the Reynolds stresses are satisfied in this model. Previously expressed k- ϵ models do not use such kind of constraints. The realizable k- ϵ turbulence model based on governing equations given in Equations (2.42) and (2.43), respectively (Ansys Fluent 2009)

$$\frac{\partial}{\partial t}(\rho k) + \frac{\partial}{\partial x_j}(\rho k u_j) = \frac{\partial}{\partial x_j} \left[\left(\mu + \frac{\mu_t}{\sigma_k} \right) \frac{\partial k}{\partial x_j} \right] + G_k + G_b - \rho \varepsilon - Y_M + S_k \quad (2.42)$$

$$\frac{\partial}{\partial t}(\rho \varepsilon) + \frac{\partial}{\partial x_j}(\rho \varepsilon u_j) = \frac{\partial}{\partial x_j} \left[\left(\mu + \frac{\mu_t}{\sigma_k} \right) \frac{\partial \varepsilon}{\partial x_j} \right] + \rho C_1 S_\varepsilon - \rho C_2 \frac{\varepsilon^2}{k + \sqrt{\nu \varepsilon}} + C_{1\varepsilon} \frac{\varepsilon}{k} C_{3\varepsilon} G_b + S_{\varepsilon k} \quad (2.43)$$

where

$$C_1 = \max \left[0.43, \frac{\eta}{\eta + 5} \right], \quad \eta = S \frac{k}{\varepsilon}, \quad S = \sqrt{2 S_{ij} S_{ij}} \quad (2.44)$$

S_{ij} is the mean strain rate and defined by Equation (2.45).

$$S_{ij} = \frac{1}{2} \left(\frac{\partial V_j}{\partial x_i} + \frac{\partial V_i}{\partial x_j} \right) \quad (2.45)$$

The k equation is the same as that in the standard k - ε model except for the model constants. The form of the ε equation is quite different from those in the standard k - ε model. The model constants are:

$$C_{1\varepsilon} = 1.44, \quad C_2 = 1.9, \quad \sigma_k = 1.0, \quad \sigma_\varepsilon = 1.2$$

The degree to which ε is affected by the buoyancy is determined by the constant $C_{3\varepsilon}$. In FLUENT, $C_{3\varepsilon}$ is not specified, and calculated according to Equation (2.46).

$$C_{3\varepsilon} = \tanh \left| \frac{v}{u} \right| \quad (2.46)$$

where v is the component of the flow velocity parallel to the gravitational vector and u is the component of the flow velocity perpendicular to the gravitational vector.

2.8.2. Energy Equation in the k- ε Models

The energy equation is given in Equation (2.47).

$$\frac{\partial}{\partial t}(\rho E) + \frac{\partial}{\partial x_i} [u_i(\rho E + p)] = \frac{\partial}{\partial x_j} \left(k_{eff} \frac{\partial T}{\partial x_j} + u_i (\tau_{ij})_{eff} \right) + S_h \quad (2.47)$$

Where E is the total energy, k_{eff} is the effective thermal conductivity, S_h is the source term contains contributions from radiation, as well as any other volumetric heat sources and $(\tau_{ij})_{eff}$ is the deviatoric stress tensor, defined by Equation (2.48).

$$(\tau_{ij})_{eff} = \mu_{eff} \left(\frac{\partial v}{\partial x_i} + \frac{\partial u}{\partial x_j} \right) - \frac{2}{3} \mu_{eff} \frac{\partial V_k}{\partial x_k} \delta_{ij} \quad (2.48)$$

For the standard and realizable k-ε models, the effective thermal conductivity is calculated by Equation (2.49).

$$k_{eff} = k + \frac{c_p \mu_t}{Pr_t} \quad (2.49)$$

Where k in this case, is the thermal conductivity. The default value of the turbulent Prandtl number is 0.85.

2.9. Modeling Near Wall Regions

The turbulent boundary layer can be divided into three regions: laminar sub-layer, buffer region and turbulent layer.

Viscous shear stress is dominant and flow retains its viscous flow character in the laminar sub-layer which is very thin and located next to wall. The viscosity plays a dominant role in momentum and heat or mass transfer. The mean axial velocity rapidly increases with the distance from the wall. The buffer region is adjacent to the laminar sub-layer and an interior region between the laminar and the fully turbulent layers.

Viscous and turbulence shear stresses are equally important in this layer. The velocity changes relatively little with the distance from the wall. The outer layer in which turbulence plays a major role is known as the fully - turbulent layer. Turbulent shear stress is dominant.

Y plus (y^+) which is a mesh-dependent dimensionless distance and determines the region solved. It is defined by the Equation (2.50).

$$y^+ = \frac{\rho \cdot U_T \cdot y}{\mu} \quad (2.50)$$

where U_T is the friction velocity which is found by Equation (2.51), y is the distance between first cell and wall, ρ is the fluid density, and μ is the dynamic viscosity of fluid.

$$U_T = \sqrt{\frac{\tau_w}{\rho}} \quad (2.51)$$

where

τ_w is the wall shear stress.

The wall shear stress is based on the velocity gradient in the direction normal to the surface of the wall and found by Equation (2.52).

$$\tau_w \cong \mu \cdot \left. \frac{\partial U}{\partial y} \right|_{y=0} \quad (2.52)$$

where U is the fluid velocity along the wall.

The laminar sub-layer is valid when $y^+ < 5$. The height of the first cell is generally taken to be approximately $y^+ = 1$. In the range of $5 < y^+ < 30$, there exists a buffer region. If the boundary layer is meshed sufficiently fine so that the first cells are placed entirely in the laminar sub-layer of the boundary layer, the approach used is generally referred to as Low-Re Modeling. For meshes with a $y^+ > 30$, wall function theory may be applied. Wall functions are generally described as having two regions: the laminar sub-layer and the log-law layer. For the dimensionless velocity and

temperature within the laminar sub-layer region, Equations (2.53) and (2.54) can be used.

$$u^+ = y^+ \quad (2.53)$$

$$T^+ = \text{Pr} y^+ \quad (2.54)$$

Dimensionless velocity can be described as a function of the fluid velocity and the friction velocity and found by Equation (2.55).

$$u^+ = \frac{U}{U_T} \quad (2.55)$$

The dimensionless temperature may be calculated by Equation (2.56).

$$T^+ = \frac{T_w - T}{T^*} \quad (2.56)$$

Where T_w is the wall temperature at a certain point, T is the fluid temperature, and T^* is defined by Equation (2.57).

$$T^* \equiv \frac{\alpha \cdot q_w}{k \cdot U_T} \quad (2.57)$$

Where α is the thermal diffusivity, q_w is the wall heat flux and k is the thermal conductivity.

The region above the laminar sub-layer ($y^+ > 30$) is the log-law layer is generally described by Equation (2.58).

$$n^+ = a \ln y^+ + B \quad (2.58)$$

where n is either the dimensionless velocity or temperature. Constants A and B are usually found experimentally.

FLUENT provides enhanced wall treatment options for modeling turbulence near to wall. Enhanced wall treatment combines a two-layer model with enhanced wall functions and can be used to deal with the resolution of the boundary layer. The domain is subdivided into a viscosity affected region and a fully-turbulent region. The two-layer approach is an integral part of the enhanced wall treatment and is used to specify both ϵ and the turbulent viscosity in the near-wall cells (Ansys Fluent 2009)

2.10. Radiative Transfer Equation

The radiative intensity field within the enclosure as a function of location (\vec{r}), direction (\vec{s}) and spectral variable (wave number, η) is expressed by Radiative transfer equation.

Net radiative heat flux is radiative energy irradiating from all possible directions and wave numbers. A light beam which is traveling through a participating medium in the direction of \vec{s} loses energy by absorption and by scattering away from the direction of travel and gains energy by emission (Modest 2003). The absolute amount of absorption is directly proportional to the magnitude of the incident energy and travelling distance through the medium and calculated by Equation (2.59).

$$\left(dI_{\eta}\right)_{abs} = -K_{\eta}I_{\eta}ds \quad (2.59)$$

where the proportionality constant K_{η} is known as the (linear) absorption coefficient.

Scattered energy is calculated by Equation (2.60) (Modest 2003).

$$\left(dI_{\eta}\right)_{sca} = -\sigma_{s\eta}I_{\eta}ds \quad (2.60)$$

where the proportionality constant $\sigma_{s\eta}$ is the (linear) scattering coefficient

The emitted intensity (which is the rate of emitted energy per unit area) along any path is proportional to the length of the path, and local energy content in the medium. It is calculated by Equation (2.61) (Modest 2003).

$$(dI_\eta)_{em} = -K_\eta I_{b\eta} ds \quad (2.61)$$

The proportionality constant for emission K_η is the same as for absorption. Augmentation due to scattering has contributions from all directions and, therefore, must be calculated by integration over all solid angles. The energy flux scattered into the direction \hat{s} from all incoming directions \hat{s}_i can be find by using Equation (2.62).

$$(dI_\eta)_{sca}(\hat{s}) = ds \frac{\sigma_{s\eta}}{4\pi} \int_{4\pi} I_\eta(\hat{s}_i) \phi_\eta(\hat{s}_i, \hat{s}) d\Omega_i \quad (2.62)$$

The change in intensity can be found by using Equation (2.63) in which the emission, absorption, scattering away from the direction \hat{s} , and scattering into the direction of \hat{s} are summed (Modest 2003).

$$\begin{aligned} I_\eta(s + ds, \hat{s}, t + dt) - I_\eta(s, \hat{s}, t) = & K_\eta I_{b\eta}(s, t) ds - K_\eta I_\eta(s, \hat{s}, t) ds - \\ & \sigma_{s\eta} I_\eta(s, \hat{s}, t) ds + \frac{\sigma_{s\eta}}{4\pi} \int_{4\pi} I_\eta(\hat{s}_i) \phi_\eta(\hat{s}_i, \hat{s}) d\Omega_i ds \end{aligned} \quad (2.63)$$

The outgoing intensity is calculated from Equation (2.64).

$$I_\eta(s + ds, \hat{s}, t + dt) = I_\eta(s, \hat{s}, t) + dt \frac{\partial I_\eta}{\partial t} + ds \frac{\partial I_\eta}{\partial s} \quad (2.64)$$

Equation (2.62) can be written as in Equation (2.65).

$$\frac{1}{c} \frac{\partial I_\eta}{\partial t} + \frac{\partial I_\eta}{\partial s} = K_\eta I_{b\eta} - K_\eta I_\eta - \sigma_{s\eta} I_\eta + \frac{\sigma_{s\eta}}{4\pi} \int_{4\pi} I_\eta(\hat{s}_i) \phi_\eta(\hat{s}_i, \hat{s}) d\Omega_i \quad (2.65)$$

All quantities in Equation (2.64) may vary with location in space, time and wave number, while the intensity and the phase function also depend on direction \hat{s} and \hat{s}_i . The radiative transfer equation solved by Fluent solver is given in Equation (2.66) (Ansys Fluent 2009)

$$\frac{dI(\vec{r}, \vec{s})}{ds} + (a + \sigma_s)I(\vec{r}, \vec{s}) = an^2 \frac{\sigma T^4}{\pi} + \frac{\sigma_s}{4\pi} \int_0^{4\pi} I(\vec{r}, \vec{s}) \phi(\vec{s}\vec{s}') d\Omega \quad (2.66)$$

Following radiation models can be used in Fluent solver (Ansys Fluent 2009): Discrete Ordinates Model, Discrete Transfer Radiation Model, P-1 Radiation Model, Rosseland Radiation Model and Surface to Surface Radiation Model. Only Surface to Surface Radiation and Discrete Ordinates Models can be selected in ICEPAK.

2.10.1. The Discrete Ordinates Radiation Model

The discrete ordinates radiation model solves the radiative transfer equation for a finite number of discrete solid angles. The integral over direction in Equation (2.66) is replaced by numerical quadratures. Detailed information can be found in Radiative Heat Transfer Books. Two implementations of the discrete ordinates model are available in FLUENT: uncoupled and (energy) coupled.

2.11. Basics of Computational Fluid Dynamics

Detailed information about flow is always required in design stage of engineering systems which include fluid flow. One way to find flow properties like velocity, temperature and pressure field is solving governing equations.

Since those equations are nonlinear in the acceleration term (convection term), have singularities for high Reynolds Numbers CFD, and the pressure difference terms are difficult to solve in combination with the fluid's motion, computational tool is used. Computational Fluid Dynamics (CFD) is the simulation of systems by using modeling (mathematical form of physical problems) and numerical methods. It can be utilized in various fields like the design of aircrafts, land vehicles, study of blood flow, the analysis of the effects of pollution, the design of electronic circuits, and the design of buildings.

Special codes are generally used in specific problems and two dimensional cases in industrial applications. Generally writing reliable codes require longer time durations and this is not competitive.

In complex geometries, commercial software like FLUENT, CFX, ICEPAK, FLOTHERM, FloEFD, STAR-CD, FLOW-3D, COMSOL and CFDESIGN is

frequently used. Different disciplines like mathematics, computer science, engineering and physics are utilized in developing stage of that software.

Software reduces the development cost of new products and time between design and marketing. Relatively lower cost of a computer run and shorter run times with regard to time required for experiments are advantageous of CFD methods. Understanding calculations performed by CFD solvers develops awareness of the process involved and their usage limitations.

It should be emphasized numerical results must be verified by experimental study realized, since only validated numerical results are meaningful. In applications, numerical results are generally used after verification of one case. Then, modifications on a model with regard to CFD results can be assumed more reliable.

In this research, FLUENT and ICEPAK software packages have been used. FLUENT is a computer program written in the C computer language for modeling fluid flow and heat transfer in complex geometries. It provides complete mesh flexibility, including the ability to solve flow problems using unstructured meshes that can be generated about complex geometries with relative ease. ICEPAK software uses FLUENT solver for thermal and fluid flow calculations. FLUENT solver provides complete mesh flexibility, and allows solving complex geometries using unstructured meshes. CFD Analysis contains some sub-processes. In this section, those processes are introduced. All process takes place before the run time is called as pre-processing.

2.11.1. Geometry Preparation

The geometry may result from measurements of an existing configuration or may be associated with a design study. In a design procedure, a set of objectives and constraints are specified instead geometry. In CFD applications, some pre-processors like GAMBIT can be utilized in the preparation of CFD models. Such tools are also used for mesh generation and assignation of zones.

Also geometries generated in external sources can be read as standard geometric files like IGES, PARASOLID, ACIS, STEP files by GAMBIT. But in such circumstances, components not exposed to the flow, duplicated entities, small details should be eliminated and geometrical connectivity between parts must be rebuilt in

GAMBIT. ANSYS design modeler or other CAD software can also be used for the model generation.

ICEPAK uses own environment for model generation. It should be noted that ICEPAK can be used for only three dimensional problems. Also model generation is quite different in ICEPAK when it is compared by GAMBIT. Although there are some limitations in modeling stage, simpler mesh generation process makes ICEPAK software practical in applications.

2.11.2. Mesh Generation

Since algebraic form of partial differential equations is solved in sub domains, the computational field should be divided into subdomains (cells, elements) which is called as mesh or grid generation. Structured (hexahedral), unstructured meshes (tetrahedral), or Hybrid grids (some portions of flow field are structured (viscous regions) and others are unstructured) can be used. Two and three dimensional domains can be divided into sub-domains by using different mesh types given in Figures 2.1 and 2.2.

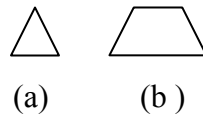


Figure 2.1. Cell shapes used in 2D geometries (a) Triangle (b) Quadrilateral (Source: Ansys Fluent 2009).

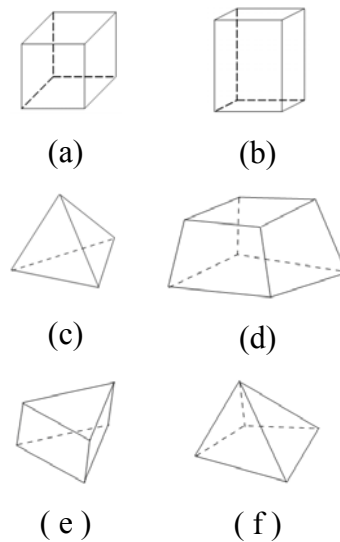


Figure 2.2. Cells used in 3D geometries (a) Cube (b) Rectangular Prism (c) Tetrahedron (d) Hexahedron (e) Prism (f) Pyramid (Source: Ansys Fluent 2009).

Cells can be defined in two principal methods: Grid based (staggered) and cell centered. In grid based cells, nodal value stored at intersection of grid lines and control volume surfaces defined midway between grid lines. In cell centered method, control volume is constructed first, and then central nodes are assigned.

Generally, solution or run time of nonlinear and coupled equations is not short since all equations are solved repeatedly until converge solution is obtained in every element. The type and quality of grid structure are important for the accurate and stable solutions.

When the number of element in a domain is small, the departure of the discrete solution from the exact solution is expected to be large. On the other hand, high number of elements increases the solution time. Therefore computation time and geometry are the main parameters in selection of mesh type. The shape of the flow domain or complexity of the geometry affects the time consumed for grid generation. Usually, the regular grids in which the grid lines are orthogonal to each other are preferred in CFD analysis. When the shape of a domain is regular like a rectangle, it can be meshed by regular grids. Mesh density effects run times in analysis. Coarse meshes are generally preferred in solid regions. Mesh density can be increased in flow regions. A special interest should be taken at walls which are faced to flow region since wall quantities (temperature and heat flux) are very sensitive to the modeling of near-wall turbulence. The number of cells near to walls is generally increased to obtain correct solution. It can be fulfilled by different ways in GAMBIT. Boundary layer tool is one way to create

dense grid and used to increase the number of cells near to wall in this study. Three parameters are defined in order to create dense mesh. First one is first row value (a) which specifies the distance between the first row and wall. The second parameter is growth factor value (G) which is the ratio b/a . “ b ” is the distance between the first and second rows. The height of any row in the boundary layer (other than the first row) is equal to the height of the previous row times the growth factor (b/a) value. The last parameter is the rows value which specifies the total number of rows to be included in the boundary layer. The second way in order to create dense mesh in special regions is using size function. When size function toolbar is used, one source is defined for starting point of mesh generation. Source can be a point, an edge or a surface. Then the target which is desired to mesh is defined. Meanwhile, the growth rate and maximum sizes are entered. The third way which requires long time is manual grid generation. It can be fulfilled by meshing lines and faces separately.

CFD modeling in ICEPAK is based on block creation. Models can be generated from solid blocks which are generally rectangular prisms, cylinders and spheres. But using rectangular prisms make mesh generation process easy. After creation of blocks, the properties of the region can be corrected. The priority is very important in mesh generation. The last created items or objects having higher priorities are meshed at the beginning. Priority is important for objects having special side properties. The most important difference in ICEPAK modeling is that all objects are generated in an environment which is called as a cabinet. The empty space inside the cabinet is defined as a default fluid in the analysis. If there is more than one fluid region in the model, all fluid regions represented by blocks should be defined as fluid and fluid properties should be settled. Mesh generation and run settings are made in the same interface. Hexa structured and unstructured grids can be created. It is important to know that grid density affects the mesh density in the other part of the cabinet.

2.11.3. Selection of Numerical Method

Governing equations can be only solved numerically. Analytical solution gives a function (continuous) while numerical solution gives a set of numbers (discrete). Three different numerical solution techniques can be used: finite difference, finite volume and finite element methods. Finite element and volume methods are more flexible according

to finite difference. They can be formulated to use both structured and unstructured grids. Finite element method is mostly used in structural mechanics. The finite volume method is popular in CFD. Since it ensures that the discretization is conservative and does not require a coordinate transformation in order to be applied on irregular meshes. Flexibility is the great advantage in generating grids in arbitrary geometries (Bilir 2009).

2.11.3.1. Finite Difference Method

Finite difference methods approximate the solutions of differential equations by replacing derivative expressions with approximately equivalent difference quotients. Unknowns are calculated at node points of a grid of coordinate lines (Figure 2.3). Therefore, finite difference method requires a structured grid arrangement and based on the Taylor series expansion about a point.

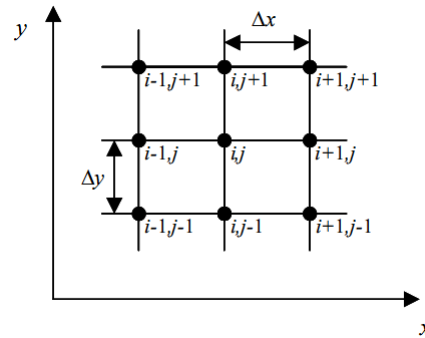


Figure 2.3. Discrete grid points for finite difference method

For two points having a small distance Δx from the central point ($(i+1, j)$ and $(i-1, j)$), unknowns can be expressed in terms of Taylor series expansion about point (i) by Equations (2.67) and (2.68) respectively (Ashgriz and Mostaghimi 2010).

$$\phi_{i+1,j} = \phi_i + \left(\frac{\partial \phi}{\partial x}\right)_i \Delta x + \left(\frac{\partial^2 \phi}{\partial x^2}\right)_i \frac{1}{2} \Delta x^2 + \left(\frac{\partial^3 \phi}{\partial x^3}\right)_i \frac{1}{6} \Delta x^3 + \dots \quad (2.67)$$

$$\phi_{i-1,j} = \phi_i - \left(\frac{\partial \phi}{\partial x}\right)_i \Delta x + \left(\frac{\partial^2 \phi}{\partial x^2}\right)_i \frac{1}{2} \Delta x^2 - \left(\frac{\partial^3 \phi}{\partial x^3}\right)_i \frac{1}{6} \Delta x^3 + \dots \quad (2.68)$$

Central difference equations for the first and the second derivatives can be found by subtracting and adding of Equations (2.67) and (2.68). Equations (2.69) and (2.70) are obtained.

$$\left. \frac{\partial \phi}{\partial x} \right|_i = \frac{\phi_{i+1} - \phi_{i-1}}{2\Delta x} - \left(\frac{\partial^3 \phi}{\partial x^3} \right) \frac{(\Delta x)^2}{6} \quad (2.69)$$

$$\left. \frac{\partial^2 \phi}{\partial x^2} \right|_i = \frac{\phi_{i+1} - 2\phi_i + \phi_{i-1}}{\Delta x^2} + O(\Delta x^2) \quad (2.70)$$

The first-order derivative can be defined by Equation (2.71) in the forward difference.

$$\left(\frac{\partial \phi}{\partial x} \right)_i = \frac{(\phi_{i+1} - \phi_i)}{\Delta x} - \left(\frac{\partial^2 \phi}{\partial x^2} \right) \frac{1}{2} (\Delta x) \quad (2.71)$$

Equation (2.72) is called backward difference.

$$\left(\frac{\partial \phi}{\partial x} \right)_i = \frac{(\phi_i - \phi_{i-1})}{\Delta x} - \left(\frac{\partial^2 \phi}{\partial x^2} \right) \frac{1}{2} (\Delta x) \quad (2.72)$$

Difference formulae are classified in two ways: (1) by the geometrical relationship of the points, namely, central, forward, and backward differencing; or (2) by the accuracy of the expressions, for instance, central difference is second-order accurate, whereas, both forward and backward differences are first-order accurate, as the higher order terms are neglected (Ashgriz and Mostaghimi 2010).

Those equations are used to produce partial differential equations describing the flow. General scalar transport equation is given by Equation (2.73).

$$\frac{\partial(\rho\phi)}{\partial t} + \nabla \cdot \rho \vec{V} \phi = \nabla \cdot (\Gamma \nabla \phi) + S \quad (2.73)$$

Where Γ is diffusion coefficient and S is the source term (generation per unit volume W/m^3).

For steady one dimensional convection/diffusion problems without any generation, the governing equation is given by Equation (2.74).

$$\frac{\partial(\rho u \phi)}{\partial x} = \frac{\partial}{\partial x} \left(\Gamma \frac{\partial \phi}{\partial x} \right) \quad (2.74)$$

From the Taylor series expansion net flux of ϕ due to diffusion into control volume can be written as in Equation (2.75).

$$\left[\frac{\partial}{\partial x} \left(\Gamma \frac{\partial \phi}{\partial x} \right) \right]_i \approx - \frac{\left(\Gamma \frac{\partial \phi}{\partial x} \right)_{i+\frac{1}{2}} - \left(\Gamma \frac{\partial \phi}{\partial x} \right)_{i-\frac{1}{2}}}{\Delta x} = - \frac{1}{\Delta x} \left(\Gamma \frac{\phi_{i+1} - \phi_i}{\Delta x} - \Gamma \frac{\phi_i - \phi_{i-1}}{\Delta x} \right) \quad (2.75)$$

$$\frac{\partial(\rho u \phi)}{\partial x} \approx \rho u \frac{\phi_{i+1} - \phi_{i-1}}{2\Delta x} \quad (2.76)$$

By using equations (2.75) and (2.76), Equation (2.74) can be written as Equation (2.77).

$$\frac{2\Gamma}{\Delta x} \phi_i = \left(-\frac{\rho u}{2} + \frac{\Gamma}{\Delta x} \right) \phi_{i+1} + \left(\frac{\rho u}{2} + \frac{\Gamma}{\Delta x} \right) \phi_{i-1} \quad (2.77)$$

2.11.3.2. Finite Volume Method

Each node is surrounded by a small volume on a mesh in finite volume method. For this reason, a flow domain is subdivided into a finite number of small control volumes. The grid defines to boundaries of the control volumes while the computational node lies at the center of the control volume. The advantage of FVM is that the integral conservation is satisfied exactly over the control volume. The finite volume method (FVM) uses the integral form of the conservation equations over the control volume. Traditionally the finite volume methods have used regular grids for the efficiency of the computations. However, recently, irregular grids have become more popular for simulating flows in complex geometries. Obviously, the computational effort is more when irregular grids are used, since the algorithm should use a table to lookup the

geometrical relationships between the volumes or element faces. The neighboring volumes are denoted as, W, volume to the west side, and E, the volume to the east side of the volume P. For the one-dimensional finite volume shown in Figure 2.4, the volume with centroid P, has four boundary faces at w, e, n, and s (Ashgriz and Mostaghimi 2010).

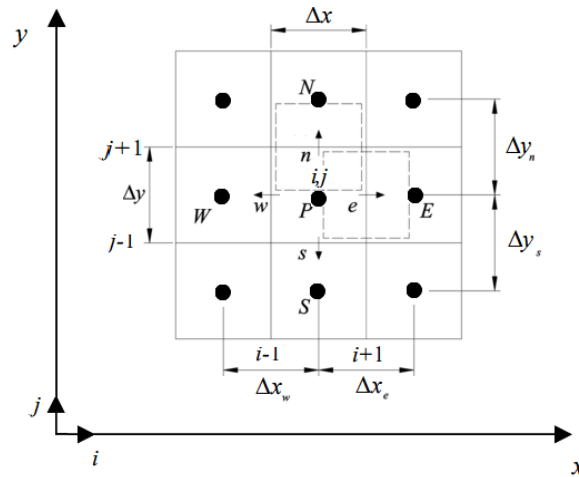


Figure 2.4. A finite volume in one dimension.

For steady two dimensional convection/diffusion problems, the governing equation is given by Equation (2.78).

$$\oint_s \frac{\partial(\rho u_i \phi)}{\partial x_i} = \oint_s \frac{\partial}{\partial x_i} \left(\Gamma \frac{\partial \phi}{\partial x_i} \right) + S \quad (2.78)$$

$$A_e u_e \phi_e - A_w u_w \phi_w + A_n v_n \phi_n - A_s v_s \phi_s = \Gamma A_e \frac{d\phi}{dx} \Big|_e - \Gamma A_w \frac{d\phi}{dx} \Big|_w + \Gamma A_n \frac{d\phi}{dy} \Big|_n - \Gamma A_s \frac{d\phi}{dy} \Big|_s + S_P \quad (2.79)$$

$$[G\phi]_e - [G\phi]_w + [G\phi]_n - [G\phi]_s = D_e(\phi_E - \phi_P) - D_w(\phi_P - \phi_W) + D_n(\phi_N - \phi_P) - D_s(\phi_P - \phi_S) + S_P \quad (2.80)$$

The values of ϕ at the faces e, w, n and s are needed. The value of the integrand is not available at the control volume faces and is determined by interpolation. Using a piecewise-linear interpolation between control volume centers give

$$\begin{aligned} & \frac{1}{2}G_e(\phi_E + \phi_P) - \frac{1}{2}G_w(\phi_P + \phi_W) + \frac{1}{2}G_n(\phi_N + \phi_P) - \frac{1}{2}G_s(\phi_P + \phi_S) = \\ & D_e(\phi_E - \phi_P) - D_w(\phi_P - \phi_W) + D_n(\phi_N - \phi_P) - D_s(\phi_P - \phi_S) + S_P \end{aligned} \quad (2.81)$$

This equation can now be simplified to

$$A_P\phi_P = A_E\phi_E + A_W\phi_W + A_N\phi_N + A_S\phi_S + S_P = \sum_{nb} a_{nb}\phi_{nb} + b \quad (2.82)$$

where

$$A_E = D_e - \frac{G_e}{2}, A_W = D_w + \frac{G_w}{2}, A_N = D_n - \frac{G_n}{2}, A_S = D_s + \frac{G_s}{2}, A_P = A_E + A_W + (G_e - G_w)$$

In Equation (2.82), the neighboring cells are represented by the subscript “nb”. The coefficients a_{nb} and b will be different for every cell in the domain at every iteration. For one dimensional convection problems and upwind differencing, Equations (2.83) and (2.84) can be written.

$$\phi_w = \begin{cases} \phi_W, G_w > 0 \\ \phi_P, G_w < 0 \end{cases} \quad (2.83)$$

$$A_E = D_e + (G_e, 0)_{\max}, A_W = D_w + (G_w, 0)_{\max} \quad (2.84)$$

2.11.4. Identification of Flow Conditions and Properties

Usually, dimensional flow conditions are used in industrial applications. Rapid but accurate solutions are needed. Such solutions are generally obtained by commercial CFD software. Solutions with non-dimensional variables are preferred in research codes.

Flow conditions (inviscid, viscous, laminar, or turbulent, etc.), zone types (fluid or solid zones) are defined at the beginning of the computational runs. A fluid zone is the group of cells in which all equations are solved. While a solid zone is a group of cells for which only heat conduction equation is solved. The material being treated as solid may be fluid, but it is assumed that no convection takes place. Fluid or material properties (density, specific heat, thermal conductivity and for fluid viscosity) are required data for solid and fluid zones.

2.11.5. Defining Initial and Boundary Conditions

The state of pressure (p) or initial velocity (u,v,w) at all points in the flow is specified by initial conditions. Boundary conditions describe how the simulation will behave at the edges of the computational domain and specified variables about the physical model like velocity, pressure and temperature. Appropriate boundary conditions are required in order to obtain an accurate CFD solution. Following boundary conditions can be used to define the flow conditions on the computational domain.

- No slip or wall boundary condition
- Inflow boundary condition (velocity inlet, mass flow rate, constant pressure, etc.)
- Outflow boundary condition
- Periodic boundary condition

No slip or wall boundary condition defines the borders of solid regions or obstacles. Velocity is set to zero on the wall boundaries. Several heat transfer conditions can be also defined at wall boundaries such as specified heat flux, specified temperature, convective heat transfer coefficient and free stream temperature etc (Bilir 2009)

For fixed temperature boundary condition, the heat flux from a fluid cell to the wall is computed by Equation (2.85).

$$q = h_f (T_w - T_f) + q_{rad} \quad (2.85)$$

Where

h_f :fluid-side local heat transfer coefficient

T_w : wall surface temperature

T_f : local fluid temperature

q_{rad} :radiative heat flux

When the heat flux at the wall surface is specified, Equation (2.86) is used to find the wall surface temperature adjacent to a fluid cell.

$$T_w = \frac{q - q_{rad}}{h_f} + T_f \quad (2.86)$$

The heat flux is computed by using Equation (2.87) if the convective heat transfer coefficient boundary condition at a wall and external heat sink temperature are specified. The wall is assumed as having zero thickness.

$$q = h_f (T_w - T_f) + q_{rad} \quad (2.87)$$

$$q = h_{ext} (T_{ext} - T_w) \quad (2.88)$$

where

h_{ext} : external heat transfer coefficient defined by users

T_s : external heat-sink temperature defined by users

Inflow boundary conditions can be used for sources and positive normal velocity is specified. Outflow boundary condition can be used for sinks and negative normal velocity is specified. Symmetry boundary conditions can be used when symmetry has been expected from the solution. A zero flux of all quantities across a symmetry boundary is defined, so no input is required at symmetry boundaries. Periodic boundary conditions are used when the periodic solutions are expected. The last row and column of cells are copied to first row and column when periodic boundary condition is used. It is proper for simulating an infinite domain (Bilir 2009).

2.11.6. Solver Selection

Fluent solves the governing integral equations for the conservation of mass and momentum, energy and other scalars such as turbulence by using a control-volume-based technique. Since pressure term is seen in each momentum equation and velocity components appears in all equations, equations are tightly coupled. Equations can be solved one after another, sequentially (segregated algorithm) or in one step simultaneously (coupled algorithm) in FLUENT.

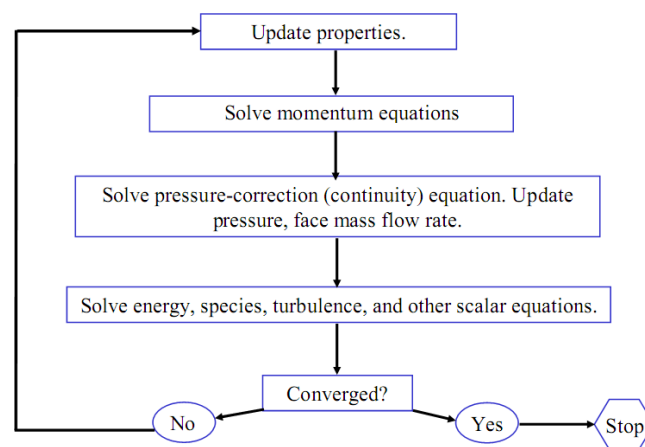


Figure 2.5. Segregated solution procedure.
(Source: Ansys Fluent 2009).

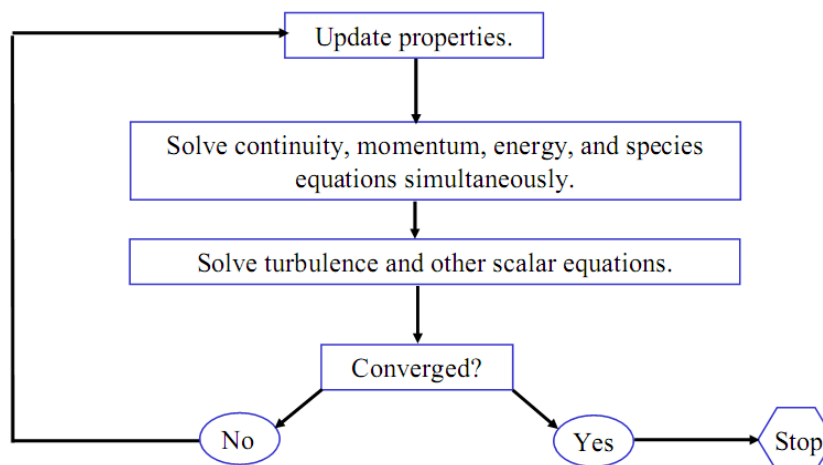


Figure 2.6. Coupled solution procedure.
(Source: Ansys Fluent 2009).

The segregated algorithm uses less memory since the discretized equations are stored in the memory once at a time. The segregated solver gives better results at low

speed flows. Coupled one is preferred when the velocity and pressure are strongly coupled (high pressures and high velocities). It gives better results in supersonic flows. But calculation times will be longer (Ansys Fluent 2009).

Unsteady and steady solvers can be applied in FLUENT. The unsteady solver is used for dynamic simulations where time is being concerned. The steady solver is designed to get steady flow solutions. Segregated and coupled algorithms can be used in both solvers.

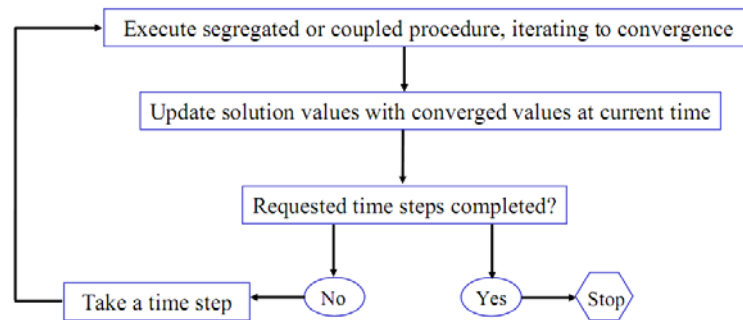


Figure 2.7. Unsteady solution procedure (Source: Ansys Fluent 2009).

Two numerical methods are available in FLUENT solver: pressure based and density based methods. Density based formulation applicable for compressible flows. Density based algorithms are summarized in Figure 2.8 (Ansys Fluent 2009). Continuity equation is used to obtain the density field. The pressure field is determined from the equation of state.

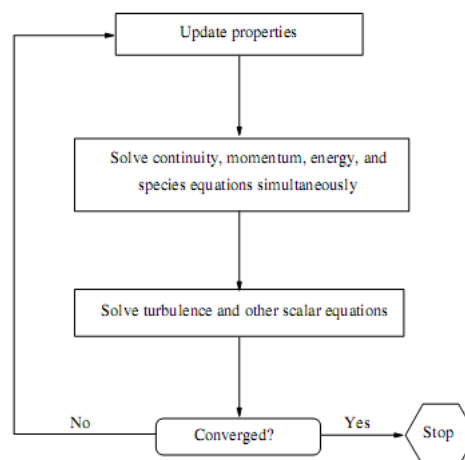


Figure 2.8. Overview of the density-based solution methods. (Source: Ansys Fluent 2009).

In the momentum equation, pressure forces appear as a source of momentum. The force terms in the momentum equation provide a link between velocity and pressure. Since there is a pressure gradient term in momentum equation, velocity depends on the pressure gradient. The momentum equation gives a link between velocity and pressure which, when substituted into the continuity equation, gives an equation for pressure. Changing pressure can be used to enforce mass conservation. Net mass flux in must increase cell pressure while net mass flux out must decrease cell pressure. The pressure field is found by solving a pressure or pressure correction equation in pressure - based solver. Pressure based algorithms are summarized in Figure 2.9 (Ansys Fluent 2009). Pressure correction equation is obtained by manipulating continuity and momentum equations. The pressure - based solver uses a solution algorithm where the governing equations are solved sequentially. It is used for incompressible flows to keep the pressure field from oscillation which may arise due to difficulties in preserving the conservation of mass or incompressibility condition as the sound speed becomes so much higher than convection velocity components.

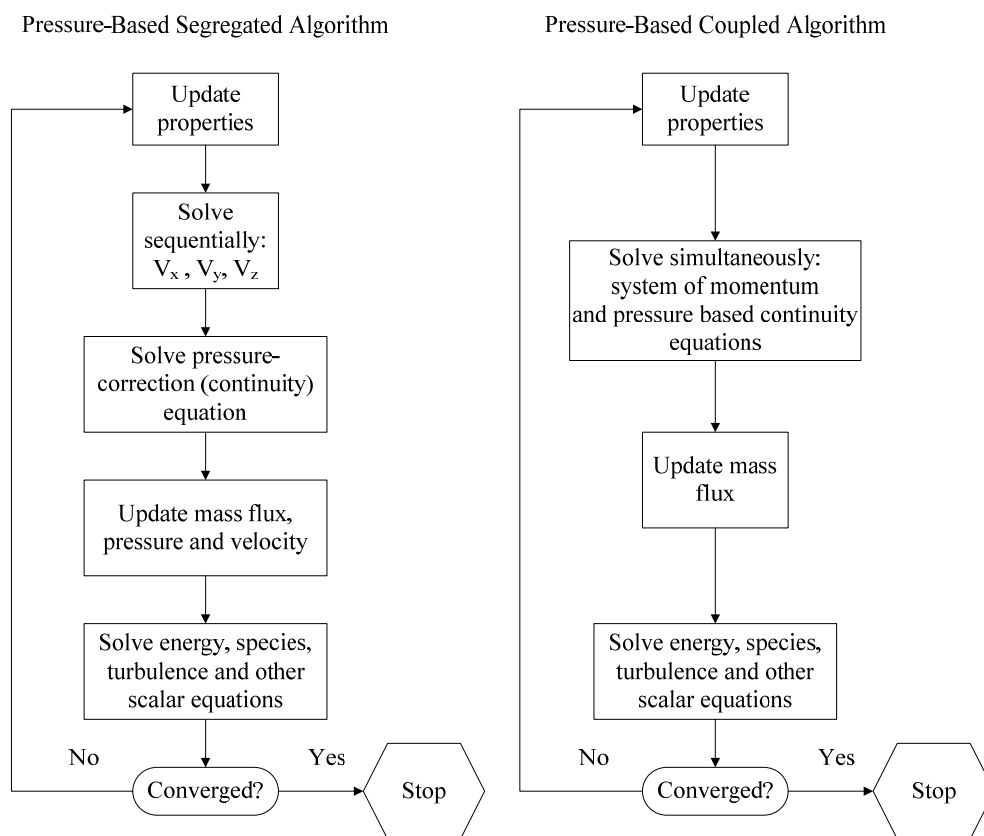


Figure 2.9. Overview of the pressure-based solution methods. (Source: Ansys Fluent 2009).

Pressure-correction algorithms are: Semi-Implicit Method for Pressure Linked Equations (SIMPLE), SIMPLE-Consistent (SIMPLEC), SIMPLER, SIMPLEX and Pressure-Implicit with Splitting of Operators (PISO).

SIMPLE algorithm uses a relationship between velocity and pressure corrections to enforce mass conservation and to obtain the pressure field. The pressure is unknown and the equations are solved according to the difference between assumed and exact pressures. Since the corrected fields are good for updating velocity (since a mass-consistent flow field is produced) but not pressure (because of the inaccuracy of the approximation connecting velocity and pressure corrections), SIMPLE scheme can be inefficient and requires considerable pressure under-relaxation. SIMPLE algorithms in steady and time dependent calculations are summarized in Figure 2.10 and 2.11 (Ansys Fluent 2009).

SIMPLER acknowledges that the correction equation is good for updating velocity but not pressure and precedes the momentum and pressure-correction equations with an equation for the pressure itself. SIMPLEC seeks a more accurate approximation to correct velocity and pressure changes. For relatively uncomplicated problems in which convergence is limited by the pressure-velocity coupling, a converged solution can be obtained more quickly by using SIMPLEC. For complicated flows involving turbulence and/or additional physical models, SIMPLEC will improve convergence only if it is being limited by the pressure-velocity coupling.

Pressure Implicit with Splitting of Operators (PISO) was originally proposed as a time-dependent, non-iterative pressure-correction. It can be more efficient for time depended calculations on highly skewed meshes. For flows having high Rayleigh number or flows in strongly curved domains, pressure staggering option (PRESTO) scheme can be selected. It uses the discrete continuity balance for a "staggered" control volume about the face to compute the "staggered" pressure. Central difference is used to approximate diffusion terms and relies on PRESTO scheme to find the pressure values at the cell faces. For triangular, tetrahedral, hybrid, and polyhedral meshes, comparable accuracy is obtained using a similar algorithm. The PRESTO scheme is available for all meshes.

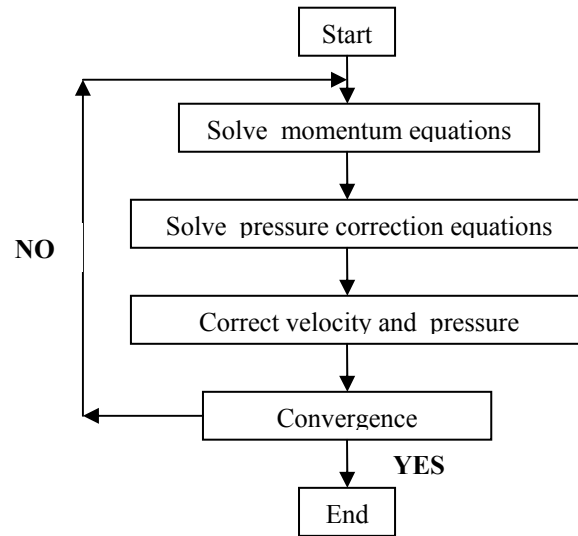


Figure 2.10. SIMPLE algorithm in steady state.
(Source: Ansys Fluent 2009).

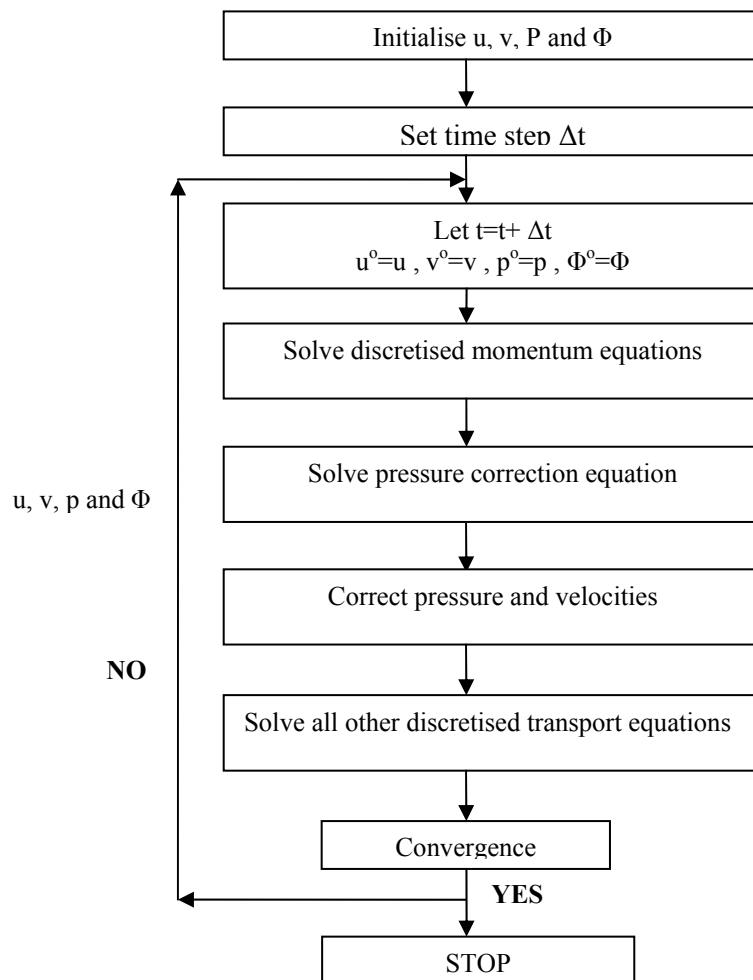


Figure 2.11. SIMPLE algorithm in transient solutions.
(Source: Ansys Fluent 2009).

2.12.7. Selection of Numerical Scheme

Face values of ϕ and $\partial\phi/\partial x$ are found by making assumptions about variation of ϕ between cell centers. Different numerical schemes can be used as given below.

- Central differencing scheme
- First-order upwind scheme
- Power-law scheme
- Second-order upwind scheme.
- QUICK scheme.

In central differencing scheme, the value of ϕ at the face is determined by linear interpolation between the cell centered values as shown in Figure 2.12-a (Bakker 2010). First order upwind schemes assumes that the cell center values of the variables represent the cell-average value and the face values of the control volume have the same value as illustrated in Figure 2.12-b.

The main advantages are that it is easy to implement and that it results in very stable calculations, but it also very diffusive. This scheme provides stability for the discretization of the pressure-correction equation. The first-order scheme is the default scheme for compressible flows. Second order upwind schemes include the second order term of a Taylor series expansion of the PDE's, and they are more accurate. The value of ϕ from the cell values in the two cells upstream of the face as shown in Figure 2.12-c (Bakker 2010).

Although the first-order discretization generally yields better convergence than the second-order scheme, the first-order discretization generally yields less accurate results. Second-order upwind is available in both pressure-based and density-based solvers. When second-order accuracy is desired, quantities at cell faces are computed using a multidimensional linear reconstruction approach. Power law scheme is based on the analytical solution of the one-dimensional convection-diffusion equation. The face value is determined from an exponential profile through the cell values as shown in Figure 2.12-d (Bakker 2010). The exponential profile is approximated by the following power law equation:

$$\phi_e = \phi_P - \frac{(1 - 0.1Pe)^5}{Pe} (\phi_E - \phi_P) \quad (2.89)$$

where Pe is the Peclet number.

In QUICK (Quadratic Upwind Interpolation for Convective Kinetics) scheme, a quadratic curve is fitted through two upstream nodes and one downstream node as given in Figure 2.12-e (Bakker 2010).

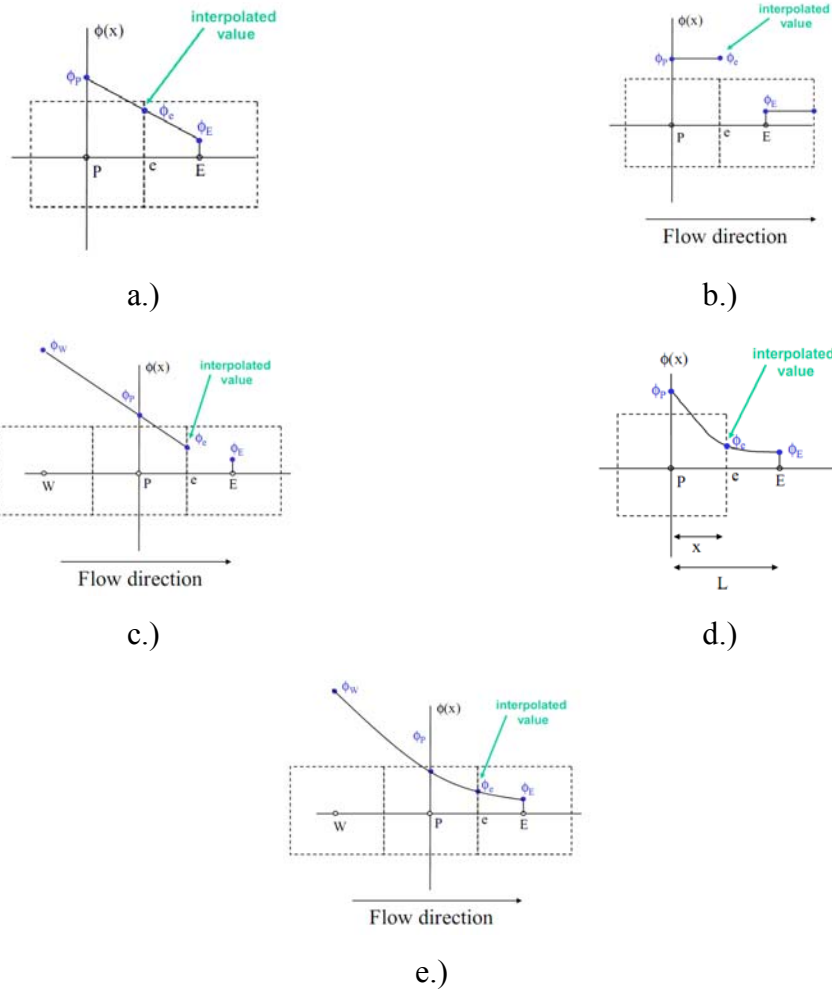


Figure 2.12. Upwind, central differencing, power law and quick schemes. (Source: Bakker 2010).

FLUENT uses an upwind/central differencing scheme, in which the convection terms are solved using upwinding, and the diffusion terms are centrally differenced.

2.11.8. Under-Relaxation Factor Settings

As a result of using nonlinear equations, some problems converge very slowly or not. First of all, it should be checked that all boundary conditions should be reflect real case. In spite of using correct boundary conditions and correct algorithms, convergence cannot be observed; new grid structure should be tried in such circumstances. Controlling the change in unknowns is one of the frequently used solution technique. The new value of a variable (ϕ^{new}) within a cell depends on the old value, ϕ^{old} , the computed change in ϕ , ($\Delta\phi = \phi^{\text{predicted}} - \phi^{\text{old}}$). The new value of variable ϕ in a cell P is calculated from Equation (2.90) at each iteration for any cell (Ansys Fluent 2009).

$$\phi_P^{\text{new,used}} = \phi_P^{\text{old}} + \alpha \cdot (\phi_P^{\text{predicted}} - \phi_P^{\text{old}}) \quad (2.90)$$

Where α is used for under-relaxation factor.

Under-relaxation factors slow down the change of ϕ produced in each iteration. The value of α does not influence the predictions obtained in the final converged solution.

- $\alpha < 1$ is under-relaxation. This may slow down speed of convergence but increases the stability of the calculation, i.e. it decreases the possibility of divergence or oscillations in the solutions.
- $\alpha = 1$ corresponds to no relaxation. One uses the predicted value of the variable.
- $\alpha > 1$ is over-relaxation. Sometimes it accelerates convergence but will decrease the stability of the calculation.

The default under-relaxation factors used in FLUENT and ICEPAK are given in Table 2.2 (Ansys Fluent 2009).

Table 2.2. Default under relaxation factors in FLUENT and ICEPAK.

	FLUENT	ICEPAK
Pressure	0.3	0.3
Density	1	1
Body Forces	1	1
Momentum	0.7	0.7
Turbulent Kinetic Energy	0.8	0.5
Turbulent Dissipation Rate	0.8	0.5
Turbulent Viscosity	1	1
Energy	1	1

Quick convergence can be experienced with higher under-relaxation factors, therefore they should be changed carefully. Lower under-relaxation factors (between 0.8 - 1.0) for temperature can be used when energy field impacts the fluid flow. ICEPAK make an automatic adjustment of under-relaxation factors for robust and fast convergence.

2.11.9. Termination Criteria and Convergence

In case unknowns in the entire flow field do not change significantly from one to the next iteration, “converged” solution is obtained. The iterative process is finished when a converged solution is found. Transport equation for ϕ can be presented in simple form as in Equation (2.91).

$$a_p \phi_p = \sum_{nb} a_{nb} \phi_{nb} + b \quad (2.91)$$

Coefficients a_p , a_{nb} depend on the solution and are updated in each iteration. At the start of each iteration, the above equality will not hold. The imbalance is called the residual (R). Residual at point p is calculated by Equation (2.92).

$$R_p = a_p \phi_p - \sum_{nb} a_{nb} \phi_{nb} - b \quad (2.92)$$

R_p becomes negligible as iterations increase. The residuals can be written as a sum off all cells as shown in Equation (2.93).

$$R = \sum_{cells} |R_p| \quad (2.93)$$

Residuals are usually scaled relative to the local value of the property ϕ in order to obtain a relative error.

$$R_{p,scaled} = \frac{|a_p \phi_p - \sum_{nb} a_{nb} \phi_{nb} - b|}{|a_p \phi_p|} \quad (2.94)$$

They can also be normalized, by dividing them by the maximum residual that was found at any time during the iterative process. An overall residual in the domain is found by Equation (2.95).

$$R^\phi = \frac{\sum_{all\ cells} |a_p \phi_p - \sum_{nb} a_{nb} \phi_{nb} - b|}{\sum_{all\ cells} |a_p \phi_p|} \quad (2.95)$$

All discrete conservation equations are obeyed in all cells to a specified tolerance at convergence. The solution no longer changes with additional iterations. Convergence is controlled by tracking the change in scaled residuals. The converged solution is ensured for residuals less than 10^{-3} for all variables, except for the energy equation, in which the residuals have to be less than 10^{-6} . Depending on the model chosen, the necessary residual level for convergence varies (Ansys Fluent 2009).

From experiences of FLUENT users, first order schemes generally converged adequately when the residual level was set at 0.001. While the second order schemes required a lower residual value. If the initial conditions are close to the final solution, residuals will be small. If the initialization is very different from the final solution, there will be a larger drop in residuals. Generally convergence was monitored by the slope of the residuals and the change of value in monitored point. When the monitored point is stabilized, the solution is accepted converged.

2.11.10. CFD Errors

CFD simulations contain errors or uncertainties. Errors are given below.

- Numerical errors: They result from the differences between the exact equations and the discretised equations solved by the CFD code. Solution error, spatial discretisation error, time discretisation error, iteration error, round-off error is typical numerical errors face in CFD calculations.
- Model errors: They result from models which are used to describe phenomena like turbulence.
- User errors: They result from inadequate use of CFD software.
- Software errors: They are the result of an inconsistency between the documented equations and the actual implementation in the CFD software.
- Application uncertainties: They are related to insufficient information to define a CFD simulation (Menter 2002).

2.11.11. Post-Processing

Visualization of three-dimensional complex geometries, unsteady and turbulent flows can be quite difficult. For such cases, powerful workstations make easy the post processing procedure. In addition, some special software can also be used for generation of velocity vectors, streamlines, pressure or velocity contours, and animation of transient calculations.

CHAPTER 3

STANDARDS ON DETERMINATION OF RADIATORS HEAT OUTPUT

Heat outputs of radiators are determined experimentally. Measurements and special conditions are specified in different standards. However different heat outputs can be obtained by applying different standards even for the same radiator.

3.1. Previous Standards

Up to July 1997, standards named BS 3528, ISO 3146, 3147, 3150, DIN 4722 had been used throughout the world (Ward 1991). According to those standards, radiators had been tested for fixed supply temperature of 90°C. The mass flow rate adjusted until the return temperature is 70°C with the room temperature of 20°C (Ward 1991).

3.2. European Standard EN 442 Part 2

Starting from July 1st 1997, the heat emission of radiators manufactured in countries of European union have been determined in accordance with the EN 442 part 2 standard in which test methods, accuracy of testing and design of the test room are specified. EN 442-2 can be applied only for the heating devices use water or steam at temperatures below 120°C as a medium and supplied with by a remote heat source (European Standard EN442-2).

The standard thermal output of a radiator is defined for reference air temperature of 20°C and an inlet water temperature of 75°C and an outlet water temperature of 65°C in this standard (European Standard EN442-2).

Properties of test room which is a special test set up used for determination of heating capabilities of radiators and calculations are introduced in this section.

3.2.1. The Characteristics of Heater Test Room Specified in EN 442

Heat output of radiators are determined in special test rooms whose dimensions are 4 m (length) X 4 m (width) X 3 m (height). The outer walls are made from sandwich panels whose internal surface temperatures can be controlled. Panels include four components. Two of them (undulating shaped steel sheet and smooth steel sheet) forms water flow channels as shown in Figure 3.1 (European Standard EN442-2). The thickness of smooth and undulating shaped steel sheets are 2 mm and 1 mm, respectively.

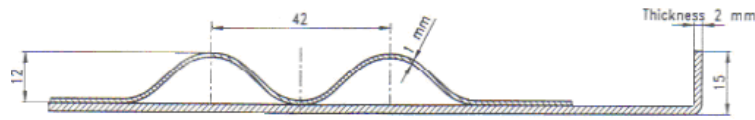


Figure 3.1. Water channels in test room panels.
(Source: European Standard EN442-2)

Smooth sheet faces with the interior of the test room. There is an insulation material around the undulating shaped steel sheet. The thickness of the insulating foam layer is 80 mm. At the outside, there is an external sheet whose thickness is 0.6 mm. The minimum overall thermal resistances of each wall, floor and ceiling are $2.5 \text{ m}^2\text{K}/\text{W}$ (European Standard EN442-2).

The temperatures of internal surfaces are controlled by water which flows through the gaps as shown in Figure 3.2 (European Standard EN442-2). Despite, there is a flow channel inside the outer wall located behind the tested radiator; the water is not circulated through this channel.

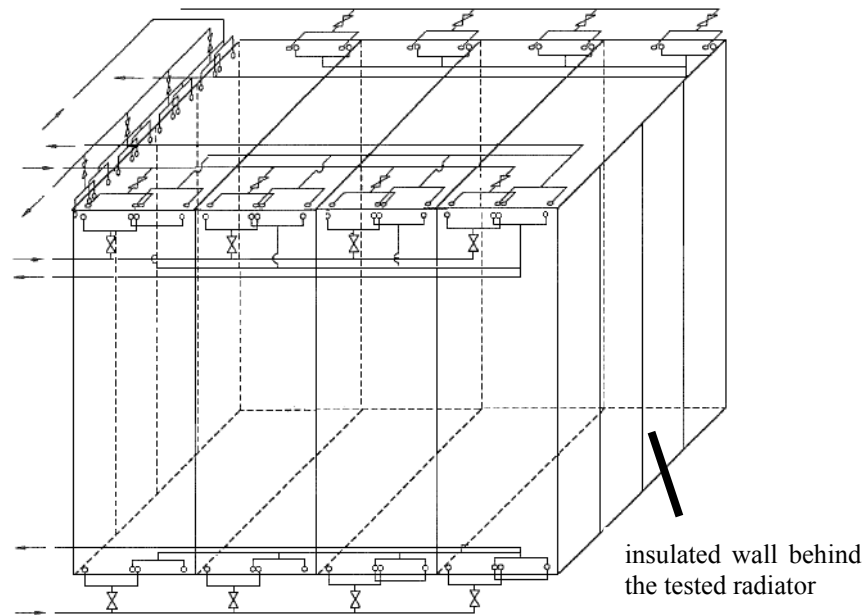


Figure 3.2. Cooling of test room panels.
(Source: European Standard EN442-2)

The test room should be independent from the environment. The only opening is entrance door which is located at the front wall and opposite to the tested radiator. The door is also insulated as described above.

The outside of the test room is not conditioned. In the standard, it is stated that the emissivity of the paint used inside surfaces is to be greater than 0.9 (European Standard EN442-2).

Radiators are placed symmetric and parallel to the wall which is not cooled. The distance between the nearest heat emitting surface of the radiator and the outer wall which is not cooled is 0.05 m. Tested radiator is positioned at a height of 0.110 m above the floor (European Standard EN442-2). Supply and return lines are connected at the same end. Water flows from the top to the bottom of the tested radiator.

3.2.2. The Determination of Standard Characteristic Equation and EN 442 Heat Output

The heat output is calculated from temperature data collected in steady state test room conditions. Therefore the main consideration in the measurements is that whether or not the temperature of a selected point in the room reaches the steady state condition. To make each measurement in equal conditions, the point on the central vertical axis of

the test room, and 0.75 m, above the floor is used as a reference point according to the standard. Also temperatures measured from 0.05 m and 1.50 m above the floor and 0.05 m below the ceiling are used to control whether the steady state conditions are reached (European Standard EN442-2).

The temperature of reference point is used to calculate excess temperature which is used in the determination of characteristic equation of a radiator. Excess temperature is the difference between the average water temperature and reference air temperature. Since mass flow rate remains constant in the measurements, the heating output of a radiator depends on only excess temperature. Equation (1.1) is used as a standard characteristic equation for any type of panel radiator in EN 442 part 2 standard.

There are two options to determine thermal output of a radiator: weighting method or electric method. Weighting method contains the measuring of the water flow rate through the heating device and determining the enthalpy difference between inlet and outlet water passed through the radiator. The uncorrected thermal output (Φ_{me}) is calculated by using Equation (3.1).

$$\Phi_{me} = \dot{m}_w \cdot (i_{in} - i_{out}) \quad (3.1)$$

where \dot{m}_w is the water flow rate, i_{in} is the enthalpy of inlet flow, and i_{out} is the enthalpy of the outlet flow. Figure 3.3 shows a schematic illustration of the experimental set up used for weighting method (European Standard EN442-2).

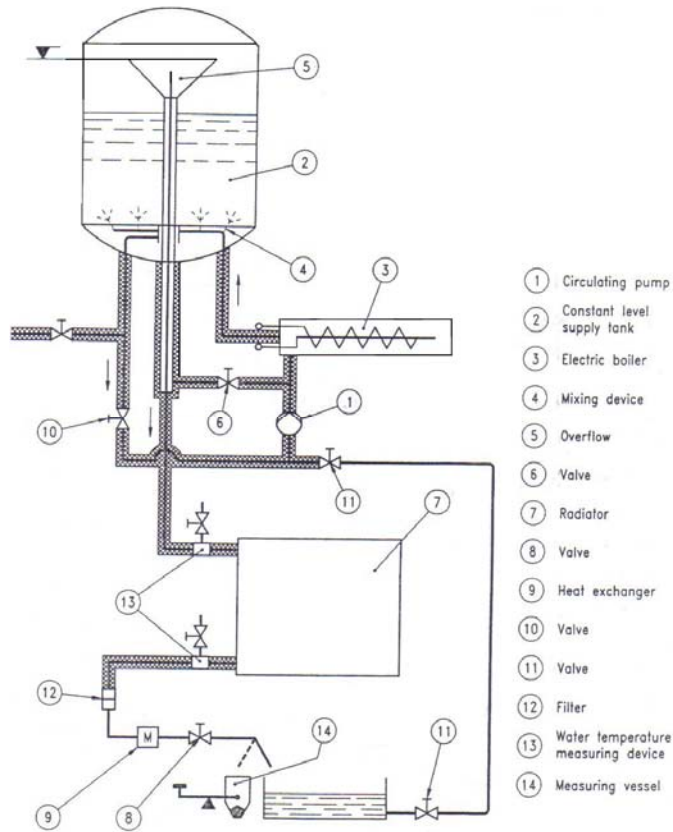


Figure 3.3. Schematic view of test set up when weighting method is applied.
(Source: European Standard EN442-2)

Thermal output depends on the ambient pressure. When it deviates from standard atmospheric pressure, the corrected thermal output (Φ) can be found by Equation (3. 2) (European Standard EN442-2).

$$\Phi = \Phi_{me} \cdot [S_k + (1 - S_k) \cdot f_p] \quad (3.2)$$

Correction factor is calculated by Equation (3.3).

$$f_p = \left(\frac{P_o}{P} \right)^{n_p} \quad (3.3)$$

The radiated heat output factor (S_k) depends only on the type of the radiator while the exponent n_p changes with radiator type and height of the radiator. Exponent n_p is almost independent from the excess temperature. Their values of radiated heat output factor and the exponent n_p are taken from the Table A.1 (European Standard EN442-2).

Values are based on the excess temperature of 50°C, but they can be used for any excess temperature.

Corrected heat outputs are calculated by Equation (3.2) and the excess temperatures (ΔT_e) are used in the determination of standard characteristic equations.

The coefficients of standard characteristic equations are calculated from the least squares regression method. First, the characteristic equation can be written in logarithmic coordinates by Equation (3.4) (European Standard EN442-2).

$$\log \Phi = \log K_M + n \cdot \log \Delta T \quad (3.4)$$

Where $\log K_M$ and n values are calculated from Equations (3.5) and (3.6) or Equations (3.7) and (3.8).

$$\log K_M = \frac{\sum(\log \Phi) \cdot \sum[(\log \Delta T)^2] - \sum(\log \Delta T \cdot \log \Phi) \cdot \sum(\log \Delta T)}{N \sum[(\log \Delta T)^2] - (\sum \log \Delta T)^2} \quad (3.5)$$

$$n = \frac{N \sum[(\log \Delta T \cdot \log \Phi)] - \sum(\log \Delta T) \cdot \sum(\log \Phi)}{N \sum[(\log \Delta T)^2] - (\sum \log \Delta T)^2} \quad (3.6)$$

where

$$K_M = 10^{\frac{A \cdot B - C \cdot D}{N \cdot B - D^2}} \quad (3.7)$$

$$n = \frac{N \cdot C - D \cdot A}{N \cdot B - D} \quad (3.8)$$

where N is the number of test points,

$$A = \sum(\log \Phi), \quad B = \sum[(\log \Delta T)^2], \quad C = \sum(\log \Delta T \cdot \log \Phi) \quad \text{and} \quad D = \sum(\log \Delta T)$$

CHAPTER 4

LITERATURE REVIEW

Internal natural convection is frequently faced phenomena in thermal engineering. In those applications, heated surfaces which dissipate energy dominate air flow in an enclosed space.

Computational fluid dynamics (CFD) methods are useful for the prediction of flow parameters in domains from small enclosures includes electronic equipment to large building spaces in practice. Although some problems require fine grids especially at near wall regions and long run times, computational solutions verified by experimental studies give meaningful results.

Many numerical studies about internal natural convection have been performed and reported with different attentions. Simpler form is two dimensional cavity problems. In computational studies, natural convection along a vertical, heated, flat plate or differentially heated, air-filled, square or rectangular tall cavities with different Rayleigh numbers are explored (Xu et al. 1998). Researches focused on the effects of aspect ratio, oriented angle, conjugated wall, radiation heat transfer, different boundary conditions in two dimensional laminar natural convection problems.

Turbulent natural convection investigated experimentally and computationally in the literature. Conducted experiments and numerical investigations on turbulent flow can be divided into two major categories: turbulent boundary layer flows and turbulent cavity flows. Although, in most cases the flow is three dimensional, two dimensional results are often satisfactory. In many of the analyses interaction of surface radiation and free convection is omitted (Balaji and Venkateshan 1993).

In this section, some important studies which assist for the accomplishment of presented study are summarized.

4.1. Studies on Two Dimensional Heat Transfer and Fluid Flows

Two dimensional natural convection heat transfer problems have been investigated experimentally, analytically, or numerically extensively since 1930 (Leong 1996). Even though many different boundary conditions have been faced in practice, researches dealing with complex boundary conditions are limited in the literature.

Natural convection in two dimensional closed cavities was classified into three groups by Mohamad et al: heating from below and cooling from above (Rayleigh–Benard problem), differentially heating, problems having cross thermal boundary conditions (Mohamad et al. 2006).

Numeric benchmark solutions for two-dimensional laminar natural convection in square and rectangular enclosures with differentially heated vertical walls and insulated horizontal walls were reported in details by Vahl Davis for air and Rayleigh numbers (Ra) of 10^3 , 10^4 , 10^5 , and 10^6 in 1968 (Davis 1968). Maximum Rayleigh number were 2×10^5 for a square cavity and 1.25×10^6 for rectangular cavity whose aspect ratio (height/thickness ratio) is 5. It was assumed that all thermodynamic properties were independent of temperature, and compressibility and dissipation effects were negligible. It was found that at sufficiently high Rayleigh number, the strong vorticity near the walls was able to sustain a weak return motion in the outer part of the boundary layer because of the well established boundary-layer flow. In this region of return flow (near the mid-height of the cavity), the opposite boundary layer was less able to influence that flow.

Markatos and Pericleous (Markatos and Pericleous 1984) solved two dimensional buoyancy-driven laminar and turbulent flows computationally. In that study, the heat transfer in a square cavity with differentially heated side walls with insulated horizontal walls was examined. Horizontal walls were insulated while vertical wall on the left hand side was hot. Rayleigh numbers changed between 10^3 and 10^{16} . The flow was assumed laminar for $Ra \leq 10^6$ or turbulent for $Ra > 10^6$. Radiation and variable property effects were neglected. Reference fluid properties were calculated at the ambient temperature of 20°C. A uniform 30 x 30 grids was found adequate for $Ra = 10^3$, but not for higher values. An improved 30 x 30 grid was used for all Rayleigh number cases up to $Ra = 10^6$, with closer spacing near the walls, to increase boundary layer resolution. 40 x 80, 60 x 120 and 100 x 160 grids were used and grid-independent

results were obtained using 60 x 120 grid for all $Ra \geq 10^8$. For Rayleigh numbers above 10^6 , a two-equation turbulence model $k-\epsilon$ was applied. The ‘SIMPLEST’ algorithm was used instead of “SIMPLE” algorithm in the solution of momentum equations. Heat flux at the wall was calculated by using wall-functions. The three and five point formulae were used for resolving the wall temperature gradient in order to calculate Nu number. According to their study, the five-point formula gave very close results to calculated results for Ra up to 10^8 , but it became erroneous, for the high Rayleigh numbers. Velocity and temperature distributions were also compared in addition to heat flux and Nusselt numbers to understand whether the solution is correct or not. The maximum velocity was seen closer to the wall and its amplitude increased as Rayleigh number increased while the velocity between the two maxima becomes progressively smaller. At Rayleigh numbers greater than 10^6 , reverse flow was observed immediately outside the boundary layers (Markatos and Pericleous 1984). Temperature contours (isotherms) and stream functions found in different Rayleigh numbers are presented in Figure 4.1 and Figure 4.2, respectively (Markatos and Pericleous 1984).

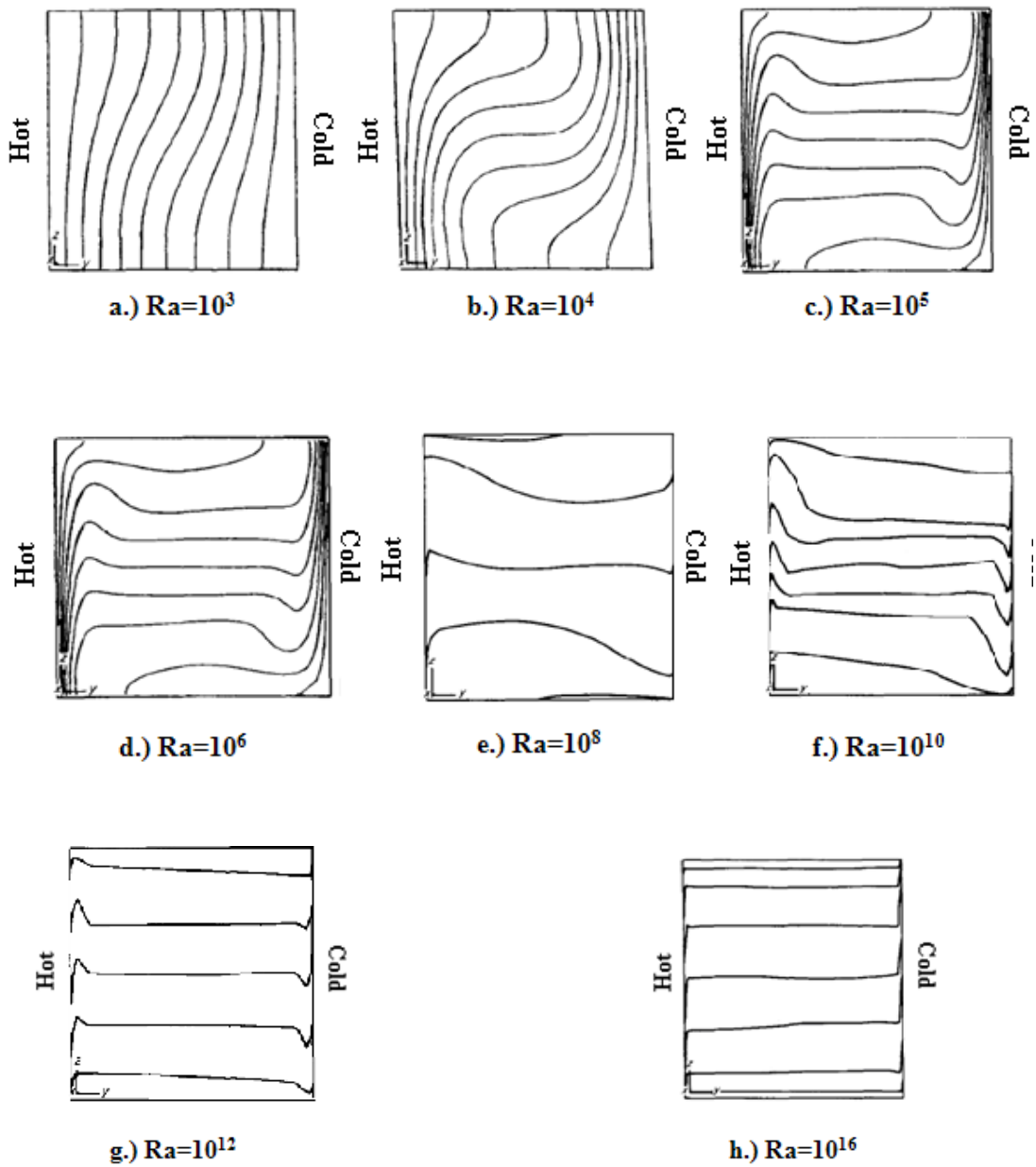


Figure 4.1. Temperature contours (isotherms) at different Rayleigh numbers.
 (Source: Markatos and Pericleous 1984)

Within the thermal boundary layers, the temperature profiles had very steep slope for high Ra numbers, and become steeper as increasing Rayleigh numbers. For those flows, the temperature profiles are almost horizontal at the outside of the boundary layers.

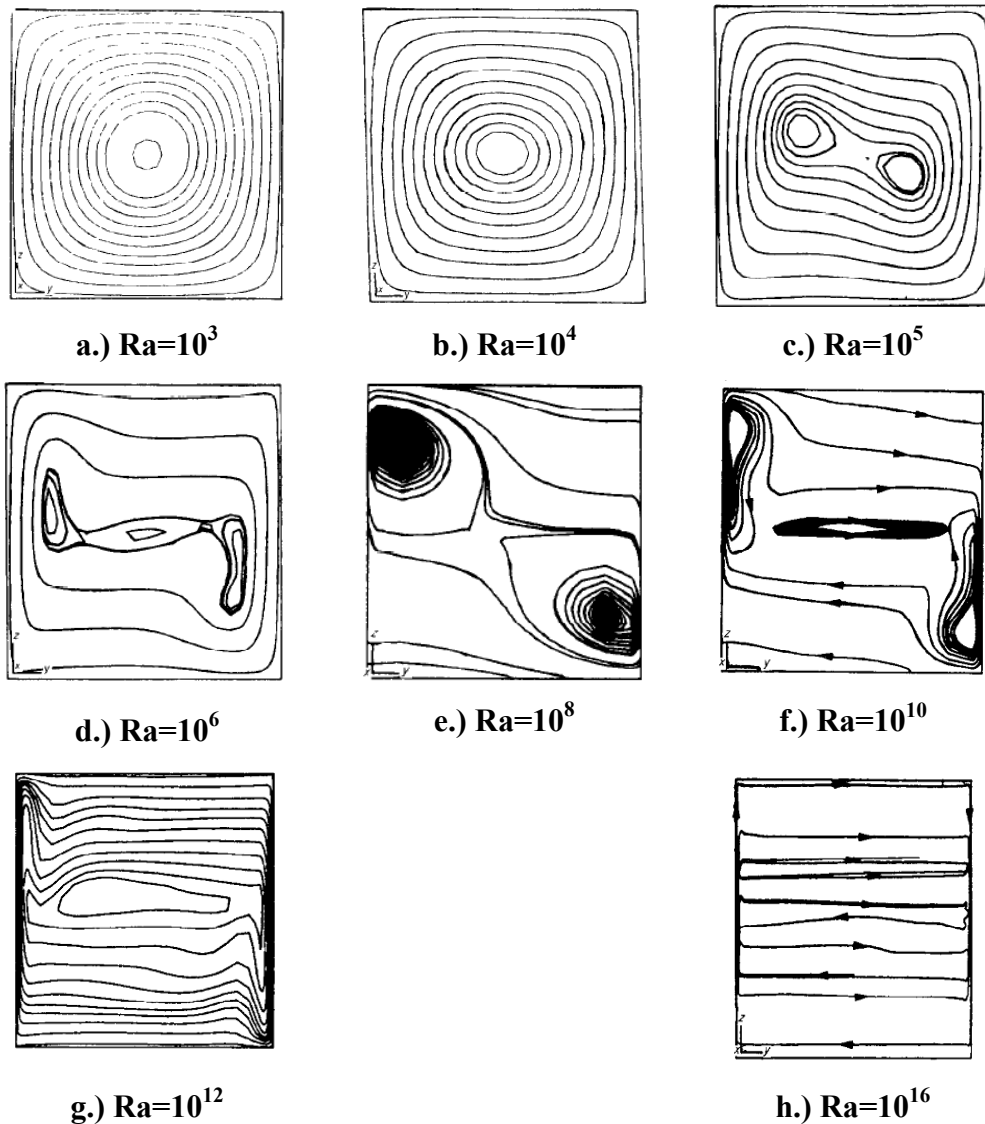


Figure 4.2. Stream functions at different Rayleigh numbers.
 (Source: Markatos and Pericleous 1984).

November and Nansteel studied the natural convective flow in a water filled square enclosure partially heated from below and cooled from one of the vertical wall in 1987 (November and Nansteel 1987). Remaining walls were insulated. Since the small temperature difference between hot and cold walls, Boussinesq approximation was used. Time dependent governing equations were used in dimensionless form. They compared their solutions with the solutions obtained for the enclosure cooled below and heated one of the vertical sides by Kimura and Bejan. They found that high rate of heat transfer occurred even though a substantial portion of the lower surface was insulated. It was also mentioned that Nusselt number reached a maximum when the insulation spans slightly more than half of the lower surface (November and Nansteel 1987)..

Balaji and Venkateshan carried out a numerical investigation of free convection coupled with surface radiation in a rectangular enclosure. They concluded that calculations that include radiation are more realistic, since it is impossible in practice to have a surface with zero emissivity (Balaji and Venkateshan 1993).

In 1995, steady state natural convection analysis in an enclosure heated from below and symmetrically cooled from the sides was conducted by Ganzarolli and Milanez (Ganzarolli and Milanez 1995). The boundary condition for the floor was uniform temperature or uniform heat flux while the side walls were cooled at a uniform temperature. Nusselt number and maximum value of the stream function are related to the Rayleigh number and the influence of the Prantl number was verified. Ra numbers was changed by using the aspect ratio between 1 and 9. By this way, cases with Ra numbers between 10^3 and 10^6 were obtained. Author showed a little influence of the Prantl number on the heat transfer and on the flow circulation inside the cavity. They found that the boundary condition at the cavity floor, uniform surface temperature or uniform heat flux, does not strongly affect the flow or isotherm contours in square cavity.

Steady natural convection of air in a two dimensional enclosure isothermally heated from one side and cooled from the ceiling was analyzed numerically by Aydin et al in 1999. Based on numerical predictions, the effects of Rayleigh number and aspect ratio on flow pattern and energy transport are investigated for Rayleigh numbers ranging from 103 to 107, and for five different aspect ratios of 0.25, 0.50, 1, 2, and 4. The effect of Rayleigh number on heat transfer is found to be more significant when the enclosure is shallow and the influence of aspect ratio stronger when the enclosure is tall and the Rayleigh number is high (Aydin et al. 1999).

Hyun and Lee researched transient natural convection in a square cavity with differentially heated side at large Rayleigh number (between 104 and 106). Dimensionless forms of equations were used (Hyun and Lee 1989). The time dependence of the Nusselt number was determined. It is stated that when Rayleigh number is greater than $Pr4A-4$, where A is the aspect ratio (height/width), a oscillatory behavior was observed for Pr number greater than 1. When $Pr < 1$, an oscillatory approach to the steady state is detected only when Ra is sufficiently high to render a strongly boundary-layer-type flow.

Chang and Tsai examined differentially heated two dimensional square cavity with Ra numbers of 104 and 1010 by using PHOENICS CFD software in 1997 (Chang

and Tsai 1997, 1023). Air was modeled as an ideal gas. Boussinesq approximation and steady state form of governing equations were used. Hot and cold walls were remained isothermal at 250 and 300K, respectively. The standard k- ϵ turbulence model associated with wall function boundary conditions was used. First, 77x77 grid was used to compare calculated results for flow at $Ra=10^4$ and $Ra=10^{10}$ with the results published by Markatos et al. and Davis. They mentioned that their results matched well in maximum velocities and their locations. By using 95x95 grids, almost similar results were found. They solved problem with constant wall temperature and constant heat transfer coefficient cases. With constant heat transfer coefficient at the hot wall, the average wall temperature was used to calculate heat transfer rate. They found a relation equation between mean Nusselt number and Rayleigh number for $10^9 \leq Ra \leq 10^{11}$ and $1 W/m^2K \leq h \leq 10 W/m^2K$

$$Nu = 0.176Ra^{0.146} \left(hW/k_f \right)^{0.502} \quad (4.1)$$

When their results are compared with the results of Markatos, average Nusselt numbers found in both researches were similar at small heat transfer coefficients. The difference increases with the increasing value of heat transfer coefficients. It was observed that the temperature gradient at the hot wall was smaller for constant h case.

Peng and Davidson used k- ϵ and k- ω turbulence models to solve turbulent natural convection in a tall cavity numerically at Ra number of 5×10^{10} (Peng and Davidson 1999). They found that these models exhibit strong sensitivity to number of grids in predicting the transitional boundary layer flow along the vertical wall. They also detected that the grid sensitivity originates from the buoyant source term of the turbulent kinetic energy equation.

An experimental study was published by Tian and Karayiannis in 2000 (Tian and Karayiannis 2000). The dimension of the cavity used in this study was 0.75 m high x 0.75 m wide x 1.5 m deep as shown in Figure 4.3. The hot and cold walls were kept isothermal at 10 and 50°C, respectively. The Rayleigh number was 1.58×10^9 . At this Ra number, low level turbulent flow exists in the cavity. The room (surrounding air) temperature was controlled at 30°C. The hot and cold walls of the cavity were made of 6 mm mild steel plate. The top and bottom walls were made from 1.5 mm mild steel sheet and provided highly conducting boundaries.

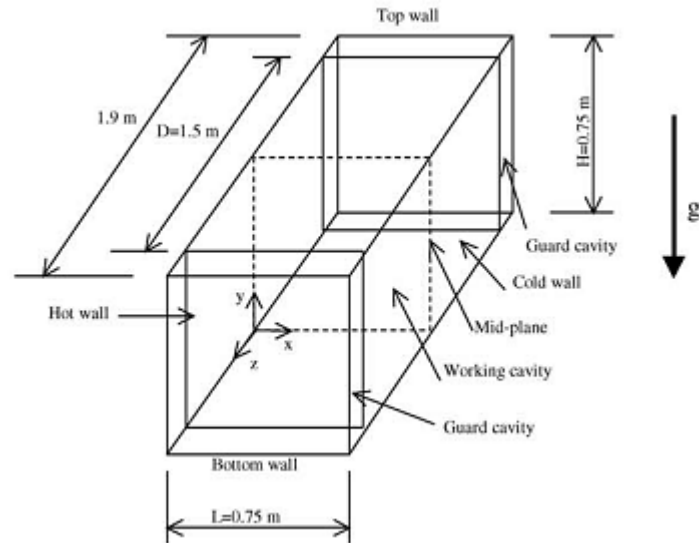


Figure 4.3. Experimental set up performed by Tian and Karaannis.
(Source: Tian and Karayiannis 2000)

The result of this study is given below.

- The flow was limited in a narrow strip along the walls where the velocity and temperature changed sharply.
- In the vertical boundary layer, the velocity reached its maximum value between the buoyant sub-layer and the outer layer and decreased to negative values at the outer edge of the boundary.
- The negative values are the result of four vortices one on each wall lying outside the boundary layer flow.
- Two additional, much smaller vortices were obtained at the hot top and cold bottom corners.
- The fluid in the cavity core was stationary and stratified.
- The temperature distribution in the cavity was nearly anti symmetrical about the cavity centre.
- The local Nu was anti-symmetrical and the agreement between the average value at the hot and cold walls was excellent.

Ampofo and Karayiannis (Ampofo and Karayiannis 2003) carried out same experiment and pointed out that the two dimensional approximation of experimental natural convection in cavities should be valid if the horizontal aspect ratio (AR_z) of the cavity is greater than 1.8. Because aspect ratio on the surface whose normal is z

direction (ARz) was 2 in their study, they mentioned that the flow was two-dimensional at the mid-section. The local velocity and temperature were simultaneously measured at different locations in the cavity by using a laser doppler anemometer (LDA) and a micro-diameter thermocouple.

LDA system consists of a laser, fiber optics, frequency shifter, signal processor, traversing system and a computer as seen in Figure 4.4. Velocity of a point is measured by using LDA system. Probe is moved after each measurement to next position. By moving the probe spatial distributions can be created. In LDA the laser beam is first divided into two beams with equal intensities. The beams are then directed to optical fibers which deliver them to the probe optics. The focal length of the probes front lens determines both the size and position of the crossing point of the two beams. Optics is used to guide the two laser beams into the measurement point where the beams cross each other. Thus the measurement volume formed by the laser beams is an ellipsoid. The beams crossing with each other form interference fringes, so that there are high intensity planes of light and between them low intensity planes which are perpendicular to the laser beam plane. The spacing between the planes is determined purely by optical parameters of the setup, namely the laser light wavelength, and the angle between the beams. The flow is seeded with small particles, which can follow the turbulent motion of the fluid. When these particles pass by the measurement volume they scatter light. The intensity fluctuation of the scattered light depends on the velocity of the particle. The time dt can relative easily be measured and then it is very simple to calculate the velocity of the particle by dividing the traveled distance d_r by the spent time dt (Laser Doppler Anemometry 2010).

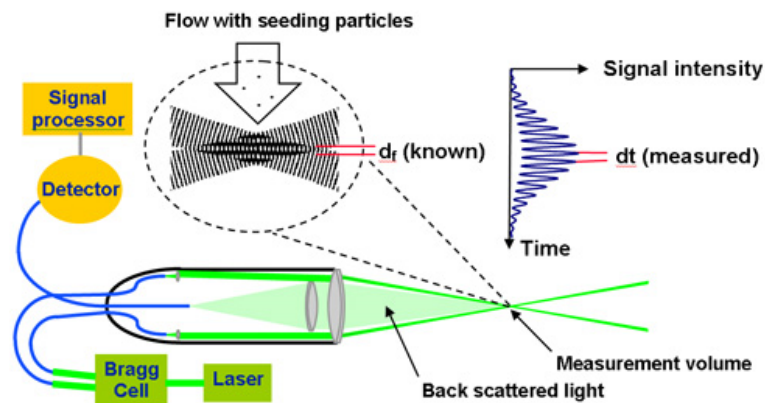


Figure 4.4. The Principle of a laser doppler anemometer.
(Source: Laser Doppler Anemometry 2010)

The authors performed an energy balance for the cavity. On the whole, heat transferred from the hot and bottom walls into the cavity were 98.12 and 21.67 W, respectively. The net heat losses from the cold and top walls were 97.77 and 22.53 W, respectively. The dimensionless temperature at the core of the cavity was 0.52, which is nearly equal to the mean temperature of vertical walls and the ambient temperature (30.7°C).

The average Nusselt numbers were 62.9, 62.6, 13.9 and 14.4 for the hot, cold, bottom and top walls, respectively. The change in Nusselt number is given in Figure 4.5 (Ampofo and Karayiannis 2003). The result of this study was used in verification of two dimensional natural convection.

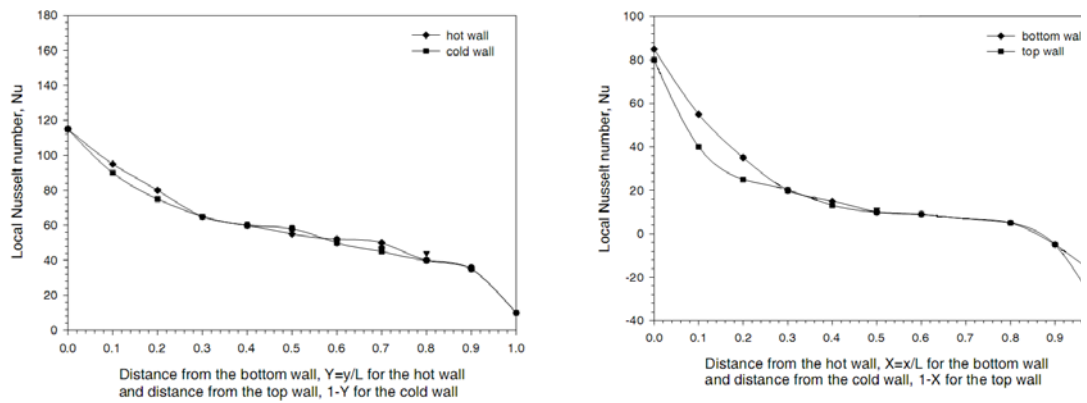
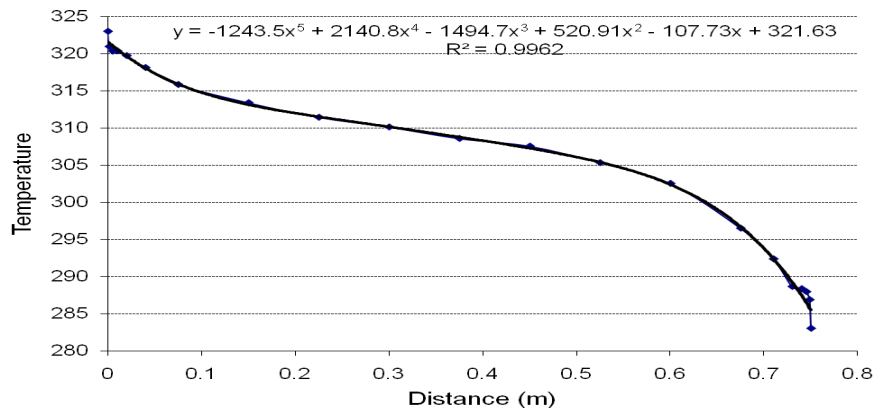
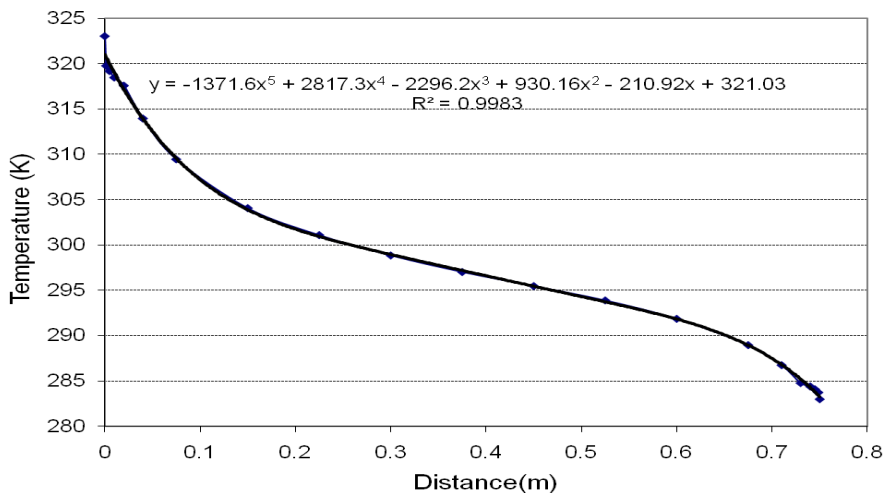


Figure 4.5. Local Nusselt numbers on vertical and horizontal walls found by Peng and Davidson (Source:Ampofo and Karayiannis 2003)



a.) Top wall



b.) Bottom wall

Figure 4.6. Wall temperatures found by Ampofo and Karaannis.

The local Nusselt numbers on each wall in the cavity were compared with the numerical results of Peng and Davidson for the same parameters (Peng and Davidson 1999). The numerical results of Peng and Davidson yields lower heat transfer rates than the experimental results. The agreement between the experimental results and numerical results presented by Peng and Davidson for the local Nusselt numbers along both the bottom and top walls of the cavity was acceptable. Vertical velocity near the hot wall was also examined in that study. Their finding is illustrated in Figure 4. As shown in this figure, vertical velocity increases steeply from the isothermal hot wall to a peak at $x=5$ mm and then decreases rapidly to zero at about $x=80$ mm from the hot wall. The profile of vertical velocity near the cold wall was almost anti-symmetrical at mid-height of the cavity.

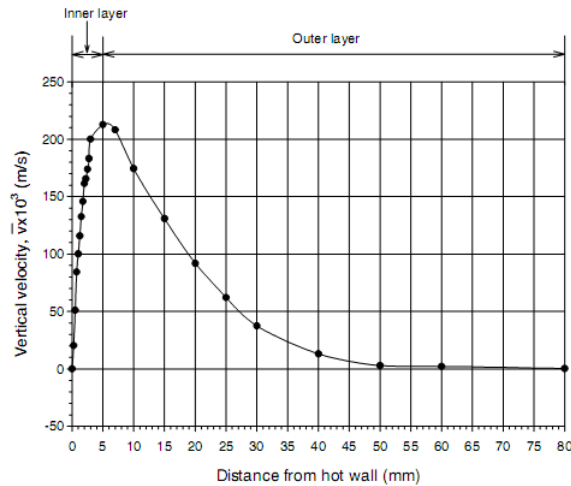


Figure 4.7. Vertical velocity profile near the hot wall.
(Source: Ampofo and Karayiannis 2003)

Ampofo and Karayiannis stated that mean quantities in the cavity was estimated by the $k-\epsilon$ model reasonably but the fluctuation and turbulence quantities cannot be predicted.

Zitzmann et al performed a numerical and experimental study on a cavity whose dimensions were 0.75 m height x 0.75 m width x 0.01 m depth, Rayleigh number of 1.56×10^9 and the results of the experimental study were compared with numerical solution (Zitzmann et al. 2005). They used $k-\omega$ turbulence model in their numerical analysis. For the $k-\omega$ model, velocity and temperature profiles were in good agreement with experiments and deviated only for the peak velocity and temperatures.

Another numerical study was performed by using ANSYS CFX software by Rundle and Lightstone (Rundle and Lightstone, 2007). The dimensions and temperature difference were chosen to yield the Rayleigh number of 1.58×10^9 . An expanding 80x80 and 140x140 grids were used. Uniform grids of 20x20 to 320x320 were also used but converged solutions were not obtained. Three different turbulence models ($k-\epsilon$, Wilcox $k-\omega$ model, Shear Stress Transport $k-\omega$ model) were tried. It was stated that by using $k-\epsilon$ turbulence model a converged solution was not gathered. They found that vertical velocity field outside of the boundary layer correctly predicted by using standard models. The Wilcox $k-\omega$ model's velocity profile had a similar width and peak velocity to the benchmark solution within the boundary layer. The peak velocity difference was smaller than the experimental uncertainty, less than 0.01%. The Stress Transport $k-\omega$ model's boundary layer was significantly thinner and had a peak velocity

that was 19% larger than the benchmark. They concluded that Wilcox $k-\omega$ model predicted the velocity profile accurately.

Beck (Beck et al. 2004) studied on the enhancement of the heat transfer by use of either one or two high emissivity sheets placed between the interior surfaces of a double radiator in 2004. They conducted experiments and two models were compared by using CFD software Fluent with the experiments. Due to time and space constraints, only two dimensional models having non-linear grid with a higher mesh concentration behind the radiator solved. Two radiators connected in series were used in the experimental set up shown in Figure 4.8 (Beck et al. 2004). Radiators were 600 mm high by 600 mm wide. Different distances between single radiators were taken into consideration.

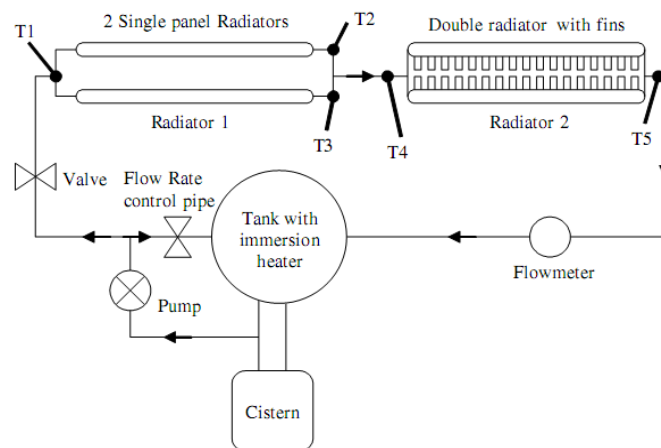


Figure 4.8. Experimental set up performed by Beck.
(Source: Beck et al. 2004)

Since only the heat transfer between the inside surfaces of the radiators was investigated, the outside surfaces of the panels were insulated to a thickness of 50 mm with expanding foam insulation with a thermal conductivity of $0.04 \text{ Wm}^{-1}\text{K}^{-1}$. The three different configurations shown in Figure 4.10 were tested using different spacing of panels and sheets (Beck et al. 2004).

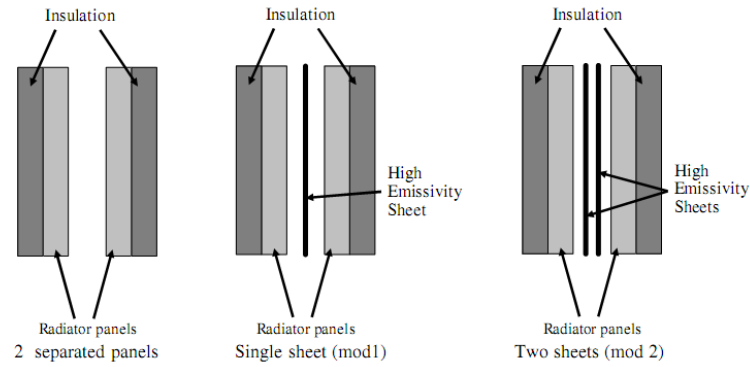


Figure 4.9. Configurations investigated by Beck.
(Source: Beck et al. 2004)

A two dimensional model of a 4 x 3 m environment was created by using a non-uniform grid structure. The grid density is higher around the radiator and the wall areas. The grid contains 56 124 cells, 112 981 faces and 58 856 nodes. Panel surfaces were remained at 70°C while room walls were held at 20°C. The surface of sheets located between panels were kept at 50°C which was the temperature measured at experiments. The k-epsilon turbulence model and the standard wall function were used (Beck et al. 2004). The near wall treatment used the standard wall function model with buoyancy terms. The discrete transfer radiation model was implemented. Because of difficulty in converging, a laminar model was used until the residuals were all below 10^{-2} and then turning on the turbulence meant that the models converged in between 25 and 30 000 iterations. Decreasing the under-relaxation helped to stabilize the convergence and ultimately, all of the residuals were brought below 3×10^{-4} . At the end of this study, it was seen that the heat output vary very little for different panel spacing. It was also presented that a single sheet raises the heat output by almost 40 % and that two sheets raise the output by 60 %. The peak velocities near the original panels were increased by the buoyancy effect of the added panels (Figure 4.10). Increased velocity decreased the thickness of the boundary layer on the heated panel and increased the heat transfer to the air (Beck et al. 2004).

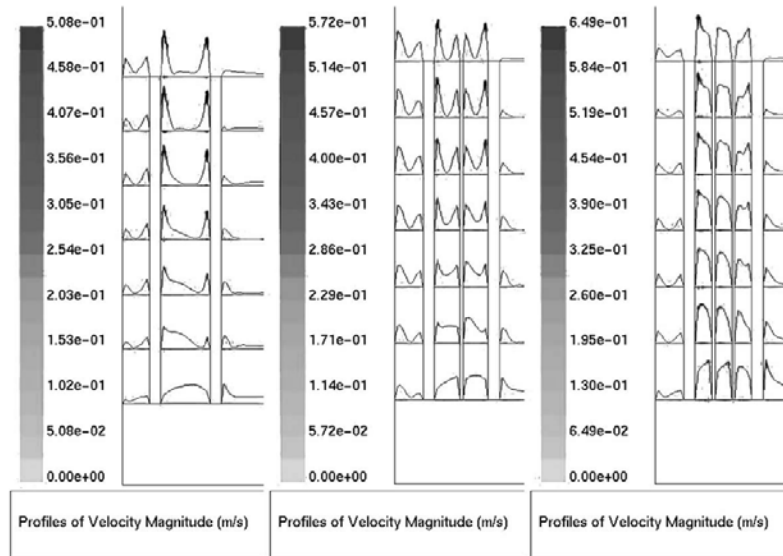


Figure 4.10. Velocity profiles with no, one and two sheets in the gap.
(Source: Beck et al. 2004)

Two separated sheets of a high emissivity placed between the panels can produce between 71 % and 88 % of the heat output of a radiator with double panel and double fin. Since they heat up by radiation and then transfer this heat to the air by free convection. In effect, the surface area that can transfer heat to the air is increased.

4.2. Studies on Three Dimensional Heat Transfer and Fluid Flows

Computational solutions of three dimensional fluid flows began with the simulation of ventilation of rooms or buildings. Also there are researches performed for other three dimensional enclosures.

Air flows in conventional turbulent type clean rooms were simulated by Murakami and Kato in 1989 (Murakami and Kato 1989). Three types of room were examined in that study. Room models, 1/6 of full scale, were used for experiments. The width of the supply outlet was 0.1 m. The height of all types of room was dimensions of the model were 0.1 m and 0.45 m (height). The velocity of the jet from the supply outlet is set to 6 ms^{-1} . Air velocity was measured and the airflow in the room model was also visualized. In numerical study, a staggered mesh system was applied. Velocity components were defined at the centre of the cell surfaces and scalar quantities were set in the centre of the cell. For momentum equations, the central difference scheme was

adopted for both the convective terms as well as other terms. The QUICK scheme, a second order up-wind scheme for convective terms, was partially adopted only near the exhaust inlets in order to remove the numerical instability. For transport equations of scalar quantities, the QUICK scheme is adopted (Murakami and Kato 1989).

Awbi (Awbi 1989) predicted the velocity and temperature distribution for a test room which was designed for evaluating the performance of ceiling diffusers in 1998. The air flow and heat transfer in two dimensional enclosures and the three dimensional flow of a wall jet over surface mounted obstacles were observed. The room had a square floor of length 4.2 and height 2.8 m. The air was supplied from a 24 mm continues slot diffuser in the ceiling spanning the width of the room and at a distance 1.2 m from the wall. A uniform load distribution occurs over the floor area. Two equation turbulence model ($k-\epsilon$) was used. For the two dimensional case, a non-uniform grid was used to produce very fine grid near the internal surface and a coarse grid in the central region. The size of the grid in the x and y directions was 42x38, respectively. In 3-D case, non-uniform grids were used in the x and y directions and a uniform grid in the z direction (20x20x11). The velocity and temperature distributions in the occupied zone of the room for different air flow rates and supply temperature is given in the study. The predicted velocity profiles are close to the experimental profiles except near the floor where the predicted values are higher particularly for the isothermal tests.

A CFD simulation of airflow and temperature field in a heated room which includes a cold surface (window) is located above a hot surface (radiator) was investigated by Weizen Lu et al in 1997 (Weizen 1997). The dimensions of room, window and ceiling were 4.74 m x 2.7 m x 3.45 m (LxHxW), 1.6 m x 2.2 m (h_wxw), and 0.6 m x 1.1 m, respectively. The room was not well insulated and heat losses existed. The effective heat flux from the hot surface was 440 W/m². The flow domain was divided into 33 x 20 x 23 cells. The outside environmental temperature and average room temperature were -3°C and 22°C. The standard k-epsilon turbulence model was applied. Computations were carried out by using a commercial CFD code, CFDS-FLOW3D. The airflow and temperature distributions in several planes were presented. They compared their results with the experimental data from the literature. They observed that some of the hot air flows along the ceiling surface and some disperses downwards due to heat exchange. A large circulation is formed under the ceiling due to the mixing of hot and cold air. A downdraught flow is formed at the cold surface to the radiator. The flow was axisymmetrical about the centre line plane. The air movement in

examined planes was separated into two main regions: the upper warm counterclockwise circulation and the lower cool clockwise circulation. The flow between these two regions was mainly towards the hot wall jet.

A transient simulation was performed by using three software simultaneously in order to model heating systems and radiators by Gritzki (Gritzki 2007). Thermal building simulation code TRNSYS was used for the heat transfer from the surrounding walls by radiation and heat conduction. The indoor air flow simulation code ParallelNS was used for the air flow calculation and Fluent was used in order to simulate the interior flow of the radiator. Two different radiator types, a multi-section radiator and a simple fluted radiator were modeled. For the discretization of the boundary condition exchange and the radiation exchange the test chamber walls are divided into small tiles (0.5 m x 0.5 m). In case of the fully coupled simulations the radiators are also divided into a large amount of very small tiles. Based on the Reynolds-averaged Navier - Stokes equations for incompressible non-isothermal fluids two different turbulence models (which include two and four extra equations) were used for calculating the effects of turbulence in air flow calculation. In the case of the k- ϵ model developed boundary layer approximations was applied to rigid walls to calculate the heat transfer. The discrete model was created by means of Finite Element method, based on linear tetrahedron elements. The radiator was completely modeled and simulated by use of the commercial CFD code FLUENT. The simulations were performed unsteady until steady state conditions were reached. Results regarding the thermal behavior of the radiator, especially the value of the thermal output are in very good agreement with the standard values given by the manufacturer. The differences between measured and simulated thermal output in all investigated cases were less than 5 %. Wall temperatures of fully coupled radiator models are presented in Figure 4.11 (Gritzki 2007).

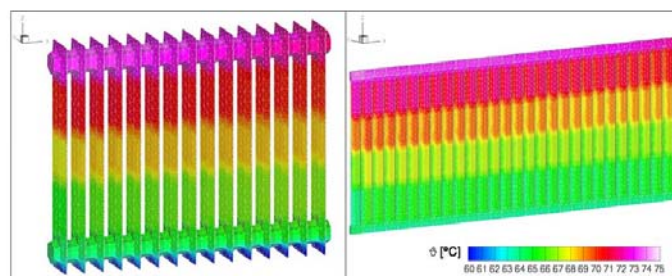


Figure 4.11. Wall temperatures of the fully coupled radiator models.
(Source: Gritzki 2007)

Simulation results are summarized in Tables 4.1 and 4.2 (Gritzki 2007).

Table 4.1. Results of simulation performed by Gritzki for the first radiator model.

	Tinlet (°C)	Toutlet (°C)	Mass flow rate (kg/h)	Thermal output (W)
Simulation	75	65	70.02	815
Reference	75	65	69.68	810

Table 4.2. Results of simulation performed by Gritzki for the second radiator model.

	Tinlet (°C)	Toutlet (°C)	Mass flow rate (kg/h)	Thermal output (W)
Simulation	75	65	81.10	945
Reference	75	65	80.64	938

Some experimental studies had been performed according to previous standards. Schlapmann (Ward 1991) calculated the heat outputs of radiators for conditions other than the standard conditions by using Equation (4.1).

$$\frac{Q}{Q_o} = \left(\frac{T_m}{T_{mo}} \right)^n \quad (4.1)$$

where o denotes the standard test condition.

The heat output of a panel radiator measured by Schlapmann over a range of temperature differences and flow rates (Ward 1991). It was concluded that the heat output could be expressed for all radiators by Equation (4.2).

$$\frac{Q}{Q_o} = \Phi \left(\frac{\Delta T_m}{\Delta T_{mo}} \right)^{n\psi} \quad (4.2)$$

Where the exponent n is 1.3.

The correction factors Φ and Ψ are dependent on the flow rate and connection type. The changes of Φ and Ψ were presented by Schlapmann in different type of connections.

Schlandlong and Barraud (Balaji and Venkateshan 1993) expressed heat output of radiators by Equation (4.3).

$$Q = B(\Delta T_1)^n m^n \quad (4.3)$$

With regard to their study, the value of m is change according to radiator type. As an example for convectors, it is 0.2. The value of n is 1.3 for most cases (Ward 1991). Ward tested a single panel radiator and a double convector type radiator with top-bottom opposite end and bottom opposite end connections in a test facility similar to recommended in BS 3528. Each radiator was tested for the six flow rates 10, 20, 30, 40, 50 and 60 lh^{-1} and for the three different water flow temperatures 80, 60, 40°C in at steady state conditions (Ward 1991). He gave diagrams for the heat outputs for each radiator type. By using these diagrams, the heat output ratios can be calculated for mass flow ratios, temperature difference between supply line and room and temperature difference between return line and room. It was concluded that at low mass flow rates and low temperature differentials, the output characteristics change from those at higher values (Ward 1991).

CHAPTER 5

EXPERIMENTAL STUDY

Heat outputs of radiators in different operating conditions are determined after tests performed for three different excess temperatures in standard test rooms specified by EN 442 part 2. Heat output of radiators with regard to test performed for the excess temperature of 50°C is called standard heat output of radiator. In this chapter, experimental studies performed in the standard test room are explained.

5.1. Test Procedure

Three types of radiators whose height and length are 600 mm and 1000 mm, respectively were tested in the experiments. Tested radiators shown in Figure 5.1 did not include top grilles and side panels. Therefore tested values were different from the catalog values of same radiators which include those additional parts.

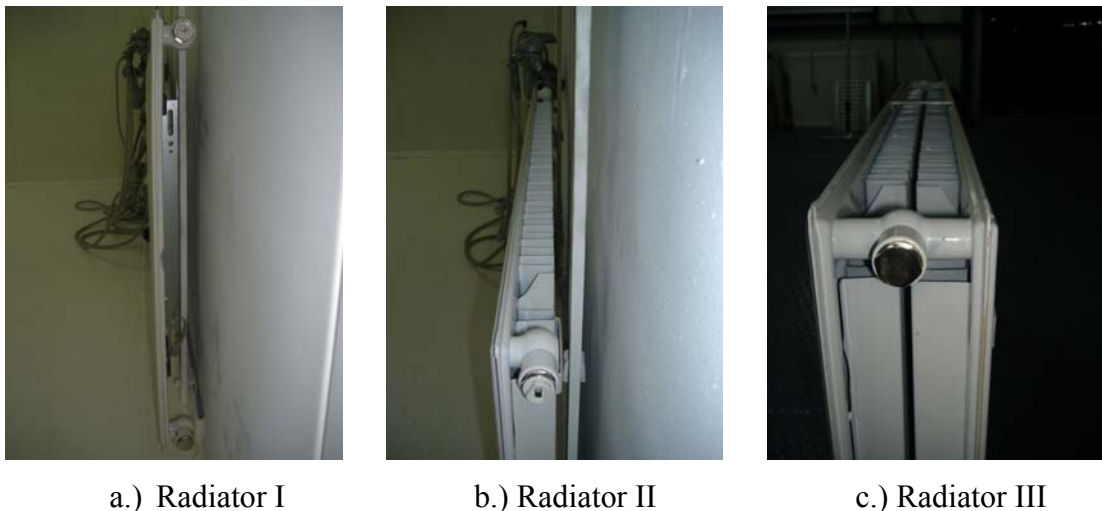


Figure 5.1. View from tested radiators.

At the beginning of each test, radiator which was being tested were fixed to proper place as illustrated in Figure 5.2 and described in EN 442 part 2 standard.



Figure 5.2. Placement of a radiator during a test procedure.

All measurements were conducted in the steady state condition. The steady state condition was followed with controlling the reference point temperature. Holding the test room on desired conditions was notoriously difficult because of number of parameters controlled simultaneously during tests. Figure 5.3 shows the measurement of reference point.



Figure 5.3. Measuring of air temperature inside the test room.

Tested radiators were attached to the circuit by using flexible connections having two temperature sensors on them. Additional temperature measuring devices connected to inlet and outlet of the radiator was used to show the reliability of the measurements. The thermal outputs of radiators were determined according to weighting method defined through the standard in this study. Water circulated in the system was heated by an immersion heater placed in the tap water tank. Water flow rate was adjusted manually by a valve which was installed outside of the test room.

Flexible connections were insulated. Therefore, all energy was transferred only from the tested radiator in the test room. The quality of these insulations was controlled

by using a thermal camera during test periods. The view which shows that there is not any heat loss is presented in Figure 5.4.

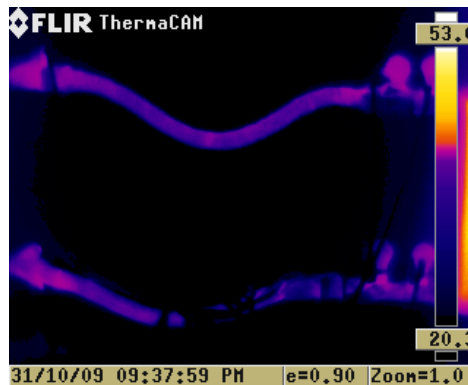


Figure 5.4. Thermal camera view from the flexible connections.

The accuracy in air pressure measuring was ± 0.2 kPa (2 mbar). The uncertainty for the excess temperature was ± 0.1 K. A weighing machine with a maximum error of 2 g at 10 kg was used to measure the water collected in the measuring vessel.

The temperature around the test room was 20°C during the tests. Three different tests for the excess temperatures of 50°C , 60°C and 30°C are required to find the characteristic equation of a radiator. Tests are named as Case 1, Case 2 and Case 3, respectively in this study. Twelve measurements were carried out in each case with regard to EN 442 part 2.

First the radiator inlet temperature was set into 75°C in the test realized for the excess temperature of 50°C (Case 1). The outlet temperature and temperature of reference point were followed. When steady state temperature had been obtained, twelve measurements were performed. The difficulty of the experiment arisen from the efforts to maintain the stability of measured values. In these twelve measurements, the excess temperature changed only $\pm 2.50^{\circ}\text{C}$. It is also stated that the temperature of reference air shall not change more than 1°C from one measurement to next. After accomplishment of test for the excess temperature of 50°C , tests for the excess temperatures of 60°C (Case 2) and 30°C (Case 3) were performed, respectively. The water flow rate measured in the first test was used in the remaining tests with the tolerance of $\pm 0.50\%$.

In this research, the tolerance value of ± 0.50 was used for the excess, reference, inlet and outlet temperatures in the measurements. Water inlet temperature was set only at the first test (Case 1). During the tests carried out for the excess

temperatures of $60^{\circ}\text{C} \pm 0.50$ (Case 2) and $30^{\circ}\text{C} \pm 0.50$ (Case 3), the inlet and outlet temperatures were not set in to any values.

5.2. Measured Values

Continuously controlled parameters were mass water flow rate, reference air temperature, inlet and outlet water temperatures in the tests performed with regard to standard. They were kept in certain tolerance values. The flow rates read in steady state conditions are presented in Figure 5.5, 5.8 and 5.11. The reference air temperatures in steady state conditions for three different cases are presented in Figure 5.6, 5.9 and 5.12. Mean water temperatures in steady state conditions are given in Figures 5.7, 5.10 and 5.13.

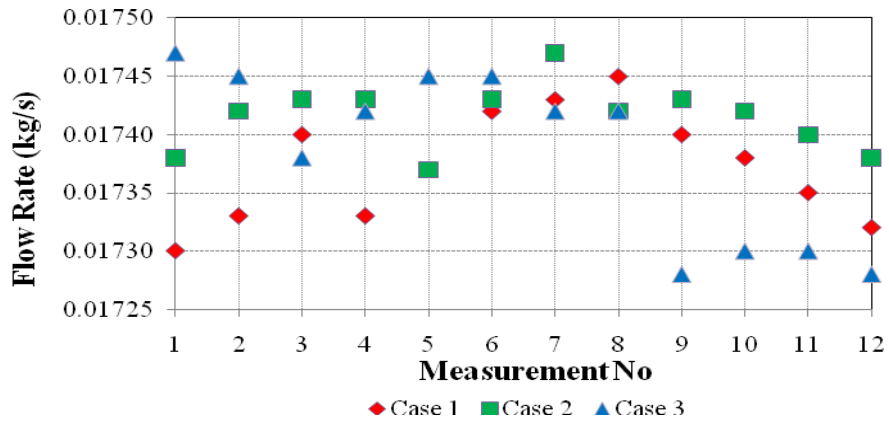


Figure 5.5. Flow rates in tests of radiator I.

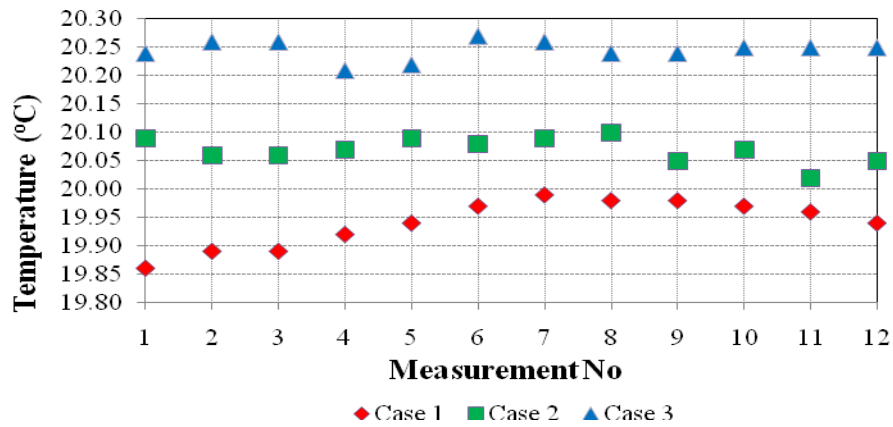


Figure 5.6. Reference air temperatures in tests of radiator I.

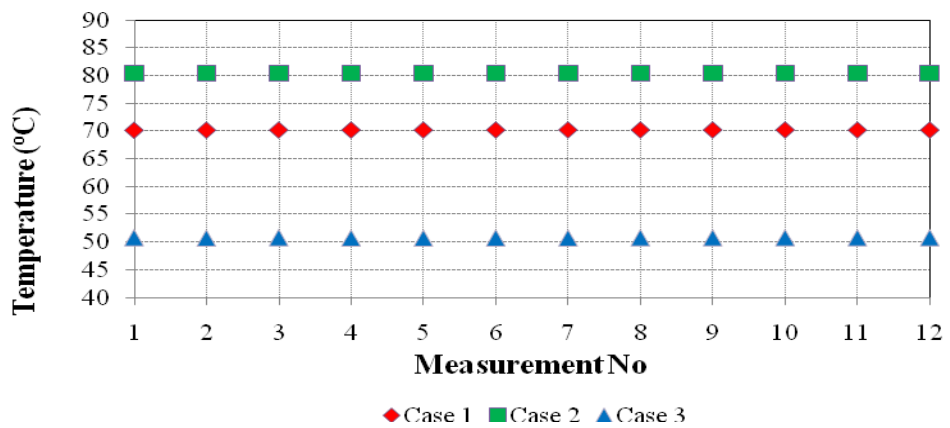


Figure 5.7. Mean water temperatures in tests of radiator I.

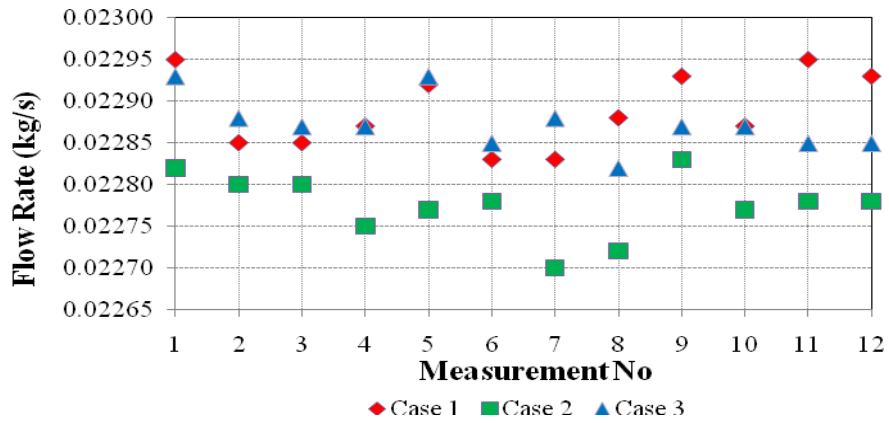


Figure 5.8. Flow rates in tests of radiator II.

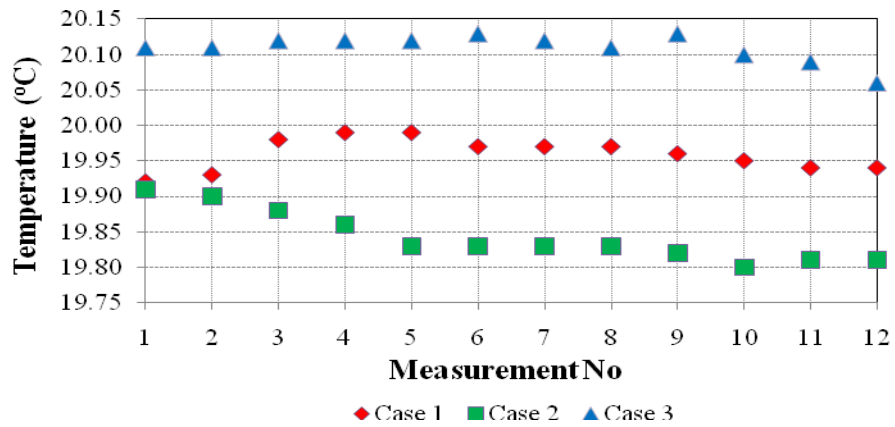


Figure 5.9. Reference air temperatures in tests of radiator II.

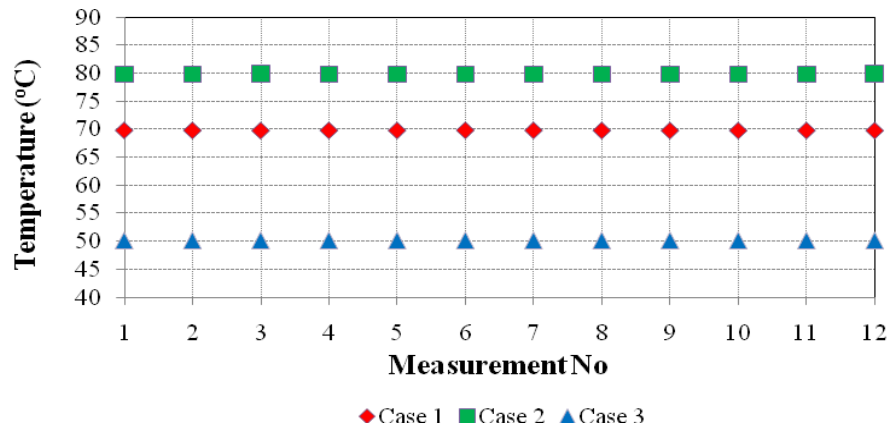


Figure 5.10. Mean water temperatures in tests of radiator II.

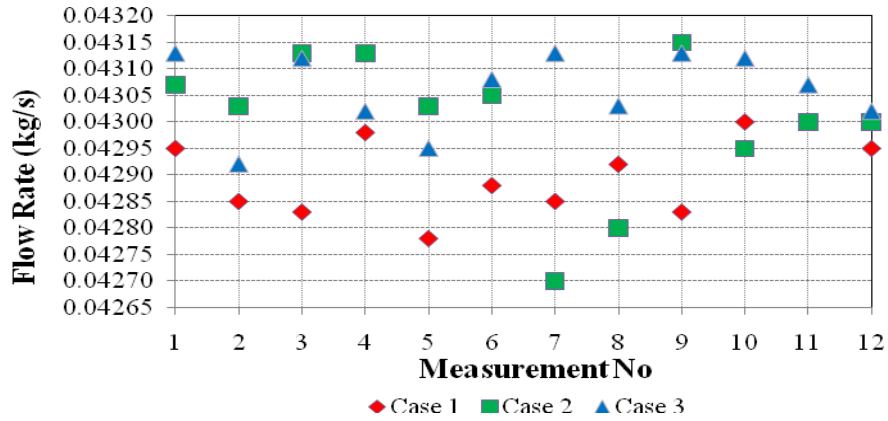


Figure 5.11. Flow rates in tests of radiator III.

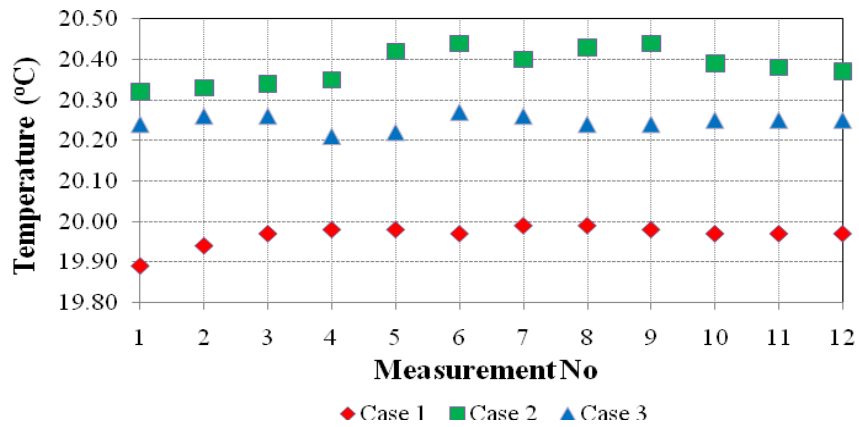


Figure 5.12. Reference air temperatures in tests of radiator III.

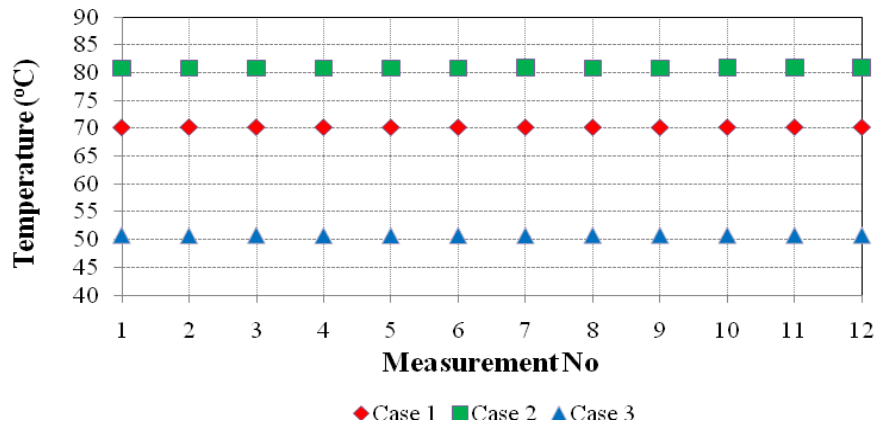


Figure 5.13. Mean water temperatures in tests of radiator III.

The surface temperatures of front faces of tested radiators were also observed by a thermal camera during the tests. The screen views which were taken during tests of radiator I are given in Figure 5.14. The temperature distribution was not uniform on the

front surface of the radiator I and the temperature was decreasing to the lower part of the front surface. Similar temperature distributions are observed in radiator II and radiator III.

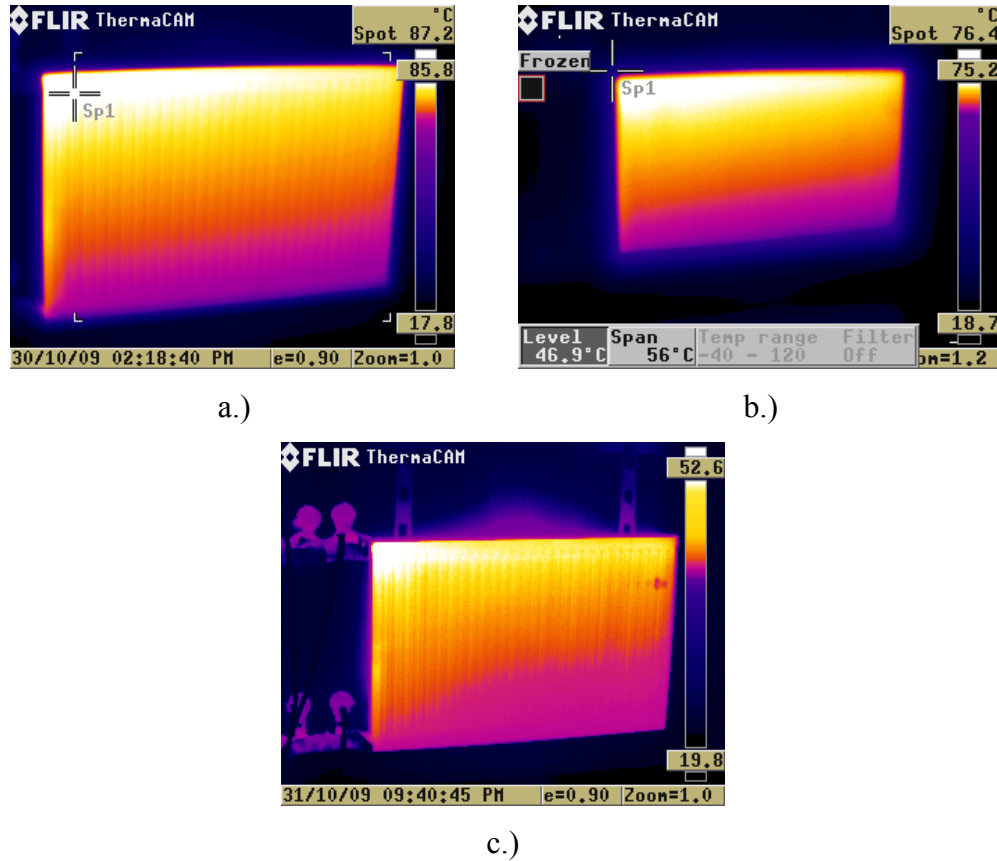


Figure 5.14. Temperature distributions on the front surface of radiator I.

5.3. Calculation of Experimental Heat Outputs

Mass flow rate found in the first case was settled at the beginning of Case 2 and Case 3. Experimental heat outputs of tested radiators were found by using Equation (5.1). Results are given in Tables 5.15, 5.16 and 5.17.

$$\Phi_{\text{exp}} = \dot{m}_w c \Delta T \quad (5.1)$$

Values of mass flow rate, specific heat and temperature differences are presented in Tables B.4, B.7 and B.10 for Case 1; Tables B.5, B.8 and B.11 for Case 2; and Tables B.6, B.9, and B.11 for Case 3 in Appendix B.

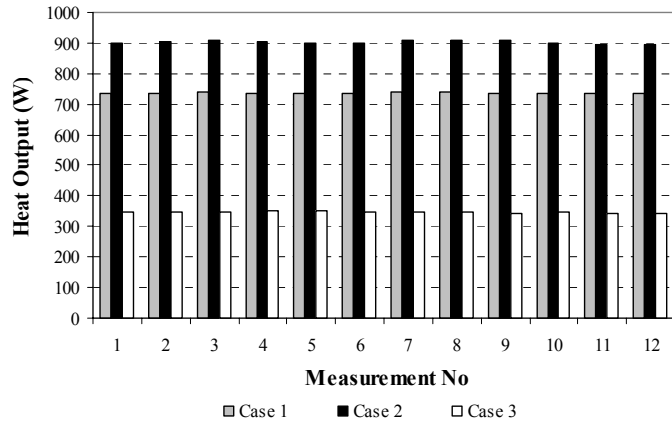


Figure 5.15. Experimental heat outputs of radiator I (W).

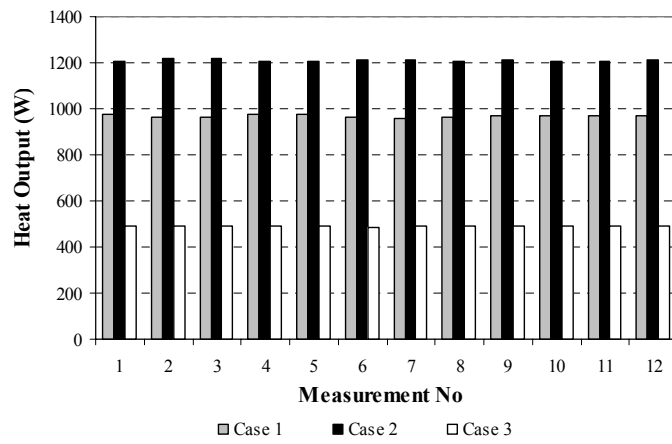


Figure 5.16. Experimental heat outputs of radiator II (W).

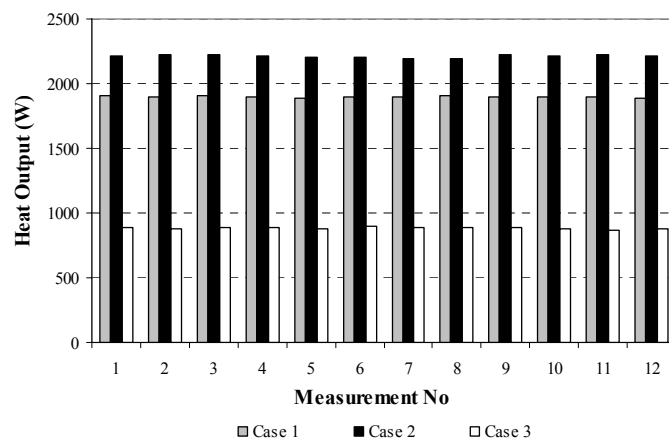


Figure 5.17. Experimental heat outputs of radiator III (W).

As seen from figures given above, experimental heat outputs is increased as addition of extended surface and panel. Enhancement in percentage is shown in Figure

5.18 and Figure 5.19. The enhancement is between 30%-35% when extended surfaces are attached to single panel for Case1.

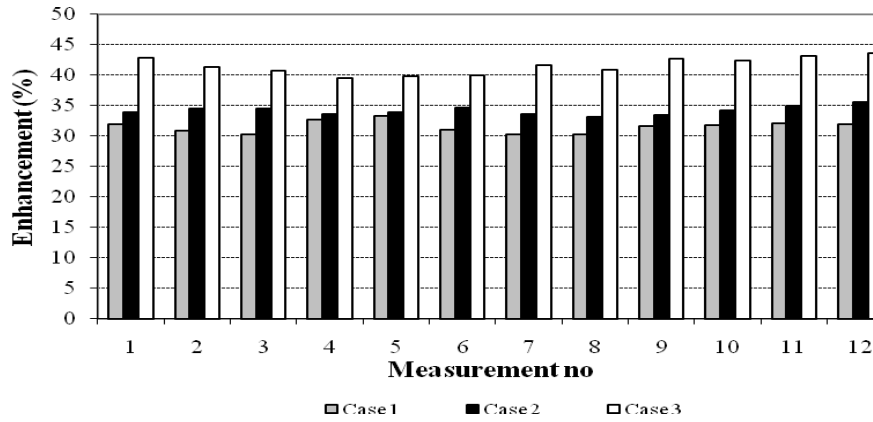


Figure 5.18. Enhancement in the heat transfer rates when radiator II is compared with radiator I (in percentage).

Enhancement in experimental heat output when double panel with double extended surface is used instead of single panel is nearly 95% as shown in Figure 5.19 for Case 1.

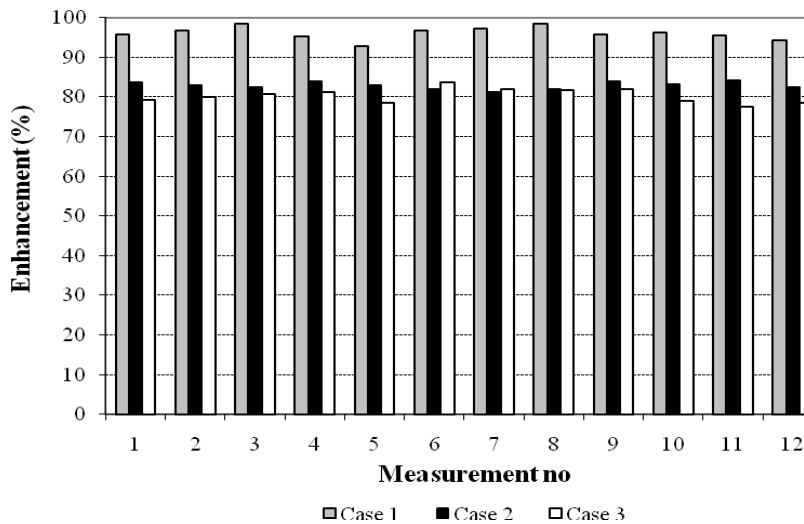


Figure 5.19. Enhancement in the heat transfer rates when radiator III is compared with radiator I (in percentage).

To compare the computational results found in this study, the mean values of experimental heat outputs given in Table 5.1. are used.

Table 5.1. Mean experimental heat outputs (Φ_{exp}) of investigated radiators (W).

Radiator	Case 1	Case 2	Case 3
I	736.51	902.13	346.05
II	968.42	1 210.25	489.87
III	1 898.58	2 213.56	883.25

5.4. Calculation of EN 442 Standard Heat Outputs

Standard characteristic equations were found by using excess temperatures for each tested radiator. Factors used in the formulations are presented in Table 5.2. These values were taken from Table A.1 given in Appendix A. Coefficients used for finding standard characteristic equations are given in Table 5.3.

Table 5.2. The radiated heat output factor (S_k), the exponent n_p and test pressure for investigated radiators.

Radiator	S_k	n_p
I	0.50	0.50
II	0.35	0.60
III	0.20	0.70

Table 5.3. Coefficients used in Equation (3.7) and (3.8) for tested radiators.

Radiator	A	B	C	D
I	100.35	99.10	166.83	59.55
II	105.12	98.70	174.31	59.43
III	114.85	99.22	190.91	59.60

Standard characteristic equations for tested radiators are given in Table 5.4. EN 442 heat outputs of tested radiators (Φ) are presented in Table 5.5. Pressure is integrated to experimental heat outputs to find EN 442 heat output as explained in Chapter 3. Pressure was 100.8 kPa during experiments.

Table 5.4. Standard characteristic equations for tested radiators.

Radiator	Characteristic Equation
I	$Q = 2.795 \bullet \Delta T^{1.4152}$
II	$Q = 5.5751 \bullet \Delta T^{1.3167}$
III	$Q = 7.908 \bullet \Delta T^{1.3846}$

Table 5.5. EN 442 heat outputs (Φ) of tested radiators (W).

CASE	Radiator I	Radiator II	Radiator III
1	709.22	962.24	1780.45
2	917.99	1223.32	2291.75
3	344.20	491.11	877.71

EN 442 heat outputs of tested radiators are compared with experimental heat outputs by using Equation (5.2). The results are given in Table (5.6).

$$Difference\% = \frac{|\Phi - Q_{exp}| \cdot 100}{Q_{exp}} \quad (5.2)$$

Table 5.6. Comparison of experimental and EN 442 heat outputs of tested radiators in three cases (in percentage).

Radiator	Case 1	Case 2	Case 3
I	3.7	1.8	0.5
II	0.6	1.1	0.3
III	6.2	3.5	0.6

EN 442 heat outputs are found relatively similar to experimental heat outputs. The maximum difference between the compared values is 6.2%. Difference results from integration of operating pressure into calculations.

CHAPTER 6

VERIFICATION OF TWO DIMENSIONAL NATURAL CONVECTION IN CAVITY

Before the calculation of heat output of tested radiators by numerical methods, some two dimensional cavity problems are solved by using FLUENT software. CFD solutions are compared with the results of previous studies explained in Chapter 4. Closeness of results is the main reason to use this finite volume solver in the CFD analysis of virtual test room.

6.1. Two Dimensional Differential Heating

Initially, two dimensional natural convection problems with differentially heating in various Rayleigh numbers (from laminar to turbulent flow) were investigated. Rayleigh numbers depend on mainly the characteristic length and temperature differences as mentioned in Chapter 2. Therefore, those parameters are changed as made in literature to obtain predefined Rayleigh numbers.

Thermo-physical properties of air at the average wall temperature are used in order to calculate Rayleigh numbers. Gravitational acceleration (g) is 9.806 ms^{-2} in each case. The hot and cold wall temperatures and characteristic lengths give laminar flows in investigated Rayleigh numbers are presented in Table 6.1. Coefficients used for the calculation of Rayleigh numbers in those cases are given in Table 6.2. Thermo-physical properties of air used in the computational runs are shown in Table 6.3.

Boundary conditions for two dimensional natural convection are given below.

Horizontal Walls:

$$y = 0, 0 < x < L, V_x = V_y = 0; \frac{dT}{dy} = 0$$

$$y = H, 0 < x < L, V_x = V_y = 0; \frac{dT}{dy} = 0$$

Vertical Walls:

$$x = 0, 0 \leq y \leq L, V_x = V_y = 0; T = T_{\text{Cold}}$$

$$x = L, 0 \leq y \leq L, V_x = V_y = 0; T = T_{\text{hot}}$$

The length (L) changes in each cases. They are given in Table 6.1.

Table 6.1. Details about two dimensional domains in investigated Rayleigh numbers.

	Rayleigh Number				
	10^2	10^3	10^4	10^5	10^6
T_{hot} (K)	305.0313	311.4066	337.0092	380.7926	395.46
T_{cold} (K)	300	300	300	300	300
T_{average} (K)	302.5156	305.7033	318.5046	340.3963	347.73
ΔT	5.0313	11.4066	37.0092	80.7926	95.46
L (m)	0.006	0.01	0.0155	0.0285	0.06

Table 6.2. Coefficients used for the calculation of Rayleigh numbers.

Rayleigh Number	T (K)	β (K^{-1})	α ($m^2 \cdot s^{-1}$)	ν ($m^2 \cdot s^{-1}$)
10^2	302.5156	0.00343	2.2×10^{-5}	1.602×10^{-5}
10^3	305.7033	0.0033	2.243×10^{-5}	1.632×10^{-5}
10^4	318.5046	0.0031	2.421×10^{-5}	1.753×10^{-5}
10^5	340.3963	0.0029	2.739×10^{-5}	1.968×10^{-5}
10^6	347.7300	0.0029	2.849×10^{-5}	2.042×10^{-5}

Table 6.3. Air properties in two dimensional computational runs.

Rayleigh Number	T (K)	Density (kg/m ³)	Heat Conductivity (W/mK)	Dynamic Viscosity (kg / m s)
10^2	302.5156	1.1665	0.02583	1.87×10^{-5}
10^3	305.7033	1.1544	0.02607	1.884×10^{-5}
10^4	318.5046	1.1080	0.02701	1.943×10^{-5}
10^5	340.3963	1.0367	0.02861	2.040×10^{-5}
10^6	347.7300	0.0029	0.02914	2.072×10^{-5}

Table 6.4. Discretization scheme employed in the computational runs of two dimensional problems.

Variable	Scheme
Pressure	Simple
Momentum	First Order Upwind
Energy	First Order Upwind

Different numbers of elements are used in x and y directions. The temperature of middle point of the cavity is followed in addition to heat transfer balance to decide whether or not steady state condition is reached. Heat transfer rates and Nusselt numbers are presented for each mesh size (number of elements in x direction times number of elements in y direction). Default under-relaxation factors are used in those runs. The steady state conditions are observed at maximum 3000 iterations which can be completed within two hours with a computer having Pentium 3 processor and 6 GB Ram.

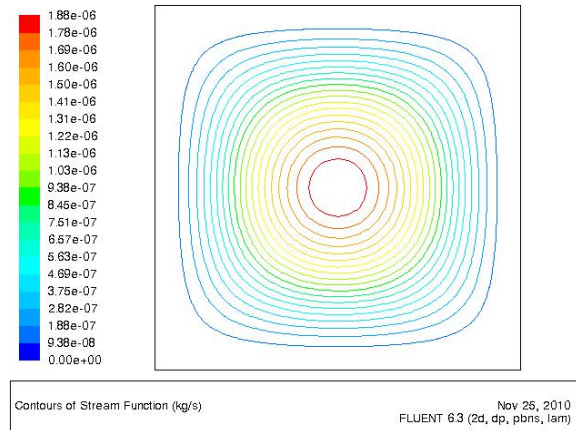
Table 6.5. Heat transfer rates and mean Nusselt number on hot and cold walls for different number of elements and $Ra=10^2$

a.) Heat transfer rate for $Ra=10^2$ (W)

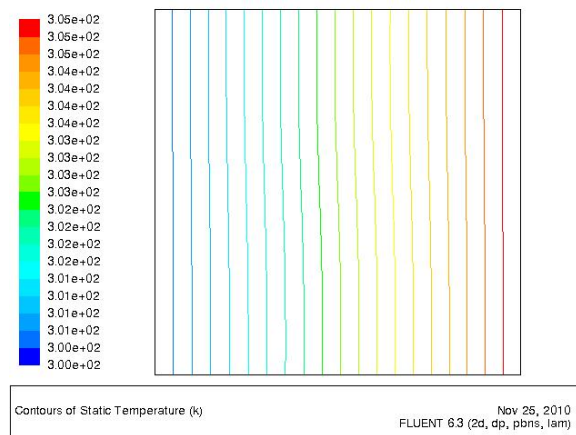
Number of elements	25 x 25	50 x 50	75 x 75	150 x 150	250 x 250
Cold Wall	-0.131	-0.131	-0.130	-0.130	-0.130
Hot Wall	0.131	0.131	0.130	0.130	0.130

b.) Nusselt number for $Ra=10^2$

Number of elements	25 x 25	50 x 50	75 x 75	150 x 150	250 x 250
Cold Wall	0.970	0.989	0.995	1.000	1.000
Hot Wall	0.970	0.989	0.995	1.000	1.000



a.)Contours of stream function



b.)Contours of temperature

Figure 6.1. Contours obtained for $Ra=10^2$.

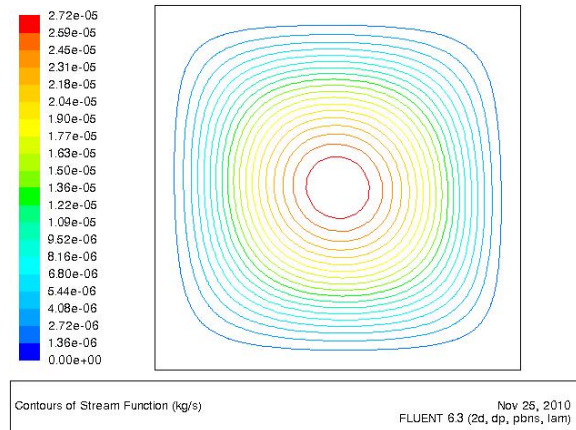
Table 6.6. Heat transfer rates and mean Nusselt number on hot and cold walls for different number of elements and $Ra=10^3$.

a.) Heat transfer rate for $Ra=10^3$ (W)

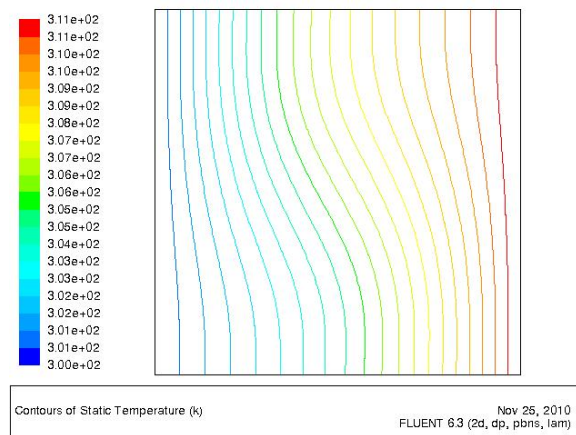
Number of elements	25 x 25	50 x 50	75 x 75	150 x 150	250 x 250
Cold Wall	-0.338	-0.334	-0.334	-0.333	-0.333
Hot Wall	0.338	0.334	0.334	0.333	0.333

b.) Mean Nusselt number for $Ra=10^3$

Number of elements	25 x 25	50 x 50	75 x 75	150 x 150	250 x 250
Cold Wall	1.0903	1.104	1.11444	1.1187	1.119
Hot Wall	1.0903	1.104	1.11444	1.1187	1.119



a.)Contours of stream function



b.)Contours of temperature

Figure 6.2. Contours obtained for $Ra=10^3$

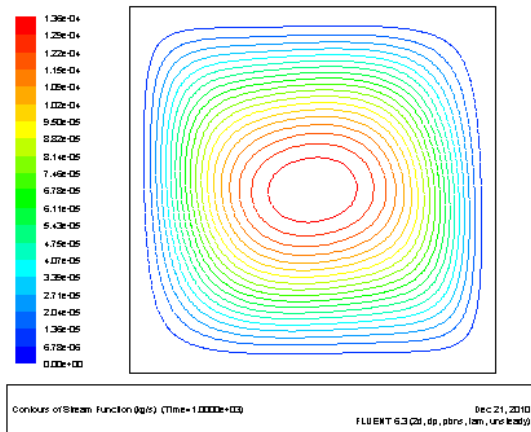
Table 6.7. Heat transfer rates and mean Nusselt number on hot and cold walls for different number of elements and $Ra=10^4$

a.) Heat transfer rates for $Ra=10^4$ (W)

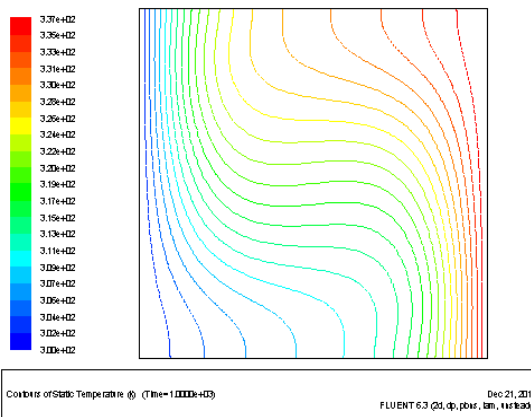
Number of elements	25 x 25	50 x 50	75 x 75	150 x 150	250 x 250
Cold Wall	-2.279	-2.252	-2.246	-2.242	-2.242
Hot Wall	2.2790	2.252	2.246	2.242	2.242

b.) Mean Nusselt number for $Ra=10^4$

Number of elements	25 x 25	50 x 50	75 x 75	150 x 150	250 x 250
Cold Wall	2.207	2.222	2.230	2.239	2.240
Hot Wall	2.207	2.222	2.230	2.239	2.240



a.) Contours of stream function



b.) Contours of temperature

Figure 6.3. Contours obtained for $Ra=10^4$.

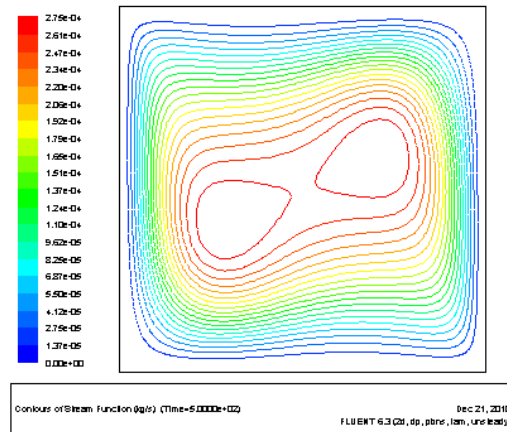
Table 6.8. Heat transfer rates and mean Nusselt number on hot and cold walls for different number of elements and $Ra=10^5$

a.) Heat transfer rates for $Ra=10^5$ (W)

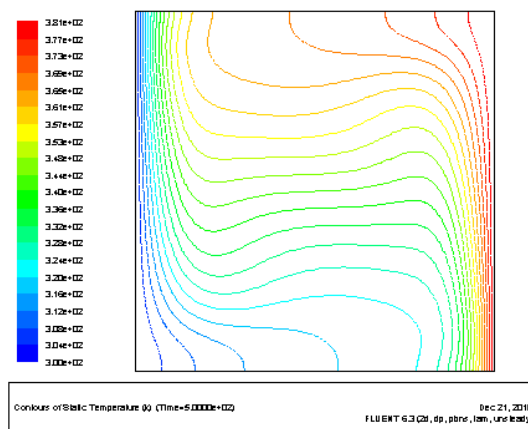
Number of elements	25 x 25	50 x 50	75 x 75	150 x 150	250 x 250
Cold Wall	-11.035	-10.586	-10.503	-10.452	-10.452
Hot Wall	11.0345	10.586	10.503	10.452	10.452

b.) Mean Nusselt number for $Ra=10^5$

Number of elements	25 x 25	50 x 50	75 x 75	150 x 150	250 x 250
Cold Wall	4.614	4.518	4.51	4.512	4.5123
Hot Wall	4.614	4.518	4.51	4.512	4.5123



a.)Contours of stream function



b.)Contours of temperature

Figure 6.4. Contours obtained for $Ra=10^5$.

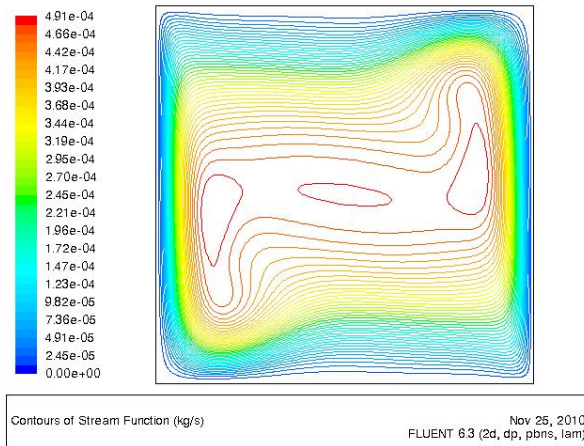
Table 6.9. Heat transfer rates and mean Nusselt number on hot and cold walls for different number of elements and $Ra=10^6$.

a.) Heat transfer rates (W) for $Ra=10^6$

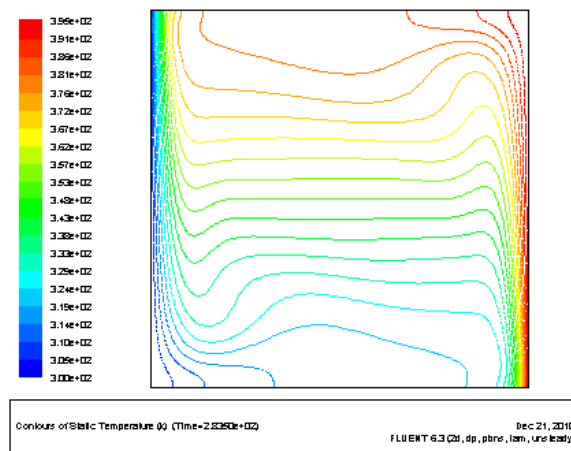
Number of elements	100 x 100	150 x 150	250 x 250	300 x 300
Cold Wall	-24.707	-24.583	-24.528	-24.530
Hot Wall	24.707	24.583	24.528	24.530

b.) Mean Nusselt number for $Ra=10^6$

Number of elements	100 x 100	150 x 150	250 x 250	300 x 300
Cold Wall	8.836	8.827	8.812	8.813
Hot Wall	8.836	8.8217	8.812	8.813



a.)Contours of stream function



b.)Contours of temperature

Figure 6.5. Contours obtained for $Ra=10^6$.

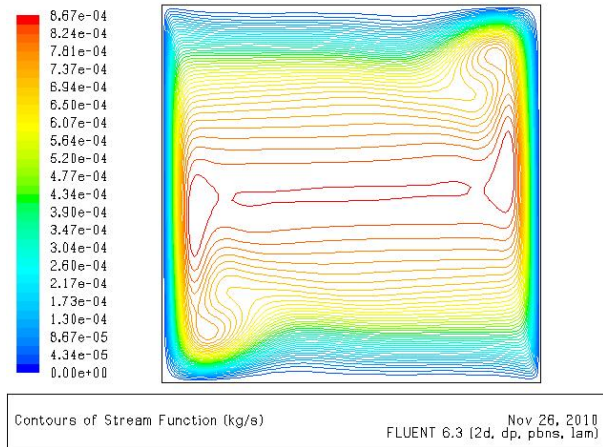
Table 6.10. Heat transfer rates and average Nusselt number on hot and cold walls for different number of elements and $Ra=10^7$.

a.) Heat transfer rates (W) for $Ra=10^7$

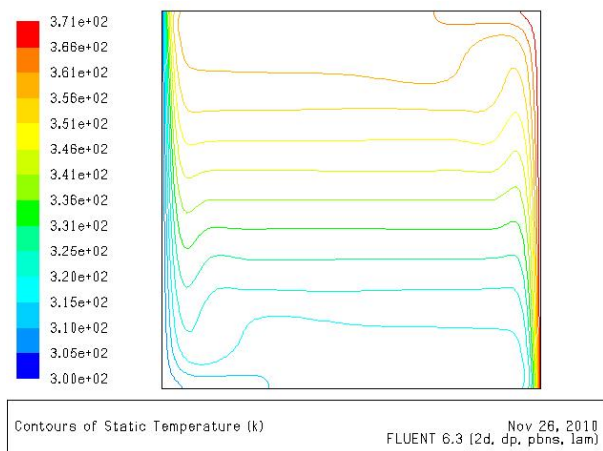
Number of elements	100 x 100	200 x 200	300 x 300	400 x 400
Cold Wall	-33.607	-33.3143	-33.2969	-33.2971
Hot Wall	33.607	33.3143	33.2969	33.2971

b.) Mean Nusselt number for $Ra=10^7$

Number of elements	100 x 100	200 x 200	300 x 300	400 x 400
Cold Wall	16.5837	16.5418	16.531	16.5304
Hot Wall	16.5837	16.5418	16.531	16.5304



a.)Contours of stream function



b.)Contours of temperature

Figure 6.6. Contours obtained for $Ra=10^7$.

Findings summarized in Tables 6.7-b,6.8-b, 6.9-b and 6.10-b are compared with results published in literature (Xu et al. 1998), (Xundan et al. 2003). It is evaluated that solutions obtained by FLUENT are similar and logical.

Table 6.11. Comparison of the predicted mean Nusselt number on the hot or cold walls of a cavity

Ra	10^4	10^5	10^6	10^7
De Vahl Davis	2.243	4.519	8.80	-
Nag et al.	2.24	4.51	8.82	-
J.M. Khodadadi	2.247	4.532	8.893	16.935
This Study	2.24	4.51	8.81	16.53

Table 6.12. Total heat transfer rates and mean Nusselt number on hot and cold walls for $Ra=10^8$.

a.) Heat transfer rate for $Ra=10^8$

Number of elements	150 x 150	250 x 250	350 x 350
Cold Wall	-100.326	-99.872	-99.87
Hot Wall	100.326	99.872	99.87

b.) Nusselt number for $Ra=10^8$

Number of elements	150 x 150	250 x 250	350 x 350
Cold Wall	31.8215	31.7022	31.7
Hot Wall	31.8215	31.7022	31.7

In Figure 6.7, change in temperature is shown for $Ra=10^8$.

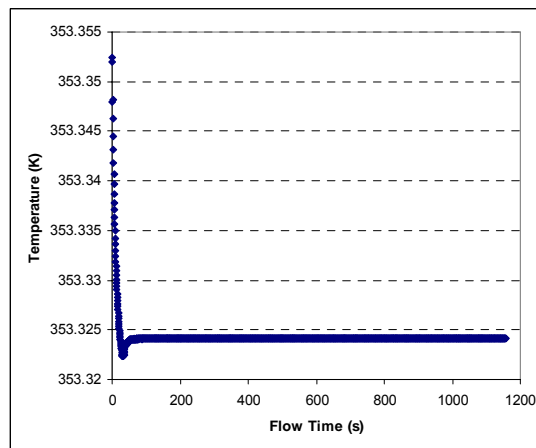
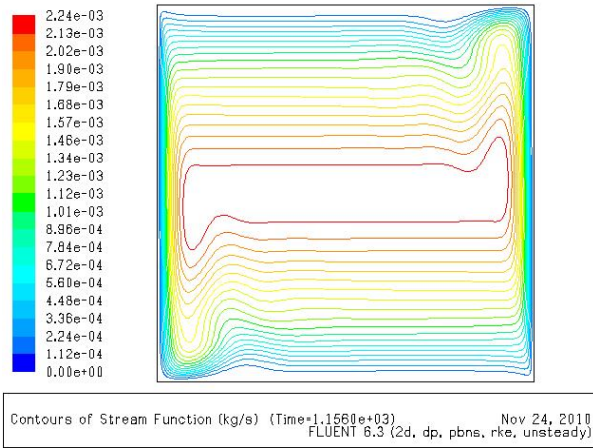
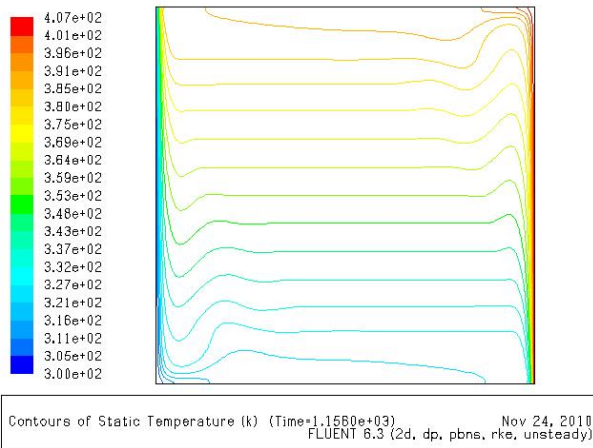


Figure 6.7. Change in middle point temperature for $Ra=10^8$.



a.) Contours of stream function



b.) Contours of temperature

Figure 6.8. Contours obtained for $Ra=10^8$.

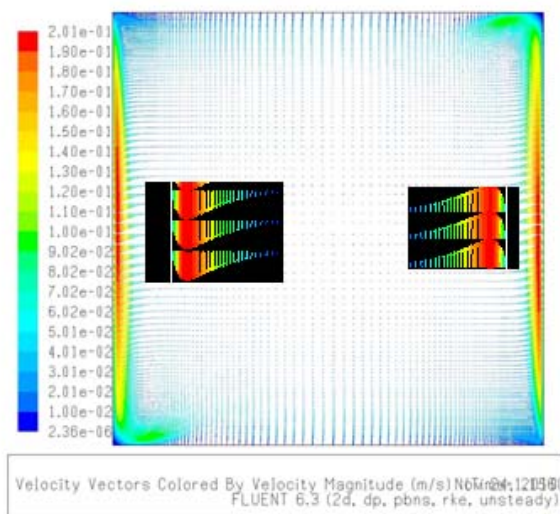


Figure 6.9. Velocity vectors for $Ra=10^8$.

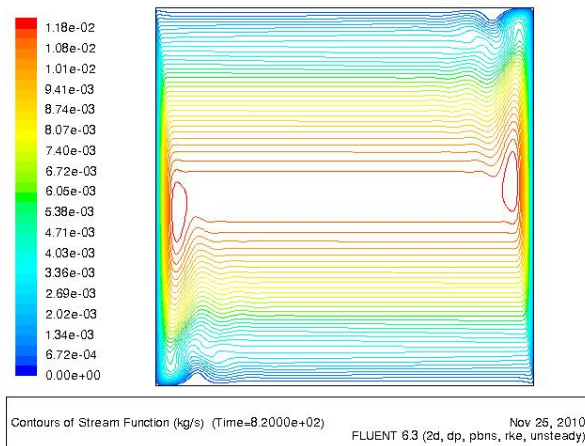
Table 6.13. Total heat transfer rates and mean Nusselt number on hot and cold walls for $Ra=10^{10}$.

a.) Heat transfer rate for $Ra=10^{10}$

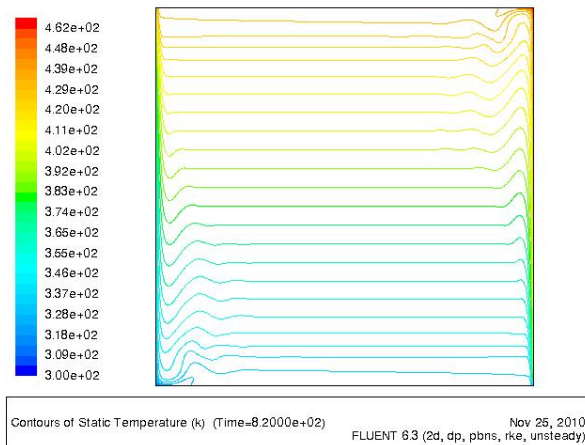
Number of elements	150 x 150	250 x 250	350 x 350
Cold Wall	-766.494	-685.36	-684.94
Hot Wall	766.494	685.36	684.94

b.) Nusselt number for $Ra=10^8$

Number of elements	150 x 150	250 x 250	350 x 350
Cold Wall	149.997	134.4532	134.453
Hot Wall	149.997	134.4532	134.453



a.) Contours of stream function



b.) Contours of temperature

Figure 6.10. Contours obtained for $Ra=10^{10}$.

The second validation is realized for flow in a rectangular cavity with the aspect ratio of 1 as shown in Figure 6.11. The vertical wall temperatures were 10°C and 50°C, respectively. However, for horizontal walls different boundary conditions are applied.

First, horizontal walls are assumed adiabatic (BC 1). Next, overall heat transfer coefficient is calculated with making an assumption for the thickness of wood block used on horizontal walls (BC 2). Then heat gain from bottom wall and heat lost from the top wall given by Ampofo and Karayiannis are used as a third boundary condition (BC 3).

Finally the temperature distributions ($T_1(x)$ and $T_2(x)$) given by Ampofo and Karayiannis (Chapter 4, and Appendix B) are identified as a fourth boundary condition (BC 4) at the horizontal walls. Since only the definition of constant temperature wall condition is possible in FLUENT, a code (user defined function –UDF) is used to define temperature profiles along the horizontal walls. Those codes are presented in Appendix I (Figure A-1).

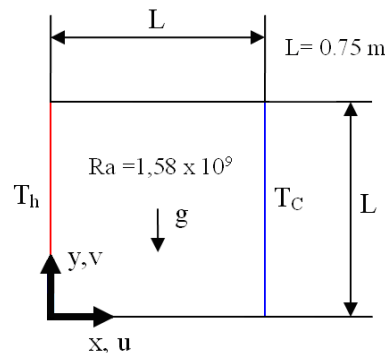


Figure 6.11. The schematic view of problem solved numerically to verify computational results with experimental results.

Boundary conditions for this problem:

	BC 1) $\frac{dT}{dy} = 0$
$y = 0, 0 < x < W, u = v = 0;$	BC 2) $Q = Q_{top}$
	BC 3) $h = 0.74 \text{ W/m}^2\text{K}$
	BC 4) $T = T_1(x)$
	BC 1) $\frac{dT}{dy} = 0$
$y = H, 0 < x < W, u = v = 0;$	BC 2) $Q = Q_{top}$
	BC 3) $h = 0.74 \text{ W/m}^2\text{K}$
	BC 4) $T = T_2(x)$

$$x = 0 \text{ and } 0 \leq y \leq H, \quad u = v = 0; \quad T = T_h$$

$$x = W, \quad 0 \leq y \leq H, \quad u = v = 0; \quad T = T_c$$

where

$$T_1(x) = -1371.6x^5 + 2817.3x^4 - 2296.2x^3 + 930.16x^2 - 210.92x + 321.03$$

$$T_2(x) = -1243.5x^5 + 2140.8x^4 - 1494.7x^3 + 520.91x^2 - 107.73x + 321.63$$

Temperature profiles ($T_1(x)$ and $T_2(x)$) are taken from Figure 4.8. In the simulations performed, the effect of radiation heat transfer is not included. The enhanced wall treatment is used in order to make $k - \epsilon$ turbulence model suitable for wall-bounded flow and solve flow near the wall accurately. Three different grid structures are used as seen in Table 6.14. Near wall regions, number of grid is increased in computational domain. The grid structure is illustrated in Figure 6.12. In Table 14, the result of CFD runs are summarized. The central temperature and total heat transfer rates from walls are taken into consideration during CFD runs in addition to residuals. When total heat flux is equal to zero and central temperature is constant, it is decided that the steady state solution is obtained.

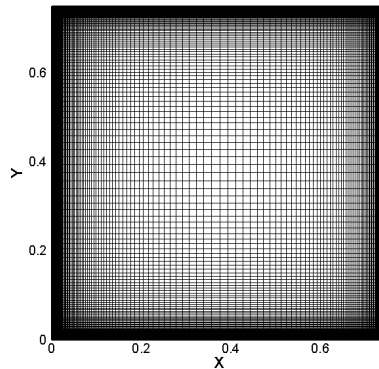


Figure 6.12. Grid structure (when the number of elements is 22 500) for investigated problem.

Table 6.14. Total heat transfer rates on hot and cold walls for different number of cells (W).

Wall	Experimental	Number of Cells		
	Heat transfer Rate (W)	22 500	40 000	62 500
Bottom	21.67	0	0	0
Cold	97.77	-95.78	-95.9	-95.9
Hot	98.12	95.78	95.9	95.9
Top	22.53	0	0	0

In the second column of Table 6.14, the experimental heat transfer rates taken from the article is presented.

In Figure 6.13, temperature and y velocity contours are presented. Similar temperature contours are obtained in previous analysis in which Ra is equal to 10^8 . Y velocity contour shows that the flow moves up near the hot wall and down near the cold wall. The velocity vectors seen in Figure 6.14 show that the velocity decreases towards to walls and center axis. Y plus values are given drawn in Figure 6.15. Since they are smaller than 1, enhanced wall treatment is used to solve the boundary layer.

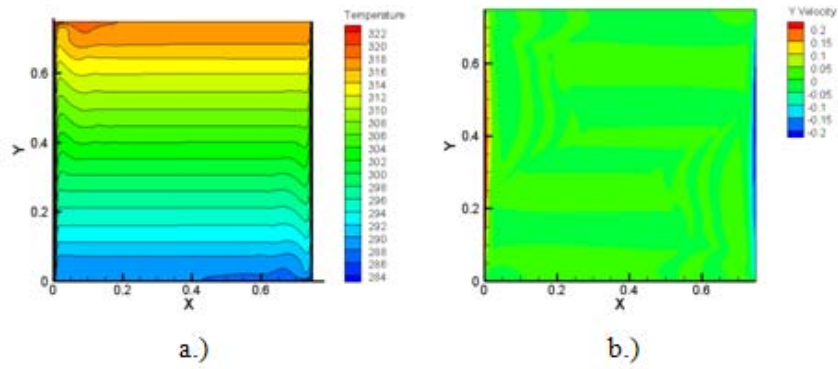
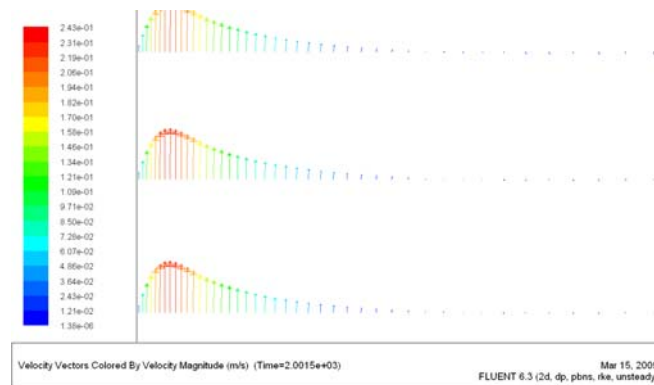
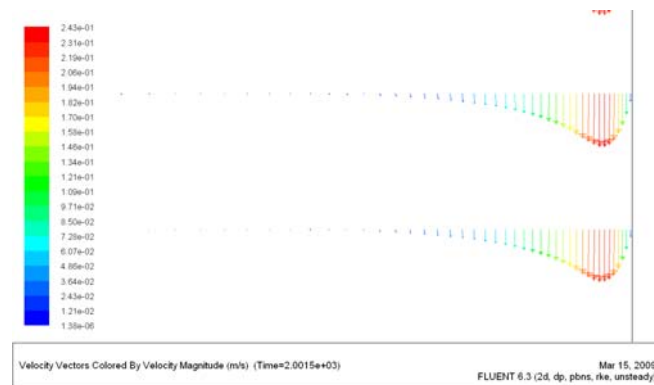


Figure 6.13. Contours for adiabatic horizontal walls (the number of elements is 22500).

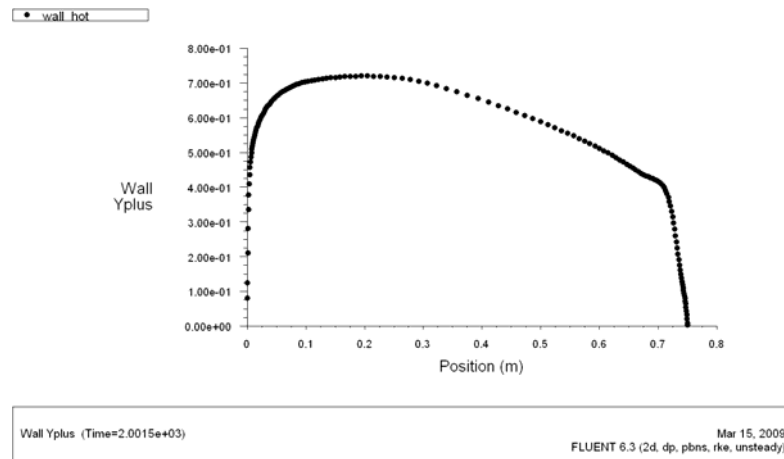


a.) Hot wall

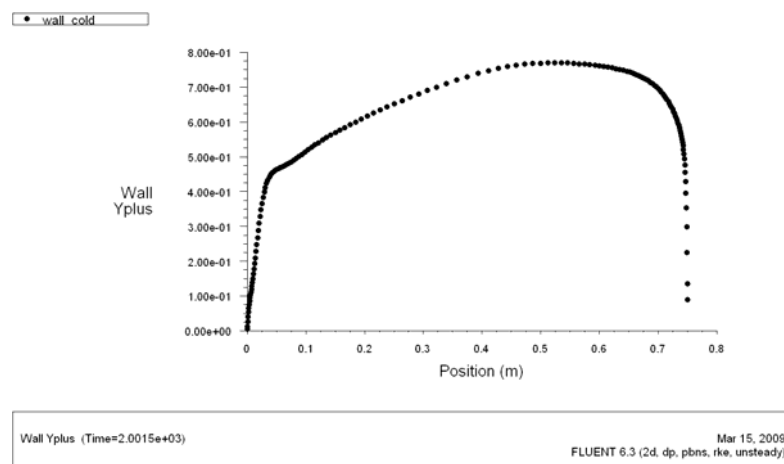


b.) Cold wall

Figure 6.14. Velocity vectors near the vertical walls (the number of elements is 22500).



a.) At the hot wall



b.) At the cold wall

Figure 6.15. Changing of Y plus values on vertical walls.

From Figure 6.15, it is seen that the boundary layer is meshed sufficiently fine (Low-Re Modeling). Since the first grid cells have a dimensionless height of $y^+ \approx 1$ along the hot and cold walls, they are in the laminar sub-layer. Wall functions are not applied. It should be noted that meshes with a $y^+ > 30$, wall functions must be applied.

First, adiabatic boundary conditions for horizontal walls are taken into consideration. For computational runs, three different grid structures are tried. In each structure, the number of grid is changed. In those analyses, local Nusselt numbers are found along vertical walls. Local Nusselt numbers are given in Figure 6.16. Total heat transfer rates in steady state conditions are presented in Table 6.15. Since there are heat transfers from insulated horizontal walls in the experimental study, different boundary conditions are also examined for one of the mesh structure examined before for the adiabatic boundary conditions. Total heat transfer rates and mean Nusselt numbers are

given for different boundary conditions in Table 6.16 and Table 6.17, respectively. In Figures 6.16, 6.17, 6.18 and 6.19, change of local Nusselt numbers are given for four different boundary conditions. It is seen that nearly similar local Nusselt numbers are obtained for vertical walls. However mean Nusselt numbers horizontal walls for BC 4 are closer to values obtained by experimental study. The source for the difference is researched. It is thought that the difference can stem from the turbulence model used. Since the heat flow rates and mean Nusselt numbers obtained by BC 4 are much closer to values obtained by an experimental study. Therefore total heat transfer rates and mean Nusselt numbers are compared in different turbulence models for BC4 and number of elements of 40 000. The results are given in Table 6.18 and 6.19.

Table 6.15. Mean Nusselt numbers for three different grid sizes in adiabatic boundary conditioned horizontal walls.

Wall	Experimental	Number of cells		
		22 500	40 000	62 500
Hot	62.9	61.61	61.67	61.672
Cold	62.6	61.61	61.69	61.691

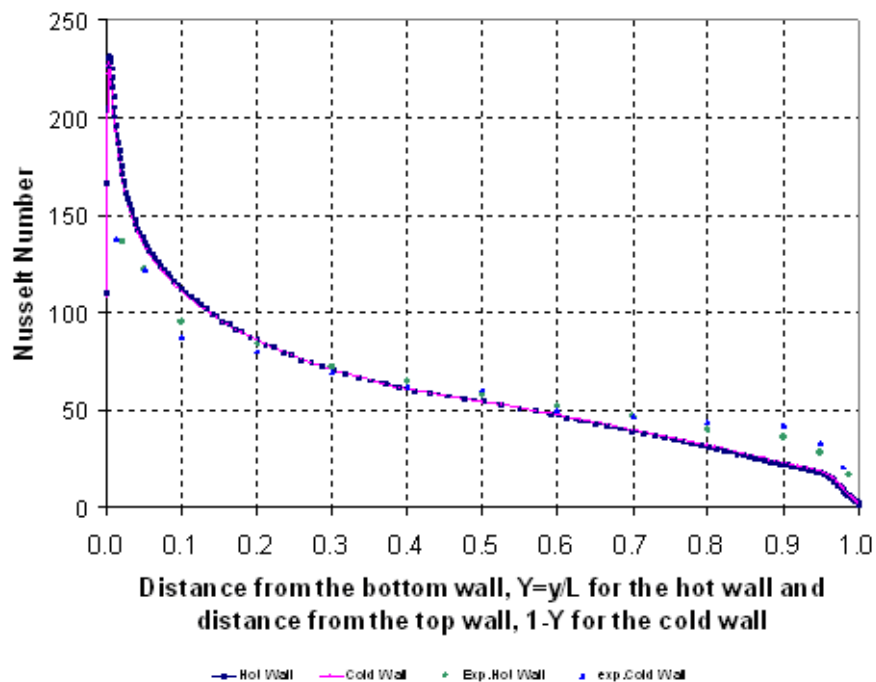


Figure 6.16. Local Nusselt numbers on the vertical walls for the adiabatic boundary condition (Number of cell is 22 500).

Table 6.16. Total heat transfer rates (W) from the walls and reference temperatures for different boundary conditions (Number of cells is 40 000).

	Experimental	Boundary Conditions			
		BC 1	BC 2	BC 3	BC 4
Bottom wall	21.67	0	21.67	7.45	17.71
Cold wall	97.77	95.9	83.81	92.22	85.82
Hot wall	98.12	95.9	84.67	91.97	85.28
Top wall	22.53	0	-22.53	-7.2	-17.17

Table 6.17. Mean Nusselt numbers for three different grid sizes in different boundary conditions (Number of cells is 40 000).

	Experimental	BC 2	BC 3	BC 4
Cold wall	62.6	53.95	61.54	55.2
Hot wall	62.9	54.49	61.54	54.83
Bottom wall	13.9	13.95	0.015	11.45
Top wall	14.4	14.5	0.015	11.09

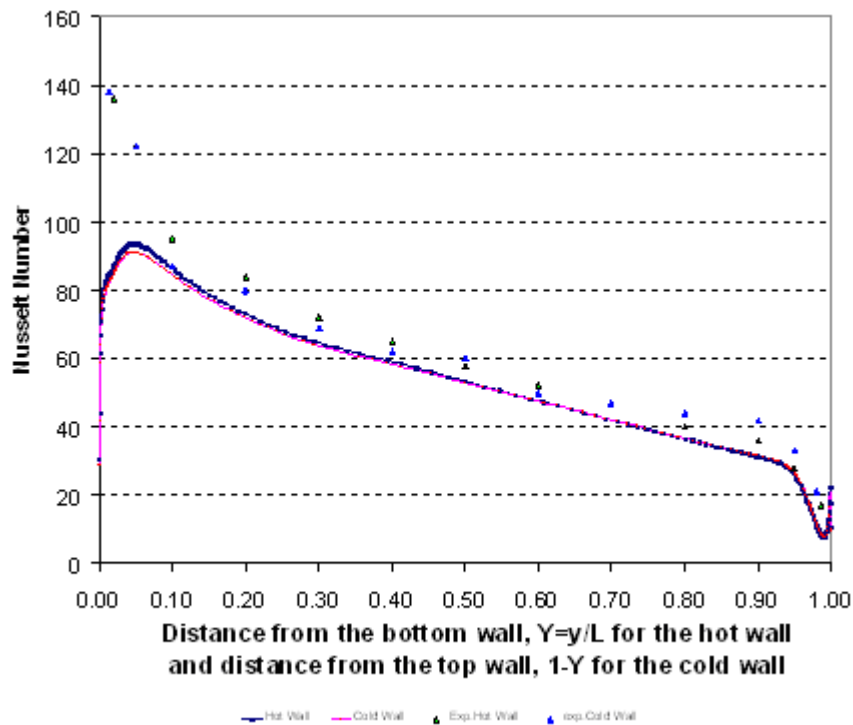


Figure 6.17. Nusselt numbers for the boundary condition 2.

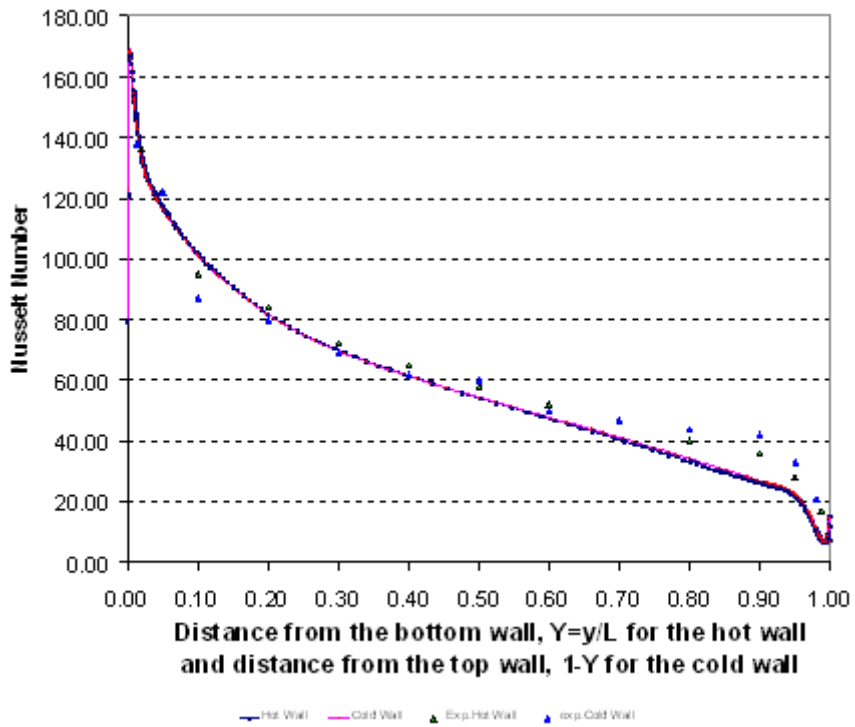


Figure 6.18. Nusselt numbers for the boundary condition 3.

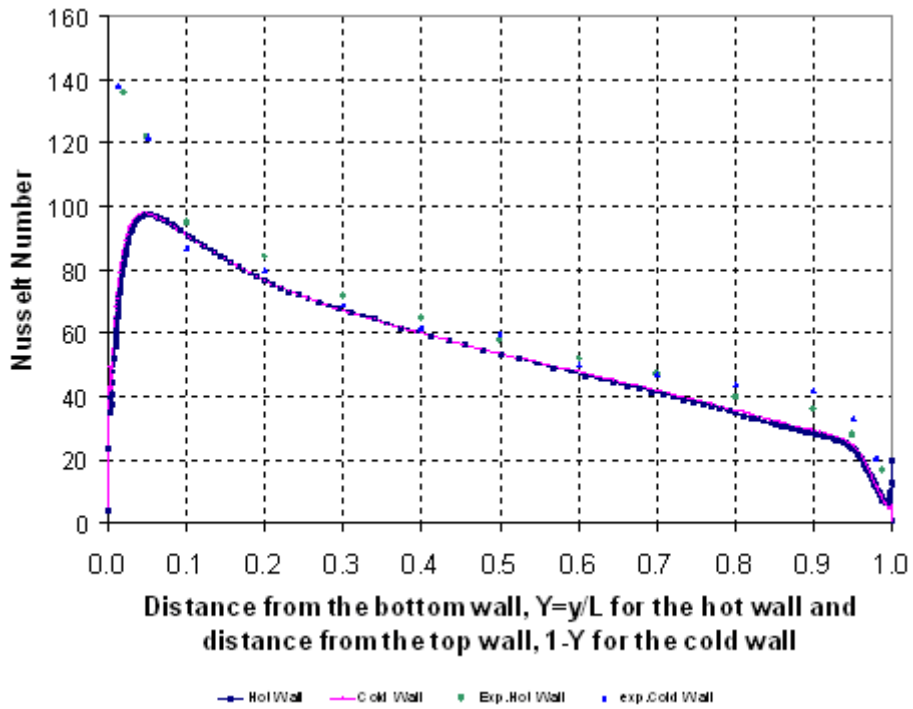


Figure 6.19. Nusselt numbers on the vertical walls (k-epsilon turbulence model and viscous effects are neglected).

Table 6.18. Total heat transfer rates (W) from the walls for investigated turbulence models (for boundary condition IV and number of cells is equal to 40 000).

Wall	k- ϵ	Standard k-w	SST k-w
Bottom	17.71	16.48	16.06
Cold	85.82	84.37	84.82
Hot	85.28	83.71	84.22
Top	17.17	15.81	15.46

Table 6.19. Mean Nusselt numbers for different turbulence models (for boundary condition 4).

Wall	k- ϵ	Standard k-w	SST k-w
Bottom	11.45	10.66	10.39
Cold	55.2	54.27	54.55
Hot	54.83	53.82	54.15
Top	11.09	10.21	9.99

As a result of applying different two equation turbulence models, close values are found for mean and local Nusselt number as seen in Table 6.19. The difference can be sourced from 3D turbulent flow in experimental set up. They used cross sectional area to find 2D flow as explained in Chapter 4. It is evaluated that using correct boundary conditions in computational solutions gives realistic results.

CHAPTER 7

BOUNDARY CONDITIONS AND COMPUTATIONAL DETAILS

The computational study is accomplished for the tested radiators by using ICEPAK software. Before some preliminary analyses are realized to solve three dimensional natural convection problem.

7.1. Pre-Analysis

Since, only one side which is located at the behind of the radiator is insulated in the examined problem, two dimensional cavity whose one of the vertical sides is hot and remaining three sides are colder is solved at the beginning. Then the hot wall is replaced by partially heated wall. Finally, the hot wall is replaced by insulated wall and there is a rectangular domain whose surface temperature is being constant. All two dimensional cases are model in GAMBIT and solved by FLUENT. When two dimensional results are found logical, three dimensional case with an internal object having constant surface temperature is solved.

7.1.1. Natural Convection in Cavity with Three Cold and One Hot Sides

Three cases are examined. The boundary conditions of first case are given below. Temperatures of cold sides are 293 K (20°C). The hot side temperature is 343 K (70°C).

On vertical walls;

$$y = 0, 0 < x < L, V_x = V_y = 0; T = T_c \quad (L=4\ 000\ \text{mm}),$$

$$y = H, 0 < x < L, V_x = V_y = 0; T = T_c \quad (H=3\ 000\ \text{mm})$$

At horizontal walls;

$$x = 0, 0 \leq y \leq H, V_x = V_y = 0; T = T_C$$

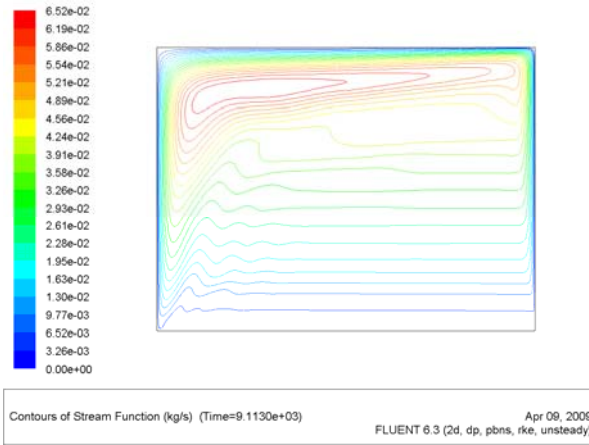
$$x = L, 0 \leq y \leq L, V_x = V_y = 0; T = T_h$$

Since one of the termination criteria is total heat transfer from the cavity, the heat transfer rates at each wall are followed during analysis. At steady state, the net heat transfer rates from the cavity is zero. The heat transfer rates at steady state are given in Table 7.1. The heat transferred to outside of the cavity is denoted by minus sign.

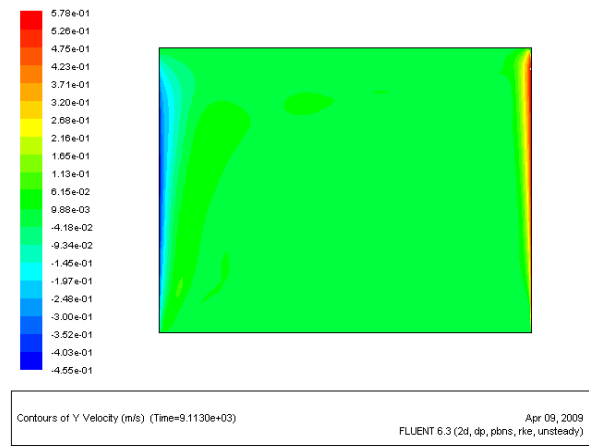
Table 7.1. Total heat transfer rates from the walls and reference temperatures in different number of elements for two dimensional cavity which has three cold and one hot sides (W).

Number of cells	30 000	58 800	82 400
Bottom cold wall	-21.78	-21.75	-21.765
Left Cold wall	-183.32	-184.25	-184.28
Hot wall	545.3	547.59	547.56
Top cold wall	-340.18	-341.57	-341.58
Reference Temp. (K)	306.28	306.29	306.293

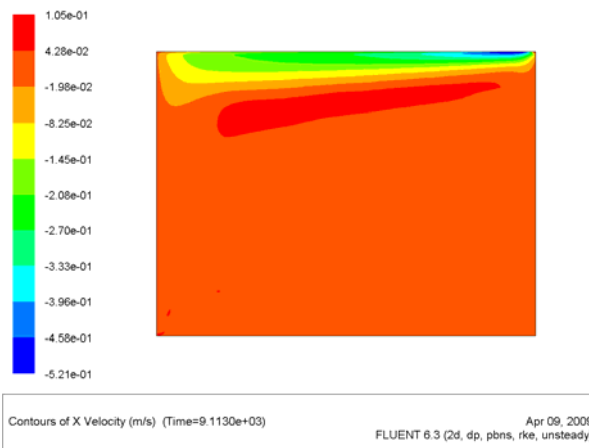
Contours of stream function is given in Figure 7.1 a. Contours of y and x velocities are plotted in Figure 7.1 b.) and 7.1 c.), respectively.



a.)



b.)



c.)

Figure 7.1. Contours obtained for the cavity whose three side is cold and the other side is hot.

7.1.2. Cavity with Three Cold and One Partially Heated Sides

The second case in which air is heated from some part of the one vertical wall and cooled from three sides is solved next. The boundary conditions of the second case are explained below. Temperatures of cold sides are 293 K (20 °C). The hot side temperature is 343 K (70 °C).

Horizontal walls;

$$y = 0, 0 < x < L, u = v = 0; \quad T = T_c$$

$$y = H, 0 < x < L, u = v = 0; \quad T = T_c$$

Vertical walls;

$$x = 0, 0 \leq y \leq H, u = v = 0; \quad T = T_c$$

$$x = L, 0 \leq y \leq 1000, u = v = 0; \quad T = T_h$$

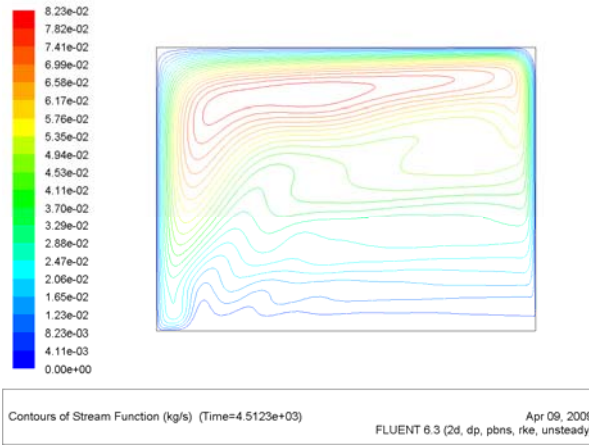
$$x = L, 1000 \leq y \leq H, u = v = 0; \quad \frac{dT}{dx} = 0$$

$$L=4000 \text{ mm}, H=3000 \text{ mm}$$

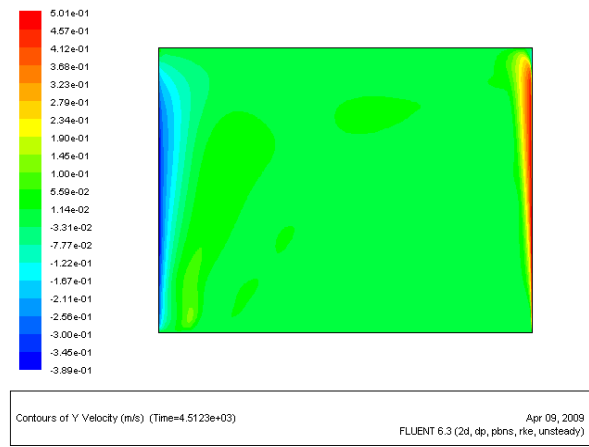
In Table 7.2, total heat transfer rates from walls are summarized for the steady state condition. Stream function, temperature and Y velocity contours are plotted in Figure 7.2.

Table 7.2. Total heat transfer rates (W) from the walls and reference temperatures for two dimensional domain which has three cold and one partially heated side.

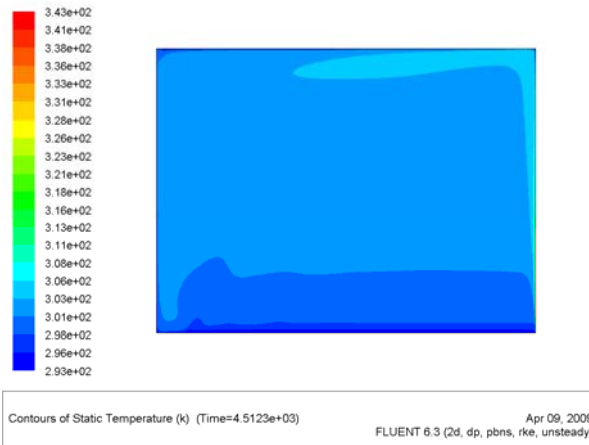
Number of cells	30 000	58 800	82 400
Bottom cold wall	-22.4	-23.06	-23.08
Left cold wall	-88.23	-86.56	-86.54
Hot wall	254.74	255.47	255.4
Top cold wall	-144.07	-145.68	-145.63
Insulated Wall	0	0	0



a.)



b.)



c.)

Figure 7.2. Contours obtained for the cavity which has three cold and one partially heated side.

7.1.3. Natural Convection in the Cavity with Internal Heated Body

The schematic view of the investigated case is given in Figure 7.3. In this case, the internal body has constant surface temperature (343 K, 70 °C). The temperatures of cold sides are 293 K (20 °C). The rectangular shaped body does not include any mesh since only the flow around the body is solved. During the analysis the reference temperature has been followed as heat transfer rates from walls. In Table 7.3, those values are presented. Contours for the considered case are plotted in Figure 7.4.

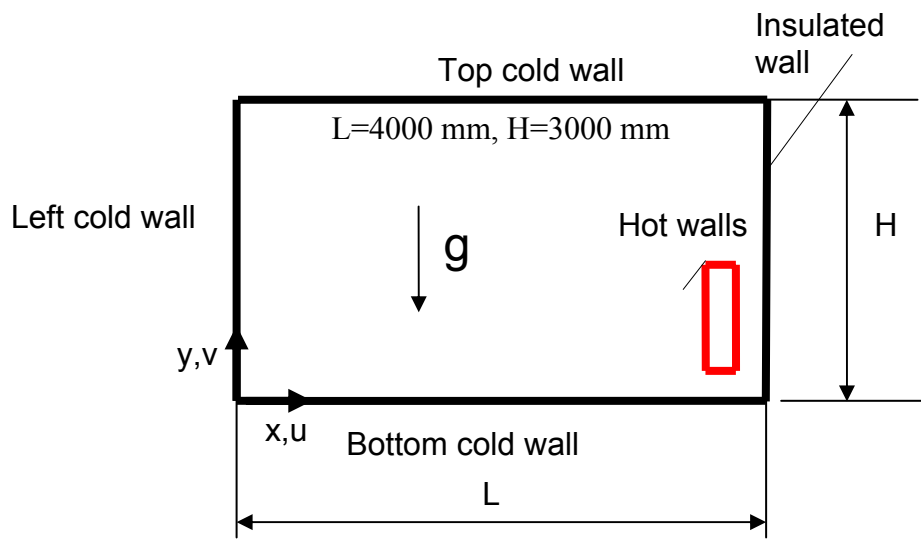
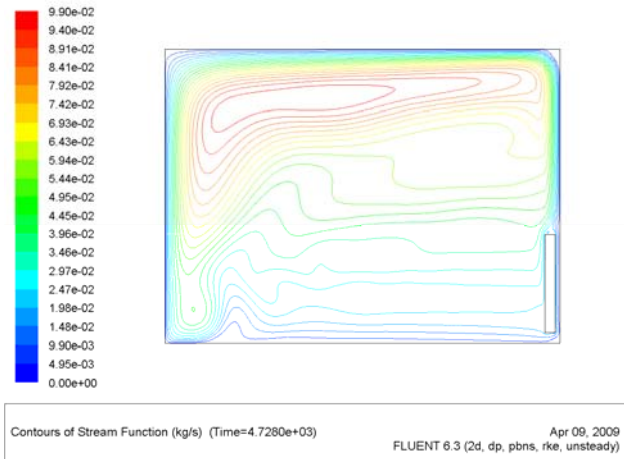


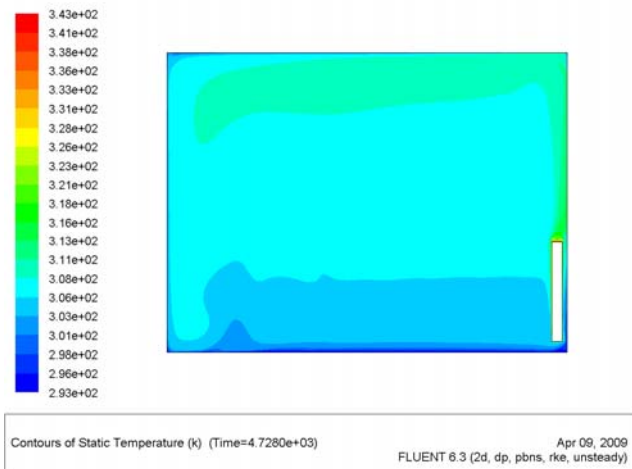
Figure 7.3. The schematic view of cavity with internal heated body.

Table 7.3. Total heat transfer rates from the walls (W) and reference temperatures for cavity with internal heated body.

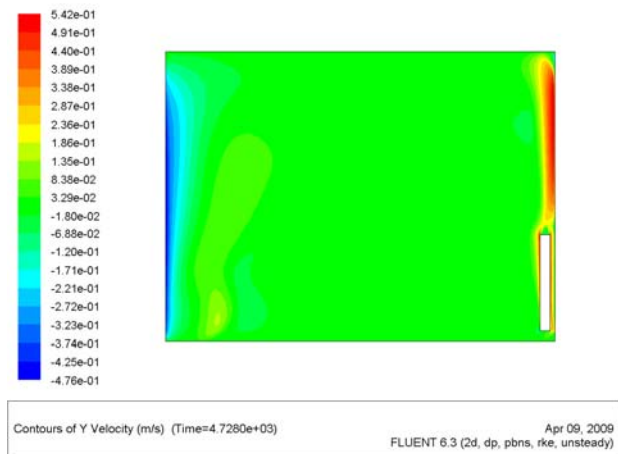
Number of cells	19 420	39 600	59 832	72 840	89 360
Bottom cold wall	-47.76	-51.11	-50.60	-55.41	-53.4
Left cold wall	-153.22	-152.94	-152.26	-155.45	-155.31
Right wall (insulated)	0	0	0	0	0
Top cold wall	-247.49	-249.75	-253.78	-256.44	-257.68
Hot Wall	449.11	453.71	465.01	467.57	466.62
Reference Temp. (K)	305.22	305.61	305.33	305.66	305.69



a.)



b.)



c.)

Figure 7.4. Contours for cavity with internal heated body.

It is evaluated that reasonable results are obtained for the flow in cavity with high Rayleigh numbers. Air flows from bottom to top near the hot vertical wall while

from top to bottom horizontal walls near the cold vertical wall. Circular stream function contours are deformed when they compared with the stream function contours obtained for square cavities.

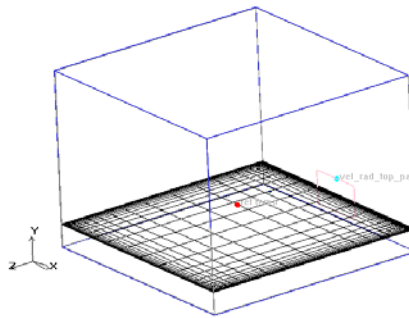
7.1.4. Natural Convection in a Three Dimensional Enclosure with an Internal Heated Body

A three dimensional object whose surface temperatures are being kept constant is investigated in this section. Dimensions of this three dimensional geometry is similar with the dimensions of single panel radiator. This problem is solved by using ICEPAK. The surface temperature is assumed to be equal to the average of inlet and outlet water temperature measured in the single panel test which is 75.22°C. The temperatures of test room walls are 18.5°C except for the wall behind the radiator. Thermal impedance of this wall is 2.5 °Cm²W⁻¹. Since there is an oscillation in residuals of some steady state solution of natural convection problems, time marching approach is used to obtain steady state solution in this problem. Analysis was realized for two different grid structures. In the second grid structure, the number of elements is decreased by 35%. Discrete ordinate radiation model was used with its default settings in the ICEPAK interface. A two equation turbulence model was used for simulation of turbulent air flow around the radiator. Body forced weighted pressure discretization is selected while first order scheme is applied in equations of momentum, energy and turbulence. Because of the natural convection heat transfer, under relaxation factors for pressure, momentum and energy are 0.3 and 0.3, 0.96, respectively. Default values are used for the other under relaxation factors (1.0 for viscosity, body forces and 0.5 for turbulent kinetic energy and turbulent dissipation rate). Bousinessq approach (Chapter 2) and double precision is used in the analysis.

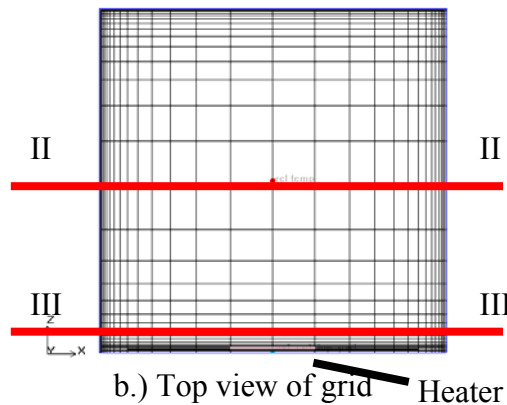
Extra two termination criteria are applied during the analysis: reference air temperature and air velocity near the top of the radiator. The stability in these criteria is taken into consideration. When stability is seen in these factors, the analysis is stopped.

Table 7.4. Number of elements in two different grid structures generated for 3D enclosure with internal body.

	GRID I	GRID II	GRID III	GRID IV
Number of Elements	29 120	44 800	156 230	951 048
Number of Nodes	32 076	48 708	158 040	989 330



a.)



b.) Top view of grid Heater

Figure 7.5. The sectional view of grid created for 3D domain (Grid II).

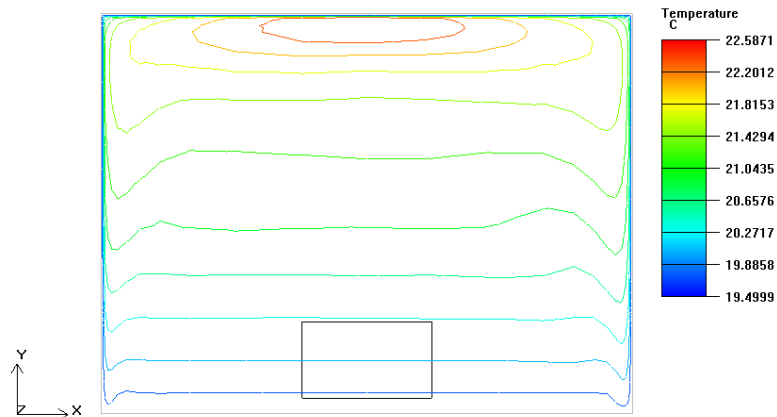


Figure 7.6. The temperature contour ($^{\circ}\text{C}$) at vertical plane (II-II) whose normal is in the z direction (Grid II).

Symetricity in temperature contours in the middle section of virtual test room occurs as expected. Nearly horizontal lines are found at the bottom part of the virtual test room.

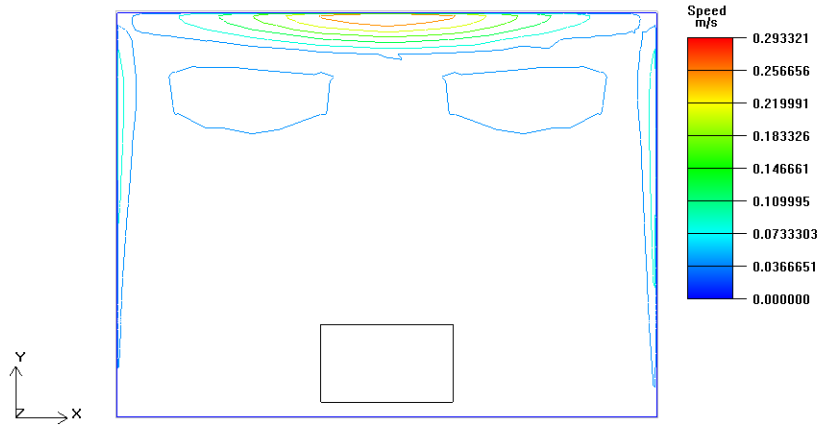


Figure 7.7. The velocity contour ($^{\circ}\text{C}$) at vertical plane (II-II) whose normal is in the z direction (Grid II).

Velocity contours in the vertical plane where the temperature of reference point is measured will be symmetrical when surface temperature is constant or uniform.

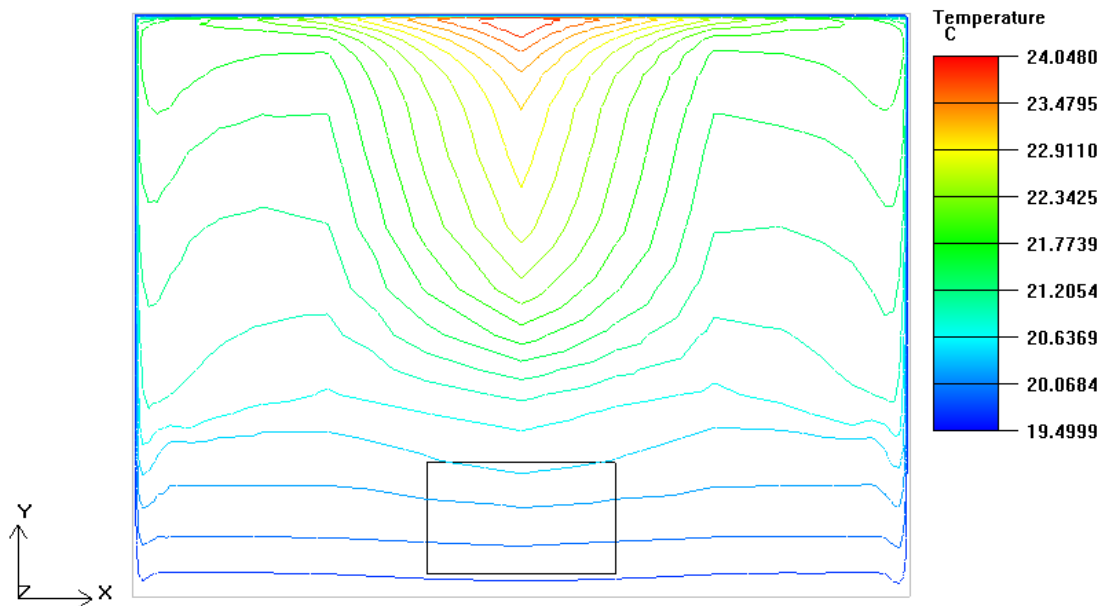


Figure 7.8. The temperature contour ($^{\circ}\text{C}$) at vertical plane (III-III) whose normal is in the x direction (Grid II)

Hot region occurs near the middle part of the top horizontal surface of the virtual test room. Symetricity in temperature contours is seen in all sections of virtual test room as occurs near the heated object.

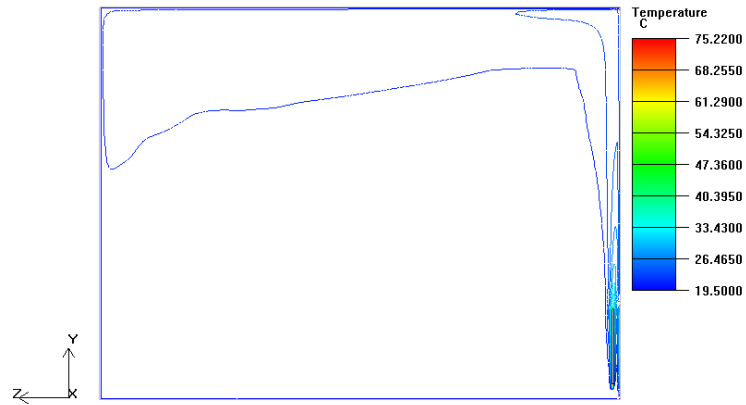


Figure 7.9. The temperature contour at vertical plane (I-I) whose normal is in the x direction (Grid II and $x=2.398$)

The hot region occurs around the heater, the air temperature throughout the virtual test room is approximately 20°C in the middle plane whose normal is in x direction.

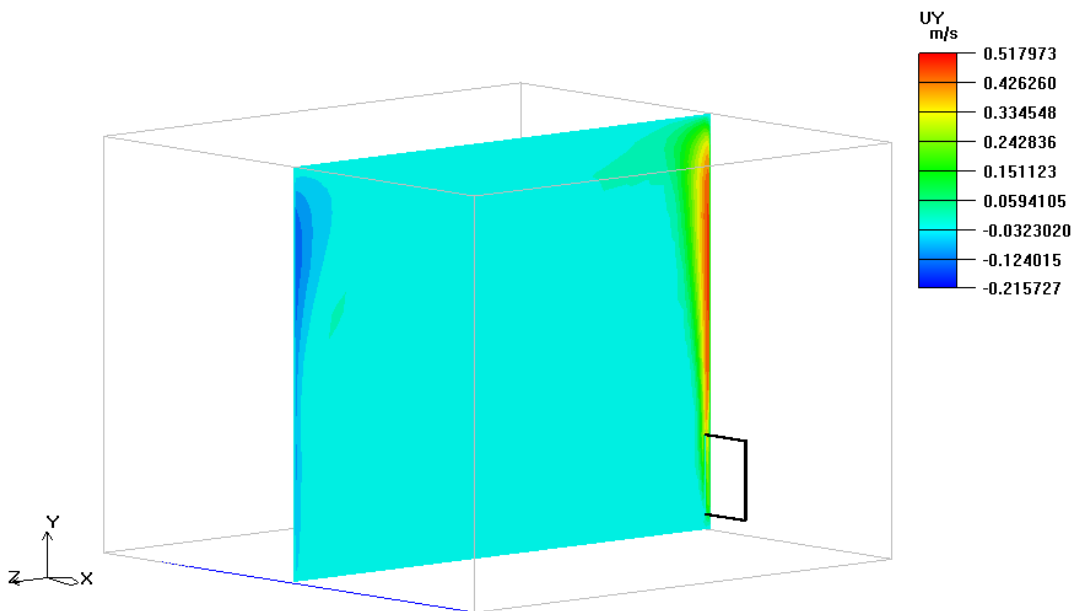


Figure 7.10. Y velocity contours at vertical plane (I-I) whose normal is in x direction (Grid II).

Hot air goes up around the heater while cold air flows to the bottom surface at the opposite side of the heater.

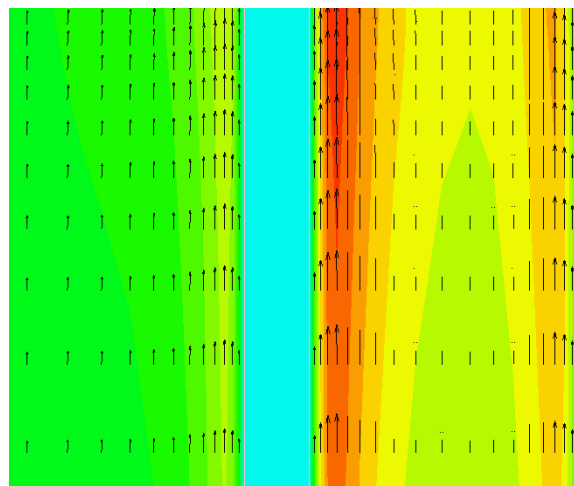
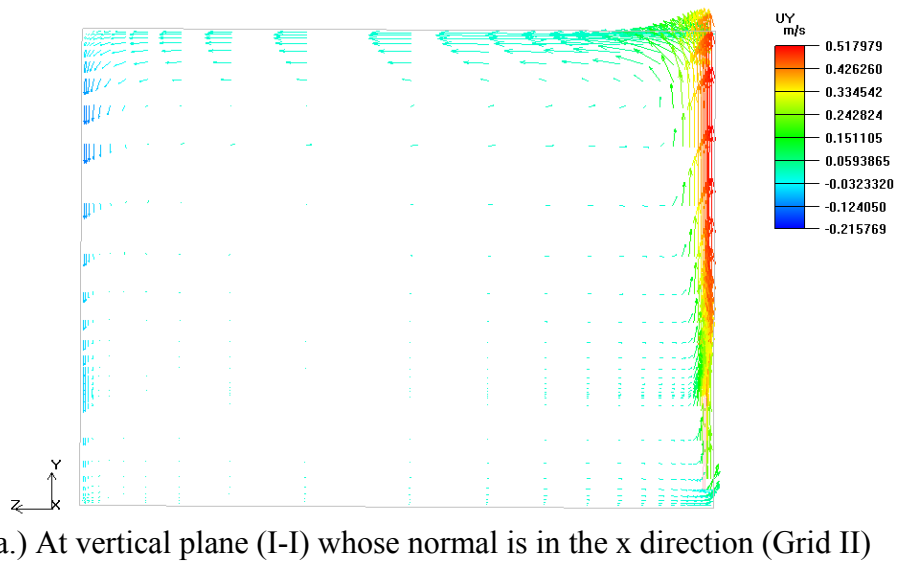


Figure 7.11. Velocity vectors (Grid II).

Table 7.5. Total heat transfer rates in different grid structures.

GRID	Turbulence Model	Heat Transfer Rate (W)
I	k- ϵ	376.225
	Realizable k- ϵ	376.30
II	k- ϵ	377.823
III	k- ϵ	377.821
IV	k- ϵ	377.820

7.2. CFD Analysis of Tested Radiators

In this section the details of computational study for tested radiators are presented.

7.2.1. ICEPAK Models for Tested Radiators

CFD models for the tested radiators (Radiator I, II and III) are shown in Figure 7.12. They are prepared in ICEPAK software. Because of the difficulties in radiator geometries rounds are ignored. Dimensions are same except at the cross sectional area of vertical water channels. Since cubical elements can be meshed properly in ICEPAK, the water volume in gaps is simplified. A detailed view of CFD model of a single panel is given in Figure 7.13.

In CFD models, air and water volumes are created from solid rectangular prisms at the beginning. Their material properties are changed from solid to fluid, later. Water is assigned as a default fluid while air is defined as a secondary fluid. Because priority is important in ICEPAK modeling. When two intersecting blocks are drawn, the late generated object whose priority is high is meshed before. Also boundary conditions and material properties of the late generated object is used in the intersection. As a result of pressing two steel sheets, a solid region is created as seen in Figure 7.14-b. Those parts are modeled by solid blocks. All steel shells which located around water channels are modeled by conducting thin plate whose thickness is zero. However thickness and conductivity are taken into consideration in the calculations. Only steel sheets shown in Figure 7.14-a are made from the solid blocks. The effective thickness and material of the thin plates are determined.

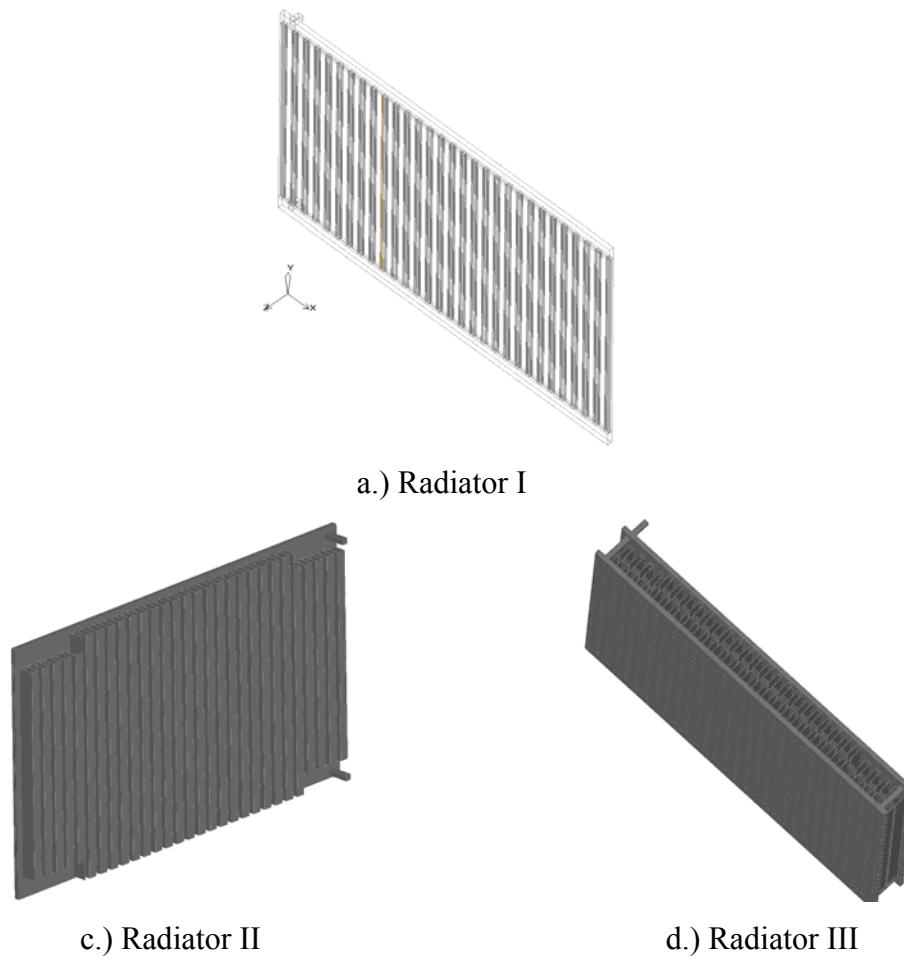


Figure 7.12. ICEPAK models of tested radiators.

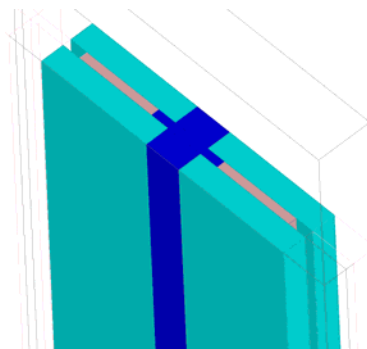


Figure 7.13. Details of CFD model of single panel.

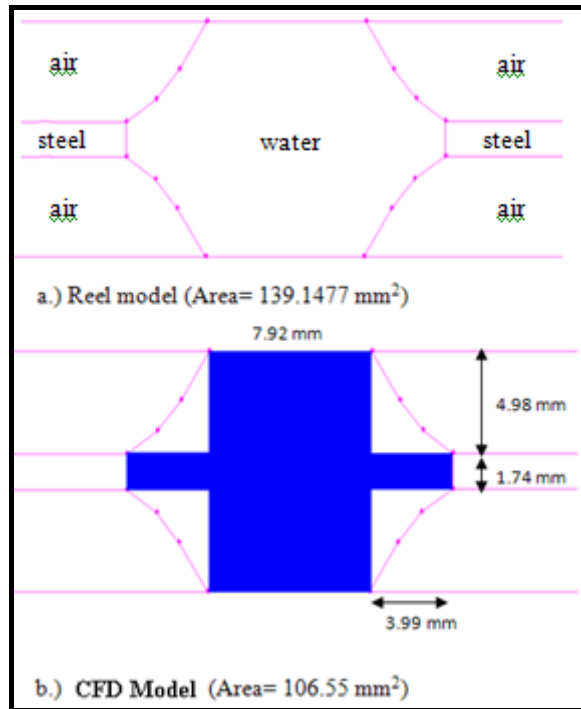


Figure 7.14. Comparison of real and CFD models.

7.2.2. Mesh Details

Four different grid structures in which number of elements is changed are tried in CFD analysis of Radiator I (case 1) as seen in Table 7.6. Since the results of last two grid structures (C-I and D-I) are similar for Case 1, other cases (Case 2 and Case 3) are solved with only C-I and D-I for Radiator I.

Table 7.6. Mesh details for Radiator I.

	A-I	B-I	C-I	D-I
Number of Elements	831 784	1 111 492	1 472 646	3 159 224
Number of Nodes	879 723	1 173 042	1 548 356	3 266 230

Uniform grid structure is preferred at the region represents the test room air in CFD model of radiator I as shown in Figure 7. 14. The grid density had been increased around the walls of the virtual test room and tested radiators as seen in Figure 7.15.

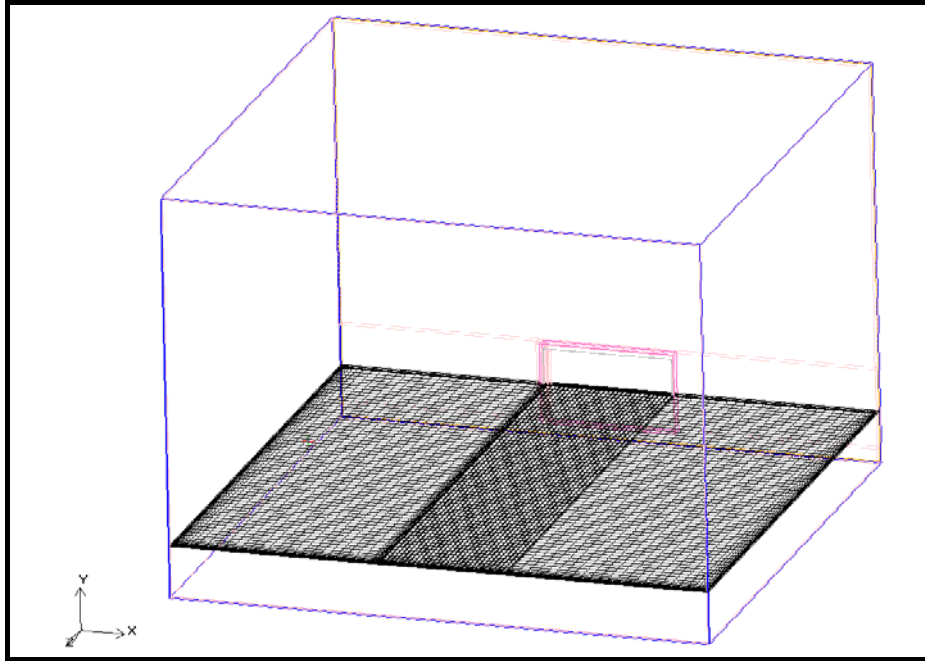


Figure 7.15. A cross sectional view of grid created in the virtual test room which includes radiator I.

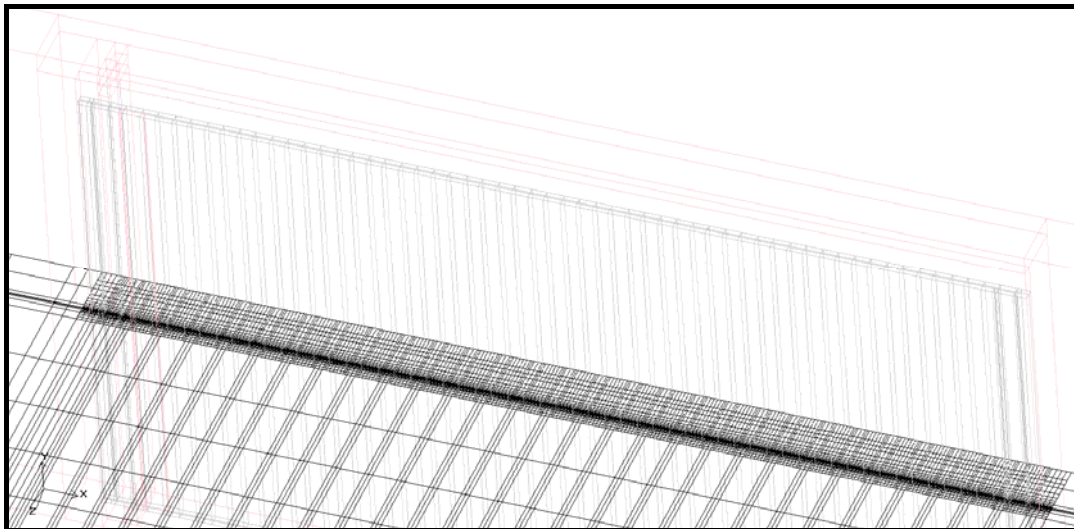


Figure 7.16. The grid density around radiator I.

Similar strategy was used in the preparation of CFD models of radiator II and III. The cross sectional views of grids are presented in Figure 7.17 and 7.19 for other CFD models of investigated radiators. Also for those models, grid densities were increased around the panel and extended surfaces as shown in Figure 7.18 and 7.20.

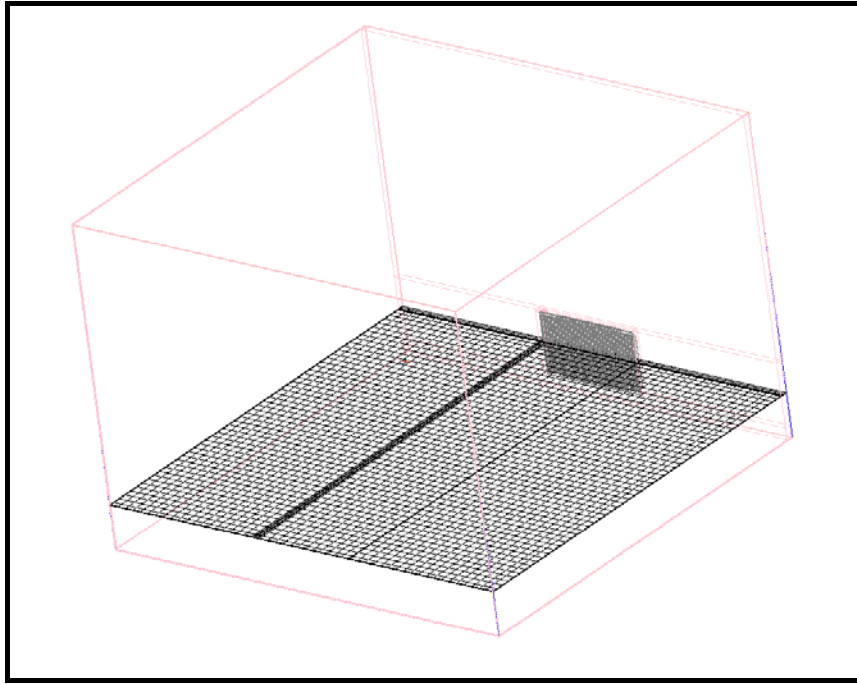


Figure 7.17. A cross sectional view of grid created for the test room includes radiator II.

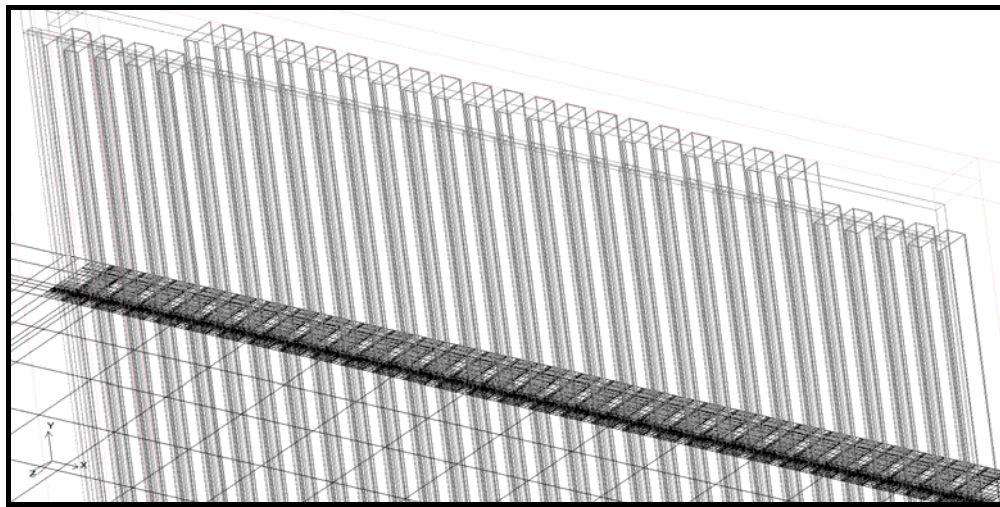


Figure 7.18. The grid density around radiator II.

Table 7.7. Mesh details for three cases of Radiator II.

	A-II	B-II
Number of Elements	1 727 060	2 147 514
Number of Nodes	1 816 385	2 248 135

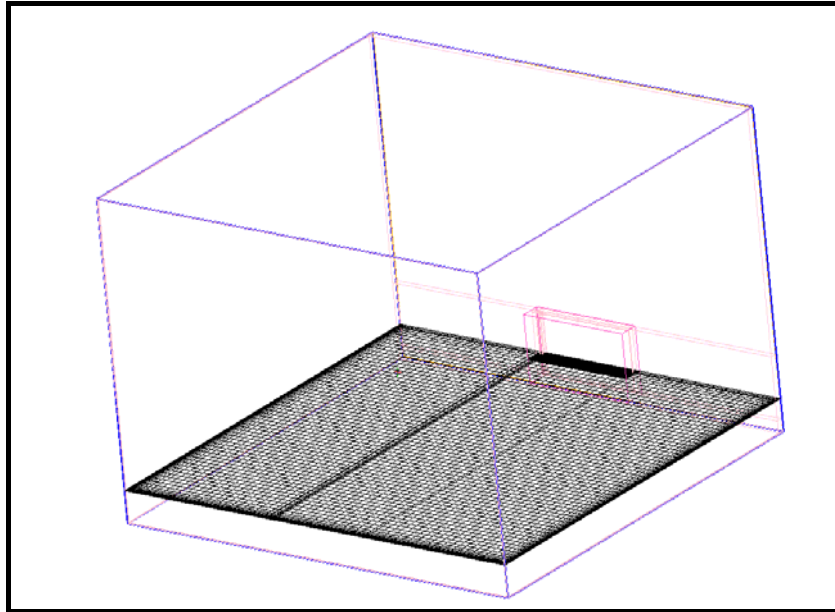


Figure 7.19. A cross sectional view of grid created for the test room includes radiator III.

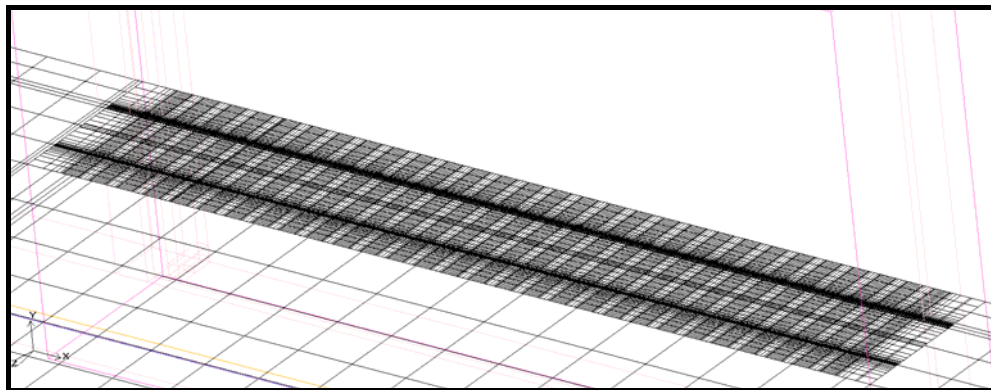


Figure 7.20. The grid density around radiator III.

Table 7.8. Mesh details for three cases and Radiator III.

	A-III	B-III
Number of Elements	2 670 998	3 198 404
Number of Nodes	2 760 778	3 303 414

7.2.3. Boundary Conditions

Since three test conditions are defined in EN 442 part 2 standard for tested radiators, the computational study is performed with applying different boundary

conditions. In each case, the inlet water velocity is defined with its temperature. Inlet velocity is calculated by using Equation (7.1).

$$V_{in} = \frac{\dot{m}_w}{\rho_w \cdot A} \quad (7.1)$$

Where ρ_w is density of water circulated through the hollow section of radiator and A is the cross-sectional area of inlet section. For the considered problem, rectangular water channels whose hydraulic diameters are equal to circular connection pipes are used in the computational study. These channels are assumed insulated as in real tests. Their cross sectional areas are 169 mm^2 . Water density is assumed 1000 kg/m^3 for the calculation of inlet velocity. The temperature values are taken from real tests. Average values are used to determine inlet boundary conditions. Velocity and temperature of inlet water are defined as summarized in Table 7.9, in the analysis.

Table 7.9. Boundary conditions at radiator inlet.

Radiator	Case	$T_{in} (^{\circ}\text{C})$	$V_{in} (\text{m/s})$
I	1	75.22	0.1028
	2	86.56	0.1031
	3	52.48	0.1029
II	1	74.81	0.1354
	2	86.15	0.1348
	3	52.70	0.1353
III	1	75.41	0.2539
	2	89.97	0.2545
	3	53.21	0.2548

Since several steady runs are performed for all models and each case. The steady state results are attained in those computational performances. At the beginning runs wall temperatures are kept at 20°C . When reference temperature is constant, the wall temperatures are changed and new iteration is initiated.

In the final runs, constant temperature boundary conditions with no slip conditions are specified at all horizontal and vertical walls of virtual test room as given in Table 7.10.

Table 7.10. Boundary conditions for the walls of virtual tests room (except wall behind tested radiators).

Radiator	Case	Temp(°C)
I	1	19.5
	2	19
	3	20
II	1	19
	2	18.5
	3	19.5
III	1	18.5
	2	18
	3	19

7.2.4. Assumptions and Solver Settings

Certain assumptions as given below are made in order to facilitate the analyses.

- Air flow is assumed incompressible turbulent.
- Ambient air is assumed 20°C.
- Boussinesq approximation is used.
- The gravity is set to 9.806 ms⁻².
- Steady state analysis are performed.
- Very small velocity on y direction (0.001 m/s) is put as an initial value at the beginning of runs.
- Because the mesh is not coarse and existence of small cells, double precision is preferred.
- SIMPLE algorithm is used to model the interaction between pressure and velocity.
- In order to speed up the solution times, first-order upwind scheme is applied for continuity, momentum and energy equations in first runs. Last runs when the first order solution approaches convergence, the second order discretisation scheme is enabled.
- k-ε turbulence model is used.

7.2.5. Convergence Criteria

Computational run for one case of a radiator was completed in 7 days by using a computer having 12 GB Ram and 3GHz Processor. Trial periods are not included to computational run times. One of the reasons for long run times is using only one processor because of the restriction when shell conduction is used in the analysis.

In this study, change in temperature of reference point and velocity near the virtually tested radiator are controlled by assignment of several points during analyses. It is observed that oscillations in temperature can be seen when coarse mesh is used. Several runs are performed for one radiator type to find steady state conditions in the virtual test room. It is evaluated that when the temperature of reference point and residuals are being controlled only, specious results can be obtained. Velocities cannot be reached steady state values although controlled temperature is being constant. In this study, the CFD runs were stopped as velocities near the tested radiator becomes. To shortened run times, several runs were performed for each radiator and case. One run was stopped when the reference air temperature became constant. The next run was initiated with last solution data and stopped when velocities were constant. Changing of scaled residuals in continuity, u velocity, v velocity, w velocity, energy, k, ϵ and discrete ordinate intensity as explained in Chapter 2 are also followed.

Changing of parameters which are followed are given in Figures 7.21, 7.22 and 7.23 for Radiator II and Case 1 as an example. In all runs, same controlling mechanism is used to understand whether the flow is reached the steady state condition. Convergence criteria for residuals of flow, energy, turbulent kinetic energy and turbulent dissipation rate are 0.0001, 10^{-7} , 10^{-7} , and 10^{-7} , respectively.

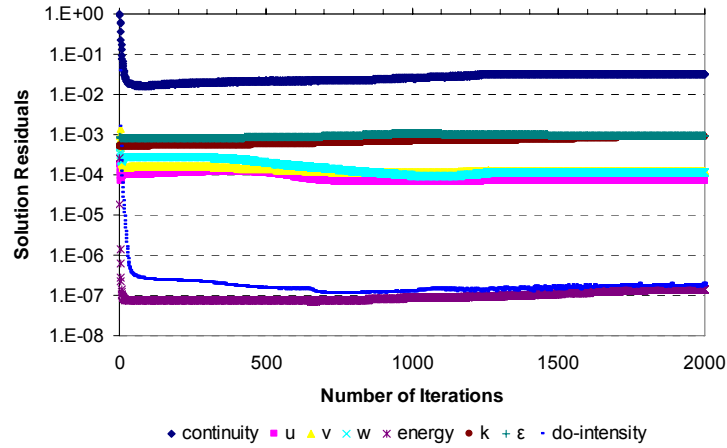


Figure 7.21. Residuals in the final CFD run for radiator II (Case 1).

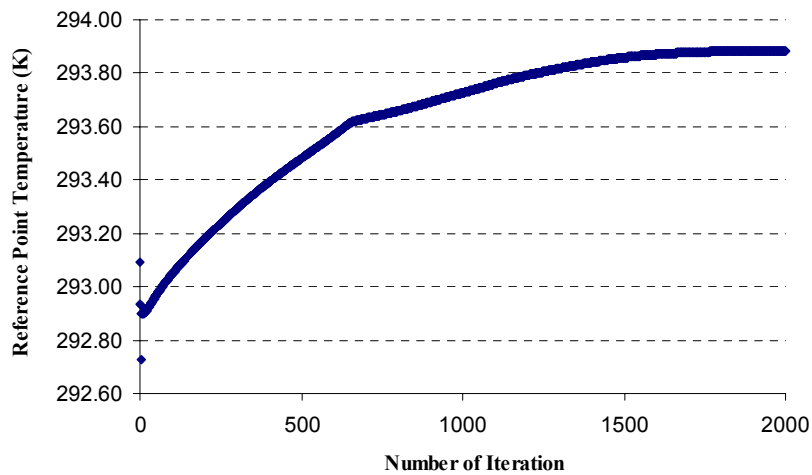


Figure 7.22. Reference point temperature in the final CFD run for radiator II (Case 1).

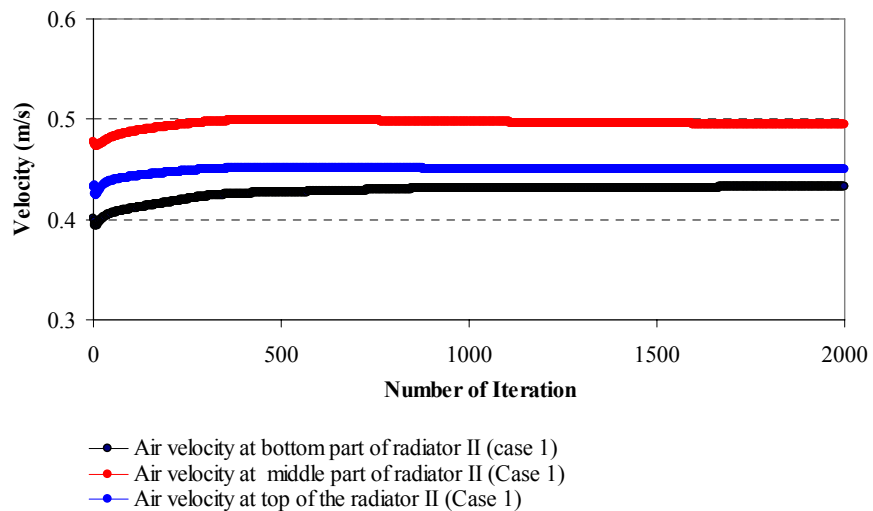


Figure 7.23. Air velocities in the final CFD run for radiator II (Case 1).

7.2.6. Comparison of Results

Computational and experimental results are compared by using Equation (7.2). By this way, the closeness of computational and experimental results is determined.

$$Difference\% = \frac{|Q_{comp} - Q_{exp}| \cdot 100}{Q_{exp}} \quad (7.2)$$

CHAPTER 8

RESULTS AND DISCUSSION

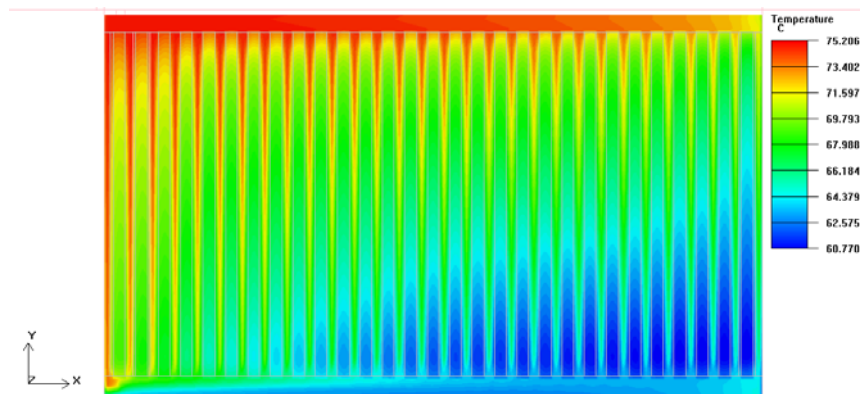
Heat outputs of tested three radiators were determined by using a commercial finite volume solver in this study. Temperature distributions at front dry surfaces and horizontal cross sections of investigated radiators were examined in the post processing part. Also velocity and temperature distributions in selected sections of the virtual test room were investigated apart from the experimental study.

Finally, experimental and computational heat outputs of tested radiators were compared to find correctness of numerical results. Since three operating conditions were taken into consideration in the experimental part, computational study was also accomplished for considered conditions. Results are presented for all examined cases.

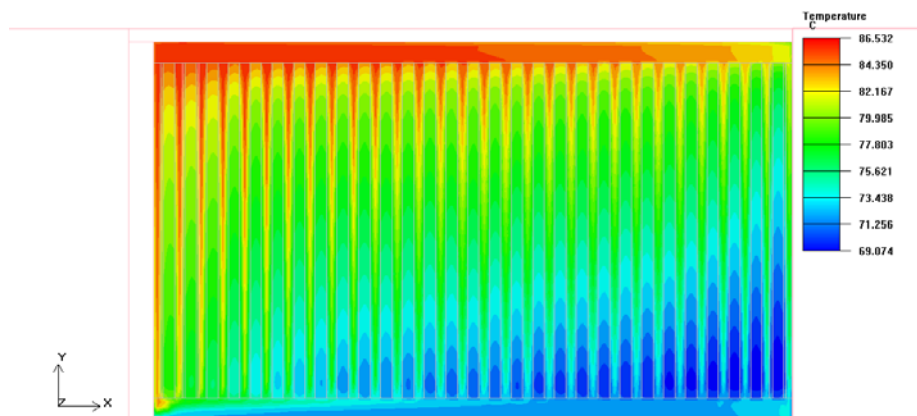
8.1. CFD Results for Radiator I

CFD model of radiator I is the simplest model examined in this study. Temperature distributions on vertical mid plane of CFD model of radiator-I are shown in Figure 8.1. It is detected that the hot water passes from the channels near to support line mostly. The bottom opposite side to the inlet section is the coolest part of radiator. Unfortunately, the temperature measurements from radiator surfaces are not specified in EN 442 standard. If temperature from the dry surfaces of the radiator is measured in the experimental study, it will be non equal in different points throughout the surface. The thermal camera views presented in Chapter 5 show non equal temperatures at the front surface. From the CFD results the non-uniform temperature distribution occurs at the front surface are also seen. Figure 8.2 in which temperature distribution at three different horizontal cross sections are drawn also illustrates that coolest water is collected at the bottom end of the radiator. Temperature distributions at two vertical mid planes are given in Figure 8.3 and Figure 8.4. Symmetric temperature contour lines are noticed in Figure 8.3. Effect of heating is shown in Figure 8.4. Temperature contours at the horizontal mid plane of virtual test room is given in Figure 8.5. The propagation of

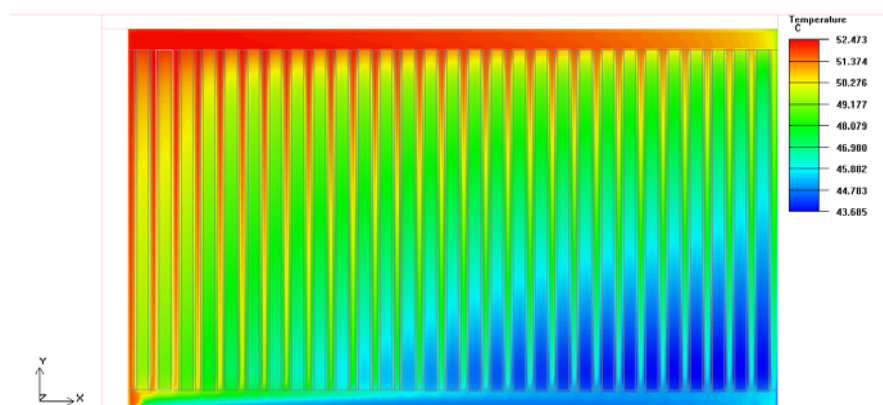
temperature fields are demonstrated clearly in this figure. The symmetric lines are also observed above the radiator.



a.)Case 1

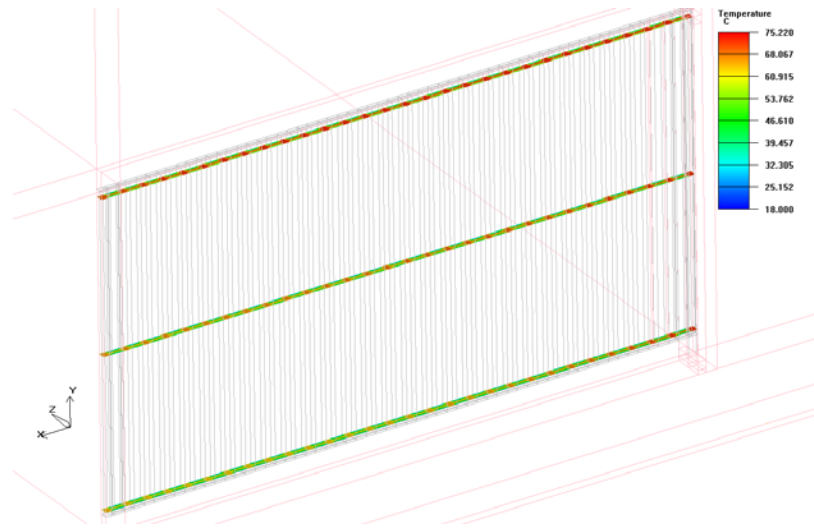


b.)Case 2

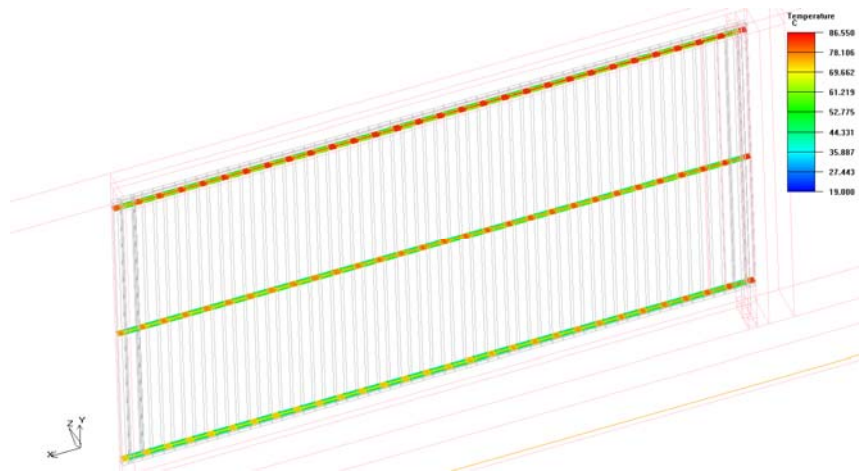


c.)Case 3

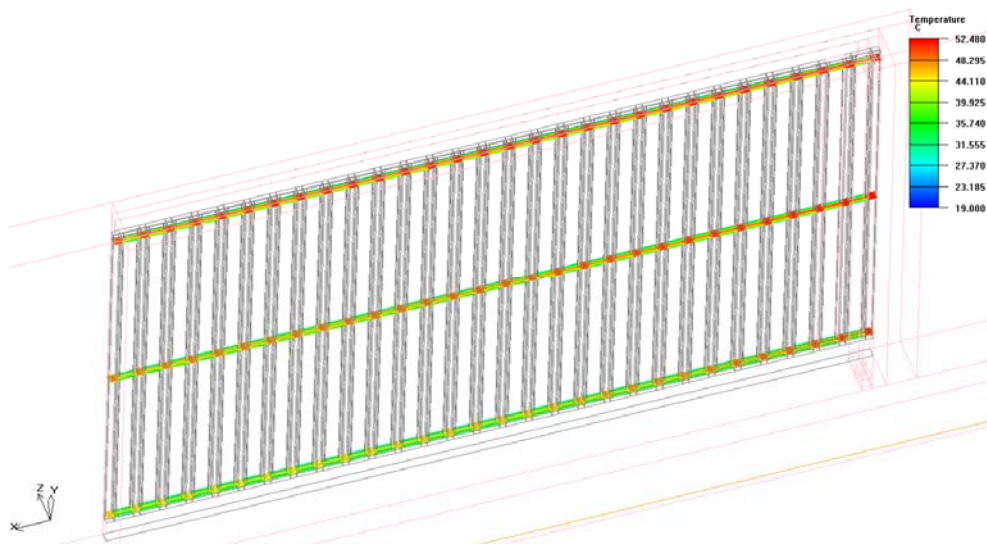
Figure 8.1. Temperature distribution on vertical mid plane of radiator I ($z=0.4559$ m).



a.)Case 1

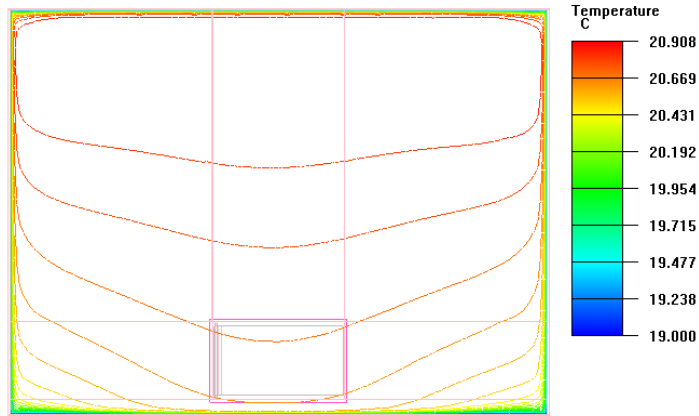


b.)Case 2

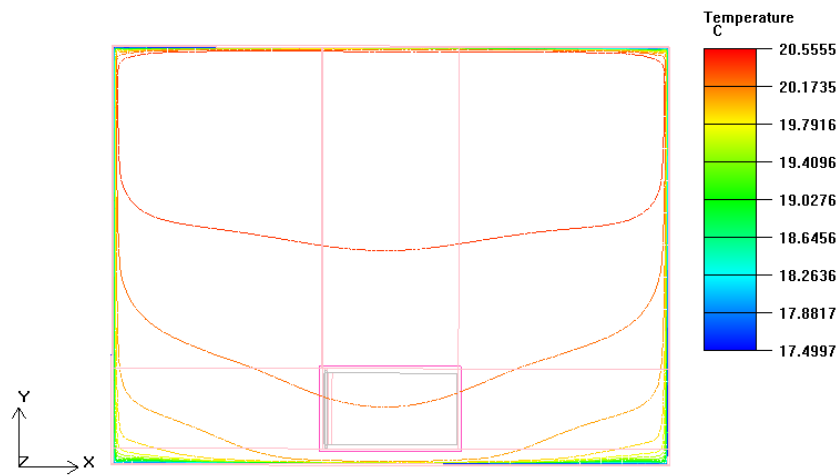


c.)Case 3

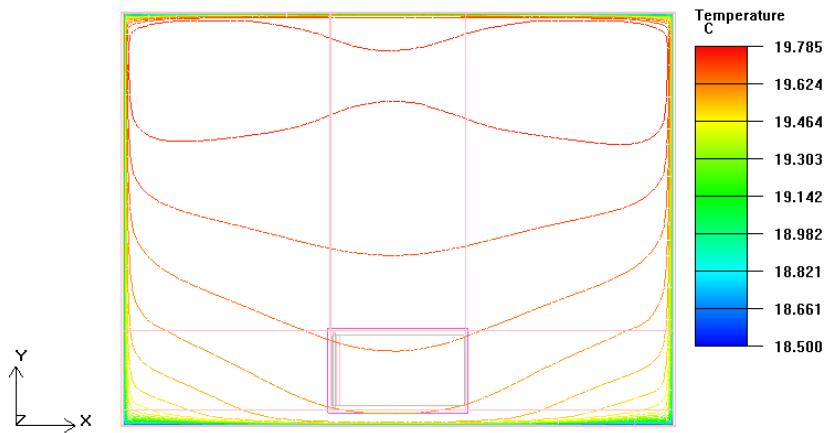
Figure 8.2. Temperature distributions at three different horizontal cross sections of radiator I.



a.) Case 1

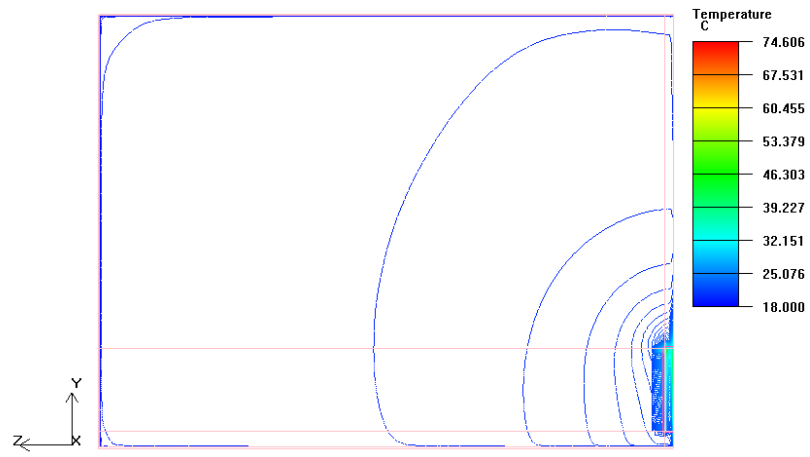


b.) Case 2

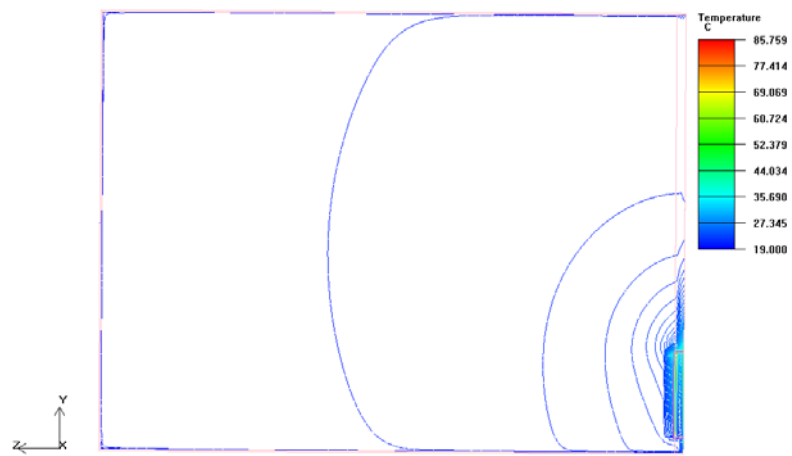


c.) Case 3

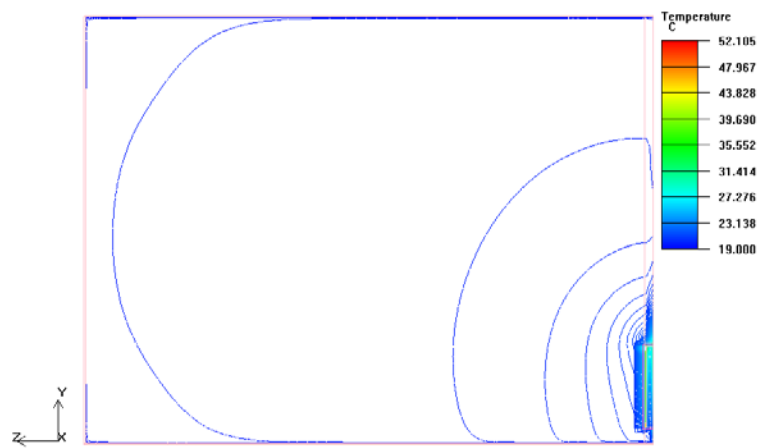
Figure 8.3. Temperature contours on the vertical mid plane of virtual test room whose normal is in z direction ($z=2.405$ m).



a.) Case 1

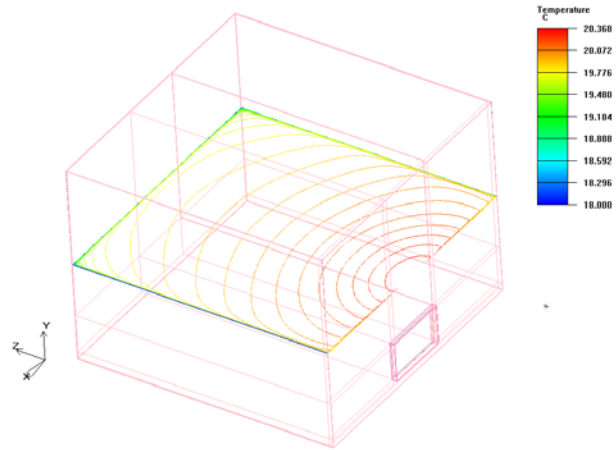


b.) Case 2

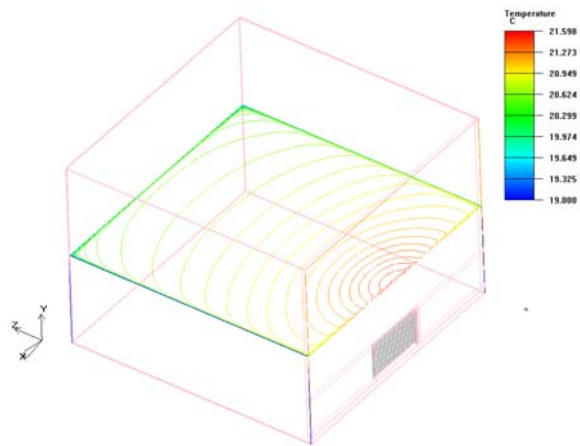


c.) Case 3

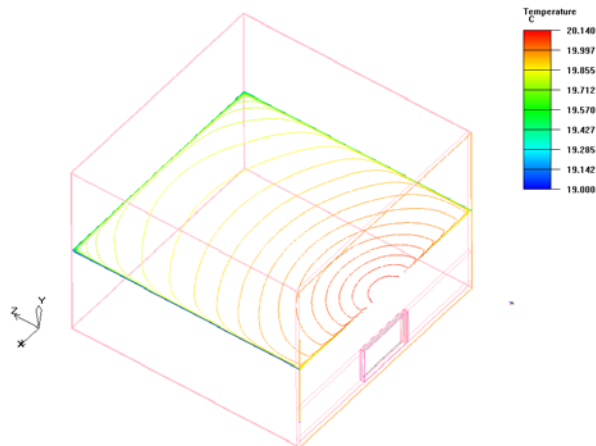
Figure 8.4. Temperature contours on the vertical mid plane of virtual test room whose normal is in x direction ($x=2.398$ m).



a.) Case 1



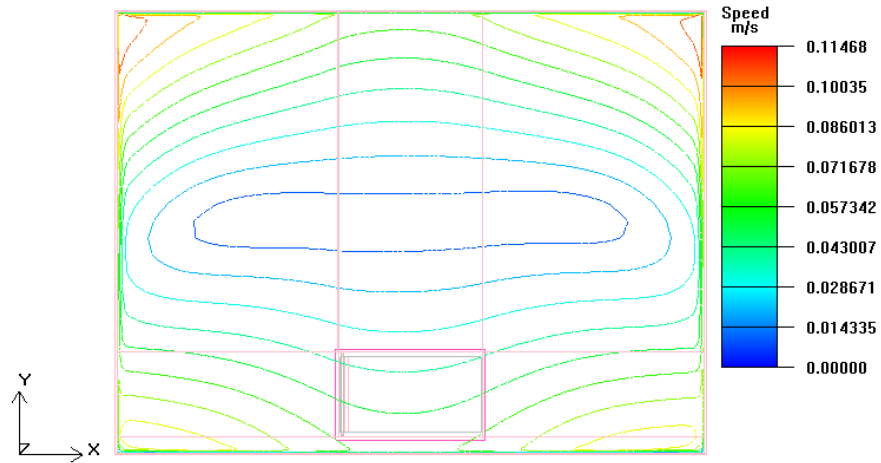
b.) Case 2



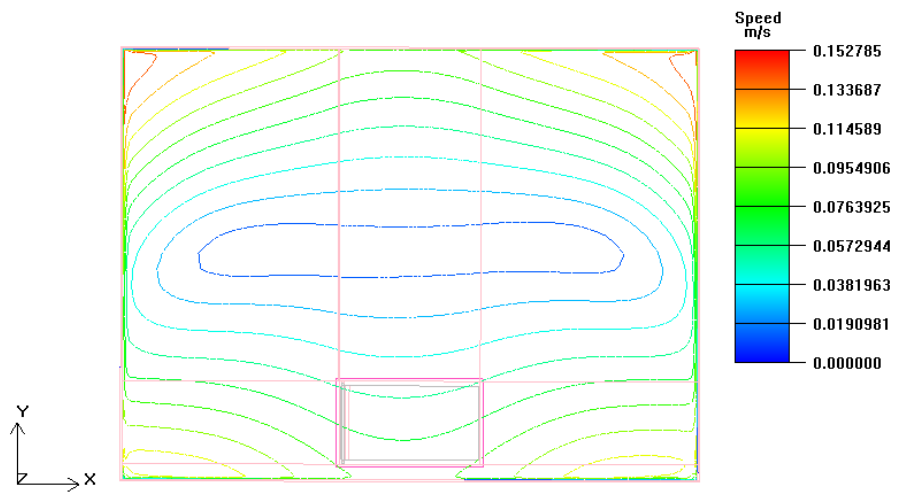
c.) Case 3

Figure 8.5. Temperature contours on the horizontal mid plane of virtual test room whose normal is in y direction ($y=1.867$ m).

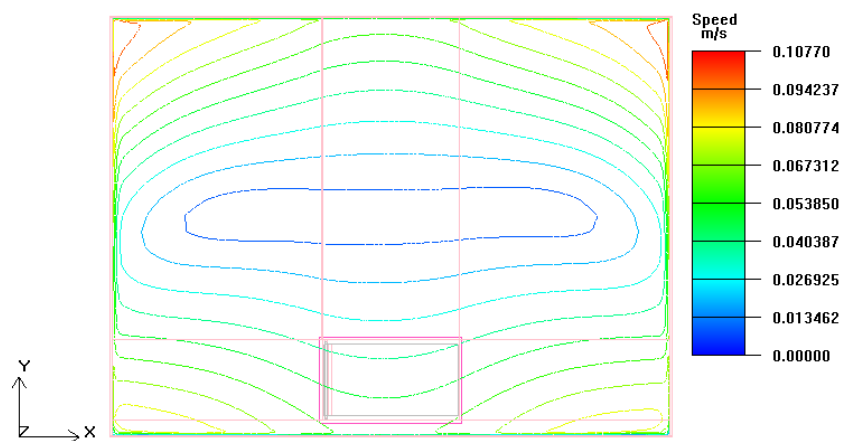
Hot region occurs the near to radiator in the virtual test room. In Figure 8.6, velocity contours are drawn with regard to velocity magnitude.



a.) Case 1



b.) Case 2



c.) Case 3

Figure 8.6. Velocity contours on the vertical mid plane of virtual test room whose normal is in z direction ($z=2.405$ m).

From Figure 8.6, it is seen that the velocity in the middle section is quite low. Velocity increases up to horizontal surfaces of virtual test room. Although there is a symmetry in velocity contours, it becomes to change.

Computational heat outputs in three different operating conditions are presented in Table 8.1. Computational (obtained from C-I grid structure) and experimental heat outputs are given together in Table 8.2.

Table 8.1. Computational heat outputs of radiator I in different grid structures (W).

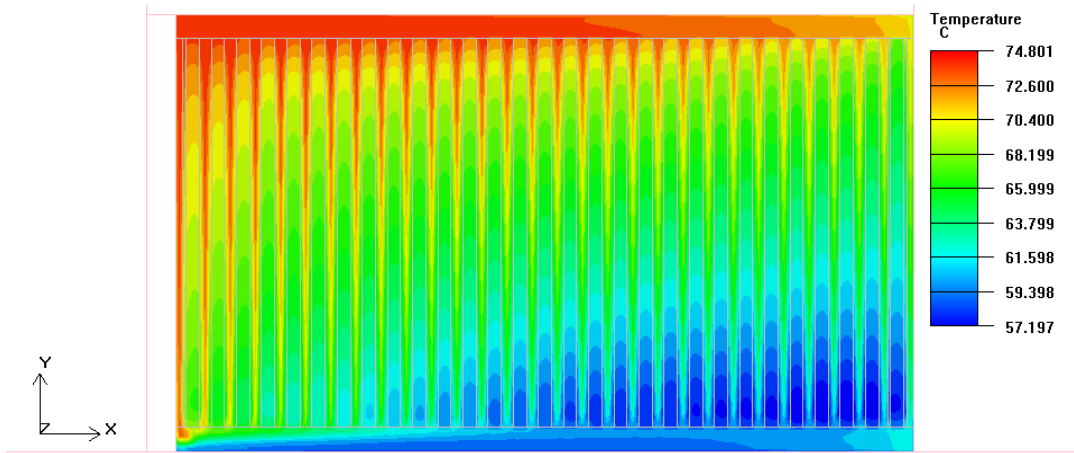
Case	Q_{A-I}	Q_{B-I}	Q_{C-I}	Q_{D-I}
1	962.33	821.15	743.27	739.8
2	-	-	964.87	953.8
3	-	-	391.15	393

Table 8.2. Compared heat outputs for radiator I (W).

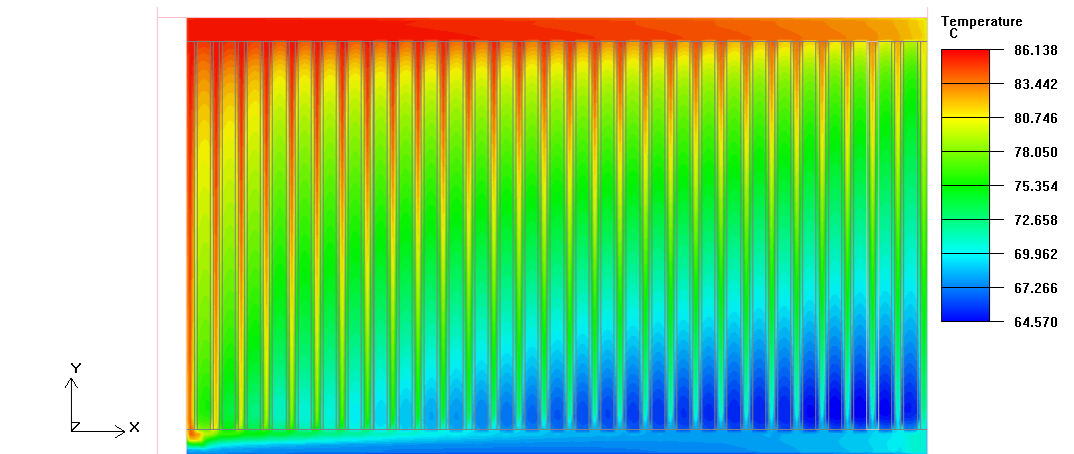
	Case I	Case II	Case III
Computational (Q_{D-I})	739.8	953.8	393
Experimental (Q_{exp})	736.5	902.1	346.0

8.2. CFD Results for Radiator II

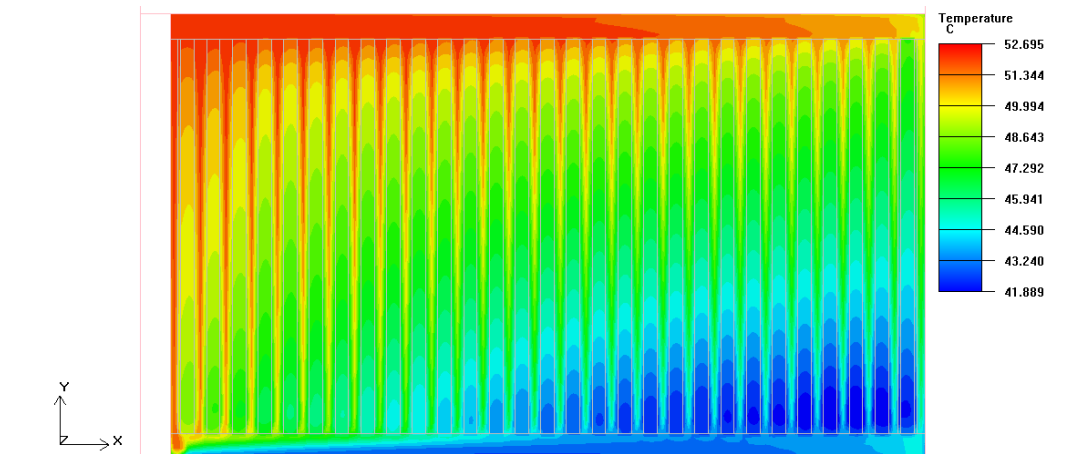
CFD model of radiator II includes fins attached to panel as described in Chapter 7. Temperature distributions on vertical mid plane of panel of radiator II are shown in Figure 8.7. Effect of extended surfaces is seen in Figure 8.7. The coolest region is closer to bottom part of the radiator. The temperature distribution on horizontal cross section is given in Figure 8.8. When those illustrations are taken into consideration same problem seen for radiator I is observed. The surface temperatures are not uniform for radiator II. Temperature distributions at several sections of the virtual test room are given in Figures 8.9 and 8.10. Velocity contours at the middle plane of the virtual test room are presented in Figure 8.11. The motion of air is shown in Figure 8.12 for radiator II. The beginning section is selected as the rear side of the radiator. Velocities are higher above the radiator. Particles move to radiator from all side of the test room



a.)Case 1

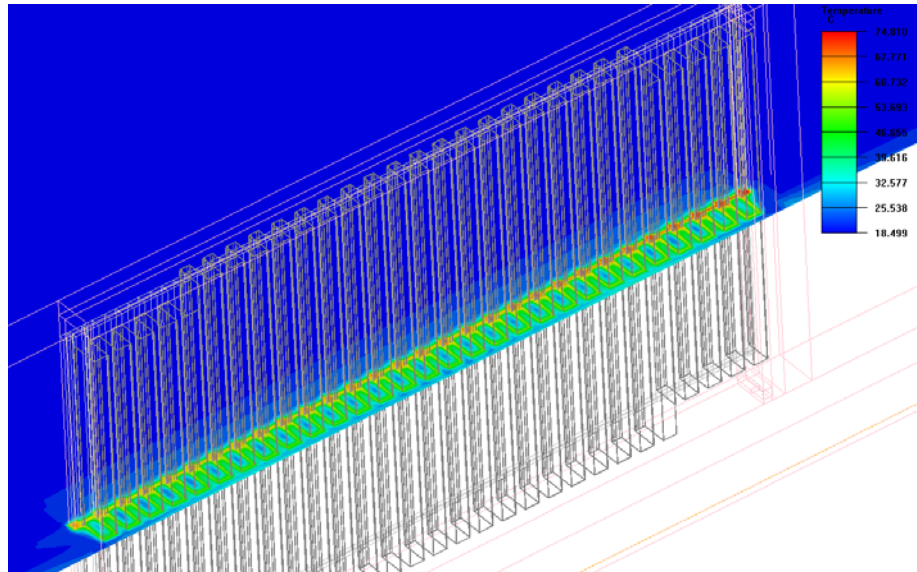


b.)Case 2

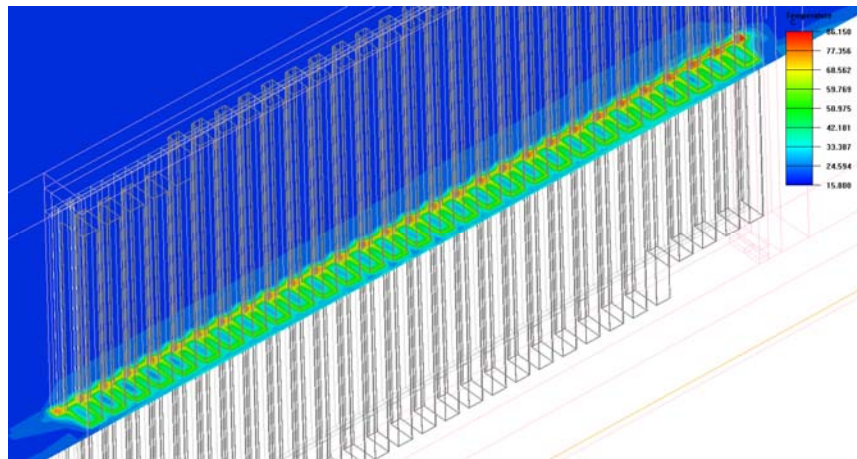


c.)Case 3

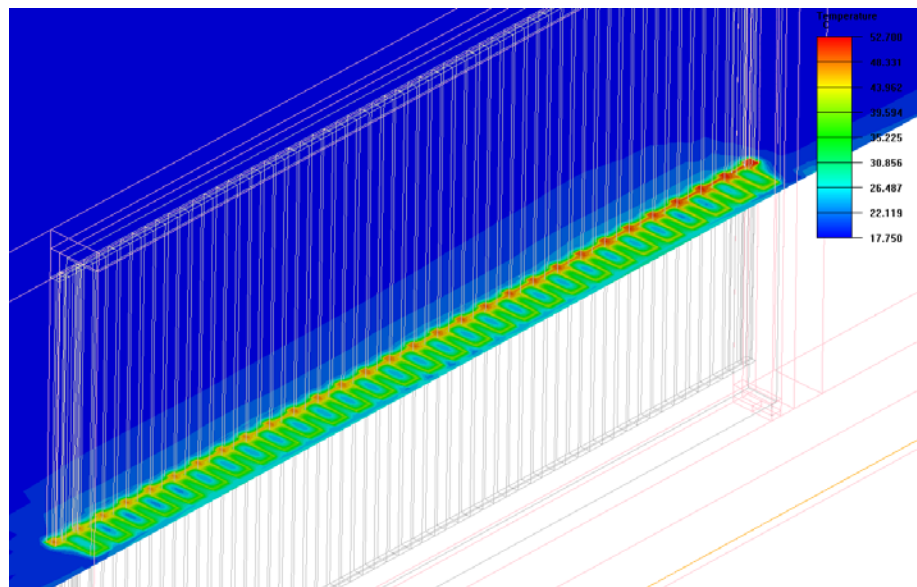
Figure 8.7. Temperature distribution on vertical mid plane of panel used in radiator II.



a.)Case 1

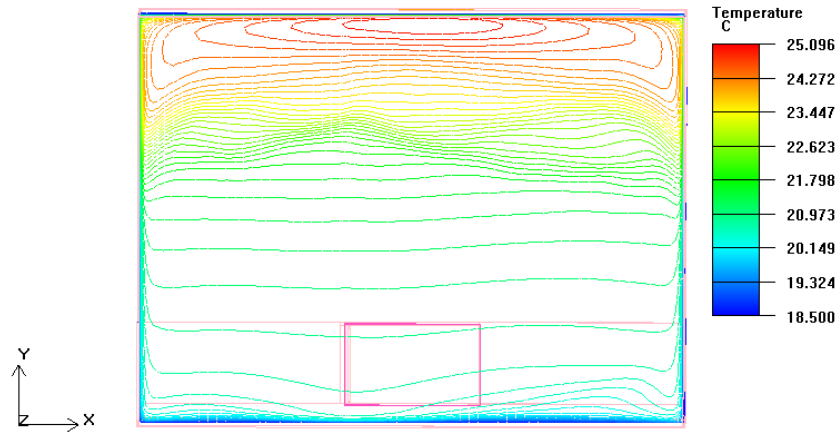


b.)Case 2

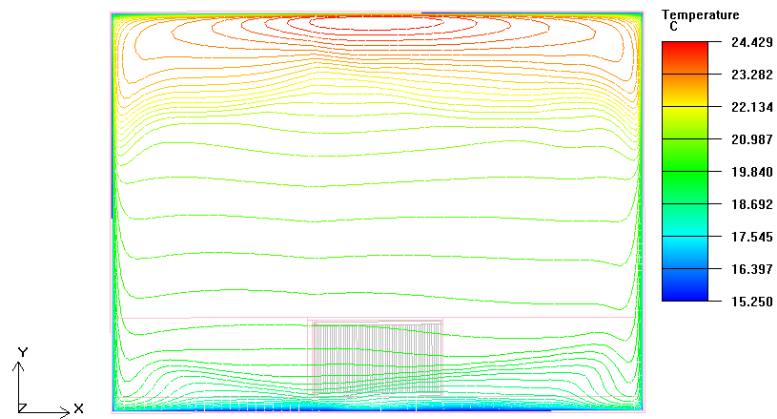


c.)Case 3

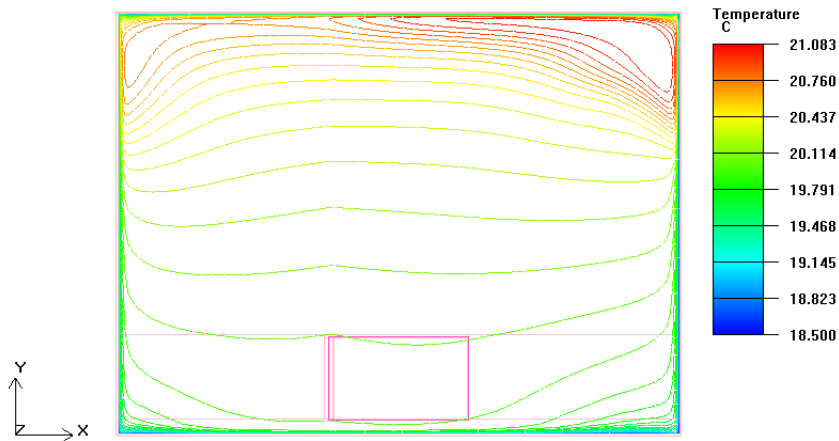
Figure 8.8. Temperature distribution on a horizontal cross section of radiator II.



a.)Case 1

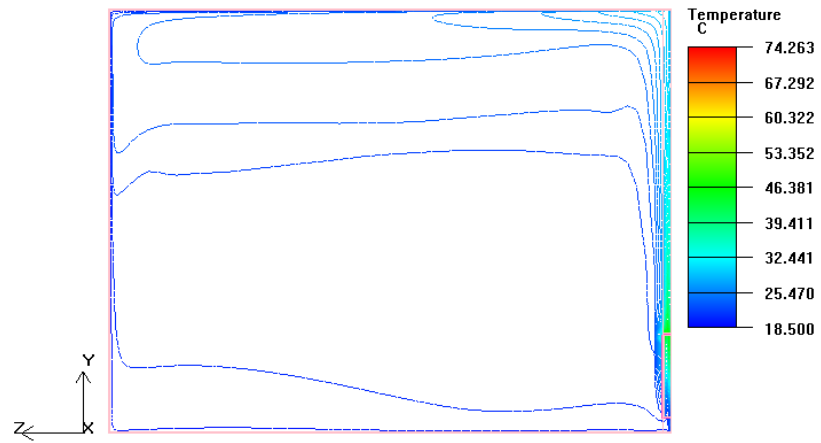


b.)Case 2

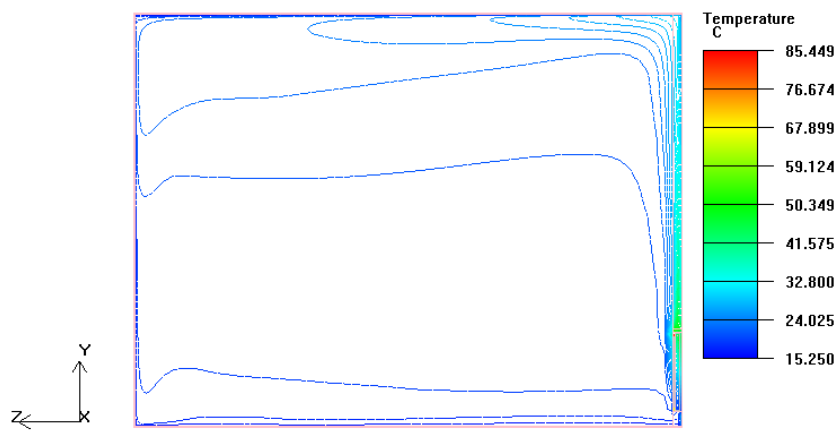


c.)Case 3

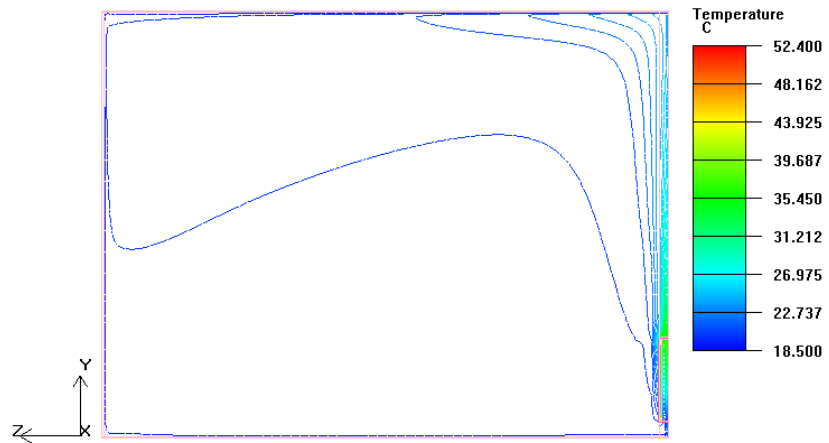
Figure 8.9. Temperature contours on the vertical mid plane whose normal is in z direction ($z=2.405$ m).



a.) Case 1

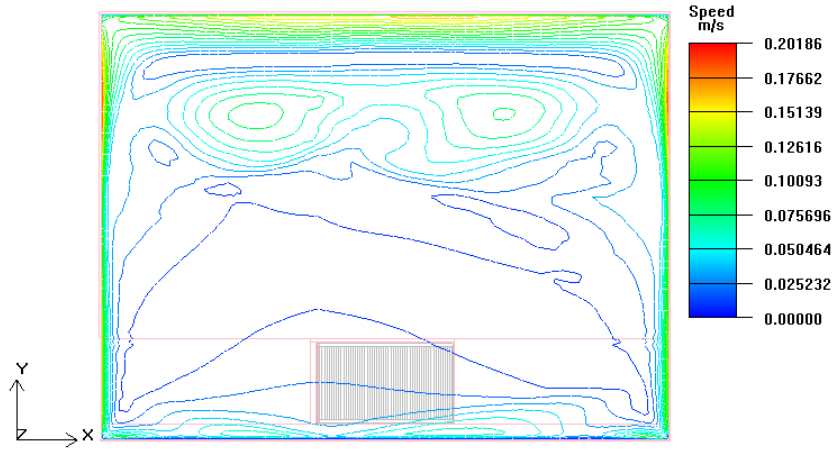


b.) Case 2

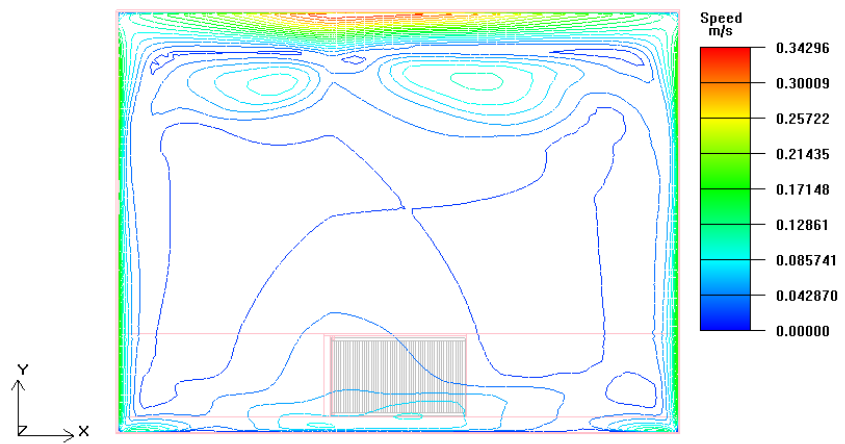


c.) Case 3

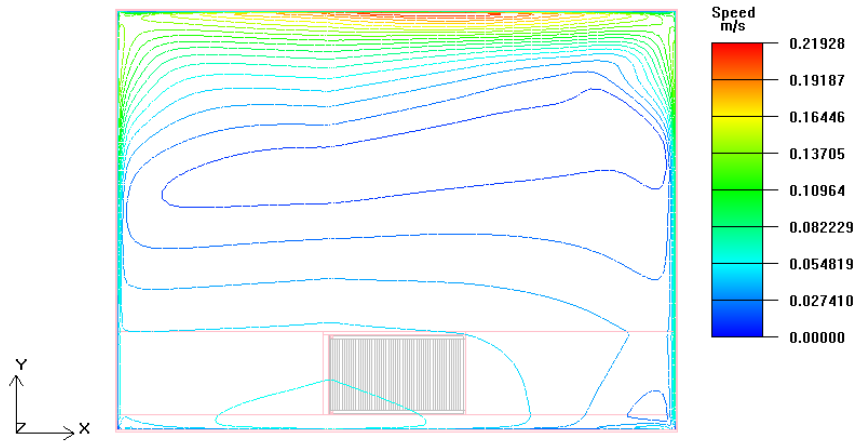
Figure 8.10. Temperature contours on the vertical mid plane whose normal is in x direction ($x=2.398$ m).



a.) Case 1



b.) Case 2



c.) Case 3

Figure 8.11. Velocity contours on the vertical mid plane whose normal is in z direction ($z=2.405$ m).

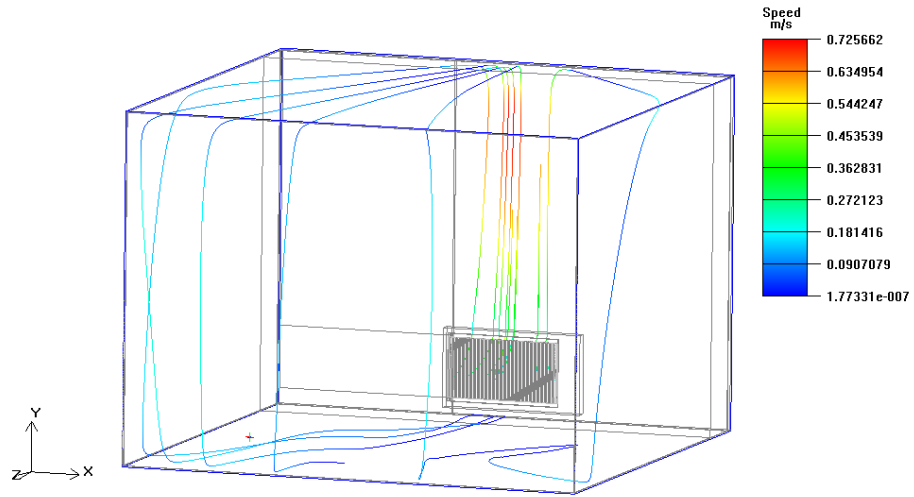


Figure 8.12. Path lines for the air motion in virtual test of radiator II.

Heat outputs in three different cases for radiator II are presented in Table 8.3. The comparisons between computational heat outputs obtained from the second grid structure with experimental heat output are given in Table 8.4.

Table 8.3. Computational heat outputs (W) of radiator II in two different grid structures.

Case	Q_{A-II}	Q_{B-II}
I	1 004.18	1 001.56
II	1 307.93	1 302.38
III	546.80	544.07

Table 8.4. Compared heat outputs for radiator II.

	Case 1	Case 2	Case 3
Computational (Q_{A-II})	1 001.56	1 302.38	544.07
Experimental (Q_{exp})	968.42	1 210.25	489.87

8.3. CFD Results for Radiator III

Path lines are given in Figure 8.13 for radiator III. As it is seen from the figure, the flow of air becomes more complicated in the virtual test of radiator III. Temperature distributions on vertical mid plane of panel used in radiator III and in Case 1, Case 2 and Case 3 are shown in Figure 8.14, Figure 8.15 and Figure 8.16, respectively. Since there are two panels in radiator III, the temperature distributions on front and back panels are given separately. Velocity and temperature contours obtained for radiator III are given in Figure 8.17 and 8.18, respectively. As it is seen from Figure 8.17, the symmetricity is broken down in excess temperature of 60°C. The computational heat outputs in three different cases are presented in Table 8.5. Experimental and computational heat outputs are given in Table 8.6. Comparison of results is given in Table 8.7.

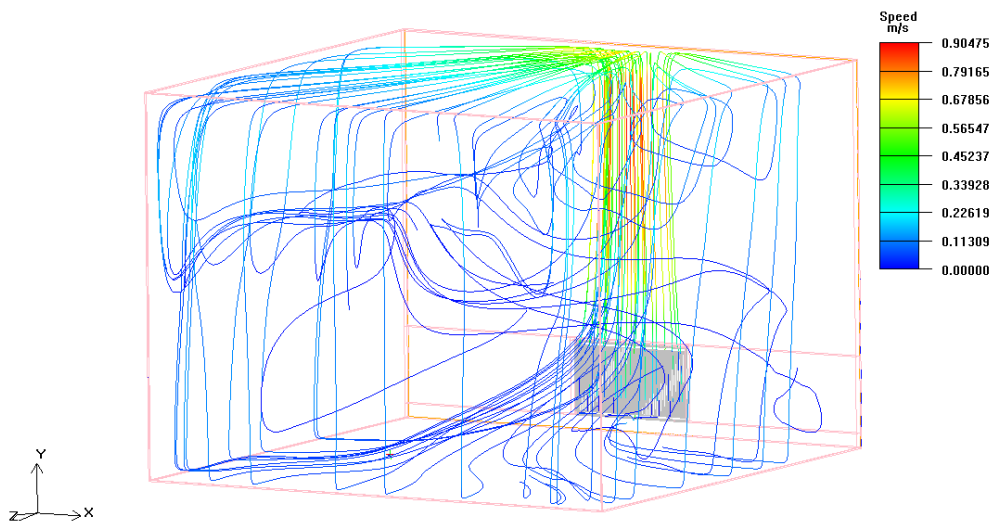
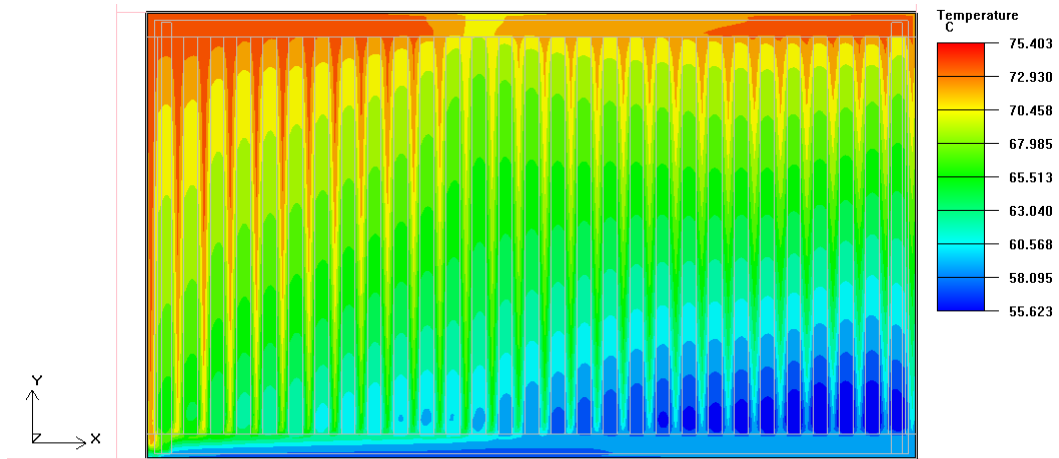
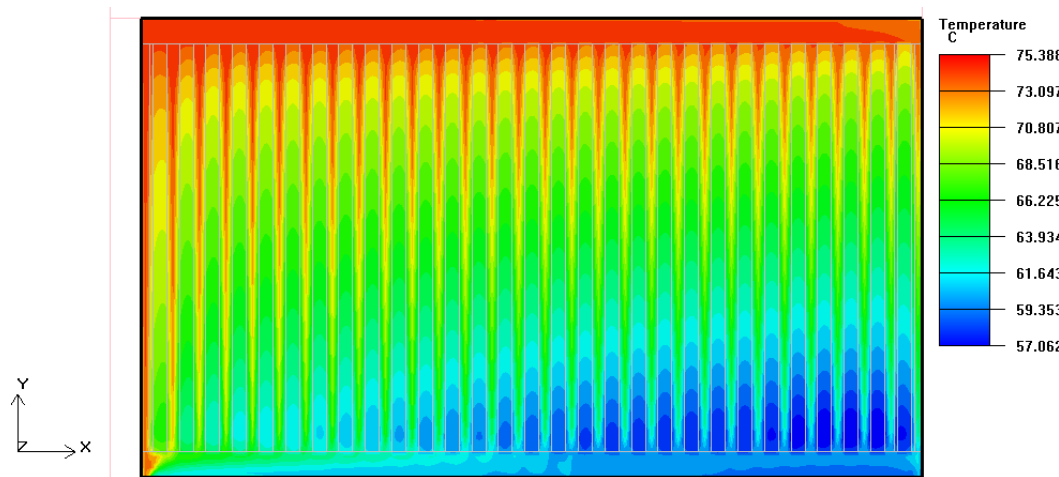


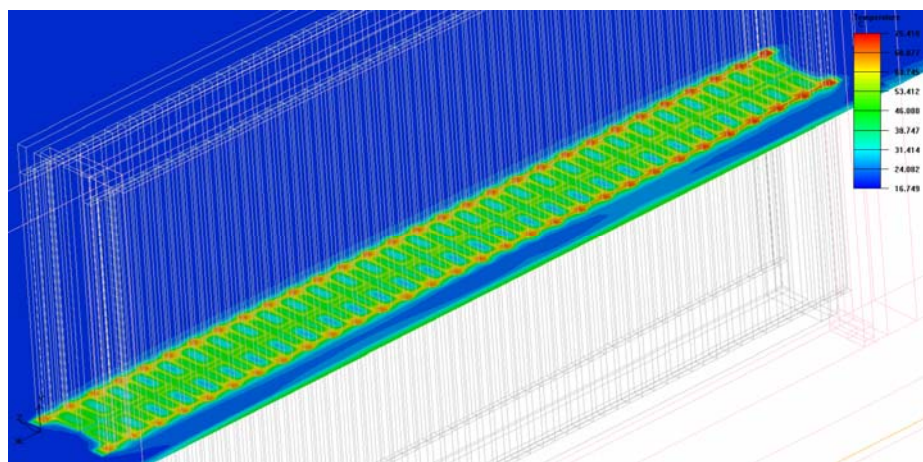
Figure 8.13. Pathlines for the air motion in virtual test of radiator III.



a.) Vertical mid plane on back panel.

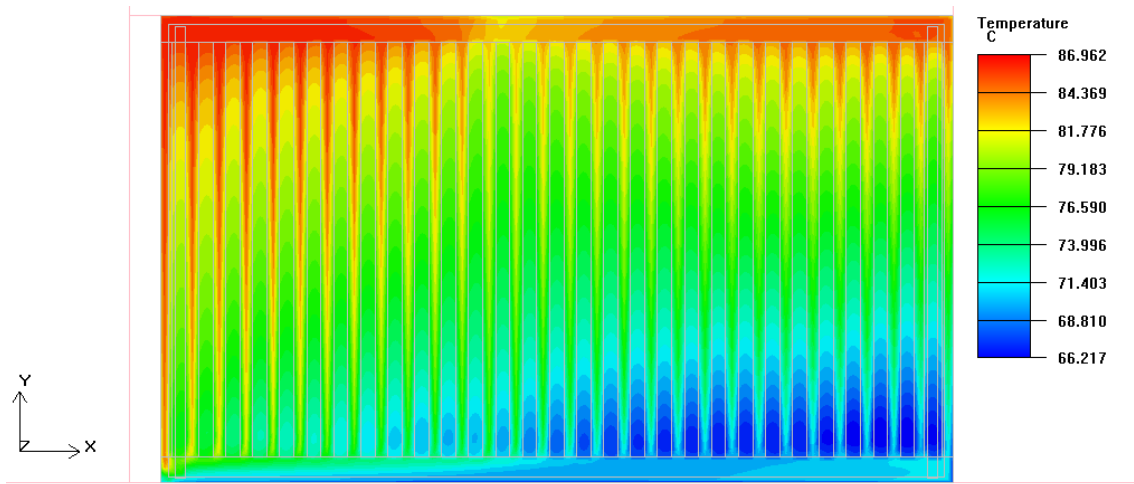


b.) Vertical mid plane on front panel.

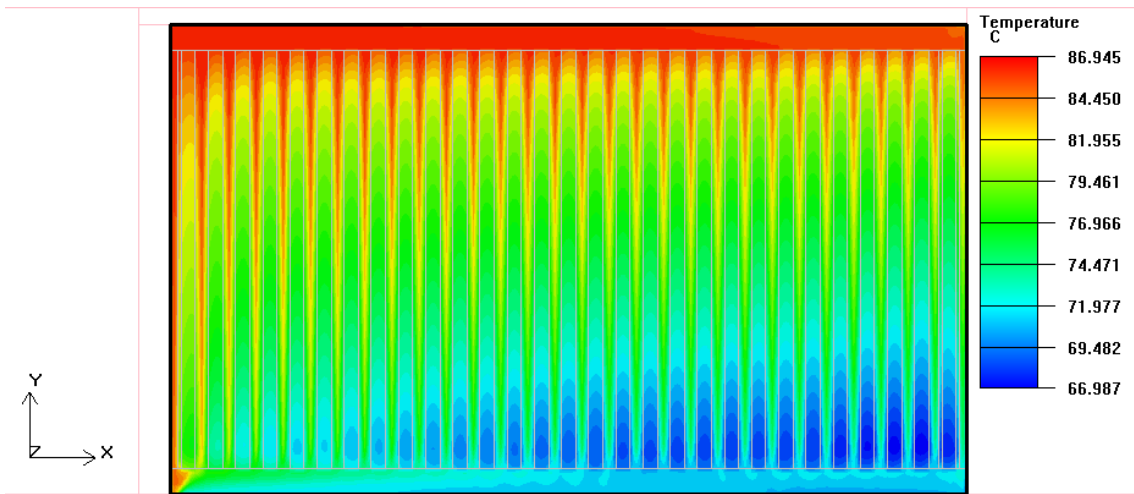


c.) Horizontal cross section.

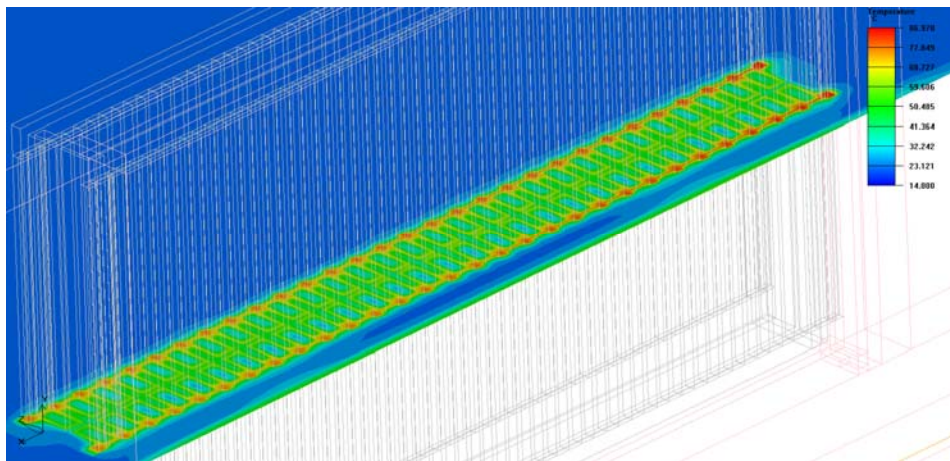
Figure 8.14. Temperature distribution on radiator III in case 1.



a.)Vertical mid plane on back panel

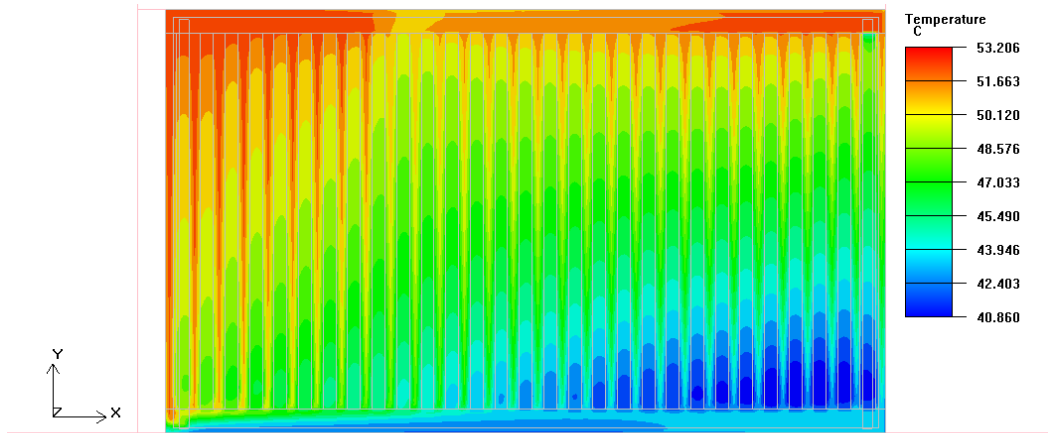


b.)Vertical mid plane on front panel

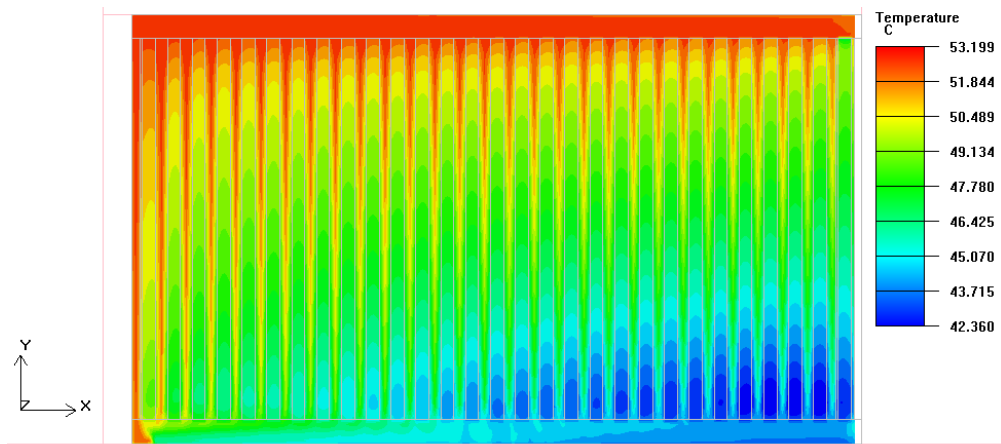


c.)Horizontal cross section

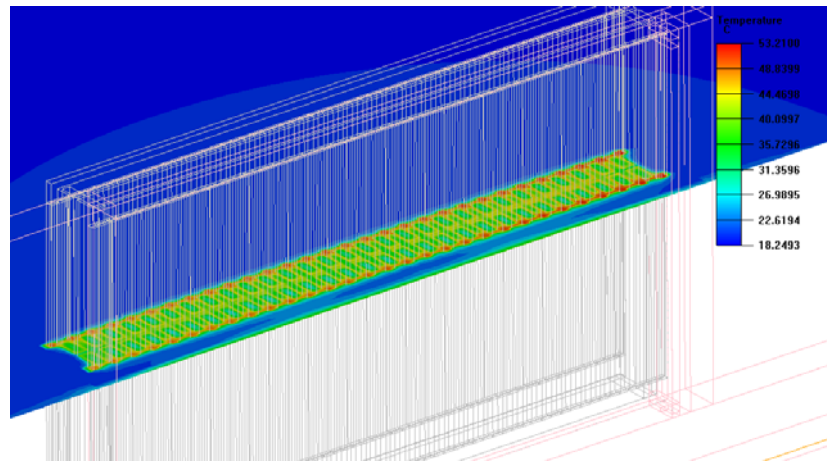
Figure 8.15. Temperature distribution on radiator III in case 2.



a.)Vertical mid plane on back panel.

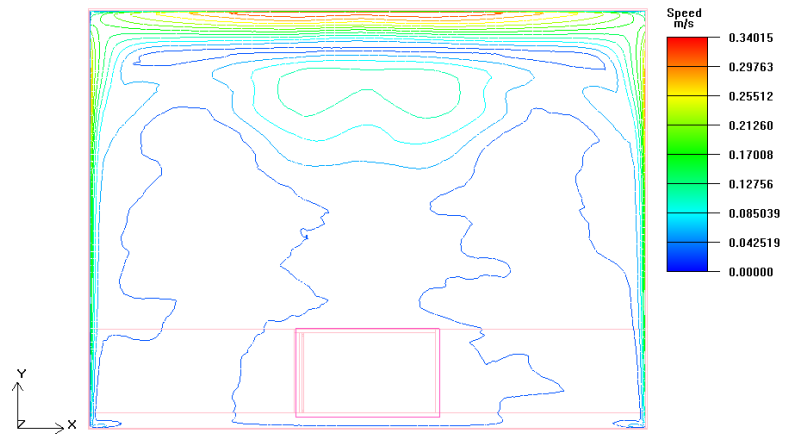


b.)Vertical mid plane on front panel.

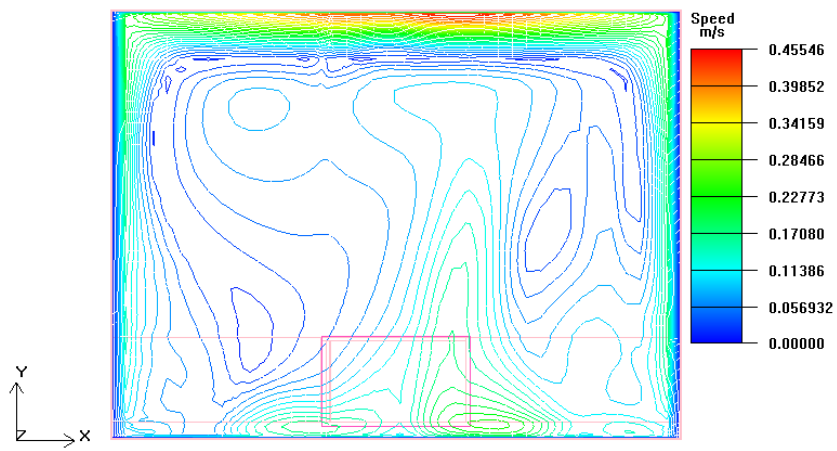


c.)Horizontal cross section.

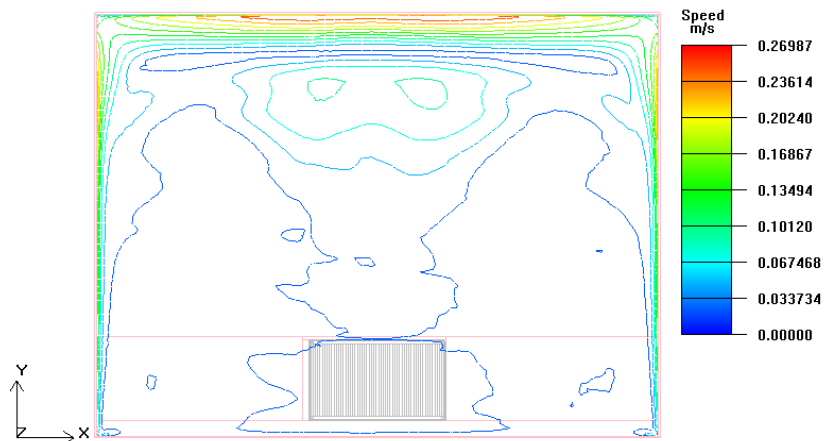
Figure 8.16. Temperature distribution on radiator III in case 3.



a.)Case 1

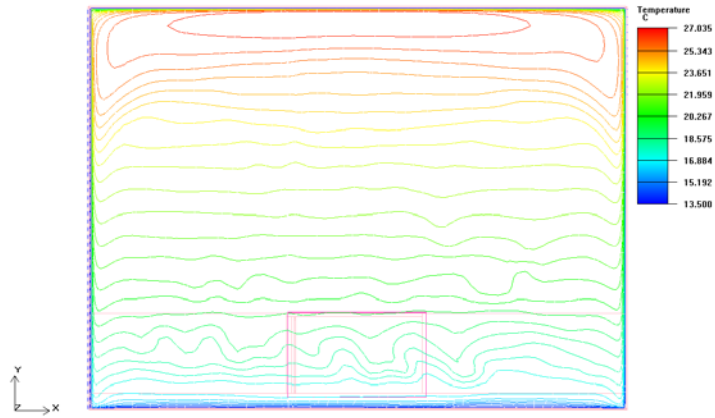


b.)Case 2

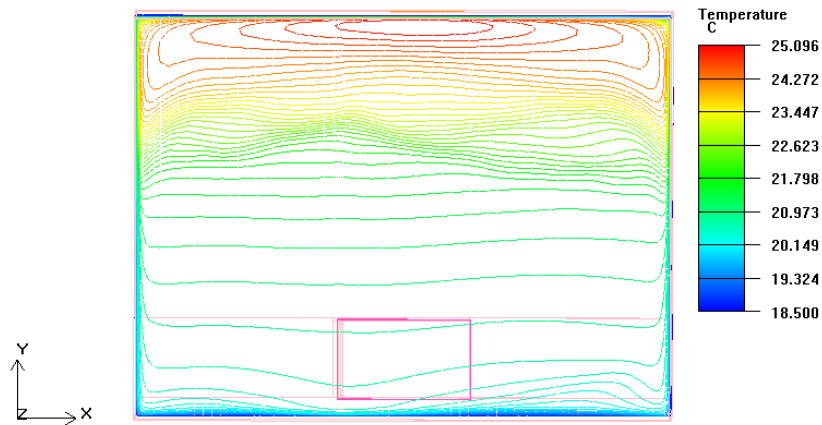


c.)Case 3

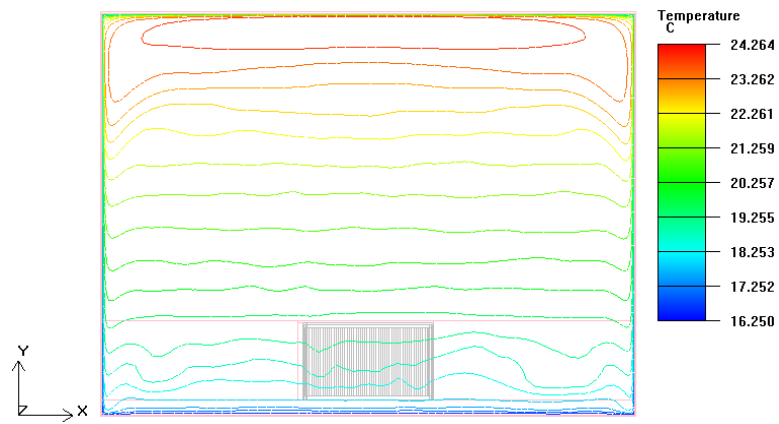
Figure 8.17. Velocity contours on the vertical mid plane whose normal is in z direction ($z=2.405$ m).



a.) Case 1



b.) Case 2



c.) Case 3

Figure 8.18. Temperature contours on the vertical mid plane whose normal is in z direction ($z=2.405$ m).

Table 8.5. Computational heat outputs of radiator III in two different grid structures (W).

Case	Q_{A-II}	Q_{B-II}
1	1 990.05	1 983.46
2	2 399.37	2 395.15
3	1 003.11	997.34

Table 8.6. Experimental heat outputs of radiator III (W).

	Case 1	Case 2	Case 3
Computational	1 983.46	2 395.15	997.34
Experimental	1 898.58	2 213.56	883.25

In Table 8.8, experimental and computational heat outputs are compared by using Equation (7.2) for all tested radiators.

Table 8.7. Comparison of heat outputs of tested radiators.

Radiator	Case 1	Case 2	Case 3
I	0.4	5.7	13.6
II	3.4	7.6	11.1
III	4.5	8.2	12.9

From the steady state analyses performed for the tested radiators, relatively closer results are obtained for the first case. It should be noted that the standard heat output of radiators are determined according to Case 1. The difference between experimental and computational heat output in percentage fluctuate between 0.4 and 13.6 for the simplest model (radiator I), 3.4 and 11.1 for the second CFD model radiator (radiator II), 4.5 and 12.9 for most complicated model investigated in this study. Quite good results are obtained for the excess temperature of 50°C and 60°C. For the lowest excess temperature, results are also in acceptable range. It is considered that difference can be sourced from turbulence model, radiation model, using Boussinesq approximation and errors seen in CFD process as mentioned in Chapter 2.

CHAPTER 9

CONCLUSION

The aim of this study is investigating whether numerical methods are applicable in the determination of heat output of radiators. One of the important advantages of using CFD software in this problem is that it enables to control flow properties like temperature and velocity at more than one point in the virtual test room. On the other hand, measuring of temperature and velocity is not easy and measuring devices require calibration. CFD solutions need experimental validation.

At the beginning, experimental heat output of radiators was determined in the test room designed with regard to EN 442 part 2 standard. Three operating conditions are taken into consideration in the test period: excess temperature of 50°C, 60°C and 30°C. The measurements specified in the standard are notoriously difficult because of the number of limitations controlled simultaneously during tests. One test for a radiator was completed approximately in six hours in this study. All tests were completed in four days. Test duration can be longer when inexperienced test operators perform tests.

First computational study was investigation of correctness of solution obtained by selected commercial software for natural convection in cavity. Since numerical results obtained by using FLUENT software well match with results given in Literature, finite volume solver of FLUENT was accepted to use in the study. Since ICEPAK uses same solver with FLUENT, it was preferred for the determination of computational heat output of radiators.

It is evaluated that the quality of the numerical predictions depends on the accurate modeling of problems and fine grid structure. One of the important advantages of using ICEPAK is that the generation of CFD models and grids are relatively simpler in ICEPAK. Although automatic mesh generation is an advantage in ICEPAK, the skewness of elements in grid structure must be checked. Manual grid generation is always advised. In addition, using different under relaxation factors automatically in ICEPAK facilitates convergence. Properties of the problem given below complicate the solution with numerical methods:

- two fluid flows,
- large solution domain,
- difficulty of mesh generation for thin walls used in the radiator geometry,
- shell conduction,
- turbulent type of natural convection
- radiation
- changing wall temperature boundary condition for virtual test room
- not applying symmetric boundary conditions

It should be mentioned that three dimensional CFD models are computationally expensive than two dimensional models. As an example, the CFD model of a single panel radiator (radiator I) was prepared in two week. The solving time was nearly one week.

CFD model of single panel radiator with single extended surface (radiator II) and double panel with double extended surface (radiator III) prepared faster since CFD model of single panel radiator has existed.

Convergence of solutions in natural convection is generally difficult with regard to forced convection applications. In the solution of natural convection problems, oscillations and difficulties in convergence can be faced. In such situations, different strategies can be applied. One approach is using time marching approximation. In this study, the steady state solver is used. The velocity of air at some points near the tested radiator is controlled in addition to change in residuals and temperature of reference air during the analysis. When the constant reference air temperature is obtained and convergence criteria for residuals are realized, it is decided that the steady state solution is obtained. However computational runs are restarted several times with previous data file and terminate up to getting constant velocities. Therefore stopping criteria are reference air temperature, residuals and velocity near tested radiators.

Controlling reference air temperature with changing wall temperatures makes CFD analysis quite difficult. Since such control mechanism is not used in commercial CFD software. Wall temperatures are settled manually and this brings about loss of time and labor.

Unknown standard mass flow rate is another difficulty faced in virtual test room. Without having mass flow rate knowledge, the CFD analysis can also be made. Number of iterations to find the proper mass flow rate can increase the solution time.

From the steady state analyses performed for the tested radiators, relatively closer results are obtained for the simplest model (radiator I). However closeness of experimental and computational heat outputs is decreased with complexity of CFD model. In spite of using non real geometries for radiators, the deviation between experimental and computational results is maximum 13.6%. The difference between experimental and computational heat output in percentage fluctuate between 0.4 and 13.6 for the simplest model (radiator I), 3.4 and 11.1 for the second CFD model (radiator II), 4.5 and 12.9 for most complicated model investigated in this study. Quite good results are obtained for the excess temperature of 50°C and 60°C. For the lowest excess temperature, results are also in acceptable range.

The results indicate that determination of heat output by numerical methods is possible and reliable but not adequate. Especially the closeness of computational and experimental standard heat output of a radiator which is determined at the excess temperature of 50°C (Case 1) is attractive. However increment in difference between experimental and numerical heat output for Case 3 is found unsatisfying. The results also show that using simpler geometries in which rounds are ignored did not affect the heat output of radiators in CFD analysis.

Non uniform temperature distribution on the front surface of tested radiators was observed in the experimental study. Similar temperature distributions were also seen at the end of the computational study as given in Chapter 8. It is considered that the uniform cross sections of vertical channels in the radiator should be reassessed in the design of new radiators.

When temperature and velocity contours are examined throughout the test room. It is seen that velocity and temperature contours in the vertical plane where the temperature of reference point is measured will be symmetrical when the heater surface has constant or uniform temperature.

Almost symmetric velocity and temperature contours are also seen when single panel radiator is used in the virtual test room. Since non uniform temperature distribution occurs in the front and back surfaces of radiator, the symmetry in velocity contours is broken down by using more complicated radiators. Especially with increasing excess temperature difference, the structure of velocity contours is extremely changed.

According to findings in this study, it is evaluated that the numerical solution of this problem can be useful in design of new types of heaters in future works. However, long solving time is accepted as a serious problem for the real life.

It is thought that the difficulties sourced from the preparation of CFD model and mesh generation will not be seen in future, parallel to development in CFD software and computers specifications. Instead of measuring only reference air temperature, measurements of velocity and temperature from more points in the real test room are planned as a future study to compare the basic characteristics of flow in the enclosure. Determination of surface emissivity of test room will be useful in the future analysis. Controlling of temperature boundary conditions of test room panels with regard to change in reference point temperature can decrease the solving time in future analysis.

REFERENCES

- Ampofo F, Karayiannis TG. 2003. Experimental benchmark data for turbulent natural convection in an air filled square cavity. *International Journal of Heat and Mass Transfer* 46: 3551-3572.
- André B. Computational Fluid Dynamics Course Notes. Dartmouth College; [cited 2010 June 10]. Available from: <http://www.bakker.org/dartmouth06/engs150>.
- ANSYS FLUENT 12.0 User and Theory Guides, April 2009.
- Ashgriz N, Mostaghimi J. An Introduction to Computational Fluid Dynamics, Chapter 20, Fluid Flow Handbook, Department of Mechanical & Industrial Eng. University of Toronto.
- ASHRAE Systems and Equipment Handbook (SI). Hydronic Heat-Distributing Units and Radiators. 2000.
- Aydin O, Unal A, Ayhan T. 1999. Natural convection in rectangular enclosures heated from one side and cooled from the ceiling. *International Journal of Heat and Mass Transfer* 42: 2345-2355.
- Awbi HB. 1989. Application of Computational Fluid Dynamics in Room Ventilation. *Building and Environment*, 24(1),73-84.
- Balaji C , Venkateshan SP. 1993. Interaction of surface radiation with free convection in a square cavity. *Int. J. Heat and Fluid Flow* 14 (3): 260-267.
- Beck SMB, Grinsted SC, Blakey SG, Worden K. 2004. A novel design for panel radiators. *Applied Thermal Engineering* 24: 1291–1300.
- Bilir L. 2009. Numerical Optimization of a Finned Tube Gas to Liquid Heat Exchanger. PhD diss., Izmir Institute of Technology.
- Callister W. 1985. *Materials Science and Engineering An Introduction*. John Wiley & Sons.
- Cengel Y. 2006. *Heat and Mass Transfer A Practical Approach*, McGraw Hill, CRC PRESS.
- Chang YP, Tsai R. 1997. Natural Convection in a Square Enclosure with a Cold Surface. *Int. Comm. Heat and Mass Transfer*. 24 (7): 1019-1027.

- Dağsöz, AK. 1998. Sıcak Sulu Kalorifer Tesisatı, Demirdöküm Teknik Yayınları No:6.
- Davis V. 1968. Laminar Natural Convection in an Enclosed Rectangular Cavity. *Int.J. Heat Mass Transfer* 11:1675-1693.
- European Standard EN 442-2. 1997. Radiators and convectors- Part 2: Test methods and rating.
- Hyun J, Lee JW. 1989. Numerical solutions for transient natural convection in a square cavity with different sidewall temperatures. *Int. J. Heat and Fluid Flow.* 10 (2).
- Ganzarolli M, Milanez LF. 1995. Natural Convection in rectangular enclosures heated from below and symmetrically cooled from the sides. *Int. J Heat Mass Transfer.* 38 (6): 1063-1073.
- Gritzki R, Perschk A., Rösler M., Richter W. 2007. Modelling of Heating Systems and Radiator in Combined Simulations. *Proceedings of Clima 2007 WellBeing Indoors.*
- Kakac S, Shah RK, Aung W. 1997. *Handbook of Single –Phase Convective Heat Transfer.* John Wiley&Sons. Inc.
- Laser Doppler Anemometry [Internet]. Tampere University of Technology; [cited 2010 June 10]. Available from: <http://www.tut.fi/units/me/ener/laitteistot/EFD/LDA.html>.
- Markatos NC, Pericleous KA. 1984. Laminar and turbulent natural convection in an enclosed cavity. *International Journal of Heat and Mass Transfer.* 27(5): 755-772.
- Menter F. EUROPEAN COMMISSION. 2002. CFD Best Practice Guidelines for CFD Code Validation for Reactor Safety Applications, 5th EURATOM FRAMEWORK PROGRAMME 1998-2002.
- Modest, M.F. 2003. *Radiative Heat Transfer, Second Edition.* Academic Pres.
- Mohamad AA, Sicard J, Bennacer R. 2006. Natural convection in enclosures with floor cooling subjected to a heated vertical wall. *International Journal of Heat and Mass Transfer.* 49: 108-121
- Murakami S., Kato S. 1989. “Numerical and Experimental Study on Room Airflow-3D Predictions using the k-epsilon Turbulence Model.” *Building and Environment,* 24 (1): 85-97.

- November M, Nansteel MW. 1987 Natural convection in rectangular enclosures heated from below and cooled along one side, *International Journal of Heat and Mass Transfer*. 30: 2433-2440.
- Özişik MN. 1997. *Basic Heat Transfer*, Mc Graw Hill.
- Peach J. 1972. Radiators and other convectors, *J.I.H.V.E.* 39: 239-253.
- Peng SH, Davidson L. 1999. Computation of turbulent buoyant flows in enclosures with low-Reynolds-number $k-\omega$ models. *International Journal of Heat of Fluid Flow*. 20: 172-184.
- Radiator Connection [Internet]. ChestofBooks; [cited 2010 June 10]. Available from: <http://chestofbooks.com/homeimprovement/repairs/Mechanics-Household/Radiator-Connection.html>.
- Rundle CA, Lightstone MF. 2007. Validation of turbulent natural convection in a square cavity for application of CFD modeling to heat transfer and fluid flow in atria geometries; 2007 June 10–14; 2nd Canadian Solar Buildings Conference, Calgary.
- Tian YS, Karayiannis TG. 2000. Low turbulence natural convection in an air filled square cavity Part I: the thermal and fluid flow fields. *International Journal of Heat and Mass Transfer* 43: 849-866.
- Von Karman Institute. *Introduction to Computational Fluid Dynamic*. 2010.
- Ward IC. 1991. Domestic radiators: Performance at lower mass flow rates and lower temperature differentials than those specified in standard tests. *Building Serv. Eng. Res. Technol.* 12 (3): 84-87.
- Weizen L, Howarth AT. 1997. Prediction of air flow and temperature field in a room with convective heat source. *Building and Environment*, 32(6): 541-550.
- Leong WH. 1996. Benchmark Experiments on natural convection heat transfer across a cubical cavity. PhD diss., Waterloo, Ontario, Canada.
- Xu W, Chen Q, Nieuwstadt FTM. 1998. A new turbulence model for near-wall natural. *Int. J. Heat Transfer*. 41: 3161-3176.
- Xundan S, Khodadadi JM. 2003. Laminar Natural Convection Heat Transfer in a Differentially Heated Square Cavity Due to a Thin Fin on the Hot Wall. *Journal of Heat Transfer*, 125.

Zitzmann Y, Cook M, Pfrommer P, Rees S, Marjanovic L. 2005. "Simulation of steady state natural convection using CFD." Ninth International IBPSA Conference; 2005 August 15-18; Montreal, Canada.

APPENDIX A

TABLES FROM EN 442 STANDARD

Table A.1. S_k , n_p values for different radiator types.

Radiator Type	Radiated Heat Output Factor (S_k)	Exponent n_p Height of the Radiator	
		<400 mm	\geq 400 mm
Sectional Radiator Vertical			
	Depth $b \leq 110$ mm	0.30	0.40
	Depth $b \geq 110$ mm	0.25	0.45
Sectional Radiator Horizontal			
	Depth $b \leq 110$ mm	0.27	0.36
	Depth $b \geq 110$ mm	0.25	0.40
Sectional Radiator Front Closed	0.25	0.55	0.65
Deep Profile Panel Radiators	0.25	0.55	0.70
Pipe Grill Radiators	0.20	0.65	0.75
Panel Radiators Without Convectors	0.50	0.40	0.50
Panel Radiators with 1 Convector			
	Pitch of the Fins $b \leq 25$ mm	0.35	0.60
	Pitch of the Fins $b > 25$ mm	0.35	0.55
Panel Radiators with 2 Convectors			
	Pitch of the Fins $b \leq 25$ mm	0.25	0.65
	Pitch of the Fins $b > 25$ mm	0.25	0.55
2 Panel Radiators Without Convectors	0.35	0.60	0.75
2 Panel Radiators With 1 Convector or with 2 convectors between the panels			
	Pitch of the Fins $b \leq 25$ mm	0.20	0.60
	Pitch of the Fins $b > 25$ mm	0.20	0.55
2 Panel Radiators With 3 Convector or with 2 convectors behind each panel			
	Pitch of the Fins $b \leq 25$ mm	0.15	0.60
	Pitch of the Fins $b > 25$ mm	0.15	0.55
3 Panel and Radiators and Multi Panel Radiators without Convectors	0.20	0.40	0.55
3 Panel and Radiators and Multi Panel Radiators with 1 Convector			
	Pitch of the Fins $b \leq 25$ mm	0.15	0.55
	Pitch of the Fins $b > 25$ mm	0.15	0.50
3 Panel and Radiators and Multi Panel Radiators with more than 1 Convector			
	Pitch of the Fins $b \leq 25$ mm	0.10	0.65
	Pitch of the Fins $b > 25$ mm	0.10	0.60

APPENDIX B

MEASURED DATA

Table B.1. Collected data in the first test of radiator I (Case 1).

No	Flow Rate (kg/s)	Reference Temp (°C)	Radiator Inlet Temp (°C)	Radiator Outlet Temp (°C)	Mean Temp. (°C)	Excess Temp (°C)
1	0.01730	19.86	75.21	65.04	70.13	50.27
2	0.01733	19.89	75.21	65.06	70.14	50.25
3	0.01740	19.89	75.23	65.10	70.17	50.28
4	0.01733	19.92	75.22	65.11	70.17	50.25
5	0.01737	19.94	75.21	65.12	70.17	50.23
6	0.01742	19.97	75.22	65.12	70.17	50.20
7	0.01743	19.99	75.23	65.13	70.18	50.19
8	0.01745	19.98	75.23	65.14	70.19	50.21
9	0.01740	19.98	75.22	65.13	70.18	50.20
10	0.01738	19.97	75.24	65.13	70.19	50.22
11	0.01735	19.96	75.23	65.10	70.17	50.21
12	0.01732	19.94	75.23	65.09	70.16	50.22

Table B.2. Collected data in the second test of radiator I (Case 2).

No	Flow Rate (kg/s)	Reference Temp (°C)	Radiator Inlet Temp (°C)	Radiator Outlet Temp (°C)	Mean Temp. (°C)	Excess Temp (°C)
1	0.01738	20.09	86.55	74.19	80.37	60.28
2	0.01742	20.06	86.55	74.19	80.37	60.31
3	0.01743	20.06	86.56	74.16	80.36	60.30
4	0.01743	20.07	86.53	74.20	80.37	60.30
5	0.01737	20.09	86.54	74.20	80.37	60.28
6	0.01743	20.08	86.51	74.22	80.37	60.29
7	0.01747	20.09	86.55	74.18	80.37	60.28
8	0.01742	20.10	86.59	74.19	80.39	60.29
9	0.01743	20.05	86.61	74.20	80.41	60.36
10	0.01742	20.07	86.55	74.23	80.39	60.32
11	0.01740	20.02	86.51	74.26	80.39	60.37
12	0.01738	20.05	86.54	74.27	80.41	60.36

Table B.3. Collected data in the third test of radiator I (Case 3).

No	Flow Rate (kg/s)	Reference Air Temp (°C)	Inlet Temp (°C)	Outlet Temp (°C)	Mean Temp. (°C)	Excess Temp (°C)
1	0.01747	19.78	52.48	47.75	50.12	30.34
2	0.01745	19.79	52.46	47.72	50.09	30.30
3	0.01738	19.79	52.48	47.70	50.09	30.30
4	0.01742	19.81	52.51	47.70	50.11	30.30
5	0.01745	19.80	52.50	47.70	50.10	30.30
6	0.01745	19.84	52.47	47.71	50.09	30.25
7	0.01742	19.85	52.46	47.72	50.09	30.24
8	0.01742	19.86	52.50	47.73	50.12	30.26
9	0.01728	19.75	52.42	47.67	50.05	30.30
10	0.01730	19.75	52.52	47.75	50.14	30.39
11	0.01730	19.75	52.49	47.75	50.12	30.37
12	0.01728	19.75	52.46	47.72	50.09	30.34

Table B.4. Collected data in the first test of radiator II (Case 1).

No	Flow Rate (kg/s)	Reference Temp (°C)	Radiator Inlet Temp (°C)	Radiator Outlet Temp (°C)	Mean Temp. (°C)	Excess Temp (°C)
1	0.02295	19.92	74.83	64.71	69.77	49.85
2	0.02285	19.93	74.80	64.73	69.77	49.84
3	0.02285	19.98	74.76	64.71	69.74	49.76
4	0.02287	19.99	74.85	64.68	69.77	49.78
5	0.02292	19.99	74.86	64.67	69.77	49.78
6	0.02283	19.97	74.83	64.73	69.78	49.81
7	0.02283	19.97	74.79	64.75	69.77	49.80
8	0.02288	19.97	74.76	64.73	69.75	49.78
9	0.02293	19.96	74.78	64.70	69.74	49.78
10	0.02287	19.95	74.80	64.68	69.74	49.79
11	0.02295	19.94	74.80	64.69	69.75	49.81
12	0.02293	19.94	74.78	64.68	69.73	49.79

Table B.5. Collected data in the second test of radiator II (Case 2).

No	Flow Rate (kg/s)	Reference Temp (°C)	Radiator Inlet Temp (°C)	Radiator Outlet Temp (°C)	Mean Temp. (°C)	Excess Temp (°C)
1	0.02282	19.91	86.12	73.52	79.82	59.91
2	0.02280	19.90	86.18	73.48	79.83	59.93
3	0.02280	19.88	86.22	73.47	79.85	59.97
4	0.02275	19.86	86.14	73.52	79.83	59.97
5	0.02277	19.83	86.11	73.50	79.81	59.98
6	0.02278	19.83	86.16	73.49	79.83	60.00
7	0.02270	19.83	86.18	73.46	79.82	59.99
8	0.02272	19.83	86.14	73.48	79.81	59.98
9	0.02283	19.82	86.14	73.50	79.82	60.00
10	0.02277	19.80	86.15	73.50	79.83	60.03
11	0.02278	19.81	86.12	73.49	79.81	60.00
12	0.02278	19.81	86.20	73.51	79.86	60.05

Table B.6. Collected data in the third test of radiator II (Case 3).

No	Flow Rate (kg/s)	Reference Temp (°C)	Radiator Inlet Temp (°C)	Radiator Outlet Temp (°C)	Mean Temp. (°C)	Excess Temp (°C)
1	0.02293	20.11	52.70	47.55	50.13	30.02
2	0.02288	20.11	52.70	47.59	50.15	30.04
3	0.02287	20.12	52.71	47.60	50.16	30.04
4	0.02287	20.12	52.71	47.60	50.16	30.04
5	0.02293	20.12	52.71	47.60	50.16	30.04
6	0.02285	20.13	52.70	47.61	50.16	30.03
7	0.02288	20.12	52.70	47.59	50.15	30.03
8	0.02282	20.11	52.70	47.57	50.14	30.03
9	0.02287	20.13	52.71	47.59	50.15	30.02
10	0.02287	20.10	52.70	47.56	50.13	30.03
11	0.02285	20.09	52.70	47.56	50.13	30.04
12	0.02285	20.06	52.70	47.55	50.13	30.07

Table B.7. Collected data in the first test of radiator III (Case 1).

No	Flow Rate (kg/s)	Reference Temp (°C)	Radiator Inlet Temp (°C)	Radiator Outlet Temp (°C)	Mean Temp. (°C)	Excess Temp (°C)
1	0.04295	19.89	75.39	64.81	70.10	50.21
2	0.04285	19.94	75.44	64.88	70.16	50.22
3	0.04283	19.97	75.47	64.83	70.15	50.18
4	0.04298	19.98	75.41	64.85	70.13	50.15
5	0.04278	19.98	75.38	64.86	70.12	50.14
6	0.04288	19.97	75.42	64.84	70.13	50.16
7	0.04285	19.99	75.40	64.85	70.13	50.14
8	0.04292	19.99	75.43	64.82	70.13	50.14
9	0.04283	19.98	75.37	64.81	70.09	50.11
10	0.04300	19.97	75.42	64.86	70.14	50.17
11	0.04300	19.97	75.43	64.88	70.16	50.19
12	0.04295	19.97	75.38	64.91	70.15	50.18

Table B.8. Collected data in the second test of radiator III (Case 2).

No	Flow Rate (kg/s)	Reference Temp (°C)	Radiator Inlet Temp (°C)	Radiator Outlet Temp (°C)	Mean Temp. (°C)	Excess Temp (°C)
1	0.04307	20.32	86.93	74.67	80.80	60.48
2	0.04303	20.33	86.96	74.66	80.81	60.48
3	0.04313	20.34	86.96	74.66	80.81	60.47
4	0.04313	20.35	86.95	74.71	80.83	60.48
5	0.04303	20.42	86.94	74.73	80.84	60.42
6	0.04305	20.44	86.93	74.74	80.84	60.40
7	0.04270	20.40	87.00	74.75	80.88	60.48
8	0.04280	20.43	86.94	74.72	80.83	60.40
9	0.04315	20.44	86.98	74.68	80.83	60.39
10	0.04295	20.39	87.02	74.73	80.88	60.49
11	0.04300	20.38	87.04	74.72	80.88	60.50
12	0.04300	20.37	87.02	74.75	80.89	60.52

Table B.9. Collected data in the third test of radiator III (Case 3).

No	Flow Rate (kg/s)	Reference Temp (°C)	Radiator Inlet Temp (°C)	Radiator Outlet Temp (°C)	Mean Temp. (°C)	Excess Temp (°C)
25	0.04313	20.24	53.24	48.33	50.79	30.55
26	0.04292	20.26	53.15	48.25	50.70	30.44
27	0.04312	20.26	53.25	48.35	50.80	30.54
28	0.04302	20.21	53.18	48.26	50.72	30.51
29	0.04295	20.22	53.15	48.28	50.72	30.50
30	0.04308	20.27	53.22	48.26	50.74	30.47
31	0.04313	20.26	53.21	48.28	50.75	30.49
32	0.04303	20.24	53.23	48.29	50.76	30.52
33	0.04313	20.24	53.25	48.31	50.78	30.54
34	0.04312	20.25	53.23	48.35	50.79	30.54
35	0.04307	20.25	53.20	48.36	50.78	30.53
36	0.04302	20.25	53.22	48.34	50.78	30.53

Table B.10. Experimental heat outputs for the first test data of radiator I (Case 1).

No	Flow rate (kg/s)	Specific heat (J/kg/K)	ΔT (K)	Q_{exp} (W)
1	0.01730	4 190.08	10.17	737.21
2	0.01733	4 190.08	10.15	737.03
3	0.01740	4 190.10	10.13	738.56
4	0.01733	4 190.10	10.11	734.13
5	0.01737	4 190.10	10.09	734.37
6	0.01742	4 190.10	10.10	737.21
7	0.01743	4 190.11	10.10	737.64
8	0.01745	4 190.11	10.09	737.76
9	0.01740	4 190.11	10.09	735.64
10	0.01738	4 190.11	10.11	736.25
11	0.01735	4 190.10	10.13	736.43
12	0.01732	4 190.10	10.14	735.88

Table B.11. Experimental heat outputs for the second test data of radiator I (Case 2).

No	Flow rate (kg/s)	Specific heat (J(kg/K))	ΔT (K)	Q_{exp} (W)
1	0.01738	4 197.30	12.36	901.65
2	0.01742	4 197.30	12.36	903.72
3	0.01743	4 197.29	12.40	907.17
4	0.01743	4 197.30	12.33	902.05
5	0.01737	4 197.30	12.34	899.67
6	0.01743	4 197.30	12.29	899.12
7	0.01747	4 197.30	12.37	907.05
8	0.01742	4 197.31	12.40	906.65
9	0.01743	4 197.33	12.41	907.91
10	0.01742	4 197.31	12.32	900.80
11	0.01740	4 197.31	12.25	894.66
12	0.01738	4 197.33	12.27	895.09

Table B.12. Experimental heat outputs for the third test data of radiator I (Case 3).

No	Flow rate (kg/s)	Specific heat (J(kg/K))	ΔT (K)	Q_{exp} (W)
1	0.01747	4 181.05	4.73	345.49
2	0.01745	4 181.04	4.74	345.83
3	0.01738	4 181.04	4.78	347.35
4	0.01742	4 181.04	4.81	350.33
5	0.01745	4 181.04	4.80	350.20
6	0.01745	4 181.04	4.76	347.29
7	0.01742	4 181.04	4.74	345.23
8	0.01742	4 181.05	4.77	347.42
9	0.01728	4 181.02	4.75	343.18
10	0.01730	4 181.06	4.77	345.02
11	0.01730	4 181.05	4.74	342.85
12	0.01728	4 181.04	4.74	342.46

Table B.13. Experimental heat outputs for the first test of radiator II (Case 1).

No	Flow rate (kg/s)	Specific heat (J/kg/K)	ΔT (K)	Q_{exp} (W)
1	0.02295	4 189.86	10.12	973.11
2	0.02285	4 189.86	10.07	964.09
3	0.02285	4 189.84	10.05	962.17
4	0.02287	4 189.86	10.17	974.51
5	0.02292	4 189.86	10.19	978.56
6	0.02283	4 189.87	10.1	966.11
7	0.02283	4 189.86	10.04	960.37
8	0.02288	4 189.85	10.03	961.51
9	0.02293	4 189.84	10.08	968.42
10	0.02287	4 189.84	10.12	969.72
11	0.02295	4 189.85	10.11	972.15
12	0.02293	4 189.84	10.1	970.34

Table B.14. Experimental heat outputs for the second test of radiator II (Case 2).

	Flow rate (kg/s)	Specific heat (J/kg/K)	ΔT (K)	Q_{exp} (W)
1	0.02282	4 196.86	12.6	1 206.73
2	0.0228	4 196.86	12.7	1 215.24
3	0.0228	4 196.88	12.75	1 220.03
4	0.02275	4 196.86	12.62	1 204.94
5	0.02277	4 196.85	12.61	1 205.04
6	0.02278	4 196.86	12.67	1 211.31
7	0.0227	4 196.86	12.72	1 211.82
8	0.02272	4 196.85	12.66	1 207.16
9	0.02283	4 196.86	12.64	1 211.09
10	0.02277	4 196.86	12.65	1 208.87
11	0.02278	4 196.85	12.63	1 207.48
12	0.02278	4 196.89	12.69	1 213.23

Table B.15. Experimental heat outputs for the third test of radiator II (Case 3).

	Flow rate (kg/s)	Specific heat (J(kg/K))	ΔT (K)	Q_{exp} (W)
1	0.02293	4 181.05	5.15	493.74
2	0.02288	4 181.06	5.11	488.84
3	0.02287	4 181.06	5.11	488.62
4	0.02287	4 181.06	5.11	488.62
5	0.02293	4 181.06	5.11	489.90
6	0.02285	4 181.06	5.09	486.28
7	0.02288	4 181.06	5.11	488.84
8	0.02282	4 181.06	5.13	489.46
9	0.02287	4 181.06	5.12	489.58
10	0.02287	4 181.05	5.14	491.49
11	0.02285	4 181.05	5.14	491.06
12	0.02285	4 181.05	5.15	492.02

Table B.16. Experimental heat outputs for the third test of radiator III (Case 1).

	Flow rate (kg/s)	Specific heat (J(kg/K))	ΔT (K)	Q_{exp} (W)
1	0.04295	4190.06	10.58	1904.01
2	0.04285	4190.10	10.56	1896.00
3	0.04283	4190.09	10.64	1909.47
4	0.04298	4190.08	10.56	1901.75
5	0.04278	4190.07	10.52	1885.72
6	0.04288	4190.08	10.58	1900.91
7	0.04285	4190.08	10.55	1894.20
8	0.04292	4190.08	10.61	1908.08
9	0.04283	4190.05	10.56	1895.10
10	0.043	4190.08	10.56	1902.63
11	0.043	4190.10	10.55	1900.84
12	0.04295	4190.09	10.47	1884.23

Table B.17. Experimental heat outputs for the second test of radiator III (Case 2).

	Flow rate (kg/s)	Specific heat (J(kg/K))	ΔT (K)	Q_{exp} (W)
1	0.04307	4 197.64	12.26	2216.51
2	0.04303	4 197.65	12.3	2221.68
3	0.04313	4 197.65	12.3	2226.85
4	0.04313	4 197.66	12.24	2215.99
5	0.04303	4 197.67	12.21	2205.44
6	0.04305	4 197.67	12.19	2202.85
7	0.0427	4 197.70	12.25	2195.71
8	0.0428	4 197.66	12.22	2195.45
9	0.04315	4 197.66	12.3	2227.89
10	0.04295	4 197.70	12.29	2215.78
11	0.043	4 197.70	12.32	2223.78
12	0.043	4 197.71	12.27	2214.75

Table B.18. Experimental heat outputs for the third test of radiator III (Case 3).

	Flow rate (kg/s)	Specific heat (J(kg/K))	ΔT (K)	Q_{exp} (W)
1	0.04313	4 181.16	4.91	885.44
2	0.04292	4 181.14	4.9	879.33
3	0.04312	4 181.16	4.9	883.43
4	0.04302	4 181.14	4.92	884.97
5	0.04295	4 181.14	4.87	874.56
6	0.04308	4 181.15	4.96	893.41
7	0.04313	4 181.15	4.93	889.04
8	0.04303	4 181.15	4.94	888.78
9	0.04313	4 181.16	4.94	890.85
10	0.04312	4 181.16	4.88	879.82
11	0.04307	4 181.16	4.84	871.60
12	0.04302	4 181.16	4.88	877.78

APPENDIX C

ADDITIONAL CODE USED IN FLUENT

```
#include "udf.h"

DEFINE_PROFILE(top_wall_temp, thread, position)
{
    real x[ND_ND];      /* this will hold the position vector */
    real a;
    face_t f;

    begin_f_loop(f, thread)
    {
        F_CENTROID(x,f,thread);
        a = x[0];
        F_PROFILE(f, thread, position) = -1243.5*pow(a,5)+2140.8*pow(a,4)-1494.7*pow(a,3)+520.91*pow(a,2)-107.73*a+321.63;
    }
    end_f_loop(f, thread)
}

#include "udf.h"

DEFINE_PROFILE(bottom_wall_temp, thread, position)
{
    real x[ND_ND];      /* this will hold the position vector */
    real a;
    face_t f;

    begin_f_loop(f, thread)
    {
        F_CENTROID(x,f,thread);
        a = x[0];
        F_PROFILE(f, thread, position) = -1371.6*pow(a,5)+2817.3*pow(a,4)-2296.2*pow(a,3)+930.16*pow(a,2)-210.92*a+321.03;
    }
    end_f_loop(f, thread)
}
```

Figure B.1. User defined function utilized to assign predefined temperature profiles to horizontal walls of two dimensional cavity investigated in Chapter 6.

VITA

PERSONAL INFORMATION

Surname, Name: ERDOĞMUŞ, Abdullah Berkan
Nationality: Turkish (TC)
Date and Place of Birth: 07.07.1975, Bornova-Izmir
E-mail: berkanerdogmus@gmail.com

EDUCATION

Degree	Institution	Year of Graduation
MS	İzmir Institute of Technology	2003
BS	Dokuz Eylül University	1999

WORK EXPERIENCE

Year	Place	Enrollment
September 2007 – Present	Aselsan Inc., Ankara	R&D Engineer
December 2000 – September 2007	Izmir Institute of Technology	Research Assistant
September 1999 - June 2000	Yates Inc., Izmir	Project Engineer
1998	BMC, Izmir	Trainee
1997	Akdöküm, Izmir	Trainee

FOREIGN LANGUAGES

English (Advanced), German (Beginner)

PUBLICATIONS

Erdogmus, A. B., Ozerdem, B., Ilken, Z., The Determination of Characteristic Equation and Heat Output of a Single Panel Radiator, 01-03 December 2010. 41st International HVAC Congress. Belgrade, Serbia (Oral Presentation), Presented by Ozerdem B.

Erdogmus, A. B., Sahin M., Colakoglu A., Erentürk, B., The Improvement of Cooling Performance of a Flash Pumped Laser Using: Nd:Yag, The ASME 2010 10th Biennial Conference on Engineering Systems Design and Analysis (ESDA 2010), 12-14 July 2010, Yeditepe University, Istanbul/Turkiye (Oral Presentation)

Ocak M., **Erdogmuş B.**, Çolakoğlu A., Platform Instrumentation on Flight Tests (in Turkish), 1. Aviyonik Sistem Enstrümantasyon Sempozyumu (ASES 2010), 28-30 Nisan 2010, Hava Harp Okulu, Istanbul/ Turkey (Oral Presentation), Presented by Ocak M.

Erdogmus, B. , Toksoy, M. , Ozerdem, B. , Aksoy, N., Economic assessment of geothermal district heating systems: A case study of Balçova-Narlıdere, Turkey, Energy and Buildings, Volume 38, Issue 9, Page 1053-1059